AUBURN UNIVERSITY
Samuel Ginn College of Engineering

Research Report

CHARACTERIZATION OF CONCRETE CREEP AND SHRINKAGE OF THE BIRMINGHAM I-59/I-20 SEGMENTAL BRIDGE

Submitted to

The Alabama Department of Transportation

Prepared by

Paul S. Beauchamp
Grant M. Cooper
Anton K. Schindler
Robert W. Barnes

DECEMBER 2023

Highway Research Center
Harbert Engineering Center
Auburn, Alabama 36849

1. Report No. 930-989	**2. Government Accession No.**	**3. Recipient Catalog No.**
4. Title and Subtitle Characterization of Concrete Creep and Shrinkage of the Birmingham I-59/I-20 Segmental Bridge		**5. Report Date** December 2023 **6. Performing Organization Code**
7. Author(s) Paul S. Beauchamp, Grant M. Cooper, Anton K. Schindler, and Robert W. Barnes		**8. Performing Organization Report No.** 930-989
9. Performing Organization Name and Address Highway Research Center Department of Civil Engineering 238 Harbert Engineering Center Auburn, AL 36849		**10. Work Unit No. (TRAIS)** **11. Contract or Grant No.**
12. Sponsoring Agency Name and Address Alabama Department of Transportation 1409 Coliseum Boulevard Montgomery, Alabama 36130-3050		**13. Type of Report and Period Covered** **14. Sponsoring Agency Code**

15. Supplementary Notes
Project performed in cooperation with the Alabama Department of Transportation.

16. Abstract

The objective of this study is to accurately predict the creep and shrinkage behavior of concrete in the I-59/I-20 segmental bridge located in downtown Birmingham, Alabama. Concrete samples were collected on four sampling dates throughout the bridge's construction for creep and shrinkage testing. Concrete specimens were loaded at 7, 28, 91, and 182 days for creep testing. Shrinkage testing began for concrete specimens as soon as specimens were exposed to drying after initial curing. All concrete specimens were cured using increased temperatures for the first 24 hours after casting. Creep and shrinkage measurements were collected at set time intervals over five years. To accurately predict creep and shrinkage, eight commonly used models were evaluated during this project: AASHTO LRFD, ACI 209, B3, B4, CEB MC 1990, CEB MC 90-99, CEB MC 2010, and GL 2000. A statistical analysis was performed to compare each model to the measured data, and it is concluded that the CEB MC 90-99 model most accurately predicts the measured creep and shrinkage. Calibration to improve prediction was performed on the CEB MC 90-99 model, as well as the CEB MC 1990 model because it is commonly used in bridge design software. It is recommended to use the calibrated CEB MC 90-99 model to predict the creep and shrinkage of the concrete cast in segments of the Birmingham I-59/I-20 segmental bridge.

17. Key Words Compliance, prediction, compressive strength, elastic modulus, shrinkage strain, laboratory testing		**18. Distribution Statement** No restrictions.	
19. Security Classification (of this report) Unclassified	**20. Security Classification (of this page)** Unclassified	**21. No. of Pages** 313	**22. Price** None.

Research Report

CHARACTERIZATION OF CONCRETE CREEP AND SHRINKAGE OF THE BIRMINGHAM I-59/I-20 SEGMENTAL BRIDGE

Submitted to

The Alabama Department of Transportation

Prepared by

Paul S. Beauchamp
Grant M. Cooper
Anton K. Schindler
Robert W. Barnes

DECEMBER 2023

DISCLAIMERS

The contents of this report reflect the views of the authors who are responsible for the facts and accuracy of the data presented herein. The contents do not necessarily reflect the official views or policies of Alabama DOT, Auburn University, or the Highway Research Center. This report does not constitute a standard, specification, or regulation. Comments contained in this paper related to specific testing equipment and materials should not be considered an endorsement of any commercial product or service; no such endorsement is intended or implied.

NOT INTENDED FOR CONSTRUCTION, BIDDING, OR PERMIT PURPOSES

Anton K. Schindler, Ph.D., P.E.
Robert W. Barnes, Ph.D., P.E.
Research Supervisors

ACKNOWLEDGEMENTS

Material contained herein was obtained in connection with a research project “Characterization of Concrete Creep and Shrinkage of the Birmingham I-59/I-20 Segmental Bridge,” ALDOT Project 930-989, conducted by the Auburn University Highway Research Center. Funding for the project was provided by the Alabama Department of Transportation (ALDOT). The funding, cooperation, and assistance of many individuals from each of these organizations are gratefully acknowledged. The authors particularly acknowledge the contributions of the following individuals:

Tim Colquett	ALDOT, State Bridge Engineer
Berhanu Woldemichael	ALDOT, Bridge Bureau
DeJarvis Leonard	ALDOT, East Central Region Engineer
Kidada Dixon	ALDOT, State Research and Development Engineer
Gary Smith	ALDOT, East Central Region
Stacey Glass	ALDOT, Construction Bureau
Eric Johnson	Corven Engineering, Bridge Designer
Adam Patterson	Volkert Engineering, Project Manager
Lloyd Pitts	Volkert Engineering, Vice President

ABSTRACT

The objective of this study is to accurately predict the creep and shrinkage behavior of concrete in the I-59/I-20 segmental bridge located in downtown Birmingham, Alabama. Concrete samples were collected on four sampling dates throughout the bridge's construction for creep and shrinkage testing. Concrete specimens were loaded at 7, 28, 91, and 182 days for creep testing. Shrinkage testing began for concrete specimens as soon as specimens were exposed to drying after initial curing. All concrete specimens were cured using increased temperatures for the first 24 hours after casting. Creep and shrinkage measurements were collected at set time intervals over five years. To accurately predict creep and shrinkage, eight commonly used models were evaluated during this project: AASHTO LRFD, ACI 209, B3, B4, CEB MC 1990, CEB MC 90-99, CEB MC 2010, and GL 2000. A statistical analysis was performed to compare each model to the measured data, and it is concluded that the CEB MC 90-99 model most accurately predicts the measured creep and shrinkage. Calibration to improve prediction was performed on the CEB MC 90-99 model, as well as the CEB MC 1990 model because it is commonly used in bridge design software. It is recommended to use the calibrated CEB MC 90-99 model to predict the creep and shrinkage of the concrete cast in segments of the Birmingham I-59/I-20 segmental bridge.

TABLE OF CONTENTS

LIST OF TABLES

LIST OF FIGURES

Chapter 1

INTRODUCTION

1.1 PROJECT BACKGROUND

Due to the prevalence of prestressed and post-tensioned segmental bridge construction in concrete bridge design, it is important to understand and quantify the concrete behavior, including volumetric changes. These volumetric changes, which include elastic deformation, creep, and shrinkage have been studied by many researchers to gain a better understanding of how different concrete properties and mixtures affect them. This research project was conducted to add further knowledge of the quantities of creep and shrinkage of concrete in segmental bridge applications, specifically for the Alabama Department of Transportation (ALDOT). During 2018 and 2019, the I-59/I-20 interchange in Birmingham, Alabama was replaced by ALDOT to better meet the traffic needs of the area. This replacement included a precast segmental bridge, portions of which are shown in Figure 1-1 and Figure 1-2. The bridge contains over one million square feet of deck area and is comprised of 2316 typical precast segments across the entire bridge with the longest span reaching 165 feet. The volumetric changes associated with this segmental bridge are the primary topics investigated in this research project.

Figure 1-1: Birmingham I-59/I-20 segmental bridge during construction

Figure 1-2: Birmingham I-59/I-20 segmental bridge during construction

1.2 RESEARCH OBJECTIVES

The main goal of this study is to accurately characterize the creep and shrinkage of the concrete used in the I-59/I-20 segmental bridge in Birmingham, Alabama. A more detailed list of objectives is listed below:

- Quantify the creep and shrinkage behavior of concrete sampled from the I-59/I-20 bridge through testing.
- Predict the creep and shrinkage of the concrete samples tested during this project using the eight prediction models listed below:
    - AASHTO LRFD (2020),
    - ACI 209 (2008),
    - B3 (Bazant and Baweja 2000),
    - B4 (Bazant 2015),
    - CEB MC 1990 (CEB 1990),
    - CEB MC 90-99 (CEB 1999),
    - CEB MC 2010 (fib 2012), and
    - GL 2000 (Gardner and Lockman 2001).

- Identify the most accurate prediction model based on test data of the samples from the segmental bridge.
- Calibrate the most accurate model for predicting creep and shrinkage to best represent the long-term volumetric changes that may occur in the I-59/I-20 segmental bridge.

1.3 RESEARCH SCOPE

For the purposes of this research, creep and shrinkage were measured for four different concrete mixture proportions collected from the jobsite during construction of the Birmingham I-59/I-20 segmental bridge between February 21, 2018, and August 9, 2019. The four collection dates for these samples were April 10, 2018, July 9, 2018, November 19, 2018, and April 16, 2019. Prior to transport to the laboratory at Auburn University, all specimens were subjected to the same elevated curing regime at the casting yard as the bridge segments. This ensured that they were the best possible representation of the concrete used in the segments of the I-59/I-20 segmental bridge.

For creep testing, loading ages of 7 days, 28 days, 91 days, and 182 days were studied for each of the sampling dates above. All creep specimens were loaded to 40 percent of their ultimate compressive strength, which was determined immediately prior to loading. Total strains of the creep specimens were measured at specified time intervals, and shrinkage strains were measured at similar intervals by recording the deformations of unloaded concrete specimens subjected to drying. Creep strains were determined by subtracting elastic and shrinkage strains from the total strains. All measured data were compared to the eight prediction models listed in Section 1.2, and a statistical analysis was performed to evaluate each model's accuracy and determine which model could be most effectively calibrated to accurately predict creep and shrinkage in the I-59/I-20 segmental bridge.

1.4 REPORT ORGANIZATION

Chapter 2 of this report provides an overview of the volumetric changes in concrete, including their mechanisms and contributing factors. The effects of these volumetric changes in segmental bridge construction are also covered. A definition of each creep and shrinkage prediction model with the corresponding equations is provided in Chapter 3, as well as a review of literature from previous studies related to the prediction of creep and shrinkage. The experimental plan and procedures used for this research are provided in Chapter 4. The segmental bridge casting process and construction practices used in the Birmingham I-59/I-20 segmental bridge project are detailed in Chapter 5. The results from all testing performed in this study are presented in Chapter 6. These results include those from creep and shrinkage testing, as well as all fresh and

hardened concrete properties tested throughout this project. Chapter 7 presents all results from the modeling of creep and shrinkage based on the prediction models, and Chapter 8 covers the statistical comparison of the accuracy of these models. The most accurate creep and shrinkage prediction model is identified in Chapter 8. Chapter 9 presents the calibration of the most accurate model. Conclusions from this project and recommendations for continued research related to it are then discussed in Chapter 10. All testing data and a full breakdown of the results are presented in Appendices A and B, respectively. The casting and erection dates for all segments used in the I-59/I-20 segmental bridge in Birmingham, Alabama are tabulated in Appendix C.

Chapter 2

LITERATURE REVIEW

2.1 INTRODUCTION

This research studies the effects of creep and shrinkage in segmental bridge applications. In order to understand the experimental results in this expansive topic, it is important to first understand the types of volumetric changes that occur in concrete and how they impact segmental bridge construction and performance. This chapter uses literature from previous studies to detail the volumetric changes associated with a loaded concrete specimen, including the mechanisms involved, and significant factors, that affect them. It also discusses the construction methods of segmental bridges and how concrete volumetric changes affect long-term segmental bridge performance.

2.2 VOLUMETRIC CHANGES IN CONCRETE

In a standard concrete specimen under load, there are three main categories of volumetric changes: elastic strain, shrinkage strain, and creep strain. The latter two changes are time dependent. Elastic strains in concrete occur instantaneously upon loading, while creep and shrinkage strains gradually develop over time. Shrinkage strains can be divided into two main mechanisms: drying shrinkage and autogenous shrinkage (Mehta and Monteiro 2014). Creep strains are the sum of basic creep and drying creep; however, Mehta and Monteiro (2014) state, "it is a common practice to ignore the distinction between the basic and the drying creep, and creep is simply considered as the deformation under load in excess of the sum of the elastic strain and free drying shrinkage strain."

2.2.1 Elastic Volumetric Changes

Mehta and Monteiro (2014) state, "The elastic characteristics of a material are a measure of its stiffness." Because concrete is a composite material with poor tensile strength, its stress-strain relationship is nonlinear, so these properties can be difficult to quantify precisely. However, assuming a proportional limit, an estimate may be made of the modulus of elasticity, which is defined as the applied stress divided by the instantaneous strain in the concrete (Mehta and Monteiro 2014). This value can be either measured according to standards such as ASTM C469 (2014), or estimated using prediction equations, some of which are defined in Chapter 3. While concrete behaves like a nonlinear material as high stress levels are approached, these linear estimates provide sufficiently accurate values below 50 percent of the ultimate stress and only

slightly less accurate values between 50 and 75 percent of the ultimate stress. Above 75 percent, the cracks in the system, which initiate in the interfacial transition zone, have typically propagated to the point of continuity causing the stress-strain relationship to be much more significantly nonlinear (Mehta and Monteiro 2014).

Because it is not a homogeneous material, the modulus of elasticity is affected by the stiffnesses of the concrete's individual components, among other factors. The most important factor determining the elastic modulus of the aggregate phase is its porosity (Mehta and Monteiro 2014). In general, dense or low-porosity aggregates are stiffer; therefore, there is a direct relationship between the amount of dense aggregate in concrete and the concrete's modulus of elasticity. The shape, size, grading, and minerology also play a role in the stiffness of the aggregates (Mehta and Monteiro 2014). Similar to aggregates, the modulus of elasticity of the cement paste matrix is almost entirely affected by its porosity. The factors involved in determining the porosity of the cement past matrix are the water-cement ratio, chemical admixtures, degree of hydration, and air content. For normal weight aggregates, the elastic modulus of the cement paste matrix is generally lower than that of the coarse aggregates (Mehta and Monteiro 2014). The stiffnesses of the aggregates and cement paste relative to the concrete are shown in Figure 2-1. The interfacial transition zone can also affect the concrete's modulus of elasticity due to capillary voids, microcracks, and the orientation of calcium hydroxide. Mehta and Monteiro (2014) also found that when concrete specimens are tested in wet conditions, the modulus of elasticity increases by around 15 percent compared to the same specimens in dry conditions.

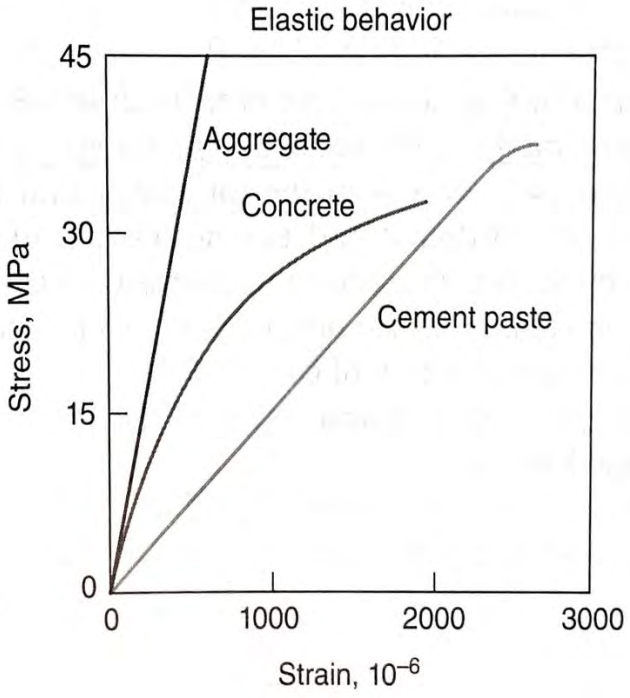

Figure 2-1: Comparison of concrete component stiffnesses (Mehta and Monteiro 2014)

2.2.2 Autogenous Shrinkage

Jensen and Hansen (1996) define autogenous shrinkage as the bulk deformation that occurs in a closed, isothermal concrete system and independently of external humidity. While it refers to the total deformation of the concrete, it is caused by a process at the molecular level called chemical shrinkage, which leads to self-desiccation (Jensen and Hansen 1996). These mechanisms associated with autogenous shrinkage and the factors affecting it are discussed in this section.

2.2.2.1 Mechanism of Autogenous Shrinkage

Autogenous shrinkage in general is associated with hydration, so the mechanisms that drive it can begin as soon as the concrete is cast. Initially, the only volume changes that occur locally without affecting the volume of the member is the process of chemical shrinkage (Neville 2011). L'Hermite (1960) states, "the reaction products formed from cement hydration occupy a smaller volume than the initial components," and Holt (2001) defines chemical shrinkage as, "the reduction of the absolute volume of the reactants due to hydration." In low water-to-cement ratio systems, chemical shrinkage leaves empty voids in concrete, which causes a decrease in the internal relative humidity (Jensen and Hansen 1996). This leads to the process of self-desiccation, which is defined by Neville (2011) as the "withdrawal of water from the capillary pores by the hydration of the hitherto unhydrated cement." Self-desiccation causes stresses in the capillary system, which build up to cause bulk shrinkage of the concrete or autogenous shrinkage. In general, as the structure of the concrete matrix becomes more rigid, the concrete can withstand the stresses caused by self-desiccation, so autogenous shrinkage decreases significantly over time (Byard et al. 2012).

2.2.2.2 Factors Affecting Autogenous Shrinkage

Because autogenous shrinkage is caused by stresses from a lack of water in the capillary voids in the concrete, one of the main factors that affects it is the water/cement ratio of the concrete. Lower water/cement ratios lead to an increase in autogenous shrinkage because stresses initiate more quickly due to the smaller amount of water before self-desiccation begins (Neville 2011). The stress development leading to autogenous shrinkage is generally accepted to not be of concern when the water/cement ratio is greater than 0.42 (Byard et al. 2012). The effect of water/cement ratio on autogenous shrinkage is presented in Figure 2-2.

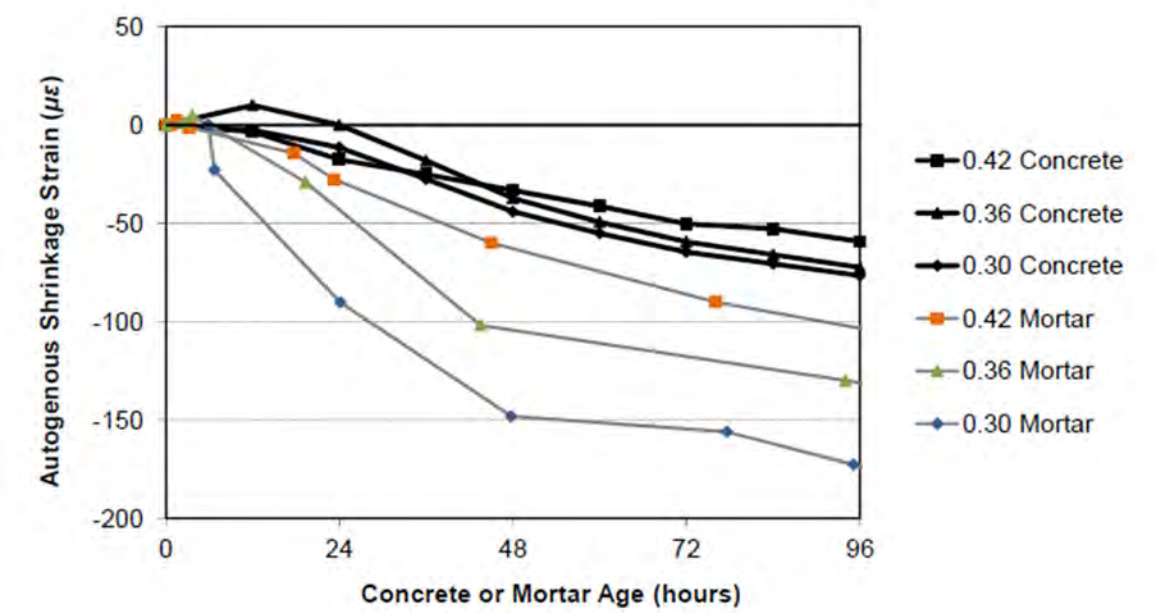

Figure 2-2: Effect of water/cement ratio on autogenous shrinkage (Byard et al. 2012)

According to Neville (2011), other factors that tend to increase autogenous shrinkage are high temperatures, high cement contents, more fine cements, and higher levels of tricalcium aluminate and tetracalcium aluminoferrite. In addition, higher fly ash contents can decrease autogenous shrinkage (Neville 2011). Autogenous shrinkage is often mitigated with internal curing. This is generally performed by pre-wetting lightweight aggregates so that the pores in the aggregates fill with water, and the stresses are not able to develop because self-dessication is prevented (Byard et al. 2012).

2.2.3 Drying Shrinkage

Drying shrinkage is defined broadly by ACI Committee 209 (2008) as “shrinkage occurring in a specimen that is allowed to dry.” Neville (2011) elaborates in defining it as shrinkage caused by “withdrawal of water from concrete stored in unsaturated air.” Unlike autogenous shrinkage, drying shrinkage is heavily dependent on the external moisture condition, so the ambient relative humidity is an important factor (Neville 2011).

2.2.3.1 Mechanism of Drying Shrinkage

The drying process can begin immediately after the environment of the concrete specimen has an ambient relative humidity lower than 100 percent. Initially, the free water in the concrete is lost due to the relative humidity gradient; however, this loss causes very little shrinkage, if any (Neville 2011). Mehta and Monteiro (2014) define free water as “the water in large voids of the order of >50 nm” and state that the removal of free water does not lead to a change in volume. As the

concrete continues to dry, the removal of adsorbed water in the hydrated cement paste occurs, which is the main driver of drying shrinkage (Neville 2011). Regarding adsorbed water, Mehta and Monteiro (2014) state, “under the influence of attractive forces, water molecules are physically adsorbed onto the surface of solids in the hydrated cement paste.” Additionally, drying can lead to the loss of some capillary water held in hydrostatic tension, which causes shrinkage on a smaller scale (Mehta and Monteiro 2014). At a constant relative humidity, drying shrinkage increases over time at a rate that decreases over time, i.e., the rate of shrinkage at early ages is much greater than the rate at late ages (Neville 2011). This relationship is presented in Figure 2-3.

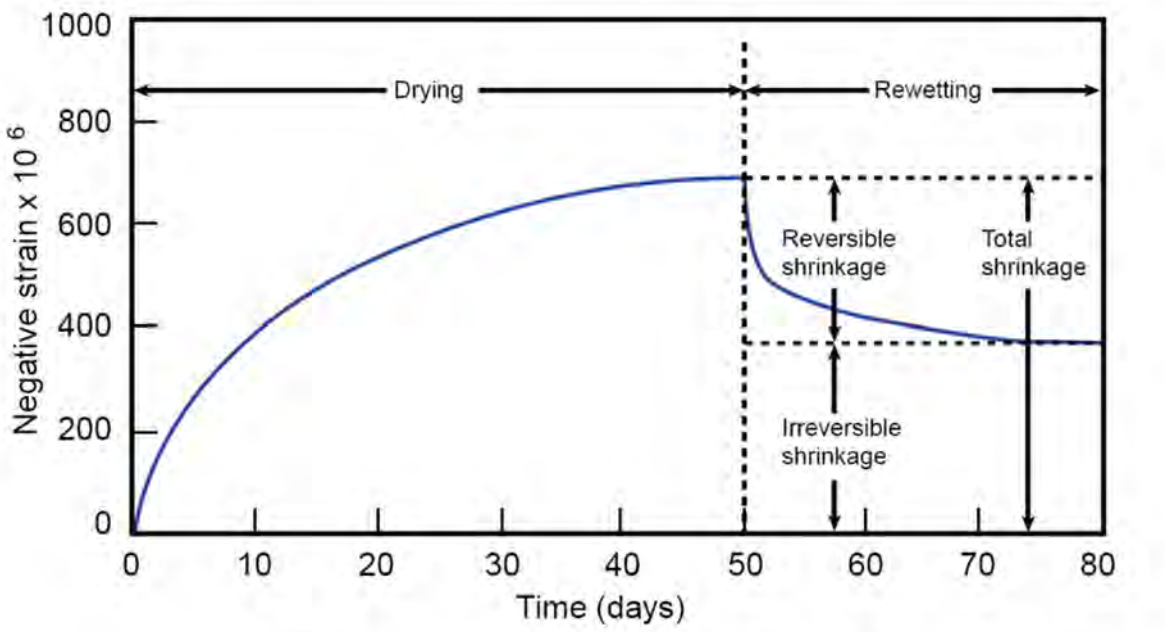

Figure 2-3: Shrinkage of an unloaded specimen (Mehta and Monteiro 2014)

2.2.3.2 Factors Affecting Drying Shrinkage

As discussed above, the driving factor in drying shrinkage is the relative humidity gradient between the concrete and the environment. Any ambient relative humidity below 100 percent leads to drying shrinkage, but a lower relative humidity causes higher drying shrinkage strains as more adsorbed water must be removed to return the system to equilibrium (Neville 2011). The relationship between ambient relative humidity and drying shrinkage is presented in Figure 2-4.

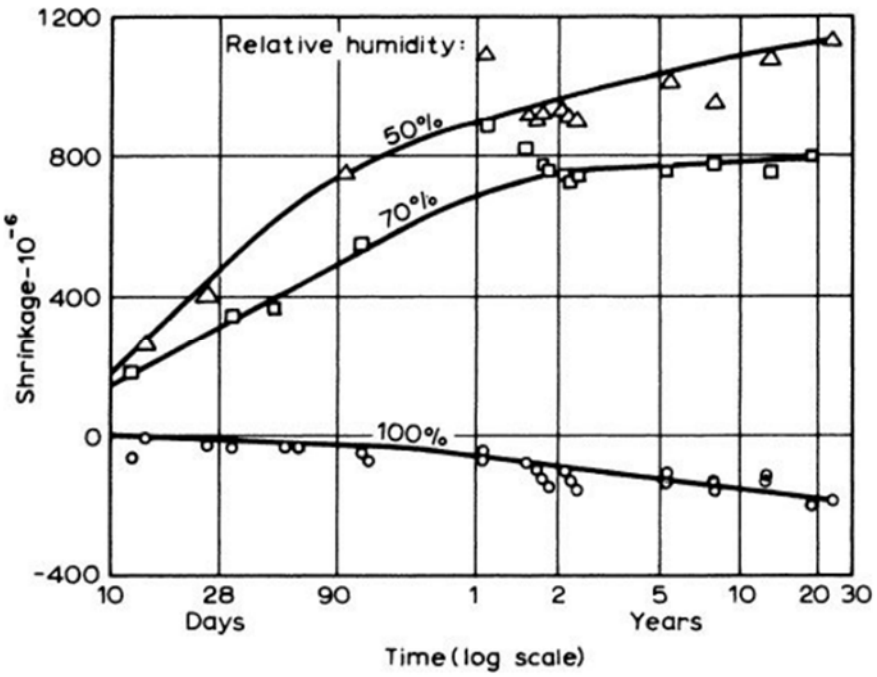

Figure 2-4: Relationship between relative humidity and drying shrinkage (Neville 2011)

While external factors such as relative humidity are the leading causes of drying shrinkage, the rate and magnitude of shrinkage strain is greatly impacted by material selections and mixture proportions (Neville 2011). One internal factor important to drying shrinkage is the water content or water/cement ratio of the concrete mixture. In general, a higher water/cement ratio leads to higher drying shrinkage strains because it "determines the amount of evaporable water in the cement paste and the rate at which water can move towards the surface of the specimen" (Neville 2011). The relationship between the water/cement ratio of a mixture and its drying shrinkage is presented in Figure 2-5.

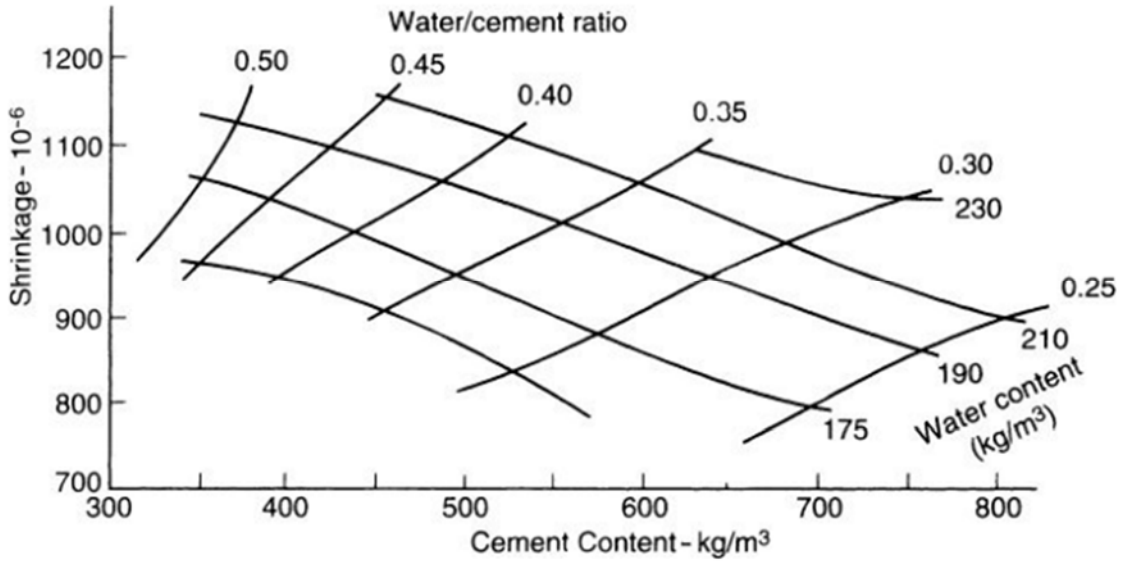

Figure 2-5: Relationship between water/cement ratio and shrinkage (Neville 2011)

The other main factor contributing to drying shrinkage related to material selection is the properties and quantities of the aggregates in the mixture (Neville 2011). Mehta and Monteiro (2014) state that the most important property of aggregates in relation to drying shrinkage is the modulus of elasticity. Aggregates with higher elastic moduli are more resistant to shrinkage, and thus, concrete mixtures with less stiff aggregates tend to shrink more (Mehta and Monteiro 2014). Lightweight aggregates tend to have lower elastic moduli due to their high porosity, so using them can lead to high shrinkage strains (Neville 2011). Because aggregates provide the stiffness to resist the drying shrinkage of the hydrated cement paste in concrete, increasing the proportion of aggregates in the mixture can lower the shrinkage strains as well (Neville 2011). The relationship between aggregate content and shrinkage at varying water/cement ratios is presented in Figure 2-6.

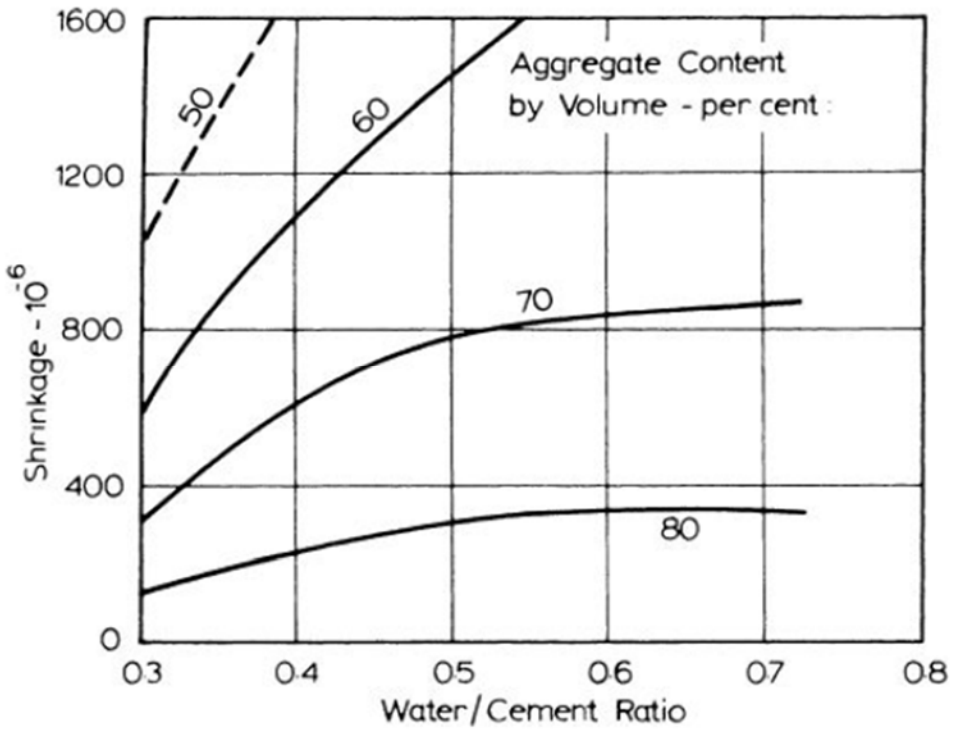

Figure 2-6: Relationship between aggregate content and shrinkage (Neville 2011)

2.2.3 Creep

ACI Committee 209 (2008) defines creep strain as “the time-dependent increase in strain under constant load taking place after the initial strain at loading.” The increase in strain due to creep can often be several times larger than the instantaneous strain at loading, so it can play an important role in the long-term behavior of many structures (Neville 2011). Creep is partially dependent on the movement of moisture out of the concrete, so it does have similar mechanisms to shrinkage. However, the sustained loading of the concrete also leads to other creep mechanisms which are independent of relative humidity (Mehta and Monteiro 2014). This section discusses these mechanisms of creep and the factors that affect it, as well as the method for quantifying the effects of creep on differently loaded structures for the purposes of comparison.

2.2.4.1 Mechanisms of Creep

In general, creep is discussed broadly as one process; however, it is made up of two very different mechanisms (Mehta and Monteiro 2014). The first of these mechanisms is basic creep, which is defined as “the time-dependent increase in strain under sustained constant load of a concrete specimen in which moisture losses or gains are prevented (sealed specimen)” (ACI Committee 209 2008). Basic creep occurs independently of moisture movement, so at a relative

humidity of 100 percent, it is the only creep mechanism that takes place (Mehta and Monteiro 2014). Basic creep is largely caused by the viscoelastic behavior of concrete due to its composite nature (Mehta and Monteiro 2014). Hedegaard (2020) states that basic creep "may be caused by some combination of crystalline flow in the aggregates and hardened cement paste, plastic flow in the cement paste" and "closing of internal voids."

The second mechanism by which creep occurs is drying creep, which is defined as "the additional creep to the basic creep in a loaded specimen exposed to a drying environment and allowed to dry" (ACI Committee 209 2008). According to Mehta and Monteiro (2014) there is some measurable creep strain caused by drying of a loaded specimen beyond the drying shrinkage strain of the unloaded specimen. "It has been observed that when a concrete is under load and is simultaneously exposed to low relative humidity environment, the total strain is higher than the sum of elastic strain, free shrinkage strain, and basic creep" (Mehta and Monteiro 2014). The mechanism for drying creep is the same as the moisture movement mechanism of drying shrinkage; however, the sustained stress causes it to occur at a higher rate (Mehta and Monteiro 2014). The interaction among all of the above mechanisms of volumetric changes in concrete is presented in Figure 2-7.

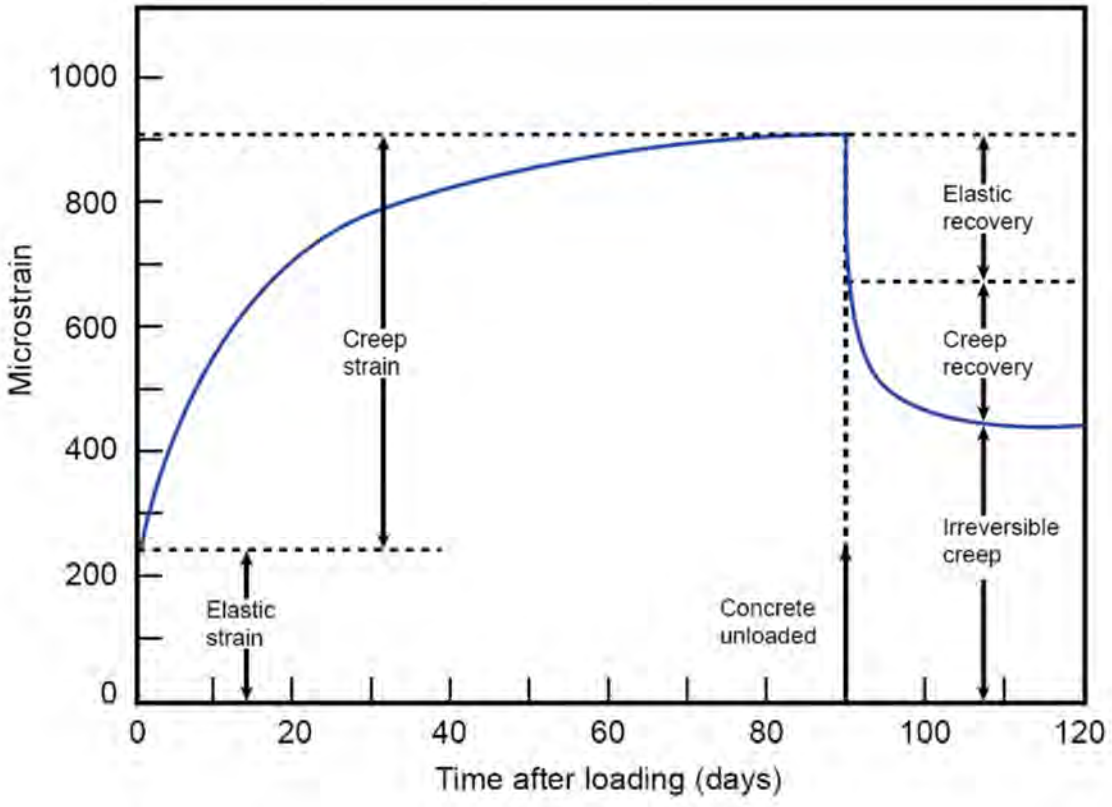

Figure 2-7: Volumetric changes of loaded concrete specimen (Mehta and Monteiro 2014)

2.2.4.2 Factors Affecting Creep

Because the mechanism of drying creep is based on the same time of moisture movement as drying shrinkage, the relationship between ambient relative humidity and shrinkage strain is very similar to drying creep strain (Mehta and Monteiro 2014). Generally, lower relative humidity values lead to higher creep values because the additional drying creep beyond basic creep increases due to the higher moisture gradient (Neville 2011). The curing history of concrete, however, can play an important role because of its effects on the interfacial transition zone. Mehta and Monteiro (2014) state “drying cycles can enhance microcracking in the interfacial transition zone and thus increase the creep.” Additionally, elevated temperatures affect the rate of creep in two different ways depending on when the structure is exposed to them (Mehta and Monteiro 2014). If the concrete is exposed to elevated temperatures during the curing process, the concrete strength increases, which decreases creep. However, if it is exposed after the load is applied, the creep strain increases (Mehta and Monteiro). For these reasons, the age at the time of loading also has a significant effect on the magnitudes of creep strains (Mehta and Monteiro 2014).

Like shrinkage, creep is heavily dependent on mixture proportions and material properties. Because the hydrated cement paste is the phase in which creep occurs, a higher aggregate content in the mixture leads to lower creep values (Neville 2011). The aggregates also provide the stiffness that resists the effects of creep, so aggregates with lower elastic moduli lead to higher creep values (Neville 2011). In comparison to normal weight aggregates, lightweight aggregates typically cause higher creep values due to the decreased stiffness caused by its increased porosity (Mehta and Monteiro 2014). Neville (2011) also found that the mineralogical properties of aggregates affect the creep of concrete, with sandstone aggregates causing the highest creep and basalt and quartz causing the lowest creep as presented in Figure 2-8.

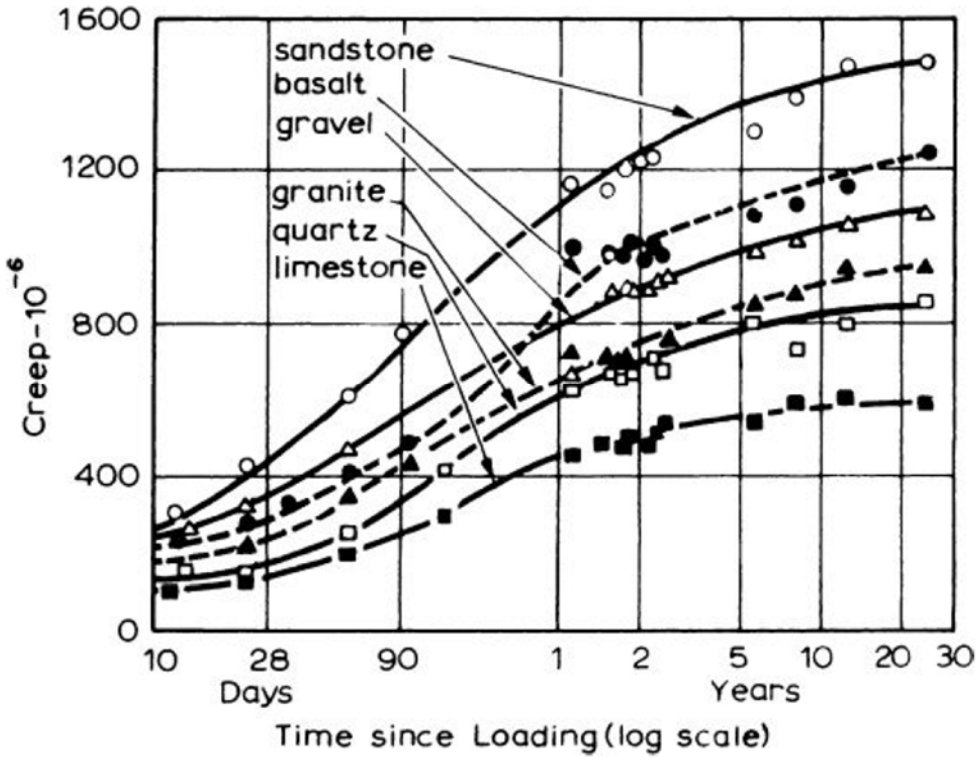

Figure 2-8: Effect of aggregate type on creep (Neville 2011)

For the reasons listed above, the water/cement ratio has the same effect on creep as it does on drying shrinkage (Neville 2011). The cement type has small effects on creep in concrete, but much is unknown about the mechanisms of these effects (Neville 2011). In general, increases in concrete strength due to the cement type decrease the creep, and vice versa (Neville 2011). For example, Neville (2011) states that a concrete specimen under a constant stress generally has lower creep values for rapid-hardening cements, and higher creep values for low heat cements. Supplementary cementitious materials such as fly ash and slag cement do not have a significant effect on creep as a whole, but they can slightly affect the separate mechanisms of creep (Neville 2011).

2.2.4.3 Compliance

When quantifying and comparing creep in different structures and concrete specimens, it is important to have a consistent way to compare it in very different scenarios and loading conditions. One quantitative creep value is known as the creep coefficient, and it is defined as "the ratio of the creep strain to the initial strain" (ACI Committee 209 2008). However, the creep coefficient does not eliminate the variability of stresses caused by loading because it does not normalize strains based on load. For this, the value of compliance is used, which is defined as "the total load induced strain (elastic strain plus creep strain) at age *t* per unit stress caused by a

unit uniaxial sustained load applied since loading age t_o" (ACI Committee 209 2008). Compliance is also given by Equation 2.1 (ACI Committee 209 2008).

$$\text{compliance} = \frac{(\text{elastic strain} + \text{basic creep} + \text{drying creep})}{\text{stress}} \qquad \text{Equation 2.1}$$

Compliance is the value that will be used to quantify and compare elastic and creep strains for the purposes of this research. A general schematic of the compliance function showing the instantaneous elastic deformation and the increasing time-dependent deformation with age is adapted from ACI 209.2R (2008) and shown in Figure 2-9.

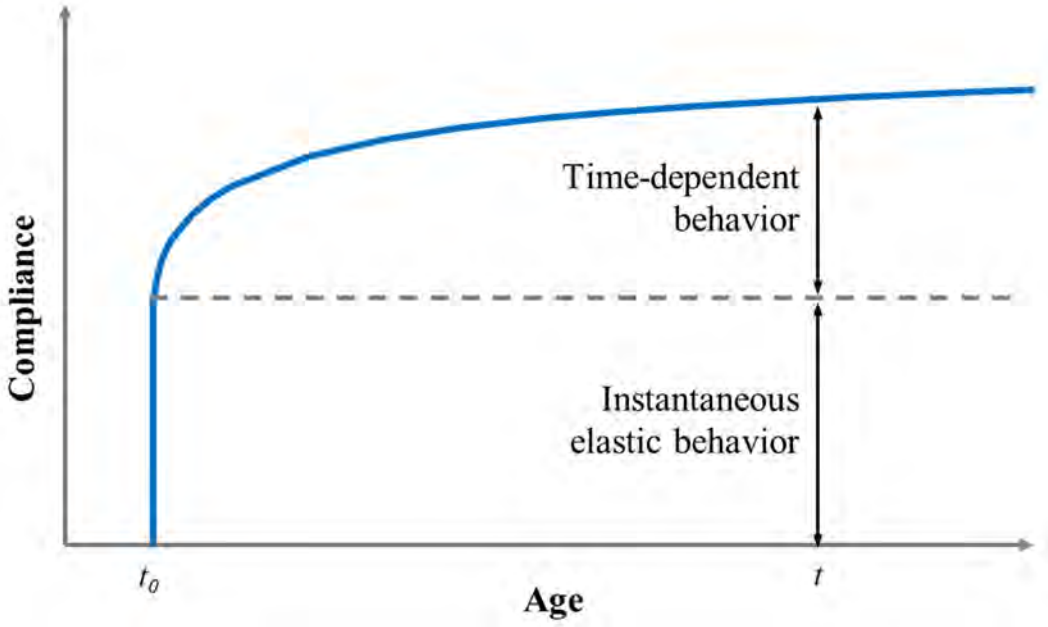

Figure 2-9: Compliance schematic adapted from ACI 209.2R (2008)

2.3 VOLUMETRIC CONCRETE CHANGES IN SEGMENTAL BRIDGES

Because this research focuses on the prediction of creep and shrinkage in segmental bridges, it is important to understand the response of segmental bridges to these volumetric changes. This section covers construction methods of post-tensioned, precast segmental bridges and the effects of creep and shrinkage on the overall performance by focusing on deflections caused by prestress losses and moment redistribution.

2.3.1 Segmental Bridge Construction

Construction of post-tensioned segmental box girder bridges is very versatile, and thus they can be constructed in a variety of ways. They are typically categorized into two main types, precast and cast-in-place. As the name suggests, the difference between these two methods is that precast segments are cast prior to placement in the bridge, either at a plant or at the construction

site, while cast-in-place segments are cast directly in their final location in the bridge. The components of a typical segmental bridge are shown in Figure 2-10.

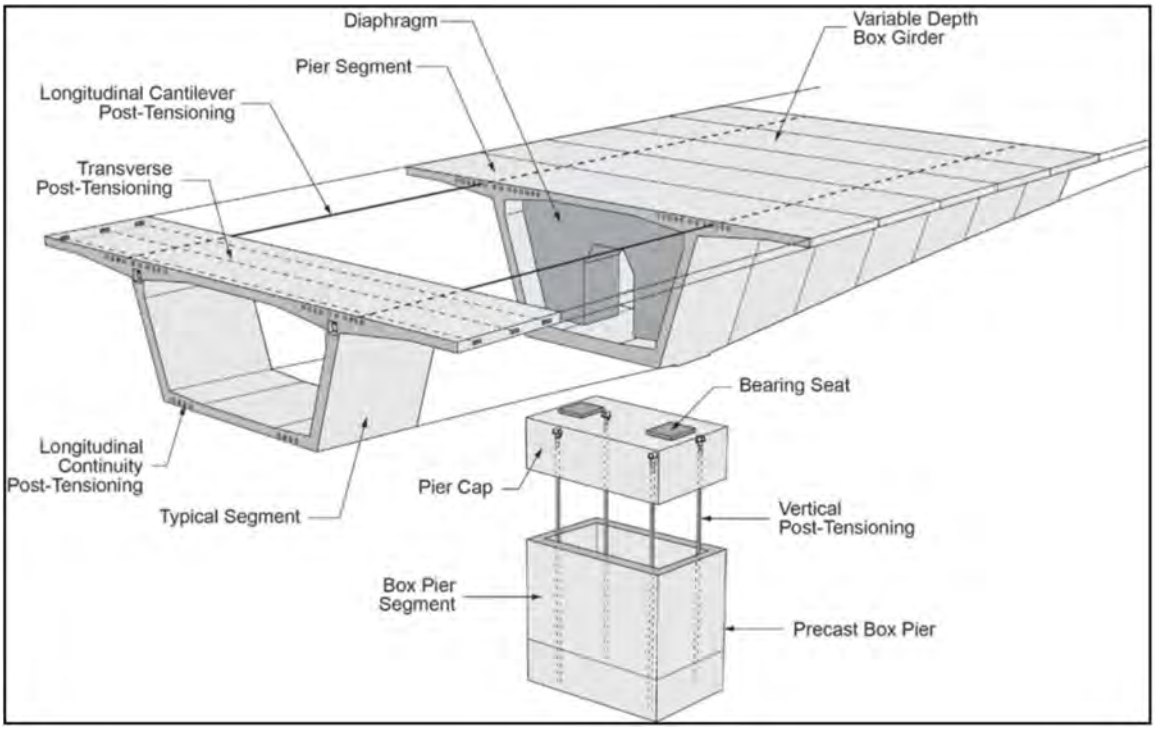

Figure 2-10: Components of typical segmental bridges (ASBI 2019)

Bridges of each of these categories can be constructed in several different methods. The three most common methods for constructing precast segmental bridges are the span-by-span method, the balanced cantilever method, and the progressive placement method (ASBI 2019).

2.3.1.1 Span-by-Span Method

According to the ASBI Construction Practices Handbook (2019), span-by-span construction is performed by constructing an entire span of segments at a time, making each span self-supporting before moving to the next. This is typically done with a temporary erection truss to support the segments until they are post-tensioned and able to support themselves. This erection process is shown in Figure 2-11.

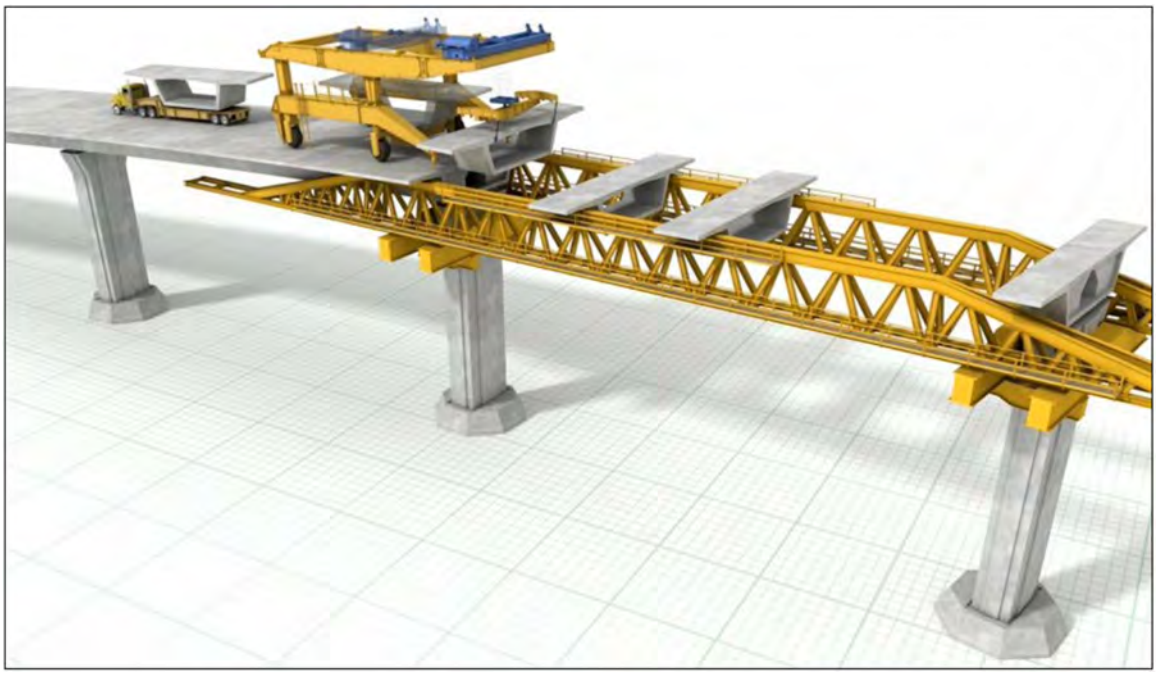

Figure 2-11: Erection process of span-by-span bridge (ASBI 2019)

Epoxy is usually applied to help seal the joints and to provide some strength to this connection until post-tensioning. This process is then repeated for every span of the bridge, and the spans are joined with cast-in-place closure joints. The placement process of the cast-in-place closure joint is shown in Figure 2-12. Span-by-span construction is advantageous mainly because of the lower costs associated with construction and the speed of construction (ASBI 2019). Span-by-span construction was the method used for the Birmingham I-59/I-20 segmental bridge, with an unbonded post-tensioning system used longitudinally and a bonded post-tensioning system used transversely.

Figure 2-12: Cast-in-place closure joint (ASBI 2019)

2.3.1.2 Balanced Cantilever Method

In balanced cantilever construction, erection initiates from a central pier, and two segments at a time are placed. These two segments are placed on both sides of pier to balance the weight and avoid a buildup of moment in the pier. Because no erection truss is used in this method, each individual segment must be post-tensioned immediately after placement and epoxying, so that it is able to support itself (ASBI 2019). A typical balanced cantilever segment cross section is shown in Figure 2-13.

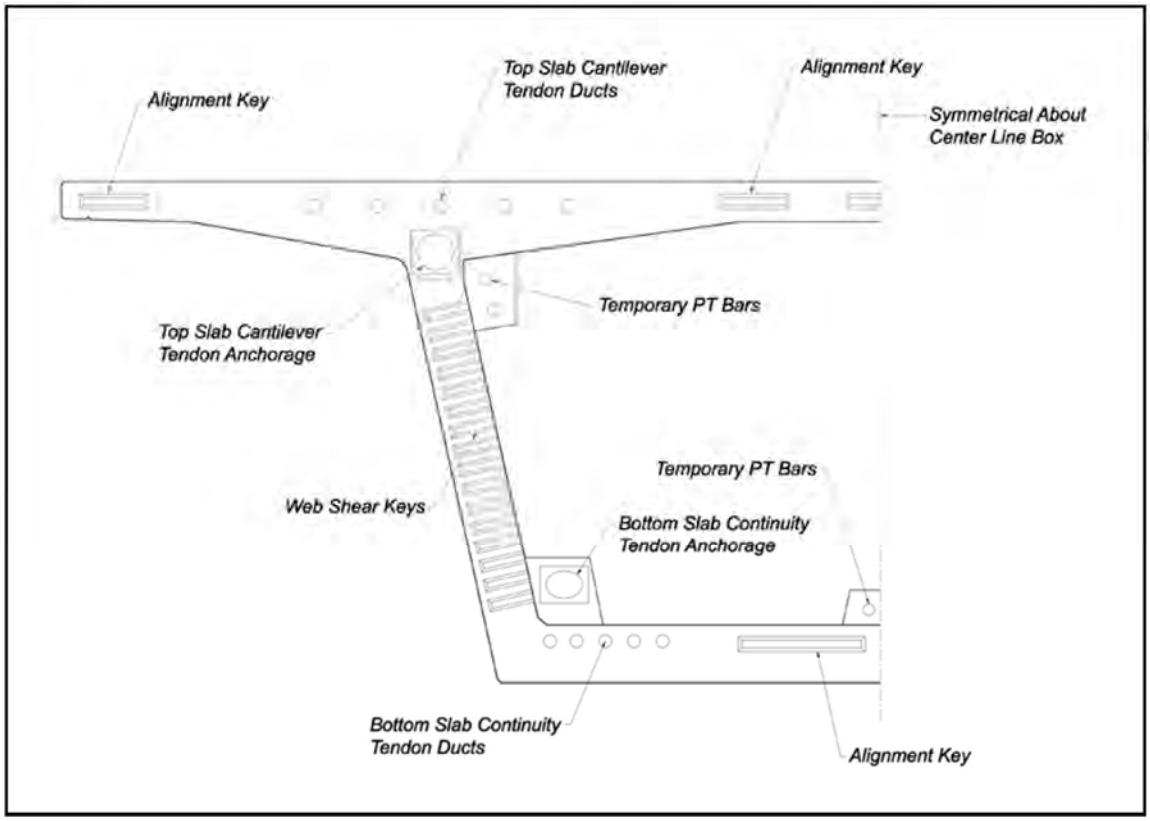

Figure 2-13: Typical balanced cantilever section (ASBI 2019)

This initial post-tensioning is typically done with high-strength steel post-tensioning bars two segments at a time, after which tendons are stressed and anchored. This repeated process is shown in Figure 2-14. Within balanced cantilever construction, there are many different methods of placement of segments including cranes, gantries, etc. However, the general construction process holds true for all balanced cantilever bridges. An example of placement using a mobile lifter is shown in Figure 2-15 (ASBI 2019).

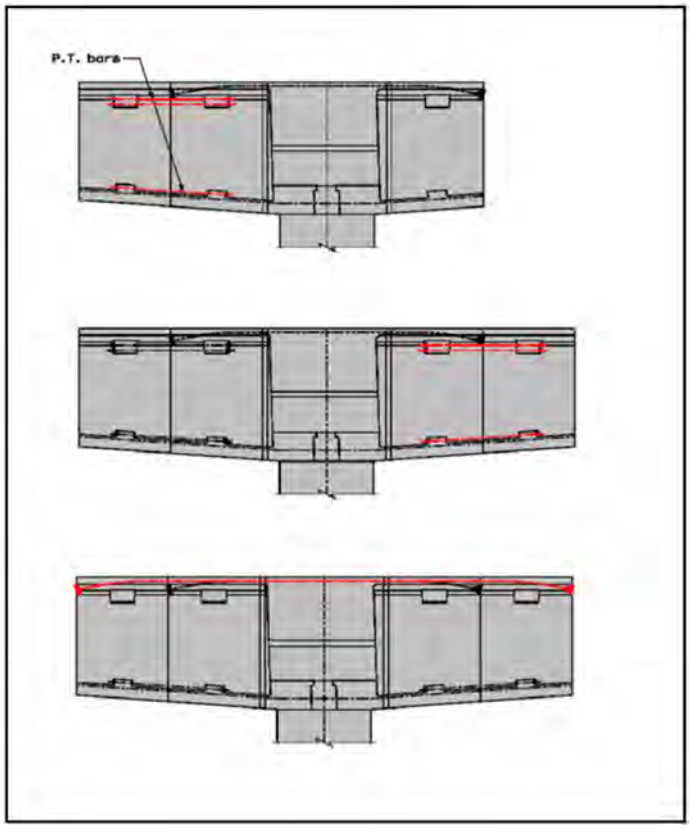

Figure 2-14: Two-segment erection cycle (ASBI 2019)

Figure 2-15: Balanced cantilever construction using mobile lifter (ASBI 2019)

2.3.1.3 Progressive Placement Method

The progressive placement construction method applies concepts from both the balanced cantilever method and the span-by-span method to erect segmental bridges in more complex or environmentally sensitive locations. The typical process of construction for this method begins at one bridge pier and continues sequentially until the span is complete. Because segments are being placed on only one side of the pier, the moments cannot balance like in the balanced cantilever method, so some type of temporary falsework is usually required until the span is completed and post-tensioned (ASBI 2019). The typical erection process for progressive placement bridges is shown in Figure 2-16.

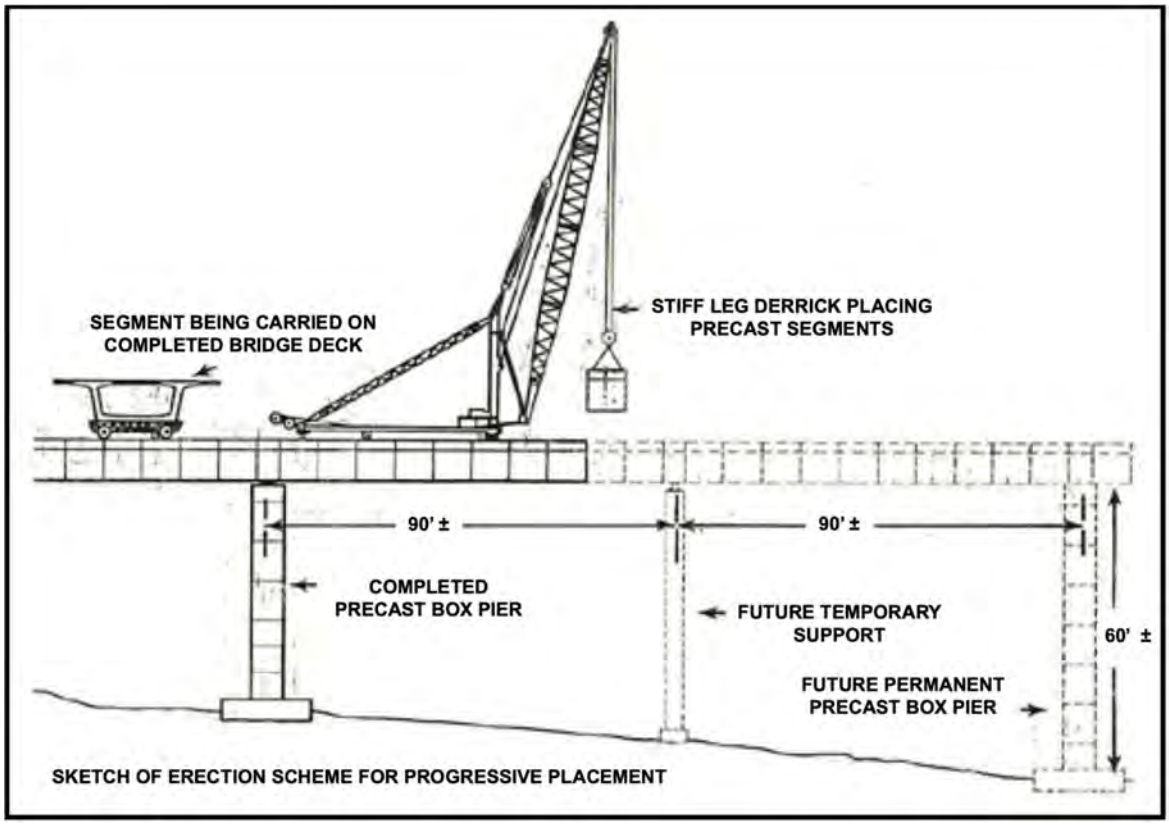

Figure 2-16: Erection process of progressive placement bridge (ASBI 2019)

2.3.2 Creep and Shrinkage in Segmental Bridges

In segmental bridge applications, creep strains are caused by the effective prestressing force of the post-tensioning tendons. These strains are time dependent and can reach significant magnitudes given enough time. When concrete is under compression, and the elastic stress is less than 40 percent of the compressive strength, it can be assumed that creep strains are

proportional to elastic strains (Wang and Fu 2014). Two major mechanisms result from creep strains that can negatively affect balanced cantilever segmental bridges if excessive (or unaccounted for): prestress losses and moment redistribution. These mechanisms may result in unanticipated long-term deflections if the time-dependent behavior of the concrete is not properly modeled (Wang and Fu 2014).

AASHTO (2020) limits the deflections of vehicular bridge spans to the span length divided by 800 in Section 2.5.2.6.2. Deflections beyond this limit are considered "excessive." Bažant et al. (2011) investigated long-term segmental bridge data and discovered 56 bridge spans exhibiting excessive deflections due to creep and shrinkage strains. One extreme example of the deflections found was the Koror-Babeldaob Bridge in Palau, which deflected 1.61 meters from its original design camber after 18 years. In that time, it also experienced an estimated prestress loss of approximately 50% due to creep and shrinkage strains (Bažant et al. 2011).

2.3.2.1 Prestress Losses Due to Creep and Shrinkage

Prestress losses can be caused by a variety of factors including elastic shortening, steel relaxation, and creep strains. Because segmental bridges are post-tensioned, there is a significant stress in the concrete caused by the force of the post-tensioning tendons. This force causes creep to initiate in the bridge immediately after post-tensioning. Shrinkage happens independently of loading, so it is already initiated at that time. However, because the creep and shrinkage strains cause the concrete to shorten, which leads to shortening of the tendons, the prestressing force goes down to ensure that the structure is in equilibrium. Because the prestressing force is responsible for the load capacity of the bridge and the in-service deflections, this unavoidable loss of prestress force must be accounted for in design to ensure the safety and the serviceability of the bridge (Ye et al. 2020).

2.3.2.2 Moment Redistribution Due to Creep and Shrinkage

Gabaldón et al. (2020) studied the mechanism of moment redistribution due to creep and shrinkage in cantilever bridges; however, this can affect any continuous segmental bridge in which closure joints are used. Each span of the bridge begins as two cantilever arms before the closure joint is cast. The high negative moments due to the self-weight of the arms is countered by the post-tensioning tendons. The casting and strength gain of the closure joints renders these two determinate cantilever arms as a single continuous and indeterminate system. The continuity of the span decreases the elastic deflections due to service loads, but it allows the creep strain caused by the prestressing force to induce a positive moment at midspan by redistributing a portion of the negative moment from the supports (Gabaldón et al. 2020). The mechanism of moment redistribution by creep and shrinkage is shown in Figure 2-17. Part (a) of Figure 2-17 shows the two cantilever arms before the closure joint is cast. Part (b) shows the cantilever arms

immediately after the closure joint is cast. Part (c) shows the deformations of the arms immediately after the closure joint is cast. Part (d) shows the moments at midspan of the continuous span due to creep.

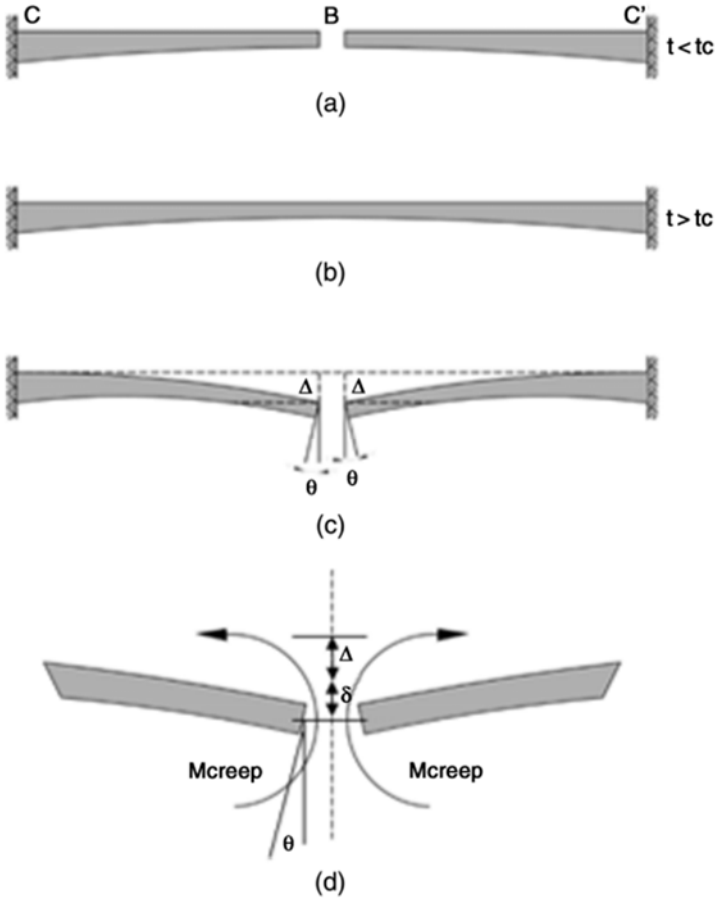

Figure 2-17: Moment redistribution mechanism (Gabaldón et al. 2020)

2.3.2.3 Vertical Displacement Due to Creep and Shrinkage

Raphael et al. (2018) studied the effects of creep and shrinkage on the bridge of Cheviré in France. The bridge of Cheviré is a segmental bridge with a central steel span of over 162 meters being supported on prestressed concrete cantilevers on both sides of the span. The total span length including the concrete cantilevers is 242 meters. A picture of the bridge is shown in Figure 2-18. The vertical displacement of the free end cantilever began being monitored three years after construction because a high displacement was detected. Over the next five years, it was observed that the vertical displacement had increased from 10 centimeters to over 18 centimeters, which was significantly more than the predicted values. Raphael et al. (2018)

determined that the excessive deflections observed in the bridge of Cheviré were caused by creep and shrinkage strains in the prestressed concrete cantilevers. The effective prestressing force in the span, along with the environmental conditions, caused shortening in the concrete due to creep and shrinkage, thus shortening the post-tensioning tendons and causing prestress loss as discussed in Section 2.3.2.1. These prestress losses caused the capacity of the cantilevers to decrease and made them susceptible to greater deflections due to loading (Raphael et al. 2018).

Figure 2-18: Bridge of Cheviré in France

Chapter 3

REVIEW OF CREEP AND SHRINKAGE PREDICTION MODELS

3.1 INTRODUCTION

The primary objective of this research is to predict creep and shrinkage strains in the Birmingham I-59/I-20 segmental bridge. This will be performed by comparisons to eight existing creep and shrinkage prediction models. This chapter outlines the eight prediction models that will be considered and reviews previous studies involving the accuracy of these models.

3.2 CREEP AND SHRINKAGE PREDICTION MODELS

Eight creep and shrinkage prediction models were selected because they are the most commonly used models in practice and research. This section outlines the details of each model, which include the required concrete properties and the equations used to determine compliance and shrinkage values. These eight models were considered:

- AASHTO LRFD (2020),
- ACI 209 (2008),
- B3 (Bažant and Baweja 2000),
- B4 (Bažant 2015),
- CEB MC 1990 (CEB 1990),
- CEB MC 90-99 (CEB 1999),
- CEB MC 2010 (fib 2012), and
- GL 2000 (Gardner and Lockman 2001).

The total number of independent variables for each prediction model is shown in Table 3-1. These quantities are separated into their respective values for creep and shrinkage.

Table 3-1: Number of independent variables for creep and shrinkage prediction models

Prediction Model	Creep Parameters	Shrinkage Parameters
AASHTO LRFD	6	4
ACI 209	9	8
B3	10	8
B4	13	13
CEB MC 1990	6	6
CEB MC 90-99	7	6
CEB MC 2010	7	6
GL 2000	5	6

3.2.1 AASHTO LRFD Prediction Model

The current standard set of specifications used by ALDOT for bridge design is AASHTO LRFD (2020). The method for determining the modulus of elasticity is based on the research of Greene and Graybeal (2013), and the methods for determining creep and shrinkage are based on Huo et al. (2001), Al-Omaishi (2001), Tadros et al. (2003), Rizkalla et al. (2007), and Collins and Mitchell (1991). All other references can be found in C5.4.2.3 of the AASHTO LRFD Bridge Design Specifications for creep and shrinkage, and C5.4.2.4 for modulus of elasticity (AASHTO 2020).

3.2.1.1 AASHTO LRFD Modulus of Elasticity

According to the AASHTO LRFD Bridge Design Specifications (AASHTO 2020), the modulus of elasticity, E_c, may be defined by Equation 3.1 for normal-weight concrete in which the design compressive strength is less than 15.0 ksi, and for lightweight concrete in which it is less than 10.0 ksi. The concrete unit weight must also be between 0.090 and 0.155 kcf.

$$E_c = 120{,}000 K_1 w_c^{2.0} f_c'^{0.33} \quad \text{Equation 3.1}$$

With,

K_1 = correction factor for source of aggregate to be taken as 1.0,

w_c= unit weight of concrete (kcf), and

f_c'= compressive strength of concrete for use in design (ksi).

3.2.1.2 AASHTO LRFD Creep Prediction Model

The AASHTO LRFD (2020) model used to predict creep results in a creep coefficient, $\psi(t, t_i)$, which when applied to the compressive strain caused by permanent loads, produces the strain due to creep. The equation for the creep coefficient function can be found in Equation 3.2. The

creep coefficient is a function of four factors: k_s, k_{hc}, k_f, k_{td}, which are based on component size, concrete strength, humidity, and time development. The equations for these factors can be found in Equations 3.3 through 3.6.

$$\psi(t, t_i) = 1.9 k_s k_{hc} k_f k_{td} t_i^{-0.118} \quad \text{Equation 3.2}$$

With,

t_i = age of concrete at time of load application (days) and

k_s = factor for the effect of the volume-to-surface ratio of the component defined as:

$$k_s = 1.45 - 0.13(V/S) \geq 1.0 \quad \text{Equation 3.3}$$

Where,

V/S = volume-to-surface ratio (in.). The maximum V/S to be considered is 6.0 in. (AASHTO 2020).

k_{hc} = humidity factor for creep defined as:

$$k_{hc} = 1.56 - 0.008H \quad \text{Equation 3.4}$$

Where,

H = average annual ambient relative humidity (percent).

k_f = factor for the effect of concrete strength defined as:

$$k_f = \frac{5}{1 + f_{ci}^{'}} \quad \text{Equation 3.5}$$

Where,

$f_{ci}^{'}$ = design concrete compressive strength at time of prestressing for pretensioned members and at time of initial loading for nonprestressed members. If concrete age at the time of initial loading is unknown, $f_{ci}^{'}$ may be taken as $0.80f'_c$ (ksi).

k_{td} = time development factor defined as:

$$k_{td} = \frac{t}{12\left(\frac{100 - 4f_{ci}^{'}}{f_{ci}^{'} + 20}\right) + t} \quad \text{Equation 3.6}$$

Where,

t = maturity of concrete (day), defined as age of concrete between time of loading for creep calculations, or end of curing for shrinkage calculations, and time being considered for analysis of creep or shrinkage effects.

3.2.1.3 AASHTO LRFD Shrinkage Prediction Model

The AASHTO LRFD (2020) model used to predict shrinkage results in the strain due to shrinkage at time t, ε_{sh}, which is defined in Equation 3.7. The factors for shrinkage are the same as those

used for the creep function, except for k_{hs}, the humidity factor, which is defined in Equation 3.8. Because k_s, k_f, and k_{td} are the same for creep, their equations can be found in Equations 3.3, 3.5, and 3.6 respectively.

$$\varepsilon_{sh} = k_s k_{hs} k_f k_{td} 0.48 \times 10^{-3} \quad \text{Equation 3.7}$$

With,

k_s = factor for the effect of the volume-to-surface ratio of the component as documented in Equation 3.3,

k_{hs} = humidity factor for shrinkage defined as:

$$k_{hs} = 2.00 - 0.014H \quad \text{Equation 3.8}$$

Where,

H = average annual ambient relative humidity (percent).

k_f = concrete strength effect factor as documented in Equation 3.5, and

k_{td} = time development factor as documented in Equation 3.6.

The AASHTO LRFD Bridge Design Specifications (AASHTO 2020) state that the shrinkage determined in Equation 3.7 should be increased 20 percent if the concrete is exposed to drying before five days of curing have elapsed.

3.2.2 ACI 209 Prediction Model

The ACI 209 prediction model for creep and shrinkage was introduced in ACI 209R (1992) and was developed by Branson and Christiason (1971). It calculates the ultimate creep coefficient and shrinkage strain based on the age of concrete when drying starts, age of concrete at loading, curing method, relative humidity, volume-surface ratio, and concrete composition. Time-dependent parameters are used to predict the creep and shrinkage at any concrete age (ACI 209.2R 2008).

3.2.2.1 ACI 209 Modulus of Elasticity

The ACI 209 creep prediction model results in a creep coefficient. In order to convert this to a compliance value, the modulus of elasticity of the concrete must be determined. According to ACI 209.2R (2008), the predicted secant modulus of elasticity at time of loading, E_{cmto}, is given by Equation 3.9.

$$E_{cmto} = 33\gamma_c^{1.5}\sqrt{f_{cmto}} \quad \text{Equation 3.9}$$

With,

γ_c = unit weight of concrete (lb/ft^3) and

f_{cmto}= mean concrete compressive strength at time of loading (psi).

3.2.2.2 ACI 209 Creep Prediction Model

The ACI 209 model used to predict creep results in an ultimate creep coefficient, ϕ_u, from which the creep strain at a given time after loading, $\phi(t, t_o)$, can be determined with a time-dependent parameter. The average ultimate creep coefficient value may be taken as 2.35 (ACI 209.2R 2008), which is modified by six correction factors. The equation for the ultimate creep coefficient is given by Equation 3.10, and the equations for the correction factors associated with it are given by Equations 3.11 through 3.17.

$$\phi_u = 2.35\gamma_{c,to}\gamma_{c,RH}\gamma_{c,vs}\gamma_{c,s}\gamma_{c,\psi}\gamma_{sh,\alpha} \quad \text{Equation 3.10}$$

With,

$\gamma_{c,to}$ = age of loading factor for creep defined as:

$$\gamma_{c,to} = 1.25t_o^{-0.118} \quad \text{for moist curing} \quad \text{Equation 3.11}$$

$$\gamma_{c,to} = 1.13t_o^{-0.094} \quad \text{for steam curing} \quad \text{Equation 3.12}$$

Where,

t_o = age of concrete at loading (days).

$\gamma_{c,RH}$ = ambient relative humidity factor defined as:

$$\gamma_{c,RH} = 1.27 - 0.67h \quad \text{for } h \geq 0.40 \quad \text{Equation 3.13}$$

Where,

h = relative humidity expressed as a decimal.

$\gamma_{c,vs}$ = volume-surface ratio factor defined as:

$$\gamma_{c,vs} = \frac{2}{3}(1 + 1.13\exp\{-0.54(V/S)\}) \quad \text{Equation 3.14}$$

Where,

V/S = volume to surface area ratio (in.).

$\gamma_{c,s}$ = slump factor defined as:

$$\gamma_{c,s} = 0.82 + 0.067s \quad \text{Equation 3.15}$$

Where,

s = observed slump of fresh concrete (in.).

$\gamma_{c,\psi}$ = fine aggregate factor defined as:

$$\gamma_{c,\psi} = 0.88 + 0.0024\psi \quad \text{Equation 3.16}$$

Where,

ψ = ratio of fine aggregate to total aggregate by weight (%).

$\gamma_{sh,\alpha}$ = air content factor defined as:

$$\gamma_{sh,\alpha} = 0.46 + 0.09\alpha \geq 1 \quad \text{Equation 3.17}$$

Where,

α = air content (%)

Equation 3.18 may be used to determine the creep coefficient at any age after loading, given the corrected ultimate creep coefficient determined in Equation 3.10.

$$\phi(t, t_o) = \frac{(t - t_o)^{\psi}}{d + (t - t_o)^{\psi}} \phi_u \qquad \text{Equation 3.18}$$

With,

($t - t_o$) = time since application of load (days),

ψ = constant for member shape and size taken as 0.6, and

d = constant for member shape and size taken as 10.

3.2.2.3 ACI 209 Shrinkage Prediction Model

The ACI 209 model used to predict shrinkage uses an ultimate shrinkage strain, ε_{shu} of 780 x 10^{-6} in./in. and similar correction factors to the creep prediction model. The ultimate shrinkage strain is given by Equation 3.19, and the correction factors are given by Equations 3.20 through 3.27. Also, like the creep model, a time-ratio parameter is used to determine the shrinkage strain at any age after curing ends, $\varepsilon_{shu}(t, t_c)$, which is given by Equation 3.28.

$$\varepsilon_{shu} = 780\gamma_{sh,tc}\gamma_{sh,RH}\gamma_{sh,vs}\gamma_{sh,s}\gamma_{sh,\psi}\gamma_{sh,c}\gamma_{sh,\alpha} \times 10^{-6} \qquad \text{Equation 3.19}$$

With,

$\gamma_{sh,tc}$= initial moist curing coefficient defined by Equation 3.20 and presented in Table 3-2:

$$\gamma_{sh,tc} = 1.202 - 0.2337\log(t_c) \qquad \text{Equation 3.20}$$

Where,

t_c = moist curing duration (days)

Table 3-2: Initial moist curing coefficients (ACI 209.2R 2008)

t_c (days)	$\gamma_{sh,tc}$
1	1.2
3	1.1
7	1.0
14	0.93
28	0.86
90	0.75

$\gamma_{sh,RH}$ = ambient relative humidity factor defined as:

$$\gamma_{sh,RH} = \begin{cases} 1.40 - 1.02h & \text{for } 0.40 \le h \le 0.80 \\ 3.00 - 3.00h & \text{for } 0.80 \le h \le 1.00 \end{cases} \qquad \text{Equation 3.21}$$

Where,

h = relative humidity expressed as a decimal.

$\gamma_{sh,vs}$ = volume-surface ratio factor defined as:

$$\gamma_{sh,vs}=1.2e^{\{-0.12(V/S)\}} \quad \text{Equation 3.22}$$

Where,

V/S = volume to surface area ratio (in.).

$\gamma_{sh,s}$ = slump factor defined as:

$$\gamma_{sh,s} = 0.89 + 0.041s \quad \text{Equation 3.23}$$

Where,

s = observed slump of fresh concrete (in.).

$\gamma_{sh,\psi}$ = fine aggregate factor defined as:

$$\gamma_{sh,\psi} = 0.30 + 0.014\psi \quad \text{for } \psi \leq 50\% \quad \text{Equation 3.24}$$

$$\gamma_{sh,\psi} = 0.90 + 0.002\psi \quad \text{for } \psi > 50\% \quad \text{Equation 3.25}$$

Where,

ψ = ratio of fine aggregate to total aggregate by weight (%).

$\gamma_{sh,c}$ = cement content factor defined as:

$$\gamma_{sh,c} = 0.75 + 0.00036c \quad \text{Equation 3.26}$$

Where,

c = cement content (lb/yd^3).

$\gamma_{sh,\alpha}$ = air content factor defined as:

$$\gamma_{sh,\alpha} = 0.95 + 0.008\alpha \geq 1 \quad \text{Equation 3.27}$$

Where,

α = air content (%).

Equation 3.28 may be used to determine the shrinkage strain at any concrete age after curing upon determining the ultimate shrinkage strain.

$$\varepsilon_{shu}(t,\, t_c) = \frac{(t\ -\ t_c)^{\alpha}}{f + (t\ -\ t_c)^{\alpha}}\varepsilon_{shu} \quad \text{Equation 3.28}$$

With,

$(t - t_c)$ = time since the end of curing (days),

α = constant for member shape and size taken as 1, and

f = constant for member shape and size taken as 35 for 7 days of moist curing, and 55 for 1 to 3 days of steam curing.

3.2.3 B3 Prediction Model

The B3 model used to predict creep and shrinkage was introduced by Bažant and Baweja (2000). Unlike other models, for the B3 model to be valid, several of the parameters must be within the ranges presented in Table 3-3 (Bažant and Baweja 2000), in addition to the concrete being cured for at least one day.

Table 3-3: Parameter ranges for the B3 model (Bažant and Baweja 2000)

Parameter Definition	Parameter Range
w/c = water-cement ratio by weight	$0.35 \leq w/c \leq 0.85$
a/c = aggregate-cement ratio by weight	$2.5 \leq a/c \leq 13.5$
f_c' = 28-day standard cylinder compression strength of concrete (psi)	$2{,}500 \leq f_c' \leq 10{,}000$
c = cement content (lb/ft^3)	$10 \leq c \leq 45$

The B3 model also uses the maturity method to account for changes in temperature throughout the life of the concrete. It uses two equations to define the equivalent age at loading, t_e', and the equivalent age after loading, $t_T - t_e'$. These are the values used as parameters for creep and shrinkage according to the B3 model, and they are given by Equation 3.29 and 3.30.

$$t_e' = \int_0^{t'} \beta_T(t')dt' \qquad \text{Equation 3.29}$$

With,

t' = concrete age at loading (days) and

β_T = temperature dependent coefficient defined as:

$$\beta_T = \exp\left[\frac{U_h}{R}\left(\frac{1}{T_0} - \frac{1}{T}\right)\right] \qquad \text{Equation 3.30}$$

Where,

T_0 = 293° K,

T = absolute temperature during the time period dt' (°K), and

U_h/R = 5000° K.

The equivalent age after loading, $t_T - t_e'$, is given below by Equation 3.31.

$$t_T - t_e' = \int_{t'}^{t} \beta_T'(t')dt' \qquad \text{Equation 3.31}$$

With,

t = concrete age (days),

β_T' = temperature defined coefficient defined as:

$$\beta_T' = \exp\left[\frac{U_c}{R}\left(\frac{1}{T_0} - \frac{1}{T}\right)\right] \qquad \text{Equation 3.32}$$

Where,

U_c/R = activation energy ratio defined given by Equation 3.33, in which w is the water content of the concrete in lb/ft^3.

$$U_c/R = 110w^{-0.27}f_c'^{0.54} \qquad \text{Equation 3.33}$$

3.2.3.1 B3 Modulus of Elasticity

The modulus of elasticity at loading age t' is required to predict the compliance in the B3 creep prediction model. This value, $E(t')$, is predicted by using the 28-day modulus of elasticity, and it is given by Equation 3.34.

$$E(t') = E(28)\left(\frac{t}{4 + 0.85t}\right)^{1/2} \quad \text{Equation 3.34}$$

With,

$E(28)$ = Modulus of elasticity of concrete at 28 days (psi) defined as:

$$E(28) = 57{,}000(f_c')^{1/2} \quad \text{Equation 3.35}$$

3.2.3.2 B3 Creep Prediction Model

The B3 model used to predict creep results in a compliance function which accounts for three effects: instantaneous strain, basic creep, and drying creep. This function can be used to predict the creep coefficient and creep strain at any concrete age. The compliance, $J(t, t')$, is given by Equation 3.36 (Bažant and Baweja 2000).

$$J(t, t') = q_1 + C_0(t, t') + C_d(t, t', t_0) \quad \text{Equation 3.36}$$

With,

q_1 = instantaneous strain due to unit stress ($\times 10^{-6}$ /psi),

$C_0(t, t')$ = compliance function for basic creep ($\times 10^{-6}$ /psi), and

$C_d(t, t', t_0)$ = additional compliance function due to simultaneous drying ($\times 10^{-6}$ /psi).

The instantaneous strain due to unit stress, q_1, is given by Equation 3.37.

$$q_1 = 0.6 \times 10^6 / E(28) \quad \text{Equation 3.37}$$

The compliance function for basic creep, $C_0(t, t')$, is given by Equation 3.38.

$$C_0(t, t') = q_2 Q(t, t') + q_3 \ln\left[1 + (t - t')^n\right] + q_4 \ln\left(\frac{t}{t'}\right) \quad \text{Equation 3.38}$$

With,

q_2 = aging viscoelastic compliance defined as:

$$q_2 = 451.1c^{0.5} f_c'^{-0.9} \quad \text{Equation 3.39}$$

q_3 = non-aging viscoelastic compliance defined as:

$$q_3 = 0.29(w/c)^4 q_2 \quad \text{Equation 3.40}$$

q_4 = flow compliance defined as:

$$q_4 = 0.14(a/c)^{-0.7} \quad \text{Equation 3.41}$$

n = empirical parameter taken as 0.1, and

$Q(t, t')$ = function affecting aging viscoelastic compliance defined as:

$$Q(t, t') = Q_f(t')\left[1 + \left(\frac{Q_f(t')}{Z(t, t')}\right)^{r(t')}\right]^{-1/r(t')} \quad \text{Equation 3.42}$$

Where,

$$r(t') = 1.7(t')^{0.12} + 8 \quad \text{Equation 3.43}$$

$$Z(t, t') = (t')^{m}\ln\left[1 + (t - t')^{n}\right] \quad \text{Equation 3.44}$$

$$Q_f(t') = \left[0.086(t')^{2/9} + 1.21(t')^{4/9}\right]^{-1} \quad \text{Equation 3.45}$$

m = empirical parameter taken as 0.5.

The compliance function for additional creep due to drying, $C_d(t, t', t_0)$, is given by Equation 3.46.

$$C_d(t, t', t_0) = q_5\left[\exp\{-8H(t)\} - \exp\{-8H(t')\}\right]^{1/2} \quad \text{Equation 3.46}$$

With,

q_5 = empirical constitutive parameter for additional creep due to drying defined as:

$$q_5 = 7.57 \times 10^5 f_c'^{-1}|\varepsilon_{sh\infty}|^{-0.6} \quad \text{Equation 3.47}$$

Where,

$\varepsilon_{sh\infty}$ = ultimate drying shrinkage strain.

The ultimate drying shrinkage strain, $\varepsilon_{sh\infty}$, is given by Equation 3.48.

$$\varepsilon_{sh\infty} = \varepsilon_{s\infty}\frac{E(607)}{E(t_0 + \tau_{sh})} \quad \text{Equation 3.48}$$

With,

t_0 = equivalent age of concrete when drying begins (days),

τ_{sh} = shrinkage half-time (days) defined as:

$$\tau_{sh} = k_t(k_s D)^2 \quad \text{Equation 3.49}$$

Where,

k_t = parameter used in the calculation of τ_{sh} defined as:

$$k_t = 190.8t_0^{-0.08}f_c'^{-1/4} \quad \text{Equation 3.50}$$

k_s = cross-section shape factor defined as:

$$k_s = \begin{cases} 1.00 & \text{for an infinite slab} \\ 1.15 & \text{for an infinite cylinder} \\ 1.25 & \text{for an infinite square prism} \\ 1.30 & \text{for a sphere} \\ 1.55 & \text{for a cube} \end{cases} \quad \text{Equation 3.51}$$

D = effective cross-section thickness or double the volume to surface area ratio.

$\varepsilon_{s\infty}$ = constant shrinkage strain defined as:

$$\varepsilon_{s\infty} = -\alpha_1\alpha_2\left[26w^{2.1}f_c'^{-0.28} + 270\right] \quad \text{Equation 3.52}$$

Where,

α_1 = cement type parameter defined as:

$$\alpha_1 = \begin{cases} 1.0 & \text{for type I cement} \\ 0.85 & \text{for type II cement} \\ 1.1 & \text{for type III cement} \end{cases} \quad \text{Equation 3.53}$$

α_2 = curing type parameter defined as:

$$\alpha_2 = \begin{cases} 0.75 & \text{for steam-curing} \\ 1.2 & \text{for sealed or normal curing in air with initial protection against drying} \\ 1.0 & \text{for curing in water or at 100\% relatvie humidity} \end{cases}$$

Equation 3.54

w = water content of concrete (lb/ft^3).

The spatial average of pore relative humidity within the cross section for any time after curing, $H(t)$, is given by Equation 3.55.

$$H(t) = 1 - (1 - h)S(t) \quad \text{Equation 3.55}$$

With,

h = relative humidity expressed as a decimal

$S(t)$ = time function for shrinkage defined as:

$$S(t) = \tanh\left(\frac{t - t_0}{\tau_{sh}}\right)^{1/2} \quad \text{Equation 3.56}$$

The spatial average of pore relative humidity within the cross section for the end of curing, $H(t')$, is given by Equation 3.57.

$$H(t') = 1 - (1 - h)S(t') \quad \text{Equation 3.57}$$

With,

$S(t')$ = time function for shrinkage defined as:

$$S(t') = \tanh\left(\frac{t' - t_0}{\tau_{sh}}\right)^{1/2} \quad \text{Equation 3.58}$$

3.2.3.3 B3 Shrinkage Prediction Model

The B3 model used to predict drying shrinkage uses the ultimate shrinkage strain to predict the shrinkage strain at any age after drying begins. Because creep due to drying shrinkage is considered in the B3 creep prediction model, the majority of the shrinkage model is defined in the

creep model. The mean drying shrinkage strain in the cross section at any age after curing is given by Equation 3.59 (Bažant and Baweja 2000).

$$\varepsilon_{sh}(t, t_0) = -\varepsilon_{sh\infty} k_h S(t) \qquad \text{Equation 3.59}$$

With,

k_h = relative humidity factor defined as:

$$k_h = \begin{cases} 1 - h^3 & \text{for } h \le 0.98 \\ -0.2 & \text{for } h = 1 \text{ (swelling in water)} \\ \text{linear interpolation} & \text{for } 0.98 \le h \le 1 \end{cases} \qquad \text{Equation 3.60}$$

3.2.4 B4 Prediction Model

The B4 model used to predict creep and shrinkage builds upon the B3 model and was introduced by Bažant (2015). Like the B3 model, several of the parameters are restricted to the ranges presented in Table 3-4 (Bažant 2015) for the model to be valid. These ranges were broadened relative to the ranges of the B3 model through calibration.

Table 3-4: Parameter ranges for the B4 model (Bažant 2015)

Parameter Definition	Parameter Range
w/c = water-cement ratio by weight	$0.22 \le w/c \le 0.87$
a/c = aggregate-cement ratio by weight	$1.0 \le a/c \le 13.2$
f_c' = 28 day standard cylinder compression strength of concrete (psi)	$2{,}070 \le f_c' \le 10{,}000$
c = cement content (lb/ft^3)	$12.5 \le c \le 93.6$
T = temperature of the environment (°C)	$-25°C \le T \le 75°C$
T_{cur} = temperature of the environment during curing (°C)	$20°C \le T_{cur} \le 30°C$
V/S = volume-surface ratio (mm.)	$12 \le V/S \le 120$

Like the B3 model, the B4 model uses a maturity function to adjust the concrete ages for temperature effects. The age at exposure, exposure duration, and age at loading are all corrected according to Equations 3.61, 3.63, and 3.65, respectively. All time-dependent factors in the creep and shrinkage models use these temperature-corrected values.

$$\tilde{t}_0 = t_0 \beta_{Th} \qquad \text{Equation 3.61}$$

With,

$\tilde{t}_0$ = temperature corrected age at exposure (days),

t_0 = age at start of environmental exposure (days),

β_{Th} = curing temperature coefficient defined as:

$$\beta_{Th} = \exp\left[\frac{U_h}{R}\left(\frac{1}{293} - \frac{1}{T_{cur} + 273}\right)\right] \qquad \text{Equation 3.62}$$

for any constant temperature $T_{cur} \in [20°C, 30°C]$

Where,

U_h/R = 4,000 K.

$$\tilde{t} = (t - t_0)\beta_{Ts} \quad \text{Equation 3.63}$$

With,

$\tilde{t}$ = temperature corrected exposure duration (days),

t = concrete age (days),

β_{Ts} = exposure temperature coefficient defined as:

$$\beta_{Ts} = \exp\left[\frac{U_s}{R}\left(\frac{1}{293} - \frac{1}{T + 273}\right)\right] \quad \text{Equation 3.64}$$

Where,

U_s/R = 4,000 K.

$$\hat{t}' = t_0\beta_{Th} + (t' - t_0)\beta_{Ts} \quad \text{Equation 3.65}$$

With,

$\hat{t}'$ = temperature corrected age at loading (days), and

t' = age at loading (days).

$$\hat{t} = \hat{t}' + (t - t')\beta_{Tc} \quad \text{Equation 3.66}$$

With,

$\hat{t}$ = temperature corrected current age (days), and

β_{Tc} = exposure temperature coefficient defined as:

$$\beta_{Tc} = \exp\left[\frac{U_c}{R}\left(\frac{1}{293} - \frac{1}{T + 273}\right)\right] \quad \text{Equation 3.67}$$

Where,

U_c/R = 4000 K.

3.2.4.1 B4 Modulus of Elasticity

The B4 creep prediction model predicts the modulus of elasticity of concrete at any age, $E(t)$, based on the 28-day elastic modulus. This 28-day value is calculated with the ACI equation for modulus of elasticity. These values are given by Equations 3.68 and 3.69 (Bažant 2015).

$$E(t) = E_{28}\left(\frac{t}{4 \text{ days} + (6/7)\,t}\right)^{1/2} \quad \text{Equation 3.68}$$

With,

E_{28} = 28-day modulus of elasticity defined as:

$$E_{28} = 57{,}000(f_c')^{1/2} \quad \text{Equation 3.69}$$

3.2.4.2 B4 Creep Prediction Model

Like the B3 model, the B4 creep prediction model predicts the compliance function as the sum of three parts: instantaneous strain, basic creep, and drying creep. However, the B4 model uses a different approach to obtain these values. The compliance function, $J(\hat{t}, \hat{t}')$, is given by Equation 3.70.

$$J(\hat{t}, \hat{t}') = q_1 + R_T C_0(\hat{t}, \hat{t}') + C_d(\hat{t}, \hat{t}', \tilde{t}_0) \quad \text{Equation 3.70}$$

With,

q_1 = instantaneous compliance ($\times 10^{-6}$ /psi),

$C_0(\hat{t}, \hat{t}')$ = basic creep compliance ($\times 10^{-6}$ /psi),

$C_d(\hat{t}, \hat{t}', \tilde{t}_0)$ = drying creep compliance ($\times 10^{-6}$ /psi), and

R_T = temperature coefficient for basic creep compliance defined as:

$$R_T = \exp\left[\frac{U_c'}{R}\left(\frac{1}{293} - \frac{1}{T + 273}\right)\right] \quad \text{Equation 3.71}$$

Where,

U_c'/R = 4,000 K.

The instantaneous compliance, q_1, is given by Equation 3.72.

$$q_1 = \frac{p_1}{E_{28}} \quad \text{Equation 3.72}$$

With,

p_1 = cement type dependent factor presented in Table 3-5.

q_2 = aging viscoelastic creep defined as:

$$q_2 = \frac{p_2}{1\text{GPa}}\left(\frac{w/c}{0.38}\right)^{p_{2w}} \quad \text{Equation 3.74}$$

Where,

p_2, p_{2w} = cement type dependent factors presented in Table 3-5.

q_3 = non-aging viscoelastic creep defined as:

$$q_3 = p_3 q_2 \left(\frac{a/c}{6}\right)^{p_{3a}} \left(\frac{w/c}{0.38}\right)^{p_{3w}} \quad \text{Equation 3.75}$$

Where,

p_3, p_{3a}, p_{3w} = cement type factors presented in Table 3-5.

Table 3-5: Creep parameters depending on cement type for the B4 model (Bažant 2015)

Parameter	R	RS	SL
p_1	0.70	0.60	0.80
p_2	58.6×10^{-3}	17.4×10^{-3}	40.5×10^{-3}
p_3	39.3×10^{-3}	39.3×10^{-3}	39.3×10^{-3}
p_4	3.4×10^{-3}	3.4×10^{-3}	3.4×10^{-3}
p_5	777×10^{-6}	94.6×10^{-6}	496×10^{-6}
p_{5H}	8.00	1.00	8.00
p_{2w}	3.00	3.00	3.00
p_{3a}	−1.10	−1.10	−1.10
p_{3w}	0.40	0.40	0.40
p_{4a}	−0.90	−0.90	−0.90
p_{4w}	2.45	2.45	2.45
$p_{5\varepsilon}$	−0.85	−0.85	−0.85
p_{5a}	−1.00	−1.00	−1.00
p_{5w}	0.78	0.78	0.78

The basic creep compliance function $C_0(t, t')$, is given by Equation 3.73.

$$C_0(\hat{t}, \hat{t}') = q_2 Q(\hat{t}, \hat{t}') + q_3 \ln\left[1 + \left(\frac{\hat{t} - \hat{t}'}{1\ \text{day}}\right)\right] + q_4 \ln\left(\frac{\hat{t}}{\hat{t}'}\right) \qquad \text{Equation 3.73}$$

q_4 = flow defined as:

$$q_4 = \frac{p_4}{1\text{GPa}}\left(\frac{a/c}{6}\right)^{p_{4a}}\left(\frac{w/c}{0.38}\right)^{p_{4w}} \qquad \text{Equation 3.76}$$

Where,

p_4, p_{4a}, p_{4w} = cement type dependent factors presented in Table 3-5.

$Q(\hat{t}, \hat{t}')$ = binomial integral which cannot be expressed analytically, but can be calculated from the following approximate explicit formula:

$$Q(\hat{t}, \hat{t}') = Q_f(\hat{t}')\left(1 + \left(\frac{Q_f(\hat{t}')}{Z(\hat{t}, \hat{t}')}\right)^{r(\hat{t}')}\right)^{-\frac{1}{r(\hat{t}')}} \qquad \text{Equation 3.77}$$

Where,

$$Q_f(\hat{t}') = \left[0.086\left(\frac{\hat{t}'}{1\ \text{day}}\right)^{2/9} + 1.21\left(\frac{\hat{t}'}{1\ \text{day}}\right)^{4/9}\right]^{-1} \qquad \text{Equation 3.78}$$

$$Z(\hat{t}') = \left(\frac{\hat{t}'}{1\ \text{day}}\right)^{-0.5} \ln\left[1 + \left(\frac{\hat{t} - \hat{t}'}{1\ \text{day}}\right)^{0.1}\right] \qquad \text{Equation 3.79}$$

$$r(\hat{t}') = 1.7\left(\frac{\hat{t}'}{1\ \text{day}}\right)^{0.12} + 8 \qquad \text{Equation 3.80}$$

The drying creep compliance function, $C_d(\hat{t}, \hat{t}', \tilde{t}_0)$, is given by Equation 3.81.

$$C_d(\hat{t}, \hat{t}', \tilde{t}_0) = q_5 \langle \exp[-p_{5H} H(\hat{t}, \tilde{t}_0)] - \exp\left[-p_{5H} H_c(\hat{t}_0', \tilde{t}_0)\right] \rangle^{0.5} \qquad \text{Equation 3.81}$$

With,

q_5 = drying creep parameter defined as:

$$q_5 = \frac{p_5}{1\text{GPa}} \left(\frac{a/c}{6}\right)^{p_{5a}} \left(\frac{w/c}{0.38}\right)^{p_{5w}} \left|k_h \varepsilon_{sh\infty}(\tilde{t}_0)\right|^{p_{5\varepsilon}} \qquad \text{Equation 3.82}$$

Where,

p_5, p_{5a}, p_{5w}, $p_{5\varepsilon}$ = cement type dependent factors presented in Table 3-5,

k_h = humidity dependent factor in which h = ambient relative humidity defined as:

$$k_h = \begin{cases} 1 - h^3 & h \le 0.98 \\ 12.94(1 - h) - 0.2 & 0.98 \le h \le 1 \end{cases} \qquad \text{Equation 3.83}$$

$\varepsilon_{sh\infty}(\tilde{t}_0)$ = ultimate shrinkage strain.

The ultimate shrinkage strain, $\varepsilon_{sh\infty}(\tilde{t}_0)$, is given by Equation 3.84.

$$\varepsilon_{sh\infty}(\tilde{t}_0) = -\varepsilon_0 k_{\varepsilon a} \frac{E(7\beta_{Th} + 600\beta_{Ts})}{E(\tilde{t}_0 + \tau_{sh}\beta_{Ts})} \qquad \text{Equation 3.84}$$

With,

ε_0 = final drying shrinkage defined as:

$$\varepsilon_0 = \varepsilon_{cem} \left(\frac{a/c}{6}\right)^{p_{\varepsilon a}} \left(\frac{w/c}{0.38}\right)^{p_{\varepsilon w}} \left(\frac{6.5c}{\rho}\right)^{p_{\varepsilon c}} \qquad \text{Equation 3.85}$$

Where,

ε_{cem}, $p_{\varepsilon a}$, $p_{\varepsilon w}$, $p_{\varepsilon c}$ = cement type dependent factors presented in Table 3-6 and

ρ = 2,350 kg/m^3.

$k_{\varepsilon a}$ = aggregate dependent parameter presented in Table 3-7, and

τ_{sh} = drying shrinkage halftime.

Table 3-6: Shrinkage parameters depending on cement type for the B4 model (Bažant 2015)

Parameter	R	RS	SL
τ_{cem} (days)	0.016	0.080	0.010
$p_{\tau a}$	-0.33	-0.33	-0.33
$p_{\tau w}$	-0.06	-2.40	3.55
$p_{\tau c}$	-0.10	-2.70	3.80
ε_{cem}	360×10^{-6}	860×10^{-6}	410×10^{-6}
$p_{\varepsilon a}$	-0.80	-0.80	-0.80
$p_{\varepsilon w}$	1.10	-0.27	1.00
$p_{\varepsilon c}$	0.11	0.11	0.11

Table 3-7: Aggregate dependent parameter scaling factors for shrinkage for the B4 model (Bažant 2015)

Aggregate type	$k_{\tau a}$	$k_{\varepsilon a}$
Diabase	0.06	0.76
Quartzite	0.59	0.71
Limestone	1.80	0.95
Sandstone	2.30	1.60
Granite	4.00	1.05
Quartz Diorite	15.0	2.20

The drying shrinkage halftime, τ_{sh}, is given by Equation 3.86.

$$\tau_{sh} = \tau_0 k_{\tau a} \left(k_s \frac{D}{1\text{mm.}} \right)^2 \qquad \text{Equation 3.86}$$

With,

D = effective thickness or double the volume-surface ratio (mm.),

$k_{\tau a}$ = aggregate dependent parameter presented in Table 3-7,

k_s = specimen geometry parameter defined as:

$$k_s = \begin{cases} 1.00 & \text{infinite slab} \\ 1.15 & \text{infinite cylinder} \\ 1.25 & \text{infinite square prism} \\ 1.30 & \text{sphere} \\ 1.55 & \text{cube} \end{cases} \qquad \text{Equation 3.87}$$

τ_0 = drying shrinkage halftime parameter defined as:

$$\tau_0 = \tau_{cem} \left(\frac{a/c}{6} \right)^{p_{\tau a}} \left(\frac{w/c}{0.38} \right)^{p_{\tau w}} \left(\frac{6.5c}{\rho} \right)^{p_{\tau c}} \qquad \text{Equation 3.88}$$

Where,

τ_{cem}, $p_{\tau a}$, $p_{\tau w}$, $p_{\tau c}$ = cement type dependent parameters presented in Table 3-6.

3.2.4.3 B4 Shrinkage Prediction Model

The main difference between the shrinkage prediction models for the B3 and the B4 models is that the B4 model separately models the effects of drying and autogenous shrinkage. The total shrinkage strain at any age, $\varepsilon_{sh,total}(\tilde{t}, \tilde{t}_0)$, is given by Equation 3.89.

$$\varepsilon_{sh,total}(\tilde{t}, \tilde{t}_0) = \varepsilon_{sh}(\tilde{t}, \tilde{t}_0) + \varepsilon_{au}(\tilde{t}, \tilde{t}_0) \quad \text{Equation 3.89}$$

With,

$\varepsilon_{sh}(\tilde{t}, \tilde{t}_0)$ = drying shrinkage strain at any age and

$\varepsilon_{au}(\tilde{t}, \tilde{t}_0)$ = autogenous shrinkage strain at any age.

The drying shrinkage strain at any age, $\varepsilon_{sh}(\tilde{t}, \tilde{t}_0)$, is given by Equation 3.90.

$$\varepsilon_{sh}(\tilde{t}, \tilde{t}_0) = \varepsilon_{sh\infty}(\tilde{t}_0) k_h S(\tilde{t}) \quad \text{Equation 3.90}$$

With,

$S(\tilde{t})$ = time curve defined as:

$$S(\tilde{t}) = \tanh\sqrt{\frac{\tilde{t}}{\tau_{sh}}} \quad \text{Equation 3.91}$$

The autogenous shrinkage strain at any age, $\varepsilon_{au}(\tilde{t}, \tilde{t}_0)$, is given by Equation 3.92.

$$\varepsilon_{au}(\tilde{t}, \tilde{t}_0) = \varepsilon_{au\infty}\left[1 + \left(\frac{\tau_{au}}{\tilde{t} + \tilde{t}_0}\right)^{\alpha}\right]^{r_t} \quad \text{Equation 3.92}$$

With,

$\varepsilon_{au\infty}$ = final autogenous shrinkage defined as:

$$\varepsilon_{au\infty} = -\varepsilon_{au,cem}\left(\frac{a/c}{6}\right)^{r_{\varepsilon a}}\left(\frac{w/c}{0.38}\right)^{r_{\varepsilon w}} \quad \text{Equation 3.93}$$

Where,

$\varepsilon_{au,cem}$, $r_{\varepsilon a}$, $r_{\varepsilon w}$ = cement type dependent parameters presented in Table 3-8.

τ_{au} = autogenous shrinkage halftime defined as:

$$\tau_{au} = \tau_{au,cem}\left(\frac{w/c}{0.38}\right)^{r_{\tau w}} \quad \text{Equation 3.94}$$

Where,

$\tau_{au,cem}$, $r_{\tau w}$ = cement type dependent parameters presented in Table 3-8.

α = autogenous shrinkage exponent defined as:

$$\alpha = r_{\alpha}\left(\frac{w/c}{0.38}\right) \quad \text{Equation 3.95}$$

Where,

r_{α} = cement type dependent parameter presented in Table 3-8.

r_t = cement type dependent parameter presented in Table 3-8.

Table 3-8: Autogenous shrinkage parameters depending on cement type for the B4 model (Bažant 2015)

Parameter	R	RS	SL
$\tau_{au,cem}$ (days)	1.00	41.0	1.00
$r_{\tau w}$	3.00	3.00	3.00
r_t	-4.50	-4.50	-4.50
r_α	1.00	1.40	1.00
$\varepsilon_{au,cem}$	210×10^{-6}	-84.0×10^{-6}	0.00×10^{-6}
$r_{\varepsilon a}$	-0.75	-0.75	-0.75
$r_{\varepsilon w}$	-3.50	-3.50	-3.50

3.2.4.4 B4* Prediction Models

The B4 prediction models provide *optional* scaling factors for certain creep and shrinkage parameters based on admixtures. These scaling factors are presented in Tables 3-9 and 3-10. Bažant (2015) states that when multiple admixtures are present, the first applicable class according to both tables "should be selected as it represents the most likely effects governing the long-term shrinkage and creep." For the purposes of this research, the models implementing these factors will be referred to as the "B4" model, and the models not implementing these factors will be referred to as the "B4*" model.

Table 3-9: Admixture dependent parameter scaling factors for creep for the B4 model (Bažant 2015)

Admixture class (% of c)	$\times p_2$	$\times p_3$	$\times p_4$	$\times p_5$
Re[a.](≤ 0.5), Fly[b.](≤ 15)	0.31	7.14	1.35	0.48
Re(> 0.5), Fly(≤ 15)	1.43	0.58	0.90	0.46
Fly(≥ 15)	0.37	2.33	0.63	1.60
Super[c.](≥ 0)	0.72	2.19	1.72	0.48
Silica[d.](≥ 0)	1.12	3.11	0.51	0.61
AEA[e.](≥ 0)	0.90	3.17	1.00	0.10
WR[f.](≤ 2)	1.00	2.10	1.68	0.45
WR(> 2, ≤ 3)	1.41	0.72	1.76	0.60
WR(> 3)	1.28	2.58	0.73	1.10

a. Re = retarder, b. Fly = fly ash, c. Super = superplasticizer, d. Silica = silica fume, e. AEA = air entraining agent, f. WR = water reducer.

Table 3-10: Admixture dependent parameter scaling factors for shrinkage for the B4 model (Bažant 2015)

Admixture class (% of c)	× r_{cem}	× $\varepsilon_{au,cem}$	× $r_{\varepsilon w}$	× r_{α}
Re(≤ 0.5), Fly(≤ 15)	6.00	0.58	0.50	2.60
Re(> 0.5, ≤ 0.6), Fly(≤ 15)	2.00	0.43	0.59	3.10
Re(> 0.5, ≤ 0.6), Fly(> 15, ≤ 30)	2.10	0.72	0.88	3.40
Re(> 0.5, ≤ 0.6), Fly(> 30)	2.80	0.87	1.60	5.00
Re(> 0.6), Fly(≤ 15)	2.00	0.26	0.22	0.95
Re(> 0.6), Fly(> 15, ≤ 30)	2.10	1.10	1.10	3.30
Re(> 0.6), Fly(> 30)	2.10	1.10	0.97	4.00
Fly(≤ 15), Super(≤ 5)	0.32	0.71	0.55	1.71
Fly(≤ 15), Super(> 5)	0.32	0.55	0.92	2.30
Fly(> 15, ≤ 30), Super(≤ 5)	0.50	0.90	0.82	1.25
Fly(> 15, ≤ 30), Super(> 5)	0.50	0.80	0.80	2.81
Fly(> 30), Super(≤ 5)	0.63	1.38	0.00	1.20
Fly(> 30), Super(> 5)	0.63	0.95	0.76	3.11
Super(≤ 5),Silica(≤ 8)	6.00	2.80	0.29	0.21
Super(≤ 5), Silica(≥ 8)	3.00	0.96	0.26	0.71
Super(≥ 5), Silica(≤ 8)	8.00	1.95	0.00	1.00
Silica(≤ 8)	1.90	0.47	0.00	1.20
Silica(> 8, ≤ 18)	2.60	0.82	0.00	1.20
Silica(> 18)	1.00	1.50	5.00	1.00
AEA(≤ 0.05)	2.30	1.10	0.28	0.35
AEA(> 0.05)	0.44	4.28	0.00	0.36
WR(≤ 2)	0.50	0.38	0.00	1.90
WR(> 2, ≤ 3)	6.00	0.45	1.51	0.30
WR(> 3)	2.40	0.40	0.68	1.40

3.2.5 CEB MC 1990 Prediction Model

The CEB MC 1990 model for predicting creep and shrinkage was introduced in the CEB-FIP Model Code 1990. This model uses the notional creep coefficient to predict the creep coefficient at any age, as well as the compliance. It also uses the ultimate shrinkage strain to predict the shrinkage strain at any age. This model accounts for member shape and size, relative humidity, compressive strength, and cement type. CEB MC 1990 also recommends the use of the equivalent age for all time inputs given by Equation 3.96 (CEB 1990).

$$t_T = \sum_{i=1}^{n} \Delta t_i \exp\left[13.65 - \frac{4000}{273 + T(\Delta t_i)/T_0}\right] \qquad \text{Equation 3.96}$$

With,

t_T = temperature adjusted concrete age which replaces t in the corresponding equations,

Δt_i = number of days where a temperature T prevails,

$T(\Delta t_i)$ = temperature during the time period Δt (°C), and

T_0 = 1°C.

3.2.5.1 CEB MC 1990 Modulus of Elasticity

To predict compliance with the CEB MC 1990 creep model, the elastic modulus at 28 days, E_{ci}, and the elastic modulus at the time of loading, $E_{ci}(t)$, are required. The predicted modulus of elasticity is based primarily on concrete strength and age of loading, along with the cement type. The CEB MC 1990 models are also in SI units, so all predicted values were converted in this work. The elastic modulus values in MPa, along with all input parameters are given by the following equations (CEB 1990).

$$E_{ci} = E_{co}[f_{cm}/10]^{1/3} \qquad \text{Equation 3.97}$$

With,

E_{co} = 21,500 MPa and

f_{cm} = mean compressive strength at 28 days (MPa).

$$E_{ci}(t) = \left[\beta_{cc}(t)\right]^{0.5} E_{ci} \qquad \text{Equation 3.98}$$

With,

$\beta_{cc}(t)$ = coefficient which depends on the age of concrete defined as:

$$\beta_{cc}(t) = \exp\left\{s\left[1 - \left(\frac{28}{t}\right)^{1/2}\right]\right\} \qquad \text{Equation 3.99}$$

Where,

s = coefficient which depends on the type of cement defined as:

$$s = \begin{cases} 0.20 & \text{for rapid hardening high strength cements (RS)} \\ 0.25 & \text{for normal and rapid hardening cements (N and R)} \\ 0.38 & \text{for slowly hardening cements (SL)} \end{cases} \qquad \text{Equation 3.100}$$

3.2.5.2 CEB MC 1990 Creep Prediction Model

The CEB MC 1990 model used to predict creep results in a notional creep coefficient, which can then be used to predict the creep coefficient and compliance at any concrete age, as well as creep strain. All concrete ages, t, are already adjusted to account for temperature based on Equation 3.96, however, this model also recommends for the concrete age of loading, t_0, to be adjusted based on the cement type. This adjustment is given by Equation 3.101 (CEB 1990).

$$t_0 = t_{0,T}\left[\frac{9}{2 + (t_{0,T})^{1.2}} + 1\right]^{\alpha} \geq 0.5 \text{ days} \qquad \text{Equation 3.101}$$

With,

$t_{0,T}$ = age of concrete at loading adjusted according to Equation 3.96 (days) and

α = power which depends on the type of cement defined as:

$$\alpha = \begin{cases} -1 \text{ for SL cements} \\ 0 \text{ for N and R cements} \\ 1 \text{ for RS cements} \end{cases} \qquad \text{Equation 3.102}$$

According to CEB MC 1990, the notional creep coefficient used to predict the creep coefficient at any concrete age, ϕ_0, is given by Equation 3.103.

$$\phi_0 = \phi_{RH}\beta(f_{cm})\beta(t_0) \qquad \text{Equation 3.103}$$

With,

ϕ_{RH} = creep coefficient based on relative humidity defined as:

$$\phi_{RH} = 1 + \frac{1 - RH/100}{0.46(h/100)^{1/3}} \qquad \text{Equation 3.104}$$

Where,

RH = ambient relative humidity (percent) and

h = notational size of member (mm.) defined as:

$$h = 2A_c/u \qquad \text{Equation 3.105}$$

Where,

A_c = cross-sectional area of member (mm.^{2}) and

u = perimeter of the member in contact with the atmosphere (mm.).

$\beta(f_{cm})$ = concrete compressive strength factor defined as:

$$\beta(f_{cm}) = \frac{5.3}{(f_{cm}/10)^{0.5}} \qquad \text{Equation 3.106}$$

Where,

f_{cm} = mean compressive strength at 28 days (MPa).

$\beta(t_0)$ = loading age factor defined as:

$$\beta(t_0) = \frac{1}{0.1 + (t_0)^{0.2}} \qquad \text{Equation 3.107}$$

According to CEB MC 1990, the creep coefficient at any concrete age, $\phi(t, t_0)$, is given by Equation 3.108.

$$\phi(t, t_0) = \phi_0\beta_c(t - t_0) \qquad \text{Equation 3.108}$$

With,

$\beta_c(t - t_0)$ = time development factor defined as:

$$\beta_c(t - t_0) = \left[\frac{t - t_0}{\beta_H + (t - t_0)}\right]^{0.3} \quad \text{Equation 3.109}$$

Where,

t = concrete age adjusted according to Equation 3.96 and

β_H = relative humidity factor defined as:

$$\beta_H = 150\left\{1 + \left(1.2\frac{RH}{100}\right)^{18}\right\}\frac{h}{100} + 250 \leq 1500 \quad \text{Equation 3.110}$$

Upon calculating the predicted creep coefficient and elastic moduli, the compliance may be given by Equation 3.111 (CEB 1990).

$$J(t, t_0) = \frac{1}{E_{ci}(t_0)} + \frac{\phi(t, t_0)}{E_{ci}} \quad \text{Equation 3.111}$$

3.2.5.3 CEB MC 1990 Shrinkage Prediction Model

The CEB MC 1990 model used to predict shrinkage results in a notional shrinkage strain, ε_{cso}, which can be used to calculate the predicted shrinkage strain at any age, $\varepsilon_{cs}(t, t_0)$. The notional shrinkage strain is given by Equation 3.112.

$$\varepsilon_{cso} = \varepsilon_s(f_{cm})\beta_{RH} \quad \text{Equation 3.112}$$

With,

$\varepsilon_s(f_{cm})$ = factor accounting for the compressive strength of concrete and cement type defined as:

$$\varepsilon_s(f_{cm}) = \left[160 + 10\beta_{sc}(9 - f_{cm}/10)\right] \times 10^{-6} \quad \text{Equation 3.113}$$

Where,

β_{sc} = coefficient which depends on the type of cement defined as:

$$\beta_{sc} = \begin{cases} 4 & \text{for SL cements} \\ 5 & \text{for N and R cements} \\ 8 & \text{for RS cements} \end{cases} \quad \text{Equation 3.114}$$

β_{RH} = coefficient which depends on relative humidity defined as:

$$\beta_{RH} = \begin{cases} -1.55\beta_{sRH} & \text{for } 40\% \leq RH \leq 99\% \\ +0.25 & \text{for } RH \geq 99\% \end{cases} \quad \text{Equation 3.115}$$

Where,

β_{sRH} = coefficient to determine relative humidity coefficient defined as:

$$\beta_{sRH} = 1 - \left(\frac{RH}{100}\right)^3 \quad \text{Equation 3.116}$$

According to CEB MC 1990, the total shrinkage strain at any concrete age is given by Equation 3.117.

$$\varepsilon_{cs}(t, t_s) = \varepsilon_{cso}\beta_s(t - t_s) \quad \text{Equation 3.117}$$

With,

$\beta_s(t - t_s)$ = coefficient to account for the development of shrinkage with time defined as:

$$\beta_s(t - t_s) = \left[\frac{(t - t_s)}{350(h/100)^2 + (t - t_s)}\right]^{0.5} \quad \text{Equation 3.118}$$

Where,

t = age of concrete adjusted according to Equation 3.96 (days) and

t_s = age of concrete at the beginning of shrinkage adjusted according to Equation 3.96 (days).

3.2.6 CEB MC 90-99 Prediction Model

The CEB MC 1990 model used to predict creep and shrinkage was modified in 1999, and for the purposes of this research, this modified prediction model is referred to CEB MC 90-99 (CEB 1999). The CEB MC 90-99 model provides small modifications to the creep portion, but the shrinkage portion is entirely new in the 1999 modification. In this model, both drying and autogenous shrinkage are modeled separately in the prediction of total shrinkage. Like the CEB MC 1990 model, the CEB MC 90-99 model also recommends the use of the same equivalent age for all time inputs previously defined in Equation 3.96. (CEB 1999).

3.2.6.1 CEB MC 90-99 Modulus of Elasticity

The prediction of the modulus of elasticity of concrete according to the CEB MC 90-99 model is very similar to that of the CEB MC 1990 model. However, a modification factor is added to account for the aggregate type of the concrete, and several of the equations are slightly adjusted. The CEB MC 90-99 prediction of the elastic modulus at the time of loading, $E_{ci}(t)$, as well as the 28-day value, E_{ci}, are defined in the equations below (CEB 1999).

$$E_{ci} = \alpha_E \cdot E_{co}\left[\frac{f_{cm}}{f_{cmo}}\right]^{1/3} \quad \text{Equation 3.119}$$

With,

$E_{co} = 2.5 \times 10^4$ MPa,

f_{cm} = mean compressive strength at 28 days (MPa),

f_{cmo} = 10 MPa, and

α_E = aggregate type coefficient defined as:

$$\alpha_E = \begin{cases} 1.2 & \text{for basalt, dese limestone} \\ 1.0 & \text{for quartzite aggregates} \\ 0.9 & \text{for limestone} \\ 0.7 & \text{for sandstone} \end{cases} \quad \text{Equation 3.120}$$

$$E_{ci}(t) = \beta_E(t) \cdot E_{ci} \quad \text{Equation 3.121}$$

With,

$\beta_E(t)$ = function to describe the development of modulus of elasticity with time defined as:

$$\beta_E(t) = \left[\beta_{cc}(t)\right]^{0.5} \quad \text{Equation 3.122}$$

The time-dependent factor used to calculate the modulus of elasticity at the time of loading, $\beta_{cc}(t)$, is given by Equation 3.123.

$$\beta_{cc}(t) = \exp\left\{s\left[1 - \left(\frac{28}{t/t_1}\right)^{1/2}\right]\right\} \quad \text{Equation 3.123}$$

With,

t = concrete age (days),

t_1 = 1 day, and

s = coefficient which depends on the strength class of cement defined as:

$$s = \begin{cases} 0.38 & \text{for 32.5 cements} \\ 0.25 & \text{for 32.5R 42.5 cements} \\ 0.20 & \text{for 42.5R 52.5 cements} \end{cases} \quad \text{Equation 3.124}$$

3.2.6.2 CEB MC 90-99 Creep Prediction Model

The CEB MC 90-99 creep prediction model does not differ much from the original CEB MC 1990 creep prediction model; however, several of the equations are slightly different such that the two models do not predict the same compliance values. The compliance function according to the CEB MC 90-99 model, $J(t, t_o)$, is given by Equation 3.125.

$$J(t, t_o) = \frac{1}{E_c(t_o)} + \frac{\phi(t, t_o)}{E_{ci}} \quad \text{Equation 3.125}$$

With,

$E_c(t_o)$ = modulus of elasticity at the time of loading and

$\phi(t, t_o)$ = creep coefficient defined as:

$$\phi(t, t_o) = \phi_o \cdot \beta_c(t, t_o) \quad \text{Equation 3.126}$$

Where,

ϕ_o = notional creep coefficient and

$\beta_c(t, t_o)$ = coefficient to describe the development of creep with time after loading.

The notional creep coefficient used to calculate the CEB MC 90-99 creep coefficient is given by Equation 3.127.

$$\phi_o = \phi_{RH} \cdot \beta(f_{cm}) \cdot \beta(t_o) \qquad \text{Equation 3.127}$$

With,

ϕ_{RH} = relative humidity factor,

$\beta(f_{cm})$ = concrete strength factor defined as:

$$\beta(f_{cm}) = \frac{5.3}{(f_{cm}/f_{cmo})^{0.5}} \qquad \text{Equation 3.128}$$

$\beta(t_o)$ = loading age factor defined as:

$$\beta(t_o) = \frac{1}{0.1 + (t_o/t_1)^{0.2}} \qquad \text{Equation 3.129}$$

Where,

t_o = adjusted concrete age at the time of loading.

The relative humidity factor used to calculate the notional creep coefficient according to the CEB MC 90-99 model is given by Equation 3.130.

$$\phi_{RH} = \left[1 + \frac{1 - RH/RH_o}{\sqrt[3]{0.1 \cdot h/h_o}} \cdot \alpha_1\right] \cdot \alpha_2 \qquad \text{Equation 3.130}$$

With,

RH = relative humidity of the ambient environment (%),

RH_o = 100%,

h = size effect factor defined as:

$$h = 2A_c/u \qquad \text{Equation 3.131}$$

Where,

A_c = cross section of the structural member (mm^2) and

u = perimeter of the structural member in contact with the atmosphere (mm).

h_o = 100 mm,

α_1 and α_2 = coefficients which depend on the compressive strength defined as:

$$\alpha_1 = \left[\frac{3.5}{f_{cm}/f_{cmo}}\right]^{0.7} \qquad \text{Equation 3.132}$$

$$\alpha_2 = \left[\frac{3.5}{f_{cm}/f_{cmo}}\right]^{0.2} \qquad \text{Equation 3.133}$$

The coefficient to describe the development of creep with time after loading, $\beta_c(t, t_o)$, is given by Equation 3.134.

$$\beta_c(t, t_o) = \left[\frac{(t - t_o)/t_1}{\beta_H + (t - t_o)/t_1}\right]^{0.3} \qquad \text{Equation 3.134}$$

With,

β_H = coefficient defined as:

$$\beta_H = 150\frac{h}{h_o}\left[1 + \left(1.2 \cdot \frac{RH}{RH_o}\right)^{18}\right] + 250\alpha_3 \leq 1500\alpha_3 \qquad \text{Equation 3.135}$$

Where,

α_3 = coefficient which depends on compressive strength defined as:

$$\alpha_3 = \left[\frac{3.5}{f_{cm}/f_{cmo}}\right]^{0.5} \qquad \text{Equation 3.136}$$

The CEB MC 90-99 creep prediction model also recommends adjusting the loading age to account for the effects of cement type in addition to the adjustments performed to account for temperature covered by the original CEB MC 1990 model. The loading age adjusted for cement type is given by Equation 3.137.

$$t_o = t_{o,T} \cdot \left[\frac{9}{2 + (t_{o,T}/t_{1,T})^{1.2}} + 1\right]^{\alpha} \geq 0.5 \qquad \text{Equation 3.137}$$

With,

$t_{o,T}$ = age of concrete at loading adjusted according to the concrete temperature,

$t_{1,T}$ = 1 day, and

a = exponent which depends on the cement type defined as:

$$a = \begin{cases} -1 \text{ for slowly hardening cement} \\ 0 \text{ for normal or rapidly hardening cement} \\ 1 \text{ for rapidly hardening high-strength cement} \end{cases} \qquad \text{Equation 3.138}$$

3.2.6.3 CEB MC 90-99 Shrinkage Prediction Model

Like the original 1990 model, the CEB MC 90-99 model used to predict shrinkage results in the shrinkage strain at any age after curing, $\varepsilon_{cs}(t, t_s)$. The main difference between the models is that the 1999 update separates the shrinkage strain into drying shrinkage and autogenous shrinkage (CEB 1999). The shrinkage strain at any age after curing is given by Equation 3.139.

$$\varepsilon_{cs}(t, t_s) = \varepsilon_{cas}(t) + \varepsilon_{cds}(t, t_s) \qquad \text{Equation 3.139}$$

With,

$\varepsilon_{cas}(t)$ = autogenous shrinkage at time t and

$\varepsilon_{cds}(t, t_s)$ = drying shrinkage at time t.

The development of drying shrinkage strain at any age after curing is given by Equation 3.140.

$$\varepsilon_{cds}(t, t_s) = \varepsilon_{cdso}(f_{cm}) \cdot \beta_{RH}(RH) \cdot \beta_{ds}(t - t_s) \qquad \text{Equation 3.140}$$

With,

$\varepsilon_{cdso}(f_{cm})$ = notional drying shrinkage coefficient defined as:

$$\varepsilon_{cdso}(f_{cm}) = \left[(220 + 110\cdot\alpha_{ds1})\cdot\exp\left(-\alpha_{ds2}\cdot\frac{f_{cm}}{f_{cmo}}\right)\right]\cdot 10^{-6} \qquad \text{Equation 3.141}$$

Where,

α_{ds1}, α_{ds2} = coefficients depending on the type of cement defined as:

$$\alpha_{ds1} = \begin{cases} 3 & \text{for slowly hardening cements} \\ 4 & \text{for normal or rapidly hardening cements} \\ 6 & \text{for rapidly hardening high-strength cements} \end{cases} \qquad \text{Equation 3.142}$$

$$\alpha_{ds2} = \begin{cases} 0.13 & \text{for slowly hardening cements} \\ 0.11 & \text{for normal or rapidly hardening cements} \\ 0.12 & \text{for rapidly hardening high-strength cement} \end{cases} \qquad \text{Equation 3.143}$$

$\beta_{RH}(RH)$ = coefficient to take into account the effect of relative humidity defined as:

$$\beta_{RH}(RH) = \begin{cases} -1.55\left[1 - \left(\frac{RH}{RH_o}\right)^3\right] & \text{for } RH < 99\% \cdot \beta_{s1} \\ 0.25 & \text{for RH} \geq 99\% \cdot \beta_{s1} \end{cases} \qquad \text{Equation 3.144}$$

Where,

β_{s1} = coefficient to take into account self-desiccation in high-performance concretes:

$$\beta_{s1} = \left(\frac{3.5 f_{cmo}}{f_{cm}}\right)^{0.1} \leq 1.0 \qquad \text{Equation 3.145}$$

$\beta_{ds}(t - t_s)$ = function to describe the time development of drying shrinkage defined as:

$$\beta_{ds}(t - t_s) = \left[\frac{(t - t_s)/t_1}{350(h/h_o)^2 + (t - t_s)/t_1}\right]^{0.5} \qquad \text{Equation 3.146}$$

The development of autogenous shrinkage strain at any age after curing is given by Equation 3.147.

$$\varepsilon_{cas}(t) = \varepsilon_{caso}(f_{cm}) \cdot \beta_{as}(t) \qquad \text{Equation 3.147}$$

With,

$\varepsilon_{caso}(f_{cm})$ = notional autogenous shrinkage coefficient defined as:

$$\varepsilon_{caso}(f_{cm}) = -\alpha_{as}\left(\frac{f_{cm}/f_{cmo}}{6 + f_{cm}/f_{cmo}}\right)^{2.5} \cdot 10^{-6} \qquad \text{Equation 3.148}$$

Where,

α_{as} = coefficient which depends on the type of cement defined as:

$$\alpha_{as} = \begin{cases} 800 & \text{for slowly hardening cements} \\ 700 & \text{for normal or rapidly hardening cements} \\ 600 & \text{for rapidly hardening high-strength cements} \end{cases} \quad \text{Equation 3.149}$$

$\beta_{as}(t)$ = function to describe the time development of autogenous shrinkage defined as:

$$\beta_{as}(t) = 1 - \exp\left(-0.2 \cdot \left(\frac{t}{t_1}\right)^{0.5}\right) \quad \text{Equation 3.150}$$

3.2.7 CEB MC 2010 Prediction Model

The CEB MC 2010 model for predicting creep and shrinkage was introduced in the CEB-FIP Model Code in 2012. This model is very similar to the CEB MC 90-99 model in predicting shrinkage. However, the prediction of creep according to the CEB MC 2010 model takes into account both basic creep and drying creep unlike the previous CEB models. The equivalent ages of the concrete based on temperature are predicted in the same way as the CEB MC 1990 model given by Equation 3.96 (fib 2012).

3.2.7.1 CEB MC 2010 Modulus of Elasticity

Like the 1999 update to the CEB MC 1990 model, the prediction of the modulus of elasticity according to the CEB MC 2010 model is very similar to its predecessors. However, as in the 1999 update, several minor changes were made to the formulation and notation of the model, while still producing very similar results. The predicted modulus of elasticity at 28 days, E_{ci}, and its development with time, $E_{ci}(t)$, are defined in the equations below (fib 2012).

$$E_{ci} = E_{c0} \cdot \alpha_E \cdot \left(\frac{f_{cm}}{10}\right)^{1/3} \quad \text{Equation 3.151}$$

With,

$E_{c0} = 21.5 \cdot 10^3$ MPa,

f_{cm} = compressive strength of concrete at 28 days, and

α_E = aggregate type coefficient defined as:

$$\alpha_E = \begin{cases} 1.2 & \text{Basalt, dense limestone aggregates} \\ 1.0 & \text{Quartzite aggregates} \\ 0.9 & \text{Limestone aggregates} \\ 0.7 & \text{Sandstone aggregates} \end{cases} \quad \text{Equation 3.152}$$

The development of the modulus of elasticity is given by Equation 3.153.

$$E_{ci}(t) = \beta_E(t) E_{ci} \quad \text{Equation 3.153}$$

With,

$\beta_E(t)$ = coefficient which depends on the age of concrete defined as:

$$\beta_E(t) = [\beta_{cc}(t)]^{0.5} \quad \text{Equation 3.154}$$

The time-dependent factor used to calculate the modulus of elasticity at any age, $\beta_{cc}(t)$, is given by Equation 3.155.

$$\beta_{cc}(t) = \exp\left\{s \cdot \left[1 - \left(\frac{28}{t}\right)^{0.5}\right]\right\} \quad \text{Equation 3.155}$$

With,

t = adjusted concrete age in days and

s = coefficient which depends on the strength class of cement presented in Table 3-11:

Table 3-11: Coefficient s used in Equation 3.155

f_{cm} [MPa]	Strength Class of Cement	s
≤ 60	32.5 N	0.38
	32.5 R, 42.5 N	0.25
	42.5 R, 52.5 N, 52.5 R	0.20
> 60	All Classes	0.20

3.2.7.2 CEB MC 2010 Creep Prediction Model

Unlike the previous CEB models, the CEB MC 2010 creep prediction model takes a different route to predict compliance of concrete. It separates the total creep into its two main mechanisms: basic creep and drying creep. The formulation of this model is defined below, and the CEB MC 2010 compliance, $J(t, t_0)$, is given by Equation 3.156 (fib 2012).

$$J(t, t_0) = \frac{1}{E_{ci}(t_0)} + \frac{\varphi(t, t_0)}{E_{ci}} \quad \text{Equation 3.156}$$

With,

$\varphi(t, t_0)$ = creep coefficient defined as:

$$\varphi(t, t_0) = \varphi_{bc}(t, t_0) + \varphi_{dc}(t, t_0) \quad \text{Equation 3.157}$$

Where,

$\varphi_{bc}(t, t_0)$ = basic creep coefficient and

$\varphi_{dc}(t, t_0)$ = drying creep coefficient.

The CEB MC 2010 basic creep coefficient, $\varphi_{bc}(t, t_0)$, is given by Equation 3.158 (fib 2012).

$$\varphi_{bc}(t, t_0) = \beta_{bc}(f_{cm}) \cdot \beta_{bc}(t, t_0) \quad \text{Equation 3.158}$$

With,

$\beta_{bc}(f_{cm})$ = coefficient based on concrete strength defined as:

$$\beta_{bc}(f_{cm}) = \frac{1.8}{(f_{cm})^{0.7}} \quad \text{Equation 3.159}$$

$\beta_{bc}(t, t_0)$ = coefficient based on loading age defined as:

$$\beta_{bc}(t, t_0) = \ln\left[\left(\frac{30}{t_{0,adj}} + 0.035\right)^2 \cdot (t - t_0) + 1\right] \quad \text{Equation 3.160}$$

Where,

t_0 = age of concrete at loading in days and

$t_{0,adj}$ = age of concrete at loading adjusted for cement type.

The adjustment of the concrete loading age for cement type is given by Equation 3.161.

$$t_{0,adj} = t_{0,T} \cdot \left[\frac{9}{2 + t_{0,T}^{1.2}} + 1\right]^{\alpha} \geq 0.5 \text{ days} \quad \text{Equation 3.161}$$

With,

$t_{0,T}$ = age of concrete at loading adjusted for temperature and

α = coefficient which depends on the type of cement defined as:

$$a = \begin{cases} \text{-1 for strength class 32.5 N} \\ \text{0 for strength classes 32.5 R, 42.5 N} \\ \text{1 for strength classes 42.5 R, 52.5 N, 52.5 R} \end{cases} \quad \text{Equation 3.162}$$

The CEB MC 2010 drying creep coefficient, $\varphi_{dc}(t, t_0)$, is given by Equation 3.163 (fib 2012).

$$\varphi_{dc}(t, t_0) = \beta_{dc}(f_{cm}) \cdot \beta(RH) \cdot \beta_{dc}(t_0) \cdot \beta_{dc}(t, t_0) \quad \text{Equation 3.163}$$

With,

$\beta_{dc}(f_{cm})$ = coefficient which depends on the concrete strength defined as:

$$\beta_{dc}(f_{cm}) = \frac{412}{(f_{cm})^{1.4}} \quad \text{Equation 3.164}$$

$\beta(RH)$ = coefficient which depends on the relative humidity defined as:

$$\beta(RH) = \frac{1 - \frac{RH}{100}}{(0.1 \cdot h/100)^{1/3}} \quad \text{Equation 3.165}$$

Where,

RH = relative humidity of the ambient environment in % and

$h = 2A_c/u$ = notional size of member in mm defined as:

$$h = 2A_c/u \quad \text{Equation 3.166}$$

Where,

A_c = cross-sectional area of member (mm.^{2}) and

u = perimeter of the member in contact with the atmosphere (mm.).

$\beta_{dc}(t_0)$ = coefficient which depends on the age at loading defined as:

$$\beta_{dc}(t_0) = \frac{1}{0.1 + t_{0,adj}^{0.2}} \quad \text{Equation 3.167}$$

$\beta_{dc}(t, t_0)$ = development of drying creep defined as:

$$\beta_{dc}(t, t_0) = \left[\frac{(t - t_0)}{\beta_h + (t - t_0)}\right]^{\gamma(t_0)} \quad \text{Equation 3.168}$$

Where,

$\gamma(t_0)$ = exponent defined as:

$$\gamma(t_0) = \frac{1}{2.3 + \frac{3.5}{(t_{0,adj})^{0.5}}} \quad \text{Equation 3.169}$$

β_h = shape factor defined as:

$$\beta_h = 1.5 \cdot h + 250 \cdot \alpha_{f_{cm}} \leq 1500 \cdot \alpha_{f_{cm}} \quad \text{Equation 3.170}$$

The strength factor, $\alpha_{f_{cm}}$, used to calculate β_h is given by Equation 3.171.

$$\alpha_{f_{cm}} = \left(\frac{35}{f_{cm}}\right)^{0.5} \quad \text{Equation 3.171}$$

3.2.7.3 CEB MC 2010 Shrinkage Prediction Model

The CEB MC 2010 shrinkage prediction model is nearly identical to the 1999 update to the CEB MC 1990 model. The only differences are slight changes in formulation and notation. Like its predecessor, it predicts the total shrinkage strain, $\varepsilon_{cs}(t, t_s)$, by separating it into its two main parts, autogenous shrinkage strain and drying shrinkage strain (fib 2012). The total predicted shrinkage strain is given by Equation 3.172.

$$\varepsilon_{cs}(t, t_s) = \varepsilon_{cas}(t) + \varepsilon_{cds}(t, t_s) \quad \text{Equation 3.172}$$

With,

$\varepsilon_{cas}(t)$ = autogenous shrinkage strain and

$\varepsilon_{cds}(t, t_s)$ = drying shrinkage strain.

The CEB MC 2010 autogenous shrinkage strain is given by Equation 3.173 (fib 2012).

$$\varepsilon_{cas}(t) = \varepsilon_{cas0}(f_{cm}) \cdot \beta_{as}(t) \quad \text{Equation 3.173}$$

With,

$\varepsilon_{cas0}(f_{cm})$ = notional autogenous shrinkage coefficient defined as:

$$\varepsilon_{cas0}(f_{cm}) = -\alpha_{as}\left(\frac{f_{cm}/10}{6 + f_{cm}/10}\right)^{2.5} \cdot 10^{-6} \quad \text{Equation 3.174}$$

Where,

α_{as} = cement type coefficient presented in Table 3-12.

Table 3-12: Shrinkage coefficients α_i

Strength Class of Cement	α_{as}	α_{ds1}	α_{ds2}
32.5 N	800	3	0.013
32.5 R, 42.5 N	700	4	0.012
42.5 R, 52.5 N, 52.5 R	600	6	0.012

$\beta_{as}(t)$ = autogenous shrinkage time function defined as:

$$\beta_{as}(t) = 1 - \exp\left(-0.2 \cdot \sqrt{t}\right) \quad \text{Equation 3.175}$$

The CEB MC 2010 drying shrinkage strain is given by Equation 3.176 (fib 2012).

$$\varepsilon_{cds}(t, t_s) = \varepsilon_{cds0}(f_{cm}) \cdot \beta_{RH}(RH) \cdot \beta_{ds}(t - t_s) \quad \text{Equation 3.176}$$

With,

$\varepsilon_{cds0}(f_{cm})$ = notional drying shrinkage coefficient defined as:

$$\varepsilon_{cds0}(f_{cm}) = [(220 + 110 \cdot \alpha_{ds1}) \cdot \exp(-\alpha_{ds2} \cdot f_{cm})] \cdot 10^{-6} \quad \text{Equation 3.177}$$

Where,

α_{ds1}, α_{ds2} = cement type coefficients presented in Table 3-12.

$\beta_{ds}(t - t_s)$ = drying shrinkage time function defined as:

$$\beta_{ds}(t - t_s) = \left(\frac{(t - t_s)}{0.035 \cdot h^2 + (t - t_s)}\right)^{0.5} \quad \text{Equation 3.178}$$

Where,

t_s = concrete age at the beginning of drying in days.

$\beta_{RH}(RH)$ = relative humidity coefficient defined as:

$$\beta_{RH} = \begin{cases} -1.55 \cdot \left[1 - \left(\frac{RH}{100}\right)^3\right] & \text{for } 40 \le RH < 99\,\% \cdot \beta_{s1} \\ 0.25 & \text{for } RH \ge 99\,\% \cdot \beta_{s1} \end{cases} \quad \text{Equation 3.179}$$

Where,

β_{s1} = strength factor defined as:

$$\beta_{s1} = \left(\frac{35}{f_{cm}}\right)^{0.1} \le 1.0 \quad \text{Equation 3.180}$$

3.2.8 GL 2000 Prediction Model

The GL 2000 prediction model for creep and shrinkage was introduced in Gardner and Lockman (2001). This model predicts the specific creep at any time after loading, which can be used to determine the compliance, and the ultimate shrinkage strain, which can be used to predict shrinkage strain at any concrete age after curing. These predicted values are based on relative humidity, element size and shape, cement type, mean compressive strength, and compressive strength at 28 days. Gardner and Lockman (2001) advise using the Arrhenius equivalent age

method to better predict the maturity of the concrete to account for any abnormal temperatures. The equivalent age in days, t_e, is given by Equation 3.181 (ASTM C1074 2019).

$$t_e = \sum_{0}^{t} \exp\left\{\frac{-E}{8.3144}\left[\frac{1}{273 + T_c} - \frac{1}{273 + T_r}\right]\right\}\Delta t \qquad \text{Equation 3.181}$$

With,

t = chronological age of concrete (days),

E = activation energy (J/mol),

T_c = average concrete temperature during time interval, Δt (°C),

T_r = reference curing temperature (°C), and

Δt = time interval (days).

3.2.8.1 GL 2000 Modulus of Elasticity

The modulus of elasticity at 28 days is required by the GL 2000 creep prediction model to obtain a specific creep value from the predicted creep coefficient. The modulus of elasticity at the time of loading is then used to convert the specific creep to a predicted compliance value. The mean modulus of elasticity, E_{cmt}, in psi at age t is given by Equation 3.182 (Gardner and Lockman 2001).

$$E_{cmt} = 500{,}000 + 52{,}000\sqrt{f_{cmt}} \qquad \text{Equation 3.182}$$

With,

f_{cmt} = mean concrete strength at age t (psi).

3.2.8.2 GL 2000 Creep Prediction Model

The GL 2000 creep prediction model results in a compliance value at any concrete age, $J(t, t_0)$, which is given by Equation 3.183. This function is based on the specific creep and the creep coefficient, which are defined in the equations following (Gardner and Lockman 2001).

$$J(t, t_0) = \frac{1}{E_{cmto}} + \text{specific creep} \qquad \text{Equation 3.183}$$

With,

E_{cmto} = modulus of elasticity at time of loading (psi) and

specific creep = creep strain per unit stress (ACI 209.2R 2008) defined as:

$$\text{specific creep} = \frac{\phi_{28}}{E_{cm28}} \qquad \text{Equation 3.184}$$

Where,

E_{cm28} = modulus of elasticity at 28 days (psi) and

ϕ_{28} = creep coefficient.

According to Gardner and Lockman (2001), the creep coefficient used to calculate specific creep, ϕ_{28}, is as defined in Equation 3.185.

$$\phi_{28} = \Phi(t_c)\left[2\left(\frac{(t-t_0)^{0.3}}{(t-t_0)^{0.3}+14}\right)+\left(\frac{7}{t_0}\right)^{0.5}\left(\frac{t-t_0}{t-t_0+7}\right)^{0.5} + 2.5(1-1.086h^2)\left(\frac{t-t_0}{t-t_0+97\cdot(V/S)^2}\right)^{0.5}\right] \quad \text{Equation 3.185}$$

With,

t = equivalent age of concrete (days),

t_0 = equivalent age of concrete loaded (days),

h = relative humidity expressed as a decimal,

V/S = volume-surface ratio (in), and

$\Phi(t_c)$ = correction factor for drying before loading defined as:

$$\Phi(t_c) = \left[1-\left(\frac{t_0-t_c}{t_0-t_c+97\cdot(V/S)^2}\right)^{0.5}\right]^{0.5} \quad \text{Equation 3.186}$$

Where,

t_c = equivalent age of concrete when drying commenced (days).

3.2.8.3 GL 2000 Shrinkage Prediction Model

The GL 2000 shrinkage prediction model is used to predict an ultimate shrinkage strain. This value is then multiplied by a humidity factor, $\beta(h)$, and a time factor, $\beta(t)$, to predict the shrinkage strain at any age after curing, ε_{sh}, which is given by Equation 3.186:

$$\varepsilon_{sh} = \varepsilon_{shu}\beta(h)\beta(t) \quad \text{Equation 3.187}$$

With,

ε_{shu} = ultimate shrinkage strain (in/in) defined as:

$$\varepsilon_{shu} = 1000\cdot K\cdot\left(\frac{4350}{f_{cm28}}\right)^{1/2}\cdot 10^{-6} \quad \text{Equation 3.188}$$

Where,

K = cement type factor defined as:

$$K = \begin{cases} 1.00 & \text{for Type I cement} \\ 0.70 & \text{for Type II cement} \\ 1.15 & \text{for Type III cement} \end{cases} \quad \text{Equation 3.189}$$

f_{cm28} = concrete mean compressive strength at 28 days (psi).

$\beta(h)$ = relative humidity factor defined as:

$$\beta(h) = (1-1.18h^4) \quad \text{Equation 3.190}$$

Where,

h = relative humidity expressed as a decimal.

$\beta(t)$ = age of concrete factor defined as:

$$\beta(t) = \left(\frac{t - t_c}{t - t_c + 97 \cdot (V/S)^2}\right)^{0.5} \quad \text{Equation 3.191}$$

Where,

V/S = volume-surface ratio (in),

t = equivalent age of concrete (days), and

t_c = equivalent age of concrete when drying commenced (days).

3.3 Overview of Previous Creep and Shrinkage Studies

3.3.1 Summary of Previous Studies Conducted at Auburn University

The following studies were all performed at Auburn University and involve assessing the accuracy of creep and shrinkage prediction models based on experimental testing. The interpretation of these studies is helpful to this research because all of them involved materials locally available to the Southeast part of the country, and more specifically, Alabama.

3.3.1.1 Mante (2016)

Mante (2016) studied and made improvements on camber predictions for precast, prestressed concrete bridge girders made with both self-consolidating concrete (SCC) and conventionally vibrated concrete (CVC). Because creep and shrinkage play an important role in camber of prestressed girders, creep and shrinkage testing was performed on six laboratory mixtures representing typical concretes used in the precast, prestressed industry. All of these mixtures contained Type III cement, along with various supplementary cementitious materials. The measured creep and shrinkage data was compared to three prediction models: AASHTO LRFD, ACI 209, and CEB MC 2010. After testing was completed, Mante (2016) found that for creep, the AASHTO LRFD and the ACI 209 models proved to be the most accurate. For shrinkage, the AASHTO LRFD model was again found to be the most accurate. Because of its accuracy and its relative simplicity compared to other models, Mante (2016) recommended that of the three models studied, the AASHTO LRFD model should be used for camber predictions of precast, prestressed concrete bridge girders (Mante 2016).

3.3.1.2 Kavanaugh (2008)

Kavanaugh (2008) performed creep testing on self-consolidating concrete specimens and compared the measured data to five prediction models: ACI 209, AASHTO LRFD, CEB MC 1990, GL 2000, and B3. Four different mixtures were used for the test specimens with varying water to cement ratios and cementitious content combinations, which included Type III cement, Class C fly ash, and slag cement. A control mixture was also prepared without viscosity-modifying admixtures (VMA) to represent a conventional-slump concrete. After testing, Kavanaugh (2008) found that the CEB MC 1990 model provided the most accurate creep predictions for both SCC and conventional-slump concrete, and the ACI 209 and the AASHTO LRFD models were the second and third most accurate, respectively (Kavanaugh 2008).

3.3.1.3 Keske (2014)

Keske (2014) studied the use of self-consolidating concrete in precast, prestressed girders. As a part of this study, creep and shrinkage testing was performed on samples of both SCC and CVC. These measured data were compared to four creep and shrinkage prediction models: ACI 209, AASHTO LRFD, NCHRP 628, and CEB MC 2010. Keske (2014) found that for creep, all four of the prediction models were relatively accurate with none significantly more so than the others for both SCC and CVC. For shrinkage, AASHTO LRFD was found to be the most accurate as all the other models tended to significantly over-predict shrinkage strain. The total time-dependent strains were also compared to the prediction models, and ACI 209 and CEB MC 2010 provided the most accurate predictions for SCC, and AASHTO LRFD provided the most accurate predictions for CVC. Based on the study, Keske (2014) concluded that AASTO LRFD was the only model to reasonably predict both creep and shrinkage (Keske 2014).

3.3.1.4 Schindler et al. (2017)

Schindler et al. (2017) studied the compliance behavior of self-consolidating concrete for prestressed applications. In this study, creep testing was performed on four SCC mixtures and one conventional-slump concrete (CSC) mixture at five different loading ages. These experimental data were compared to six creep prediction models: ACI 209, CEB MC 2010, GL 2000, B3, AASHTO LRFD, and NCHRP 628. Comparisons of accuracy were made using the standard deviation of the error (S_j) as the main statistical indicator. After testing was completed, Schindler et al. (2017) found that the CEB MC 2010 creep prediction model provided the most accurate compliance predictions for all concrete types and loading ages tested, and the ACI 209 and AASHTO LRFD models were the next-most accurate of all the models studied (Schindler et al. 2017).

3.3.2 Statistical Comparison of Creep and Shrinkage Prediction Models Using RILEM and NU-ITI Databases (Al-Manaseer and Prado 2015)

Al-Manaseer and Prado (2015) performed statistical comparisons of the accuracy of six of the creep and shrinkage prediction models: ACI 209, B3, GL 2000, CEB MC 1990, CEB MC 2010, and AASHTO LRFD. These comparisons were not based on individual testing done by them, but on the latest RILEM and NU-ITI databases at the time of the study. The goal of the study was to use several methods of statistical analysis to determine and report the most accurate prediction models (Al-Manaseer and Prado 2015).

3.3.2.1 Methods of Analysis

This study used five methods to analyze the data in comparison to the databases: the residual method, CEB coefficient of variation method, CEB mean square error method, CEB mean deviation method, and modified coefficient of variation method. The residual method was performed by simply subtracting the experimentally measured values from the predicted values. In the CEB coefficient of variation method, the data were divided into six time intervals, and the coefficient of variation, V_i, was determined for each interval. The root mean square coefficient of variation, V_{CEB}, was then determined. In the CEB mean square error method, the percent differences between predicted and measured data points, f_j, were used to calculate the mean square error, F_i, for each of the six time intervals above. This was then used to calculate the total mean square error, F_{CEB}. In the CEB mean deviation method, the average ratio of predicted to measured values, M_i, for each time interval was calculated and used to determine the total mean deviation, M_{CEB}. The modified coefficient of variation method was similar to the CEB coefficient of variation method; however, instead of performing the calculations on individual points, they were performed on populations of points to determine the total modified coefficient of variation, ω_m (Al-Manaseer and Prado 2015).

Three plans of elimination of data (A, B, and C) were implemented to use the above methods to compare the prediction models. In Plan A, all measured creep and shrinkage values of zero were excluded to avoid divide-by-zero errors in several of the analysis methods. Any repeated measurements and measurements of positive shrinkage (swelling) were also excluded. Finally, for all specimens, the 28-day modulus of elasticity was derived from the experimental 28-day compressive strength based on each model.

In Plan B, all parts of Plan A were implemented, and any points with f_j^2 of greater than 50 was excluded. In Plan C, all parts of Plans A and B were implemented, and all outliers were excluded. An outlier is defined as a data set that produces a relatively large residual and does not follow the trend of the rest of the data according to Al-Manaseer and Prado (2015).

3.3.2.2 Results from Study

The results from the statistical analyses are presented below in the following tables. Table 3-13 shows the distribution of residuals for creep and shrinkage models for 0 to 10,000 days. The distribution of residuals for this study generally represents the results from the additional statistical analysis, so the results of the other statistical methods are not shown.

Table 3-13: Residual values for creep and shrinkage

Model		RILEM						NU-ITI					
		Shrinkage			Creep			Shrinkage			Creep		
		A	B	C	A	B	C	A	B	C	A	B	C
ACI 209R-92	Overestimate, %	54	54	55	45	45	46	53	53	55	33	33	33
	Underestimate, %	46	46	45	55	55	54	47	47	45	67	67	67
B3	Overestimate, %	36	35	36	57	57	57	34	33	35	40	40	40
	Underestimate, %	64	65	64	43	43	43	66	67	65	60	60	60
GL 2000	Overestimate, %	44	43	45	59	59	60	42	42	44	46	46	47
	Underestimate, %	56	57	55	41	41	40	58	58	56	54	54	53
CEB MC 90-99	Overestimate, %	53	52	53	37	37	37	52	50	53	33	29	30
	Underestimate, %	47	48	47	63	63	63	48	50	47	67	71	70
fib MC 2010	Overestimate, %	53	52	53	35	35	35	52	50	53	28	24	25
	Underestimate, %	47	48	47	65	65	65	48	50	47	72	76	75
AASHTO 2012	Overestimate, %	37	35	35	36	36	36	37	35	36	33	33	33
	Underestimate, %	63	65	65	64	64	64	63	65	64	67	67	67

Based on the results presented above, Al-Manaseer and Prado (2015) found that for shrinkage, the ranking of models from most accurate to least accurate was ACI 209, B3, CEB MC 90-99 and CEB MC 2010, GL 2000, and AASHTO LRFD. For shrinkage, the ranking of the models from most accurate to least accurate was ACI 209, B3, GL 2000, CEB MC 90-99, CEB MC 2010, and AASHTO LRFD. When considering creep and shrinkage prediction together, the ACI 209 model was found to be the most accurate, and the AASHTO LRFD model was found to be the least accurate, with the B3 model the second most accurate (Al-Manaseer and Prado 2015).

3.3.3 Creep and Shrinkage of High-Performance/High-Strength Concrete (Suksawang et al. 2005)

Suksawang et al. (2005) investigated creep and shrinkage effects on high-performance/high-strength concrete (HP/HSC). In this study, creep and shrinkage testing was performed on concrete specimens with various supplementary cementitious materials (SCM). These experimental data were then compared to four prediction models: ACI 209, CEB 90, B3, and GL 2000. The comparisons were used to determine the best performing prediction model for this study (Suksawang et al. 2005).

3.3.3.1 Test Specimens

In total, seven different mixtures were prepared for creep and shrinkage testing. All mixtures contained Type I cement with varying types and amounts of SCMs. Three of the mixtures contained only 5%, 10%, and 15% silica fume, respectively. Three of the mixtures contained only Class F fly ash at 10%, 20%, and 30% replacement levels, respectively. One mixture was a ternary blend containing 5% silica fume and 20% fly ash. Additionally, all mixtures contained high-range water-reducing admixture (HRWR) and air entraining admixture. The compressive strengths at various concrete ages were tested, and the results are shown in Table 3-14. In general, a higher silica fume content corresponded to a higher compressive strength, and a high fly ash content corresponded to a lower compressive strength (Suksawang et al. 2005).

Table 3-14: Compressive strength: adapted from Suksawang et al. (2005)

Time (Days)	Compressive Strength (psi)						
	5SF	10SF	15SF	10F	20F	30F	5SF-20F
1	8,079	8,296	8,296	8,122	7,818	6,599	6,759
3	9,021	9,442	10,530	10,109	8,557	7,731	8,601
7	9,544	10,747	10,979	10,863	9,703	8,238	9,544
14	9,993	12,328	12,734	12,328	10,225	9,326	10,501
28	10,356	12,357	12,749	11,937	11,066	10,805	12,575
56	11,864	12,879	13,300	13,561	12,734	11,705	13,343
90	11,516	13,822	14,170	13,721	12,981	12,386	14,156

3.3.3.2 Results from Study

Suksawang et al. (2005) found that after testing, the B3 model and the GL 2000 model provided the best predictions for shrinkage with the ACI 209 model close behind. The CEB 90 model did not provide accurate predictions in this study. For creep, Suksawang et al. (2005) found that the ACI 209 model and the B3 model provided the best predictions with the CEB 90 model also predicting accurately. The GL 2000 model provided the worst predictions for creep. Suksawang et al. (2005) concluded that while some of the prediction models were relatively accurate, none of them include parameters that take into account the properties of HP/HSC. Correction factors would be necessary to do this (Suksawang et al. 2005).

3.3.4 Long-Term Prestress Loss and Camber of Box-Girder Bridge (Kamatchi et al 2014)

Kamatchi et al. (2014) studied the prediction of prestress loss and camber in box-girder bridges by comparing field results to four creep and shrinkage prediction models: the ACI 209 model, the B3 model, the CEB MC 90-99 model, and the GL 2000 model. Testing of prestress loss was performed by installing vibrating wire strain gauges throughout a typical box-girder bridge span with an effective span length of 131 feet. The configuration of these strain gauges is shown in Figure 3-1. The camber was tested with the use of a theodolite. All testing was performed for the first five years of the bridge's operation. After testing was complete, Kamatchi et al. (2014) found that the B3 model and the CEB 90-99 model predicted long-term prestress loss most accurately, of the four models studied. It was also found that the B3 model and the CEB 90-99 model predicted long-term camber most accurately, and at the latest ages studied, the CEB 90-99 model predicted camber most accurately (Kamatchi et al. 2014).

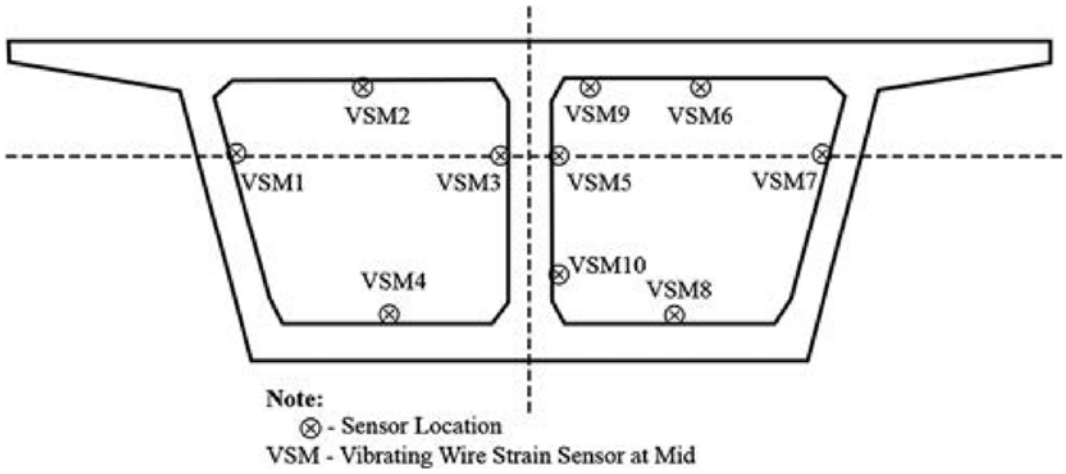

Figure 3-1: Locations of vibrating wire strain gauges at midspan of box-girder

Chapter 4

EXPERIMENTAL PLAN

4.1 INTRODUCTION

The main objective of this research is to use measured values to accurately predict creep and shrinkage strains in the I-59/I-20 segmental bridge in Birmingham, Alabama. This chapter details the experimental plan and testing procedures used for data collection and assessment of the creep and shrinkage of the concrete used in the bridge.

4.2 EXPERIMENTAL PLAN

The I-59/I-20 segmental bridge in Birmingham was under construction between February of 2018 and October of 2019. The experimental plan for this project has two main stages. The first of these stages is field specimen collection, in which specimens were collected while the segments were cast at the jobsite. Instead of mixing the concrete used for testing in a laboratory environment, samples were collected from the concrete batched on the jobsite and cured in the same environment as the segments to ensure similar properties to the concrete used in the corresponding segments. These samples were then transported to Auburn University for the laboratory testing stage of the experimental plan. This includes testing both the hardened properties of the concrete specimens and the creep and shrinkage strains in accordance with the corresponding ASTM standards. All testing during this stage was performed in controlled laboratory conditions. After the data were collected in the laboratory testing stage of the project, the statistical comparison to existing creep and shrinkage models began.

4.2.1 Specimen Type

ASTM C512 (2015) prescribes the procedure for preparing specimens used in creep testing, and it requires them to be cast in the form of 6 in. × 12 in. cylinders. After curing and removing cylinders from the molds, the ends of the cylinders must be ground to obtain a level and smooth surface. As discussed in Chapter 2, it is important to monitor both creep and shrinkage in order to isolate the creep strain from the total strain in the concrete. Therefore, both creep and corresponding shrinkage cylinders were cast for testing. In addition to the test cylinders, shrinkage strain was monitored in accordance with AASHTO T160 (2017). This method requires that the shrinkage specimens be cast in the form of 3 in. × 3 in. × 11.25 in. rectangular prisms. Two sets of shrinkage prisms were cast for the purposes of this research: one set cured alongside the bridge segments and one set cured in a lime-saturated water bath in the laboratory.

Throughout the duration of testing, these prisms were stored on wire shelves to prevent any induced restraint stress while still allowing full air contact with the concrete surface.

4.2.2 Loading Ages

As discussed in Chapter 2, the magnitudes of creep strains vary with the age of the concrete at the time of loading. To account for this effect, four loading ages were used for each sampling data set. In conjunction with previous research and considering the accelerated construction schedule of the I-59/I-20 segmental bridge, creep testing was performed with loading ages of 7 days, 28 days, 91 days, and 182 days. For the shrinkage prisms, testing began two days after each visit to the project site for prisms cured alongside the bridge segments and seven days for prisms cured in the laboratory.

4.2.3 Sample Sizing

For each field visit, two cylinders were cast on site for each loading age to monitor creep for a total of eight creep specimens. Three companion cylinders were also cast to monitor the shrinkage of the creep cylinders. Three cylinders were cast for each loading age for the purpose of determining the modulus of elasticity and strength of the concrete before creep testing. One cylinder was also cast and instrumented with a temperature sensor to monitor the internal temperature of the concrete while it cured to allow for the equivalent-age maturity of the samples to be calculated. In addition to the cylinders cast on site, six shrinkage prisms were cast, three of which were cured on site and three of which were cured in a lime bath. A summary of the number of samples for each field visit is presented in Table 4-1.

Table 4-1: Summary of number of samples for each field visit

Loading Age	6 in. × 12 in. Cylinders				Drying Shrinkage Prisms
	Creep Specimens	Shrinkage Specimens	Strength/ Elastic Modulus Specimens	Concrete Temperature	
7 Days	2	3	3	1	6
28 Days	2		3		
91 Days	2		3		
182 Days	2		3		
Column Totals	8	3	12	1	6
Total Samples	**24**				**6**

4.2.4 Sampling Dates

Throughout the duration of the bridge construction, the ALDOT-approved mixture proportions changed four times. To account for these changes, samples were collected on four separate casting dates throughout the duration of casting of the bridge segments. These four dates were April 10, 2018, July 9, 2018, November 19, 2018, and April 16, 2019. A summary of the casting of the segments with relation to their respective mixture proportions, as well as the percentage of segments cast up to the points of sample collection is presented in Figure 4-1 (courtesy of Mr. Eric Johnson, Corven Engineering). As the figure shows, the casting progression was nonlinear with respect to time, with one segment produced per day at the beginning of casting and eight segments per day at the peak of the casting schedule.

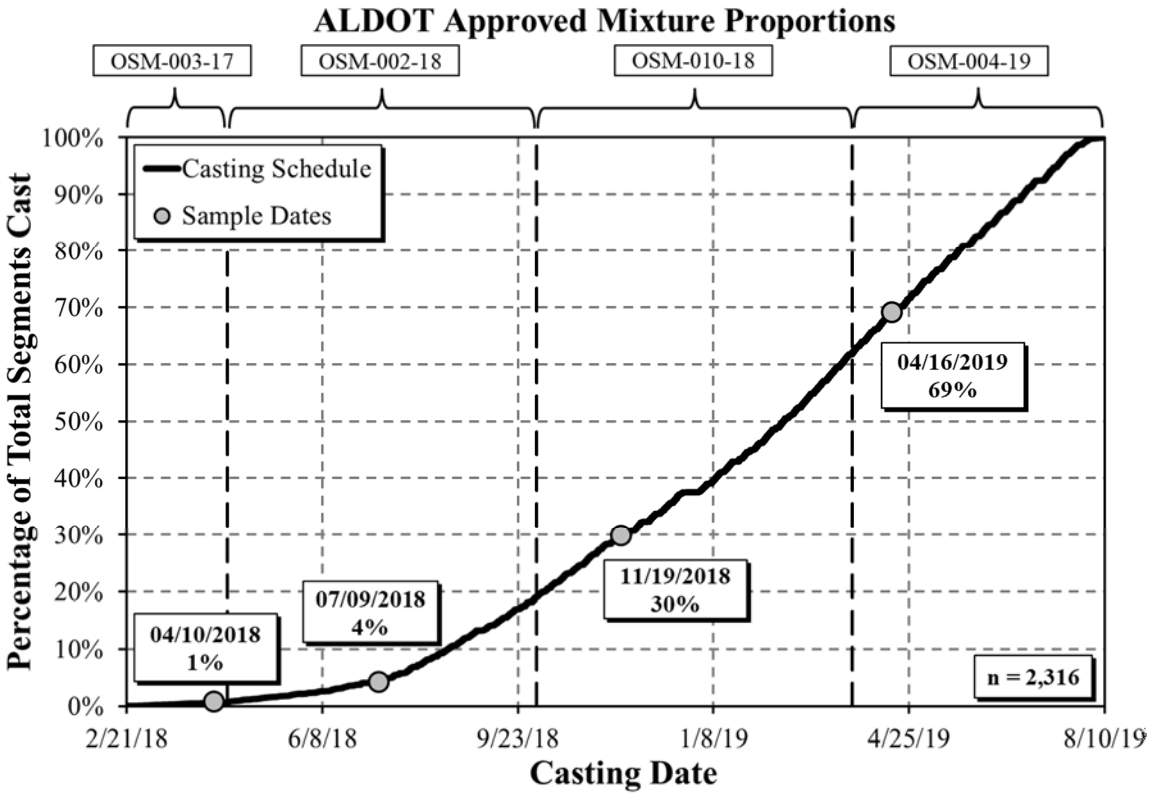

Figure 4-1: Segmental casting progression in conjunction with site visits and ALDOT approved mixture proportions

4.3 MIXTURE PROPORTIONS

The ALDOT mixture design requirements for the Birmingham I-59/I-20 segmental bridge include strength, workability, and total air content. According to the design specifications, all concrete was required to meet the following compressive strength requirements: 2,500 psi prior to the removal of formwork, 4,000 psi prior to transverse post-tensioning, and a 28-day specified compressive strength, f'_c, of 6,500 psi. The slump was required to range from 3 in. to 9 in. for all concrete cast. Additionally, all fresh concrete cast was required to have a total air content between 3 and 6 percent.

All concrete used in the I-59/I-20 segmental bridge was collected from ready-mixed concrete trucks that travelled to the site from a batch plant near the casting beds. For the casting of the specimens used for testing, the concrete was collected from the trucks using wheelbarrows. The concrete was collected from the middle of the ready-mixed truck to ensure that testing was performed on thoroughly mixed concrete. The mixture proportions were changed by the contractor at several points throughout the duration of the project. These changes were

made to increase the early-age and 28-day compressive strength, as well as to accommodate changes in availability of Type III cement, fly ash, and chemical admixtures. Based on these changes, four approved ALDOT concrete mixtures were used throughout the sample collection period. The four approved mixture proportions are presented in Table 4-2 with the sampling dates shown for each corresponding mixture proportion.

Table 4-2: ALDOT approved mixture proportions for each sampling date

Material	**ALDOT Approved Mixture Proportions**			
	OSM-003-17 04/10/2018	**OSM-002-18 07/09/2018**	**OSM-010-18 11/19/2018**	**OSM-004-19 04/16/2019**
Portland Cement (lb/yd^3)	Type I/II 682	Type I/II 682	Type III 782	Type I/II 800
Water (lb/yd^3)	264	264	283	275
Class F Fly Ash (lb/yd^3)	170	170	138	---
Coarse Aggregate* (#67 Quartzite) (lb/yd^3)	1800	1800	1750	1750
Fine Aggregate* (#100 Sand) (lb/yd^3)	878	978	955	1088
Chemical Admixtures ($oz./yd^3$)	BASF		W.R. Grace and Company	
Air-entraining Admixture	MasterAir AE 200		Daravair 1000	
	2	3	4.6	0.6
Type A	MasterPozzolith 322		Zyla 610	
	30.1	51.4	---	---
Type F	MasterPolyheed 1025		ADVA 140M	
	68	---	82.8	112
Type D	MasterSet DELVO		Recover	
	34.1	34.3	36.8	16
Type C	MasterSet AC 534		Daraset 400	
	102.2	102.2	110.4	112

Note: * All aggregates in saturated-surface dry state

4.4 SPECIMEN IDENTIFICATION SYSTEM

Because of the large number of test specimens collected for this research, an identification system was developed to give a label to each specimen. This system provided efficiency both in the data collection and in the statistical comparison to existing creep and shrinkage models. The labels for all test cylinders were based on their respective casting dates and loading ages. The labels for all shrinkage prisms were based on their respective casting dates and curing conditions. The specific convention for labeling all test specimens is presented in Table 4-3 and Table 4-4.

Table 4-3: Creep and shrinkage cylinder identification system

Creep and Shrinkage Cylinder Identification System			
Casting Date	04/10/2018*	Age at Loading	7 Day*
	07/09/2018		28 Day
	11/19/2018		91 Day
	04/16/2019		182 Day

* Specimen Label - 04/10/2018 - 7 Day

Table 4-4: Shrinkage prism identification system

Shrinkage Prism Identification System			
Casting Date	04/10/2018*	Lime Bath	Air (No Lime Bath)*
	07/09/2018		
	11/19/2018		Moist (Lime Bath)
	04/16/2019		

* Specimen Label - 04/10/2018 – Air

4.5 SAMPLE COLLECTION AND TEST METHODS

All methods for testing both fresh and hardened concrete properties for this research, as well as casting and curing methods, are described in this section. Casting and testing of fresh concrete properties were performed on the jobsite, and testing of hardened properties was performed in the Structural Concrete Materials Laboratory at Auburn University. Curing of the concrete occurred both in the field and in the laboratory.

4.5.1 Collection of Test Specimens

All test specimens were collected on the casting yard for the I-59/I-20 segmental bridge in parallel with the casting of the bridge segments. As presented in Table 4-1, 24 concrete cylinders and 6 concrete prisms were collected on each of the 4 field visits for a total of 96 cylinders and 24 prisms.

4.5.1.1 Concrete Cylinders

On each field visit, all 24 of the 6 × 12 in. concrete cylinders used for testing were prepared on the jobsite in accordance with the requirements in AASHTO T23 (2018). One cylinder on each field visit was embedded with a temperature sensor to record the curing temperatures for the first 24 to 36 hours after it was prepared. Figure 4-2 shows the preparation of several concrete test cylinders.

Figure 4-2: Preparation of concrete cylinders on the jobsite

4.5.1.2 Concrete Prisms

On each field visit, the six 3 × 3 × 11.25 in. concrete prisms were cast on the jobsite in accordance with the requirements in AASHTO T160 (2017). Figure 4-3 shows the preparation of several of the concrete prisms.

Figure 4-3: Preparation of concrete prisms on the jobsite

4.5.2 Curing and Storage Methods

Upon collecting all test specimens prepared during each field visit, it was important to ensure that they were properly cured, stored, and transported to the laboratory at Auburn University. Curing of the specimens occurred both on the jobsite alongside the corresponding bridge segments, as well as in the laboratory. All curing methods were performed in accordance with the requirements in AASHTO T23 (2018).

4.5.2.1 Field Curing

As described in Chapter 2, a specimen's curing history plays an important role in the creep and shrinkage of concrete. To give the test specimens an accurate representation of the bridge segments' curing history, it was important that they be cured using the same process. The test cylinders were sealed with tight-fitting plastic caps to prevent moisture loss while the concrete cured. The prisms, on the other hand, were covered with water-soaked burlap and wrapped in plastic. To best imitate the initial curing practices of the bridge segments, the contractor allowed the test specimens to be stored inside the formwork of the curing bridge segments. The placement of these specimens inside the forms is shown in Figure 4-4.

Figure 4-4: Placement of test specimens in segment forms for field curing

If needed to accelerate the curing process, heat was added to the concrete while it cured. Immediately after placement of the specimens in the formwork, the forms were encapsulated with blankets to aide in the heat curing. No heat was added until the initial set of the concrete occurred. After initial set, heaters were placed inside the blankets if they were deemed necessary by the contractor. The temperatures inside the forms were not to exceed 150°F, and the rate of heating was not to exceed 40°F per hour throughout the duration of initial curing. As an example, the temperature profiles for the concrete and form temperatures for the April 16, 2019, field visit is shown in Figure 4-5.

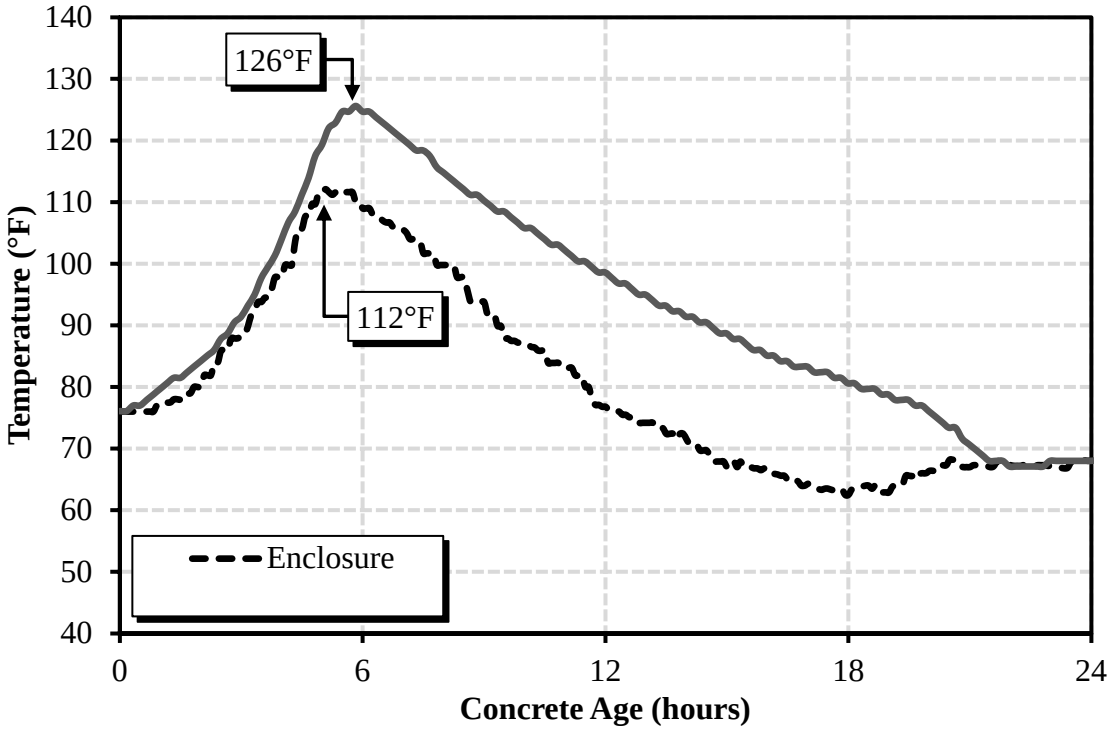

Figure 4-5: Temperature profiles for the 04/16/2019 sampling date

4.5.2.2 Laboratory Curing

After initial curing was completed at the jobsite, all test specimens were transported to the laboratory at Auburn University before demolding. Because the bridge segments did not undergo any additional curing, the concrete cylinders were demolded and placed in the creep testing room upon arrival at the laboratory. The three shrinkage prisms from each visit that were not placed in a lime bath (air-cured) were exposed immediately to drying conditions and stored on steel wire shelves in the same creep testing room as the cylinders. The remaining three (moist-cured) prisms were placed in a lime-saturated water tank for seven days for additional curing before exposure to drying. The creep testing room conditions followed the requirements in ASTM C512 (2015) and are discussed in Section 4.5.4.4.1 of this report.

4.5.3 Methods for Testing Fresh Concrete Properties

The four fresh concrete properties for which all concrete collected at the jobsite was tested were slump, total air content, unit weight, and temperature. These tests were performed by a third-party testing company to ensure that the ALDOT specifications for fresh concrete were met for all concrete used on the project.

4.5.3.1 Slump

The ALDOT requirement for slump for all concrete in the I-59/I-20 bridge segments was in the range of 3 in. to 9 in. All slump tests were performed in accordance with the specifications in AASHTO T119 (2018).

4.5.3.2 Air Content and Unit Weight

All fresh concrete samples were tested for air content and unit weight in accordance with the requirements in AASHTO T121 (2019). The standards for air content required all concrete to have a total air content in the range of 3 percent to 6 percent. Any concrete that did not meet these requirements was rejected and discarded. There was no requirement for the unit weight of the concrete.

4.5.3.3 Temperature

The fresh concrete temperature was taken for all samples, and this was performed in accordance with the requirements in AASHTO T309 (2015). The fresh concrete temperature was required to be in the range of 50°F and 95°F per the requirements in ALDOT 501 (2018). If any fresh concrete did not meet these requirements, it was rejected and discarded.

4.5.3 Methods for Testing Hardened Concrete Properties

The hardened properties tested for the purposes of this research were modulus of elasticity, compressive strength, shrinkage, and creep. All hardened concrete properties were tested in the laboratory at Auburn University.

4.5.4.1 Modulus of Elasticity

The modulus of elasticity was important for creep testing to distinguish the elastic strain due to loading from the creep and shrinkage strains in the concrete. Several of the prediction models discussed in Chapter 3 also have their own method for predicting the modulus of elasticity, so the measured value was important for comparison to the predicted values. To obtain this value, cylinders from each loading age were tested with a compressometer in accordance with the requirements in ASTM C469 (2014). The compressometer used for modulus of elasticity testing is shown in Figure 4-6. At the time of creep loading for each loading age, one cylinder's compressive strength was determined through compression testing. A second cylinder was then placed in the compressometer and loaded at 1000 lbs/sec. until a longitudinal strain of 50 microstrain was reached. The load was then recorded, and the test continued until the stress in the concrete reached 40 percent of the compressive strength of the first cylinder, and the strain

was recorded. The stress and strain values of each specimen were then used to determine the modulus of elasticity of the concrete. After this test, the cylinders were tested to determine the compressive strength.

Figure 4-6: Compressometer used to test modulus of elasticity

4.5.4.2 Compressive Strength

The compressive strength of the concrete was necessary for completing other tests and calculations. For creep testing, the target applied stress was 40 percent of the compressive strength of the concrete, so it was important to have an accurate value for each loading age. Additionally, as discussed in Chapter 3, all of the prediction models that were considered for this research use the compressive strength of concrete as a parameter for calculating creep, shrinkage, or both. Three cylinders were tested for compressive strength from each loading age as presented in Table 4-1. All testing was performed in accordance with the requirements in AASHTO T22 (2017). The specimens were prepared for testing using an end grinder to ensure smooth and level surfaces of contact between the cylinder ends and the compression machine. All cylinders were tested in a 400-kip compression testing machine at a target loading rate of 1,000 lbs/sec until failure. The maximum load was then recorded for each sample, and the average compressive strength of the three cylinders was calculated.

4.5.4.3 Drying Shrinkage

Drying shrinkage testing of the concrete rectangular prism collected at the bridge construction site was performed in accordance with the requirements in AASHTO T160 (2017). Drying of the specimens not placed in the lime bath began immediately after the removal of the molds. Measurements were taken using a standard length comparator which is shown in Figure 4-7. For the moist-cured specimens, drying began seven days after being placed in the lime-saturated water tank, and the method of measurement was the same as the air-cured specimens. As prescribed by AASHTO T160 (2017), measurement readings began immediately after exposure to drying, followed by two to six hours after exposure, once a day for the first week, once a week for the first month, once a month for the first year, and once every three months following the first year. After the three shrinkage strains were obtained for each set of prisms, the average was taken to obtain one shrinkage value at the concrete age of each measurement.

Figure 4-7: Standard length comparator used to measure drying shrinkage

In order to isolate the creep strain from the total strain, it was important to measure the shrinkage strain in additional cylinders that corresponded to the cylinders used for creep testing.

To accomplish this, three additional cylinders were collected from each field visit for drying shrinkage, and Demountable Mechanical (DEMEC) strain points were epoxied on three locations (approximately 120° apart) on each cylinder. A shrinkage cylinder with DEMEC points installed is shown in Figure 4-8, and the DEMEC strain gauge used for creep and shrinkage measurement is shown in Figure 4-9. The setup of DEMEC points was also identical on all creep specimens. The shrinkage cylinder strains were measured at the same time as the total strain measurements of loaded specimens to isolate the creep strain from the total strain.

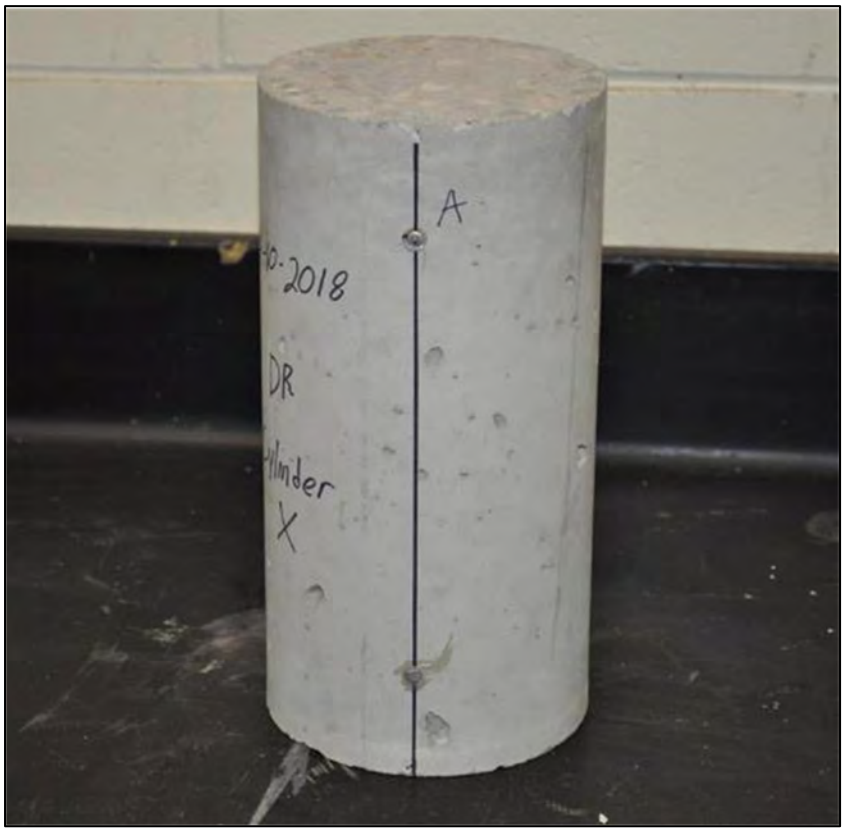

Figure 4-8: DEMEC points installed on shrinkage cylinder

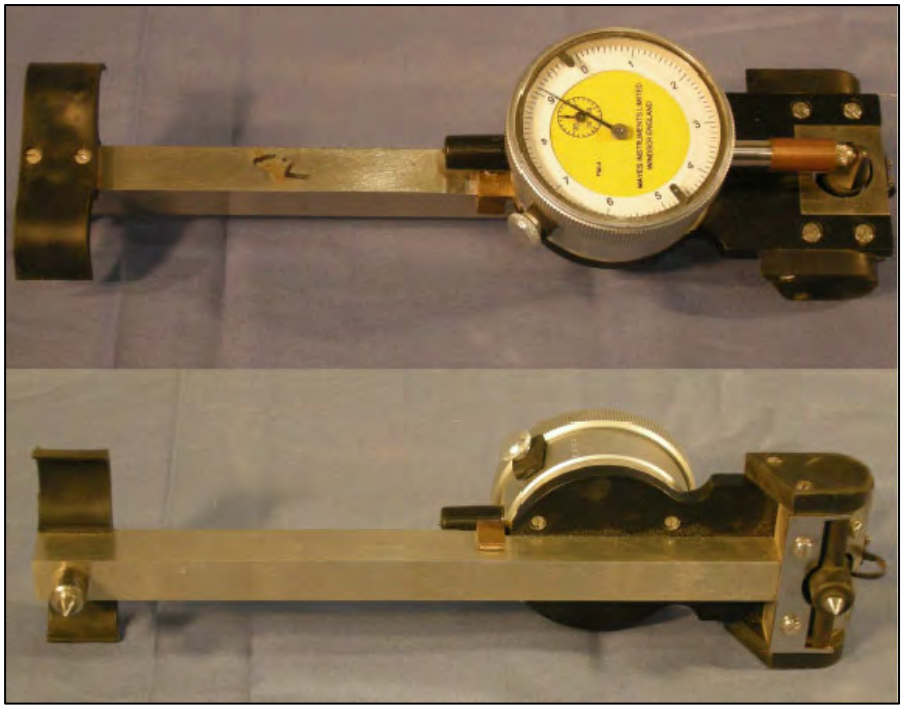

Figure 4-9: DEMEC strain gauge (Kavanaugh 2008)

4.5.4.4 Creep

All creep testing for the purposes of this research was performed in accordance with the requirements in ASTM C512 (2015). This section outlines the testing procedures used for creep testing, as well as the details of the equipment.

4.5.4.4.1 Creep Testing Room

To adhere to the standards in ASTM C512 (2015), all creep testing was performed in a temperature- and humidity-controlled room in the laboratory at Auburn University. These standards required that the temperature of the testing environment remain at 73.5°F ± 3.5°F, and that the ambient relative humidity remain at 50% ± 4%. These parameters were recorded throughout the duration of testing both to monitor compliance with the above requirements, and for use in the creep and shrinkage prediction models. The layout of the creep testing room is shown in Figure 4-10.

Figure 4-10: Creep testing room

All creep, shrinkage, and modulus of elasticity cylinder specimens were stored upright in the creep testing room until their appropriate loading ages. The shrinkage cylinders corresponding to the creep specimens can be seen with the creep testing frames in Figure 4-10. The shrinkage prism specimens were stored on wire racks along the wall of the creep testing room to expose the entire prism surface to the room environment.

4.5.4.4.2 Creep Testing Frames

For the purposes of this research, creep testing frames were required to sustain the loads on the creep cylinders and enable the measurement of the strain in each specimen. For each of the four sampling dates, four loading ages were tested for a total of 16 creep testing frames with two cylinders in each frame. Loading of each frame was performed with a hydraulic ram placed between the two upper plates of the frame; this ram was extended to induce the load on the cylinders. A 200-kip load cell was also placed in series with the hydraulic ram to monitor achievement of the desired concrete stress of 40 percent of the compressive strength. According to ASTM C512 (2015), the frames were required to maintain ± 2 percent of the target load; otherwise, the load would have to be reapplied until within the required range. The setup for the hydraulic ram is shown in Figure 4-11.

Figure 4-11: Setup of hydraulic ram and load cell on creep testing frame

The creep testing frames used for this research were assembled in a study by Kavanaugh (2008). In this study, the frames were required to have a capacity of approximately 180 kips in order to load 6 in. × 12 in. cylinders to 40 percent of their compressive strength of 16,000 psi. Therefore, each of the three rods used to hold the load after jacking were required to have a capacity of 60 kips. To achieve this, 1¾ diameter steel rods with a yield stress of 65 ksi and an ultimate stress of 80 ksi were selected (Kavanaugh 2008). These rods had a length of 90 in., and they were threaded on the lower 10 in. of the rod and the upper 50 in. The loads in each frame were secured with two 1¾ Grade 8, heavy-duty nuts on each rod; however, more were required to secure the reaction plates. These nuts were made from C 1045 steel with a minimum Rockwell hardness of C24 and a minimum ultimate tensile stress of 150 ksi (Kavanaugh 2008). Due to machine tolerance issues in the nuts, when the hydraulic ram was released, approximately two percent of the applied load was lost. To compensate for this problem, the applied load was two percent over the target load for all frames (Kavanaugh 2008). The reaction plates selected for the creep testing frames were 2¾ in. steel plates, and a six in. diameter circle was marked on the underside of the upper floating reaction plate to assist in placement of the cylinders (Kavanaugh 2008). ASTM C512 suggests that to maintain the load in each frame throughout the deformations, railroad springs should be used to allow some length change without significant load reduction. The selected springs were designed and constructed by Duer/Carolina Coil, Inc. of Reidville, South Carolina and were made from ASTM-A304, Grade 220 steel. Each spring had a height of 15 in. and an outer diameter of 8 ½ in. with a spring constant of 25,000 lbs/in. Three springs were

required for each frame. A creep testing frame image is shown in Figure 4-12, and detailed drawings of a frame are shown in Figure 4-13 and Figure 4-14.

Figure 4-12: Creep testing frame (Kavanaugh 2008)

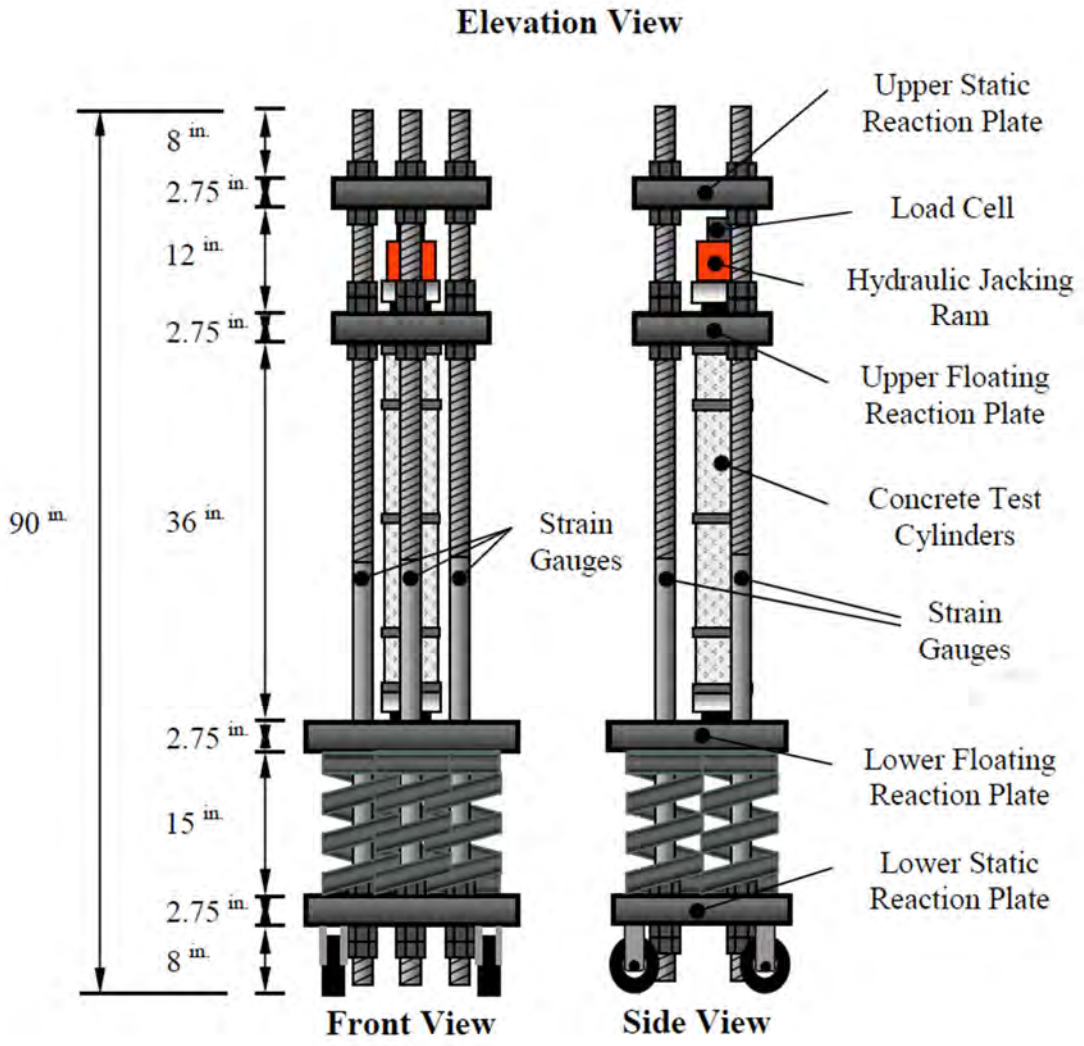

Figure 4-13: Creep frame schematic (Kavanaugh 2008)

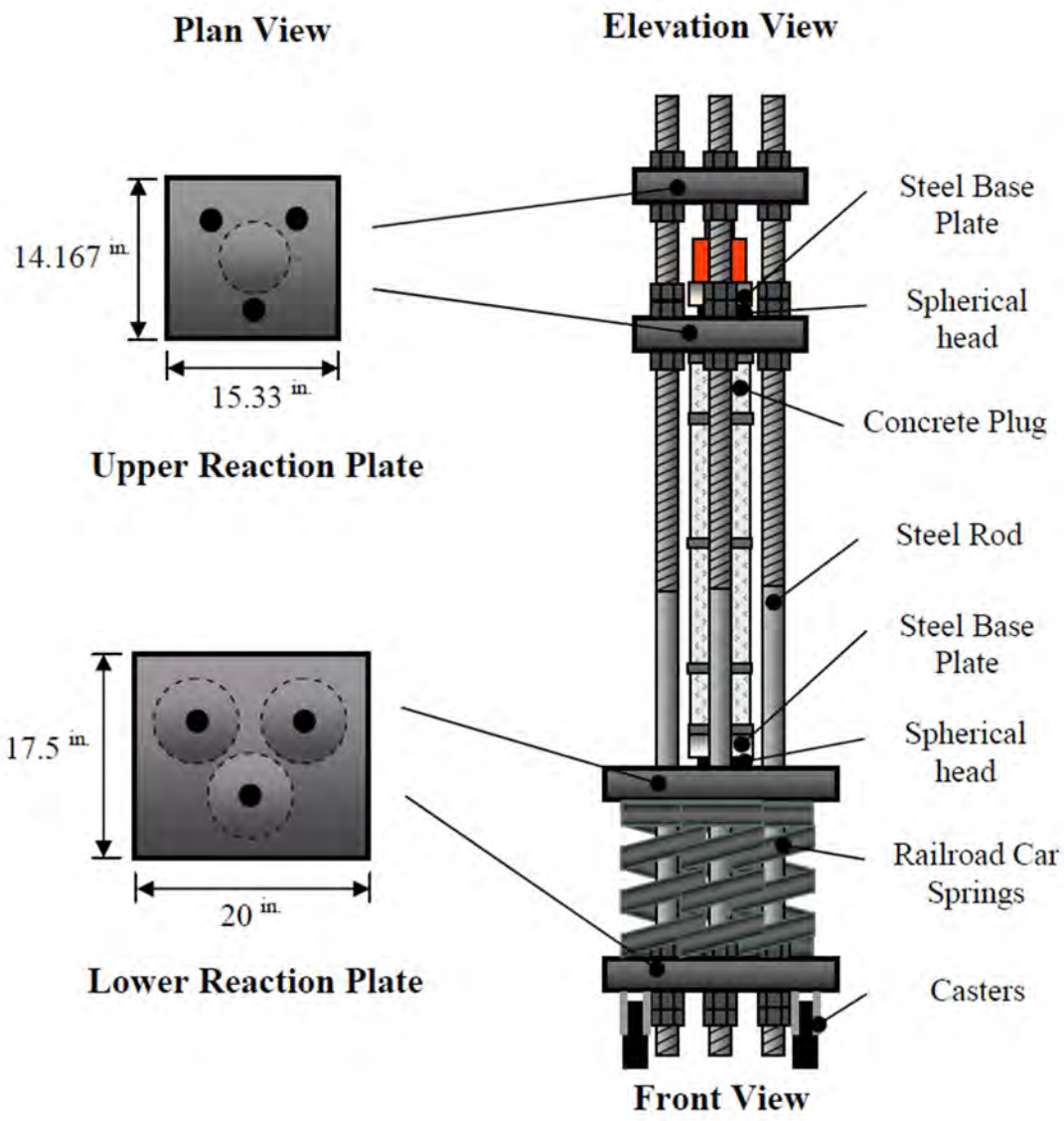

Figure 4-14: Creep frame schematic (Kavanaugh 2008)

To monitor the state of the load in each creep testing frame, DEMEC points were epoxied on two locations on each steel rod 180 degrees apart from each other. The bar strains were measured at every measurement of the creep specimens to estimate the load carried by the frame and to ensure it met the ± 2 percent requirement. A DEMEC point epoxied to the steel rods in the creep frames is shown in Figure 4-15.

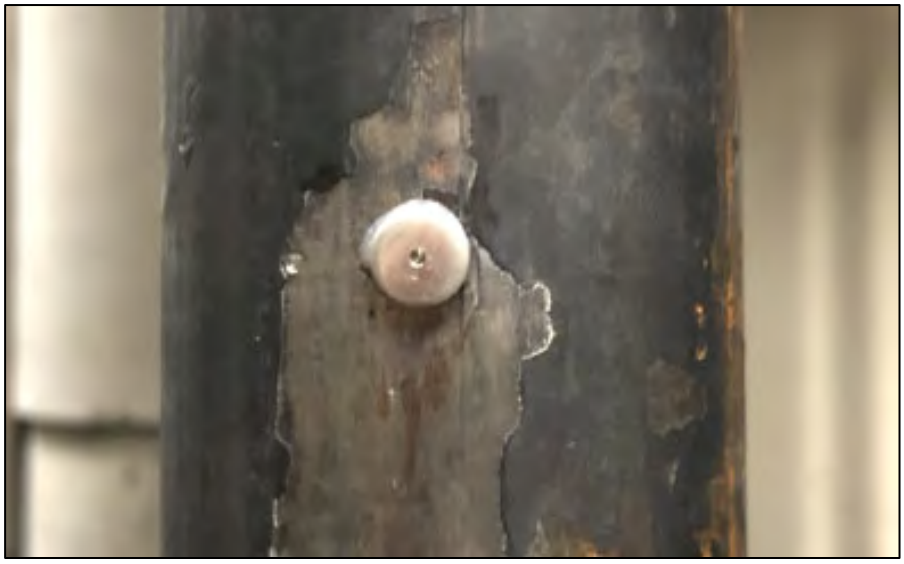

Figure 4-15: DEMEC point epoxied to steel rod for monitoring load

4.5.4.4.3 Creep Testing Procedure

In accordance with the requirements in ASTM C512, a procedural list of steps for all creep testing performed in this research is shown below. Several of the steps were adopted from a similar list developed by Kavanaugh (2008), but modifications were made for this research where applicable.

1. Obtain creep, shrinkage, and strength and elastic modulus specimens.
2. End grind each specimen to ensure a level surface and prevent eccentric loading.
3. Epoxy DEMEC points at 120-degree intervals around each creep and shrinkage cylinder. Allow epoxy to reach strength before taking readings.
4. At the time of loading, determine the ultimate compressive strength and modulus of elasticity in accordance with the requirements in AASHTO T22 (2017) and ASTM C469 (2014), respectively. Use one cylinder to determine the ultimate compressive strength and the two additional specimens for modulus of elasticity testing before testing the compressive strength.
5. Place two creep specimens into the creep frame, ensuring that the cylinders are aligned and centered on each other.
6. Lower the top floating reaction plate to make contact with the top concrete plug, ensuring that all sides of the cylinders are level.
7. Record the initial strain measurements for the creep and shrinkage specimens and steel bars before the load is applied.
8. Insert the hydraulic ram and load cell between the top two reaction plates, ensuring that the load cell rests flush with the top reaction plate.
9. Connect the load cell to the strain indicator.

10. Apply load with the hydraulic ram until 104 percent of the target load is reached. As load is applied, it is necessary to take intermediate readings of concrete strains to ensure no eccentricities have developed.
11. After reaching the desired load, tighten the nuts down to the top floating reaction plate using a pipe wrench. Lock nuts must be snug tight to the initial nuts.
12. Slowly retract the hydraulic jack, and take readings of the DEMEC points on the steel rods to ensure that the applied load remains within the two percent threshold. Reapply load if necessary.
13. Record concrete strain measurements immediately after the loading process has been completed.

Creep and shrinkage strain measurements were taken at the same intervals as the drying shrinkage specimens discussed above. After the initial load was applied, readings were taken at two to six hours after loading, once a day for the first week, once a week for the first month, once a month for the first year, and every three months following the first year. The bar strains were taken at these same intervals to ensure the required load tolerance was met. Microsoft Excel was used to convert these bar strains into bar forces, which were added together to determine the total force in each frame. If this total force was not within the two percent threshold, the hydraulic ram and load cell were used to reapply the load to the frame.

Chapter 5

CONSTRUCTION OVERVIEW OF THE BIRMINGHAM I-59/I-20 SEGMENTAL BRIDGE

5.1 INTRODUCTION

As mentioned in the previous chapter, all concrete samples were collected on-site at the Birmingham I-59/I-20 segmental bridge casting yard. Samples were collected from the same concrete mixtures that were used to cast the segmental bridge superstructure. This chapter provides an overview of the jobsite where all samples were collected as well as how the bridge was constructed.

5.2 PROJECT LOCATION

The I-59/I-20 segmental bridge project occurred at two major locations in Birmingham, Alabama. The bridge was assembled running through downtown Birmingham. With precast, segmental bridge construction it is important that the contractor have a large casting yard to store materials, equipment, and finished segments. For the Birmingham I-59/I-20 segmental bridge project all casting and storage of segments took place at an abandoned steel mill located at 1503 50th Street North Birmingham, Alabama 35212, adjacent to the Birmingham-Shuttlesworth International Airport. It was imperative to the contractor that all casting and storage would occur as close as possible to the erection site for the bridge. Portions of the abandoned steel mill were used for dry storage as well as to fabricate post-tension strand components.

5.3 CONSTRUCTION DURATION

Construction of the Birmingham I-59/I-20 segmental bridge superstructure occurred in two major phases: casting and erection of the segments. The first segment was cast on February 21, 2018, and the last segment was cast on August 9, 2019; a total casting duration of 534 days. At the peak of production eight segments were cast per day. The second major phase of the superstructure construction was the erection of segments at the bridge location on falsework. The first segment was erected on March 11, 2019, and the last segment was erected on October 14, 2019; a total erection duration of 217 days. Segments were not erected in the same order as they were cast. The duration of the two major stages of the segmental superstructure construction is presented in Figure 5-1 (courtesy of Mr. Eric Johnson, Corven Engineering).

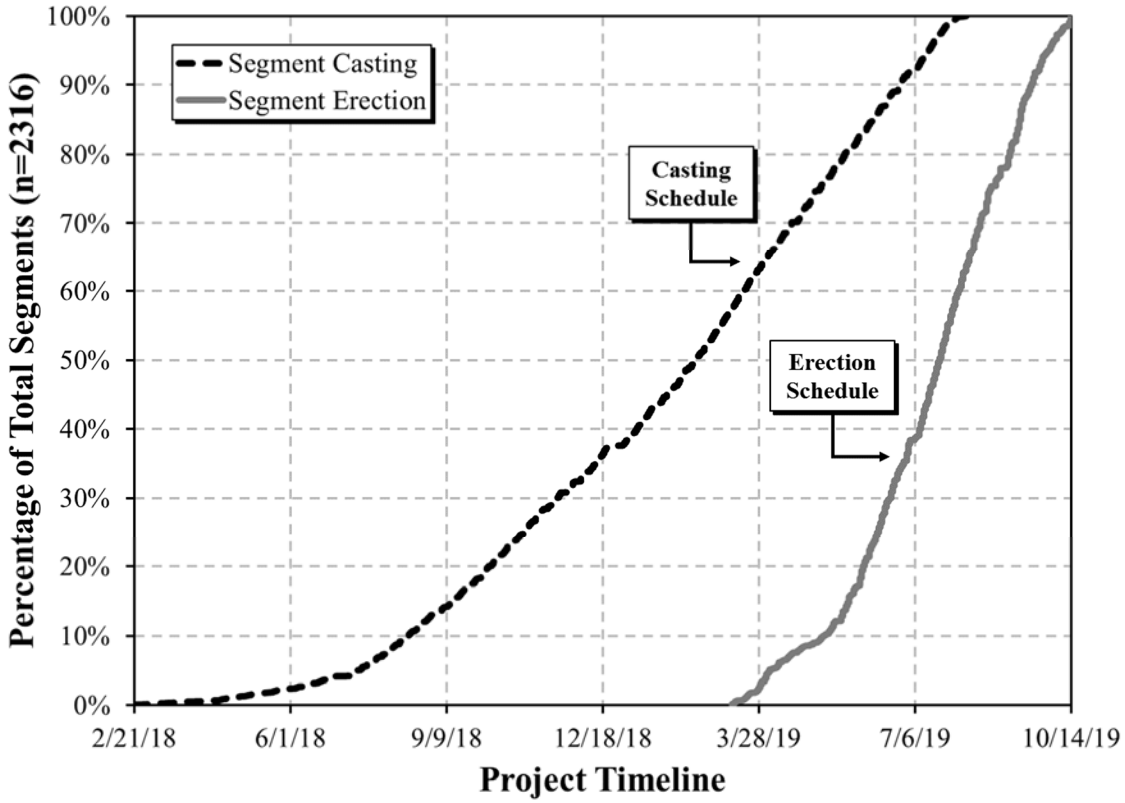

Figure 5-1: Birmingham I-59/I-20 segmental bridge superstructure construction duration

5.4 FORMWORK OF SEGMENTS

The contractor had eight primary segmental casting beds manufactured specifically for the project by a third-party contractor. Each form was equipped with adjustment points to allow for changes in grade. The formwork was also designed to have external vibrators installed on the walls to assist with proper consolidation. Typical formwork used to cast segments can be seen in Figure 5-2.

Figure 5-2: Formwork used to cast segments

After proper installation of each form, checks were made to ensure that the formwork met the desired specification. At the beginning of the casting stage all reinforcement was installed inside of the formwork. As the rate of production increased, a subsequent reinforcement fabrication box was developed to accelerate work associated with tying the reinforcement cage. The reinforcement box that matches the internal dimensions of the formwork is shown in Figure 5-3.

Figure 5-3: Reinforcement fabrication box for increased construction efficiency

5.5 CASTING OF SEGMENTS

This section outlines the standard procedure used in casting a typical bridge segment. This process was repeated for each segment with only minor differences throughout the casting stage of the project. During the peak of operation this process was repeated every day for eight casting beds.

5.5.1 Formwork Preparation

Before concrete could be placed, the formwork was prepared. The casting of each segment followed a match-casting method in which the face of one segment would be the back wall of the formwork for the next segment in a span. The formwork was then properly aligned with any minor change in orientation from the previous segment in the span. As shown in Figure 5-4, a rail system with hydraulic jacks allowed for the inside cell of the form to be removed.

Figure 5-4: System on rails used to remove internal cell of the formwork

After removing the previous segment and cleaning the formwork, a release agent approved by ALDOT was applied to all formwork surfaces. Reinforcement was then lifted from the previously mentioned box using a crane and placed into the formwork. Quality checks were completed to ensure the proper reinforcement layout and cover were achieved. Transverse post-tensioning ducts with tendons were also installed. With the use of the rail system, the internal cell of the formwork was installed. The match-cast segment can be seen with final reinforcement in the formwork in Figure 5-5.

Figure 5-5: Formwork for a segment ready for concrete placement

5.5.2 Concrete Production and Quality Assurance

Concrete placed in the segments had to meet the specific mixture proportions approved by ALDOT. With the size of the project the contractor found it beneficial to batch concrete on site. At the early stages of the project, the on-site batching plant was not operational, concrete was supplied and delivered to the segments from a third-party ready-mixed concrete producer. Once the on-site batching plant was running and approved by ALDOT, all raw materials were able to be stored locally, which allowed the delivery time to be reduced. The on-site batching plant can be seen in Figure 5-6. So long as the concrete met all ALDOT requirements, it could be placed into the formwork.

Figure 5-6: On-site batching plant for concrete production

As each batch of concrete arrived to the formwork a sample was taken for quality assurance testing. The on-site technician was responsible for testing each batch of concrete for the fresh properties required by ALDOT. Total air content, unit weight, slump, and concrete temperature was monitored and recorded. The total air content being measured on the jobsite can be seen in Figure 5-7. In addition to fresh properties, quality assurance cylinders were cast using concrete from the middle of each truck. These cylinders were used for compression testing to determine when formwork could be removed, when post-tensioning could be applied, and if the segment met the specified 28-day compressive strength.

Figure 5-7: Quality assurance testing prior to concrete placement

5.5.3 Concrete Placement

Concrete was placed from the top of each form for all typical segments, which did not allow a standard ready-mixed concrete truck to reach. Two methods were used during the project to move concrete from the truck to the top of each form. In early stages of the project a belt conveyor was used to raise concrete to the required height. The conveyor stayed in the same place and each ready-mixed concrete truck placed the batch of concrete onto the conveyor, which can be seen in Figure 5-8. As the segment was filled the arm of the conveyor belt was moved around at the top of the formwork to ensure the concrete was placed where needed.

Figure 5-8: Conveyor moving concrete to desired location at the top of the formwork

As the project progressed, it was determined that the conveyor system was inefficient and a second method of transport was implemented. The second method for moving concrete to the formwork was by using a concrete bucket and crane. The ready-mixed concrete truck discharged concrete into the bucket shown in Figure 5-9. Once filled, the bucket was lifted by a crane to the top of the formwork. Laborers quickly discharged the concrete into the form shown in Figure 5-10 and returned the bucket to be filled again. This placement method was much more efficient and was used for the remainder of the project.

Figure 5-9: Concrete bucket being filled by ready-mixed concrete truck

Figure 5-10: Concrete being placed into the formwork with a bucket

Proper consolidation was required for the concrete placed in the formwork. As discussed, each form was equipped with external vibrators attached to the walls; however, the energy from

the external vibrators was often not adequate enough to consolidate the concrete properly throughout the formwork. Therefore, portable vibrators were used in addition to the external vibrators to focus consolidation at specific points in the formwork as shown in Figure 5-11.

Figure 5-11: Consolidation using a portable vibrator

5.5.4 Finishing Techniques

The last step in constructing a segment was to strike-off and float its top, which occurred after the formwork was filled and properly consolidated. All segments were finished using standard practices throughout the project duration. An aluminum or magnesium float was used to float the tops of each segment. The proper floating of a segment is shown in Figure 5-12.

Figure 5-12: Concrete being floated using a bull float

5.6 SEGMENT CURING, PROTECTION, AND STORAGE

After each segment was cast, curing techniques were implemented according to the contractor's quality control plan. As discussed previously all segments and quality assurance cylinders were cured using an elevated temperature curing method approved by ALDOT. Thermal blankets were wrapped around all formwork, and the temperature in the enclosure was elevated using electric heaters. Upon completing the initial elevated curing cycle, the concrete cylinders corresponding to each segment were tested in compression. Concrete cylinders were required to reach a minimum compressive strength of 2,500 psi for the formwork to be removed; therefore, if cylinders tested less than the required minimum compressive strength the segment would remain in the form until the required strength was achieved. Prior to stressing of the transverse post-tensioning, concrete cylinders were required to have a compressive strength of 4,000 psi. Once forms were removed, the segment was moved to become the next match-cast segment. In order to protect the formwork from excess heat and severe weather, a roll-away canopy was used for each form of a segment as shown in Figure 5-13.

Figure 5-13: Roll-away canopy to protect each form from severe weather

After a period of 28 days, additional quality assurance cylinders were tested to determine their compressive strength. The cylinders were required to have a compressive strength of 6,500 psi at 28 days. After being used to match cast the next segment in a span, segments were stored on-site until being transported to their final erection location. A rubber-tired gantry crane was used to move segments around in the casting yard, which can be seen in Figure 5-14. The design of the crane allowed easier access around the casting yard as well as lifting the segment with minimal stressing to the concrete.

Figure 5-14: Rubber-tired gantry crane used to transport segments around the casting yard

5.7 SEGMENT CURING, PROTECTION, AND STORAGE

Erection of the Birmingham I-59/I-20 segmental bridge occurred in spans, where a complete span was erected on falsework and then post-tensioned longitudinally. The remainder of this section covers the erection of a typical span in the bridge superstructure. Falsework shown in Figure 5-15 was used on the project to support the segments of each span prior to post-tensioning. The erection schedule allowed for subsequent spans to be erected so that falsework could be recycled every two spans in the system. This allowed for rapid construction of this segmental bridge.

Figure 5-15: Falsework used to erect each span

Each segment was transported from the casting yard to the bridge site on flatbed trucks. As each segment arrived, it was erected onto the falsework. Large cranes lifted segments into place. A segment being lifted using a crane on the bridge site is shown in Figure 5-16. As each segment was erected, laborers guided the segments into place next to the match-cast segment, which is shown in Figure 5-17.

Figure 5-16: Crane lifting a segment into place

Figure 5-17: Segment being guided into place on falsework

The face of one segment was covered with an ALDOT approved water-resistant epoxy before each segment was moved into position. Additional steel bars were used to apply the stress as required by the epoxy manufacturer (ALDOT 832 2018) to ensure proper bonding. All spans were completed with a narrow closure strip between the last typical segment and the column segment. This closure strip allowed for minor geometry adjustments to be made at these locations. With all segments in place, each span was longitudinally post-tensioned along the entire simple span. After two spans were completed in sequence, the closure strip shown in Figure 5-18 between the two spans was filled using concrete delivered on-site.

Figure 5-18: Closure strip between two spans to be filled with concrete

The additional top cover in segments allowed the surface to be leveled by grinding. For this reason ALDOT required quartzite aggregate as opposed to limestone aggregate, which may lead to polishing after grinding. Additionally, grinding provided grooves of approximately 1/32 in. to meet requirements of ALDOT Standard Specifications Section 455 (2018).

Chapter 6

TEST RESULTS

6.1 INTRODUCTION

All fresh and hardened concrete testing results, as well as an overview of testing conditions, are presented in this chapter. This study consists of data collected from April 10, 2018, through October 2, 2023. The fresh concrete testing results are presented in Section 6.2, and the initial hardened concrete test results are presented in Section 6.3. Section 6.4 presents a summary of the shrinkage and creep testing conditions, and all shrinkage and creep test results are presented in Section 6.5 and Section 6.6, respectively.

6.2 FRESH CONCRETE PROPERTIES

This section presents all fresh concrete properties of the concrete mixtures from each of the four sampling dates. As presented in Table 4-2, the concrete cast on each sampling date had different ALDOT approved mixture proportions, which affected both the fresh and hardened concrete properties. A summary of all fresh concrete test results is presented in Table 6-1, and each fresh concrete property important to this study is discussed in the subsequent sections.

Table 6-1: Summary of fresh concrete properties for all sampling dates

Fresh Concrete Property	Sampling Date			
	04/10/2018	**07/09/2018**	**11/19/2018**	**04/16/2018**
Slump (in.)	5.5	6.25	6.0	6.0
Total Air Content (%)	4.4	4.2	3.4	3.8
Unit Weight (lb/ft^3)	144	141	146	145
Concrete Temperature (°F)	76	87	76	76

6.2.1 Slump

As discussed in Chapter 4, the ALDOT requirement for the slump of concrete in segmental bridges was between 3 to 9 inches. As the table above shows, the slump measurements for all sampling dates fell within this requirement. The slump of all four of the mixtures remained consistent with a typical value of approximately 6 inches.

6.2.2 Total Air Content

The ALDOT requirement for total air content in fresh concrete ranges from 3 to 6 percent. The measured air contents from each of the sampling dates fell within this requirement. The 11/19/2018 sampling date had the lowest measured air content at 3.4 percent, which corresponds to the ALDOT approved mixture that utilized Type III cement.

6.2.3 Unit Weight

Although there is no ALDOT specification requirement for a specific unit weight of fresh concrete, this value was recorded for all samples. In general, the average unit weights were the same as the theoretical values from the ALDOT approved mixture proportions in Table 4-2. The only exception was the 07/09/2018 sampling date, which had a slightly lower unit weight than the theoretical value, but this slight decrease did not affect any further testing results.

6.2.4 Temperature

As discussed in Chapter 4, the temperature of fresh concrete according to the ALDOT specifications is required to be between 50°F and 95°F. As shown in Table 4-2, the fresh concrete temperatures for all the sampling dates fell within the acceptable range.

6.3 HARDENED CONCRETE PROPERTIES

This section provides a summary of results of hardened concrete property testing. The properties discussed include compressive strength, modulus of elasticity, and maturity due to temperature. All testing for the hardened concrete properties occurred in the laboratory at Auburn University. Certain components of these properties are emphasized in the discussion for further comparison to creep and shrinkage prediction models.

6.3.1 Compressive Strength

As discussed in Chapter 4, the compressive strength was tested at each loading age to determine the loading force that corresponds to a stress of 40 percent of the strength for creep testing according to ASTM C512 (2015). A summary of all compressive strength results is presented below in Table 6-2.

Table 6-2: Compressive strength testing results

Concrete Age (Days)	Compressive Strength (psi)			
	04/10/2018	07/09/2018	11/19/2018	04/16/2019
7	5,100	5,600	6,400	7,300
28	6,100	6,700	7,200	8,000
91	6,000	7,100	7,500	8,300
182	6,400	7,100	7,400	8,100

The lowest concrete compressive strength for all samples taken was recorded at 7 days for the 04/10/2018 sampling date at 5,100 psi, while the highest compressive strength was recorded at 91 days for the 04/16/2019 sampling date at 8,300 psi. The average recorded 28-day compressive strength for all sampling dates was 7,000 psi, and the 28-day compressive strength was lower than the required 6,500 psi for the 04/10/2018 sampling date, which had an average strength of 6,100 psi. The development of compressive strength with time for the concrete samples is shown in Figure 6-1. In this figure, it is clear that the concrete compressive strength systematically increased from the first to the last sampling date. This is unusual because the 28-day strength required for this project was 6,500 psi, and this was never changed by ALDOT.

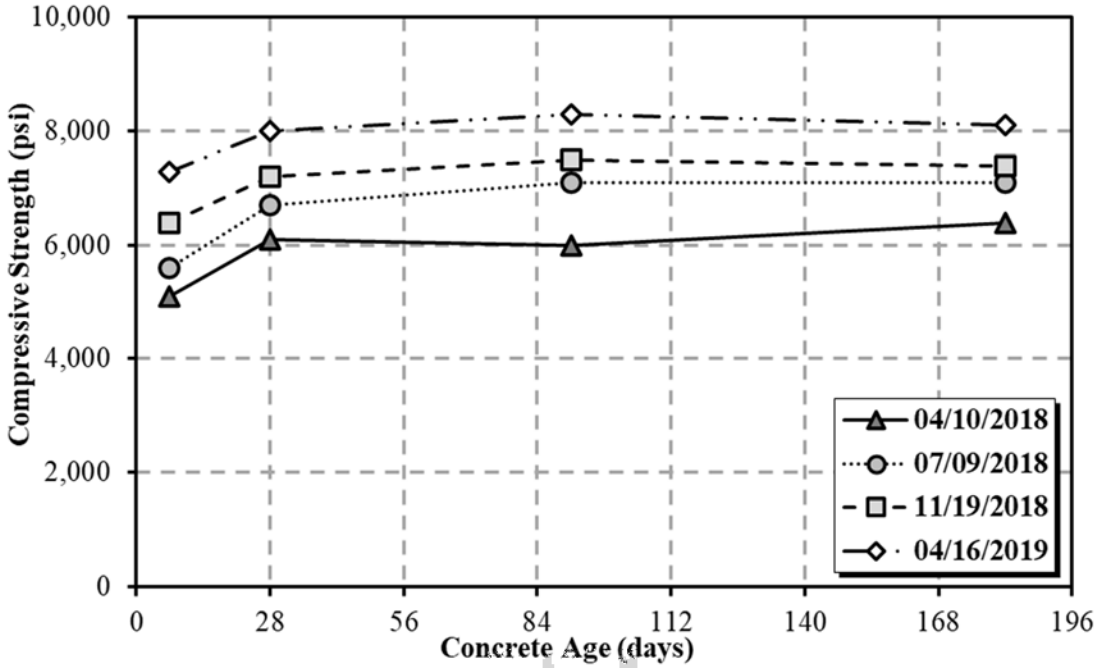

Figure 6-1: Development of compressive strength of concrete samples with time

6.3.2 Modulus of Elasticity

The modulus of elasticity was tested immediately prior to compressive strength testing for each creep-loading age. A summary of the results from modulus of elasticity testing of the concrete samples is presented in Table 6-3.

Table 6-3: Modulus of elasticity testing results

Concrete Age (Days)	Modulus of Elasticity (ksi)			
	04/10/2018	07/09/2018	11/19/2018	04/16/2019
7	3,800	4,250	4,400	5,100
28	4,050	4,250	4,600	5,300
91	3,850	4,200	4,600	5,400
182	4,150	4,300	4,500	5,400

The lowest modulus of elasticity was recorded at 7 days for the 04/10/2018 sampling date at 3,800 ksi, and the highest were recorded at 91 and 182 days for the 04/16/2019 sampling date at 5,400 ksi. The average 28-day modulus of elasticity for all sampling dates was 4,550 ksi. The development of the modulus of elasticity with time is shown in Figure 6-2.

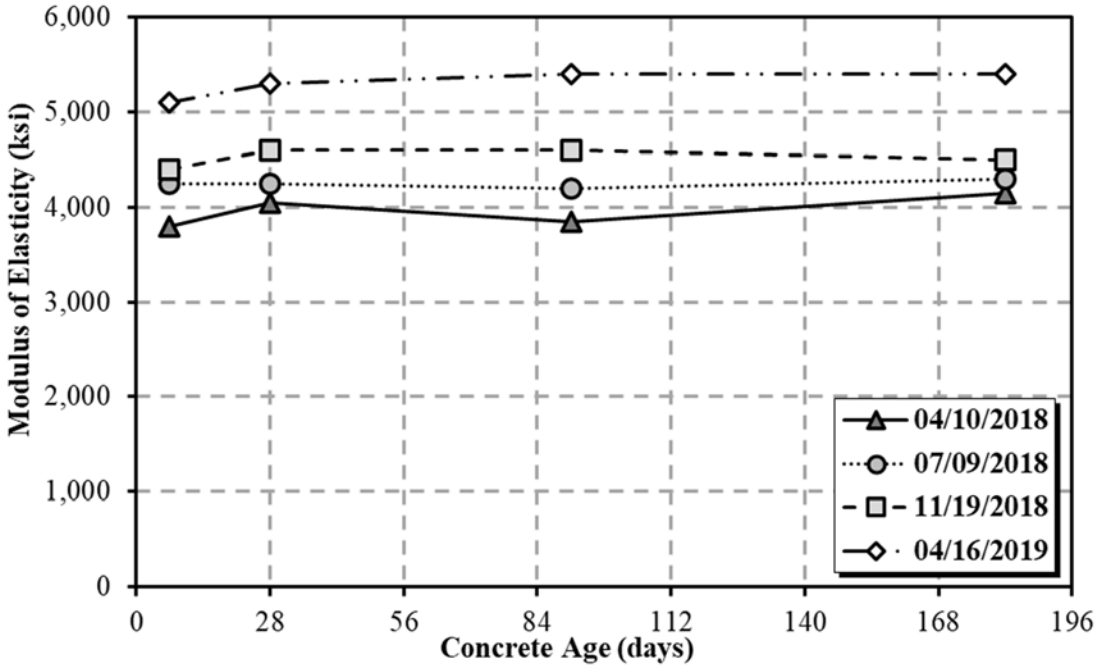

Figure 6-2: Development of modulus of elasticity of concrete samples with time

6.3.3 Maturity

The equivalent age of concrete at the time of loading, the end of curing, and throughout the service-life of the concrete is an important factor in the development of creep and shrinkage. The

maturity of concrete is a function of the temperatures to which it is exposed throughout curing. Higher curing temperatures result in higher equivalent ages, which can increase mechanical properties of the concrete such as compressive strength. To monitor the concrete temperatures during curing, a temperature sensor was placed in a concrete cylinder for each sampling date, and the temperatures were recorded for the first 24 hours after placement. The temperatures of the ambient curing environment were also recorded during this time. An overview of these temperatures is presented in Table 6-4.

Table 6-4: Summary of recorded temperatures for the first 24 hours after placement

Temperature Description		**24-Hour Curing Temperatures (°F)**			
		04/10/2018	**07/09/2018**	**11/19/2018**	**04/16/2019**
Concrete	**Maximum**	121	113	108	126
	Minimum	74	70	53	67
	Average	99	95	81	90
Ambient Environment	**Maximum**	132	109	88	112
	Minimum	69	71	49	63
	Average	98	91	71	80

The maximum recorded concrete temperature for all sampling dates was 126°F for the 04/16/2019 sampling date, and the maximum recorded temperature of the ambient curing environment was 132°F for the 04/10/2018 sampling date. All recorded temperatures of the curing environment fell under the 150°F limit specified by ALDOT. The changes in the concrete and ambient environment temperatures throughout the 24-hour curing cycle for each sampling date are shown in Figures 6-3 through 6-6.

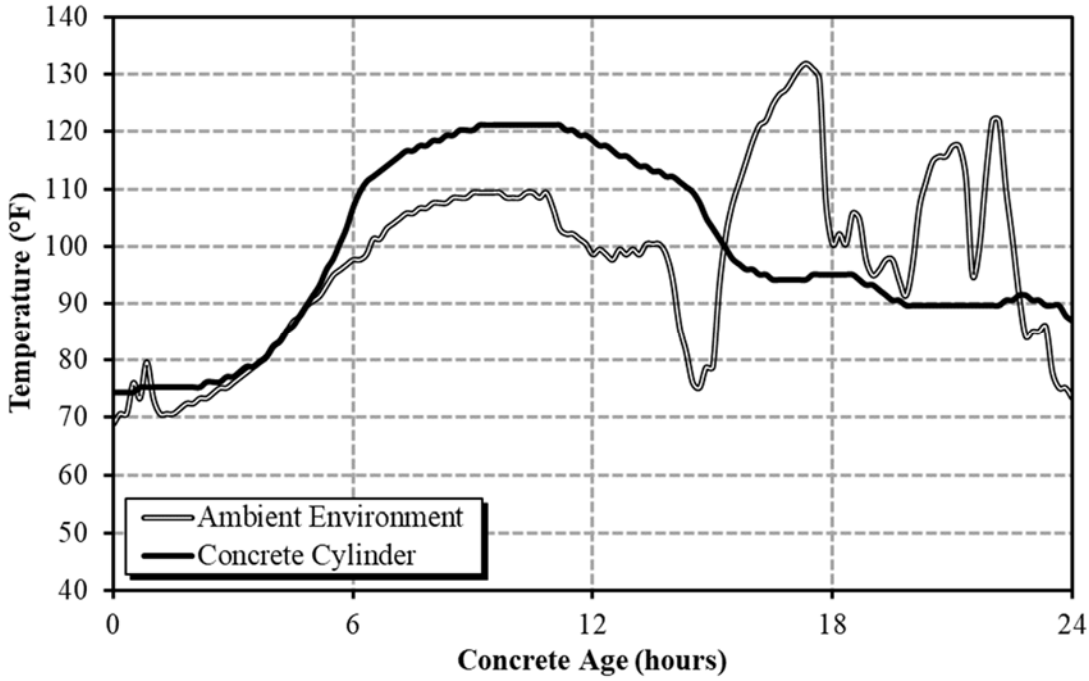

Figure 6-3: Temperature profile for the 04/10/2018 sampling date

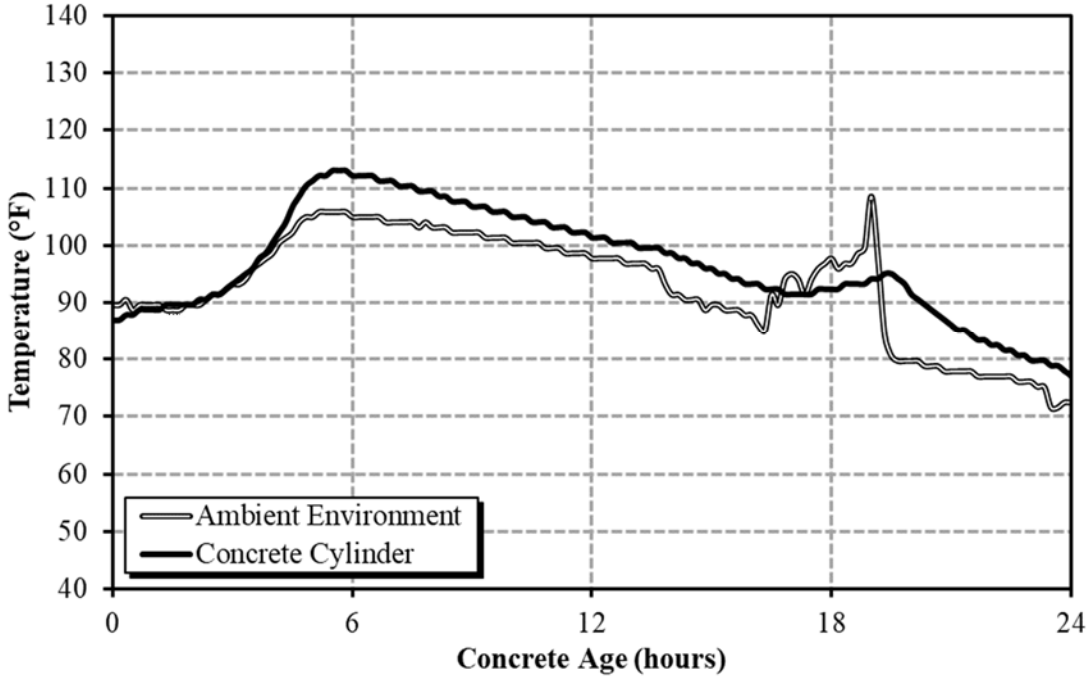

Figure 6-4: Temperature profile for the 07/09/2018 sampling date

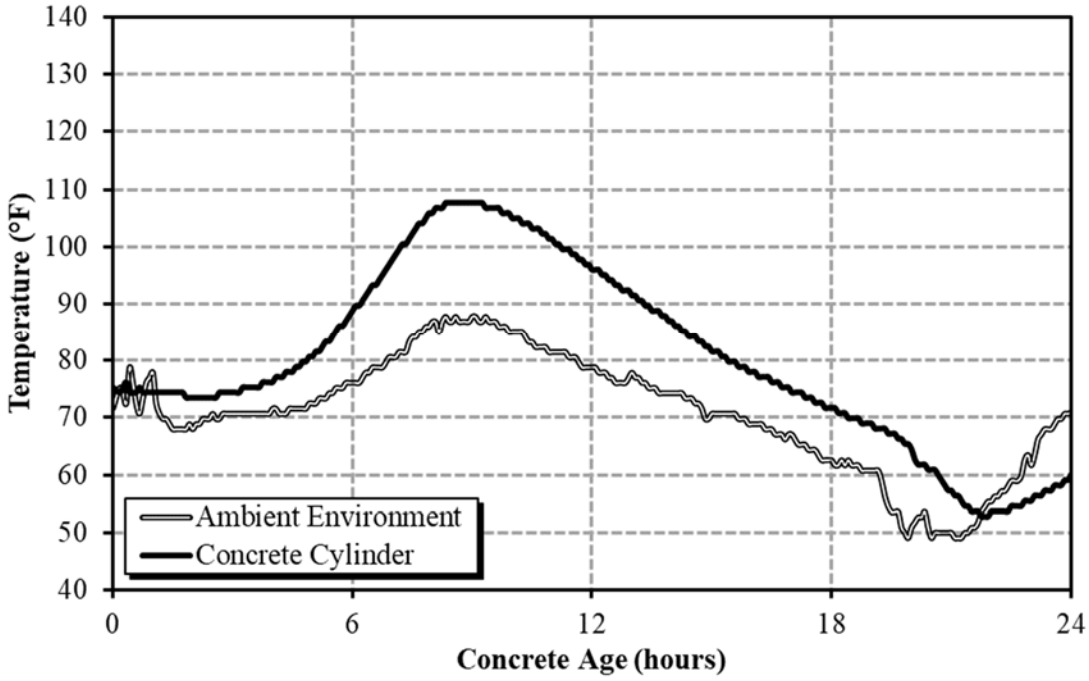

Figure 6-5: Temperature profile for the 11/19/2018 sampling date

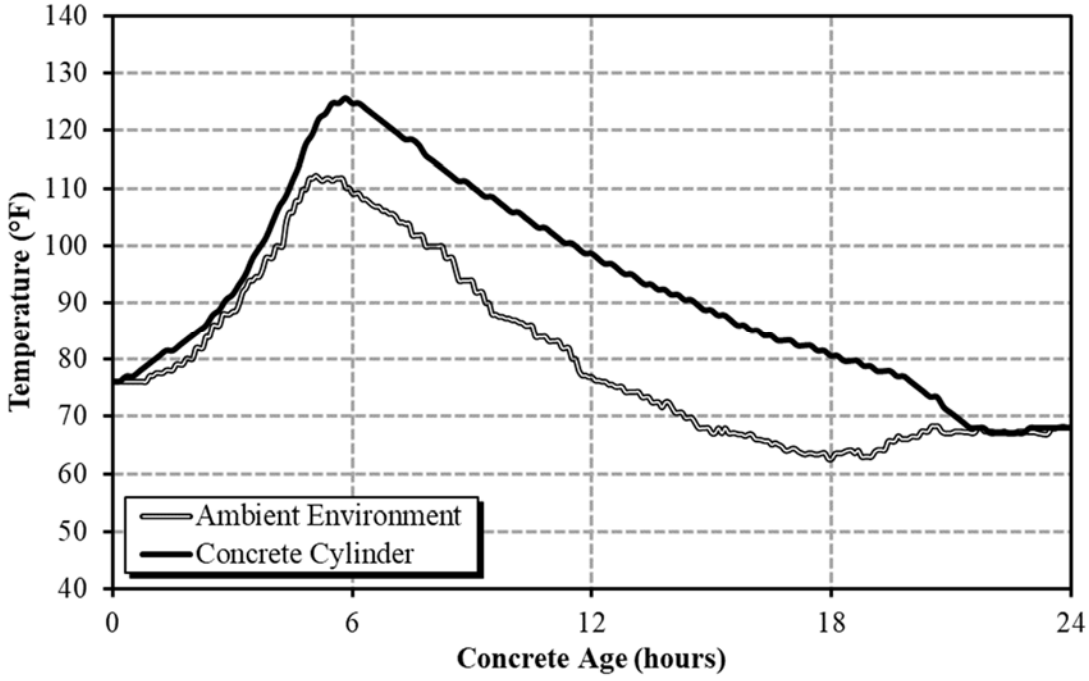

Figure 6-6: Temperature profile for the 04/16/2019 sampling date

As discussed in Chapter 3, several of the creep and shrinkage prediction models used for the purposes of this research require the use of an equivalent-age maturity method to account for the effects of the temperature on creep and shrinkage: B3, B4, CEB MC 1990, CEB MC 90-99, CEB MC 2010, and GL 2000. The equivalent ages of the concrete from each sampling date were calculated based on each of the model's maturity functions. Summaries of the equivalent ages at

the time of loading for creep specimens and at the time drying began for shrinkage specimens are presented in Tables 6-5 and 6-6, respectively. Because the three CEB MC models predict the same equivalent ages, they are represented by one entry in the tables.

Table 6-5: Equivalent age at time of loading for creep specimens

Equivalent Age at Loading (Days)				
Sampling Date	**04/10/2018**			
Method	**B3**	**B4**	**CEB MC**	**GL 2000**
7 Days	10.1	9.2	9.2	8.8
28 Days	35.1	33.4	33.4	30.1
91 Days	110.2	106.0	105.8	94.1
182 Days	218.8	210.7	210.3	186.5
Sampling Date	**07/09/2018**			
Method	**B3**	**B4**	**CEB MC**	**GL 2000**
7 Days	9.7	9.1	9.0	8.4
28 Days	34.8	33.2	33.2	29.8
91 Days	109.9	105.8	105.6	93.8
182 Days	218.4	210.5	210.1	186.2
Sampling Date	**11/19/2018**			
Method	**B3**	**B4**	**CEB MC**	**GL 2000**
7 Days	8.8	8.4	8.4	7.6
28 Days	33.9	32.6	32.5	28.9
91 Days	109.0	105.1	104.9	92.9
182 Days	217.5	209.9	209.5	185.4
Sampling Date	**04/16/2018**			
Method	**B3**	**B4**	**CEB MC**	**GL 2000**
7 Days	9.6	8.9	8.9	8.3
28 Days	34.6	33.1	33.1	29.6
91 Days	109.8	105.6	105.4	93.7
182 Days	218.3	210.4	210.0	186.1

Table 6-6: Equivalent age when drying began for shrinkage specimens

Equivalent Age when Drying Began (Days)				
Curing Type	**Air-Cured Specimens**			
Method	**B3**	**B4**	**CEB MC**	**GL 2000**
04/10/2018	2.9	2.3	2.3	2.7
07/09/2018	2.6	2.2	2.2	2.3
11/19/2018	1.7	1.5	1.5	1.5
04/16/2019	2.4	2.0	2.0	2.2
Curing Type	**Moist-Cured Specimens**			
Method	**B3**	**B4**	**CEB MC**	**GL 2000**
04/10/2018	10.1	9.2	9.2	8.8
07/09/2018	9.7	9.1	9.0	8.4
11/19/2018	8.8	8.4	8.4	7.6
04/16/2019	9.6	8.9	8.9	8.3

6.4 TESTING CONDITIONS

To ensure that all testing occurred within the relevant specifications, the loading data of the creep frames and the temperature and relative humidity of the creep room were monitored throughout the duration of testing. The results from these tests are presented and discussed in this section.

6.4.1 Loading Data

ASTM C512 (2015) specifies that the creep testing frames are required to maintain ± 2 percent of the target load. If any frame fell out of this specification, its load was reapplied; however, the majority of the frames were within the requirement. Toward the end of creep testing, the DEMEC readings on several of the frames indicated that their respective loads had either increased or decreased outside of the specification, with some indicating a deviation of up to 10 percent. Because this occurred near the end of testing and the apparent change in load did not appear to affect the creep strains, rather than reapplying the loads, this was investigated after testing concluded. At this point, each of the frames in question was unloaded to determine its load based on the steel rod strains, which indicated that all frames were within the ASTM requirement. It is believed that the apparent deviation in the frames was caused by human error, but this did not have an impact on any measured creep or shrinkage data.

6.4.2 Temperature of the Creep Room

The temperature of the creep room was measured and recorded with a data logger throughout the creep and shrinkage testing period, as discussed in Chapter 4. The average recorded temperature of the room was 73.5°F, and the maximum and minimum temperatures were 78.9°F and 68.5°F, respectively. The distribution of creep room temperatures is shown in Figure 6-7.

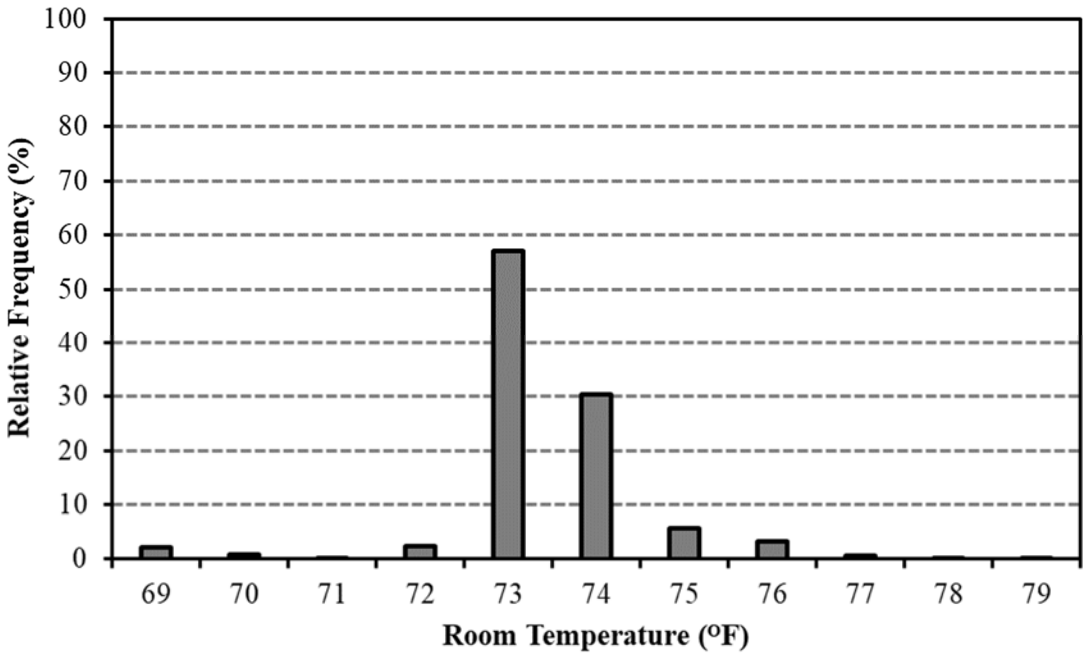

Figure 6-7: Distribution of creep room temperatures

In general, the temperatures in the creep room were maintained within the ASTM C512 (2008) specifications very well. Throughout the duration of testing, 97.8 percent of temperature readings fell within the ASTM specification of 70°F to 77°F. Recorded temperatures that fell outside the required range were likely due to sensitivity of the temperature sensor when small changes were made to the environment. Because so few data points were outside the specification, it is not likely that they had any significant effect on any creep and shrinkage data.

6.4.3 Relative Humidity of the Creep Room

The relative humidity of the creep room was monitored throughout the duration of testing with the same device used to record the temperature. The average recorded relative humidity was 46.9%, and the maximum and minimum relative humidities were 73.9% and 16.2%, respectively. The distribution of relative humidities in the creep room between the values of 42% and 58% is shown in Figure 6-8. Values outside this range are not shown due to their low occurrence. Any values outside of the specified range are primarily a result of a failure of the humidity-controlling equipment in the creep room that occurred during testing. Without functional humidity-control, the ambient relative humidity of the room rose in the warm months of the year and fell in the cool

months. This issue was addressed by installing a humidifier for the cool months and a dehumidifier for the warm months, and the relative humidity values were much more consistent for the remainder of testing. Because of their lower relative frequency, the values that fell outside the ASTM C512 (2008) requirement are not believed to have any significant effect on the measured creep and shrinkage test results.

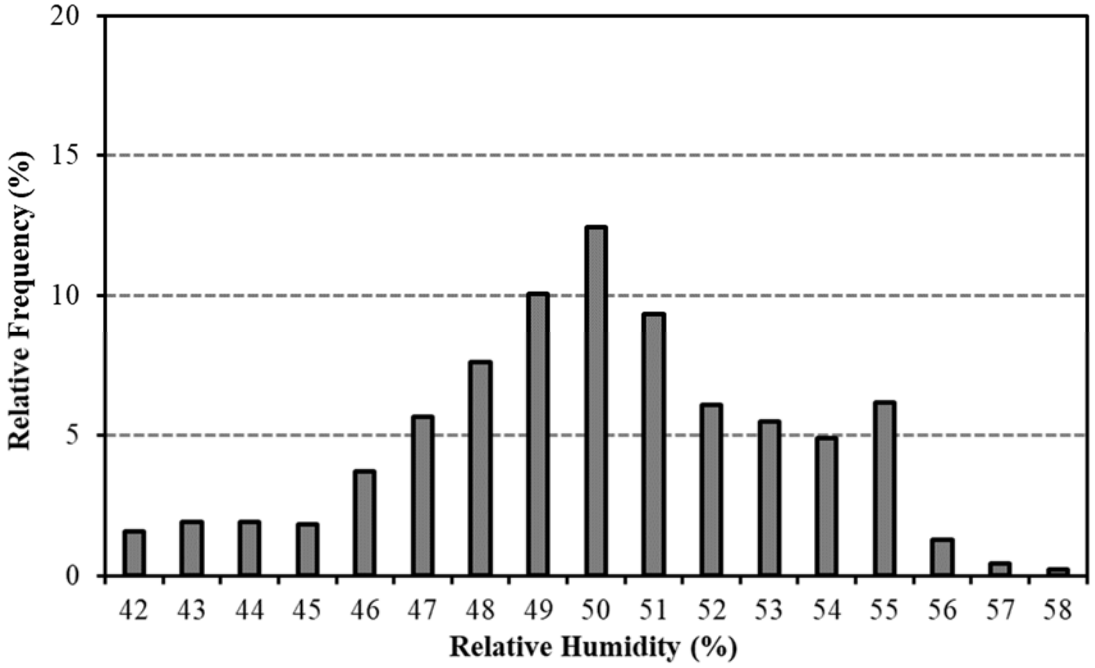

Figure 6-8: Distribution of creep room relative humidities

6.5 SHRINKAGE RESULTS

This section provides test results for all concrete shrinkage specimens, both cylinders and prisms. As discussed in Chapter 4, shrinkage cylinders were tested to accompany the creep cylinders and to isolate the creep strains in them. Additional shrinkage prims were also tested, which captured shrinkage for both air-curing and moist-curing conditions. The development of shrinkage with time for all shrinkage specimens is shown in the following sections, and for comparison purposes, the average 4-year shrinkage strain for each set of specimens is presented in Table 6-7.

Table 6-7: Average 4-year shrinkage strains for all specimens

Average 4-Year Shrinkage Strains (× 10^{-6} in./in.)			
Sampling Date	**Cylinders**	**Air-Cured Prisms**	**Moist-Cured Prisms**
04/10/2018	-573	-792	-855
07/09/2018	-542	-700	-710
11/19/2018	-481	-690	-730
04/16/2019	-442	-560	-575

As the table above shows, the maximum and minimum shrinkage strains for all specimen types corresponded to the 04/10/2018 sampling date and the 04/16/2019 sampling date, respectively. This is partially due to the inverse relationship between concrete strength and shrinkage magnitude described in Chapter 2. Because the concrete cast on 04/16/2019 had the highest average strength, and the concrete cast on 04/10/2018 had the lowest, these specimens resulted in the lowest and highest shrinkage values, respectively.

6.5.1 Shrinkage Cylinders

The development of shrinkage strain with respect to time for all creep companion shrinkage cylinders is shown in Figure 6-9. As was discussed in Chapter 4, while on the jobsite, these cylinders experienced the same initial curing regime as the bridge segments.

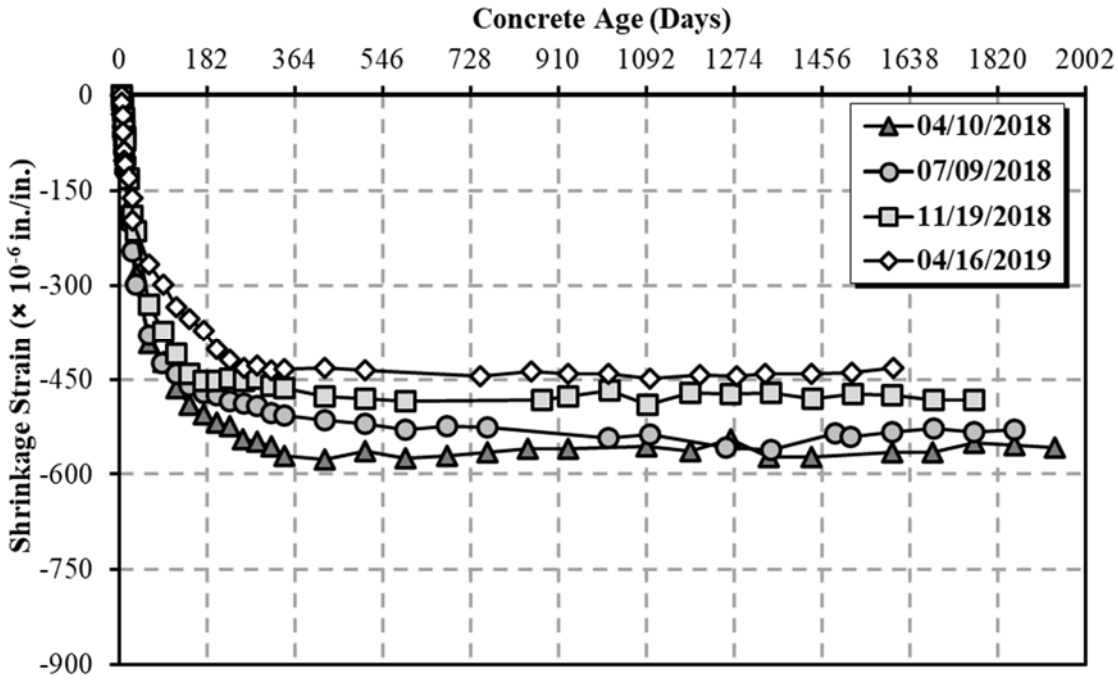

Figure 6-9: Development of shrinkage with time for creep companion cylinders

It can be seen in the figure that almost all shrinkage for all sampling dates occurred within the first year of drying. The figure also confirms that the concrete mixtures with higher strengths exhibit lower shrinkage strains, as shown in Table 6-7.

6.5.2 Shrinkage Prisms

Like the shrinkage cylinders, the highest shrinkage strains for the shrinkage prisms were recorded for the 04/10/2018 sampling date, and the lowest shrinkage strains were recorded for the 04/16/2019 sampling date, as presented in Table 6-7. In general, the moist-cured prisms exhibited higher shrinkage strains than the air-cured prisms. The development of shrinkage with time for all air-cured and moist-cured prism specimens is shown in Figure 6-10 and Figure 6-11, respectively.

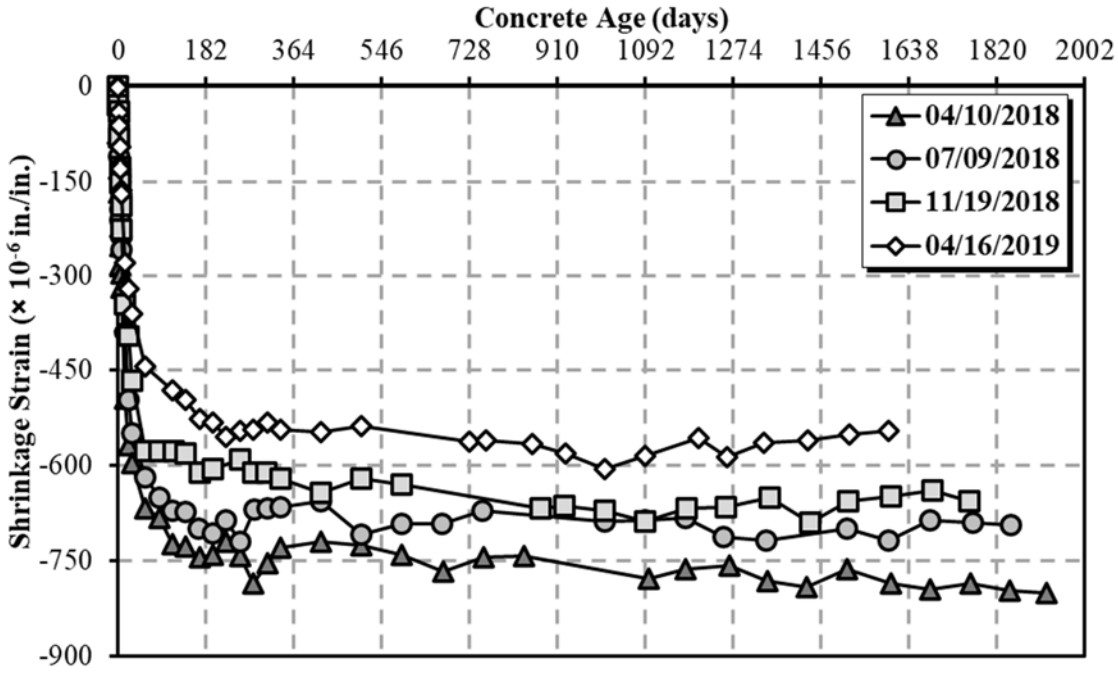

Figure 6-10: Development of shrinkage with time for air-cured prisms

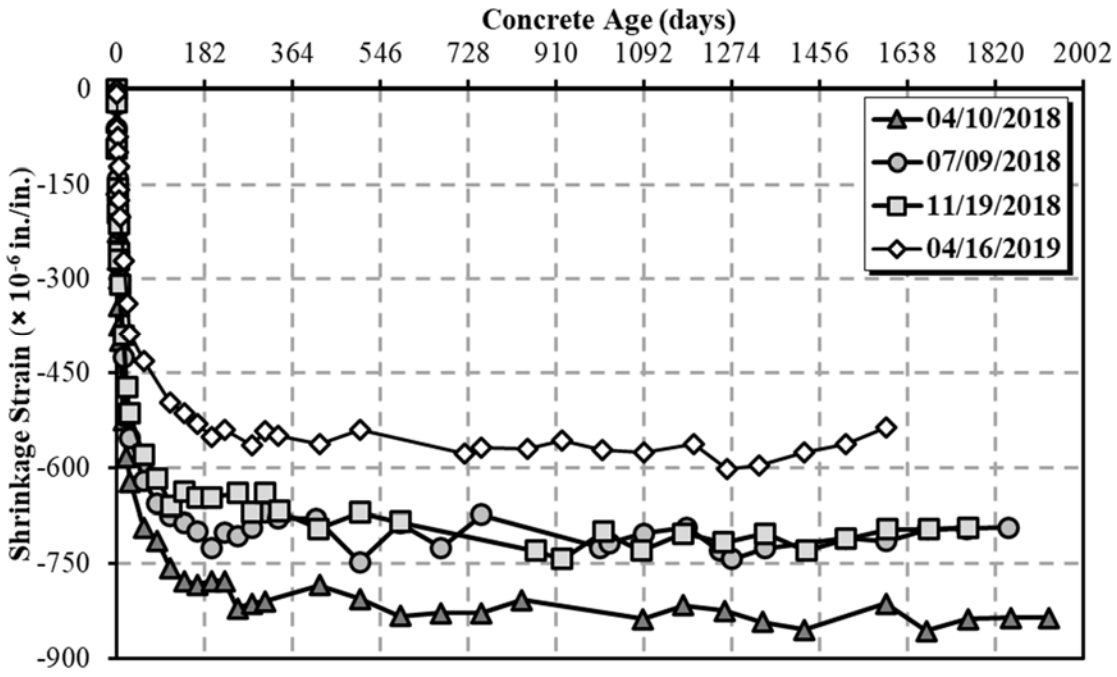

Figure 6-11: Development of shrinkage with time for moist-cured prisms

The higher shrinkage strains for the most-cured prisms compared to the air-cured prisms were likely due to the increase in absorbed water from the additional time in the lime-saturated water bath. The difference in shrinkage strains between the prisms and cylinders was due to the lower volume-to-surface area ratio for the prisms, allowing more moisture to escape because of the shorter path to the surface of the concrete.

6.6 CREEP AND COMPLIANCE RESULTS

This section provides the results from all creep testing performed for the purposes of this research. These results include both the creep strains and the compliance values corresponding to each measurement, both of which were discussed in Chapter 2. The youngest concrete tested was under load for slightly less than 4 years, while the oldest concrete was under load for more than 5 years.

6.6.1 Creep Strain Results

To accurately account for the effects of long-term loading on concrete, it is important to isolate the creep strain from elastic strain and long-term drying shrinkage strains. Creep strains are calculated by subtracting the elastic strain and the shrinkage strain of the companion cylinders from the total measured strain of the concrete. Like shrinkage, the maximum and minimum creep strain values are from the 04/10/2018 sampling date and the 04/16/2019

sampling date, respectively, which correspond to the lowest and highest average compressive strengths. In general, as the loading age increases from 7 to 182 days, the creep strain values decrease for each sampling date; however, there are exceptions at later ages. Because the sampling dates represent different ALDOT approved mixture proportions, other factors affect the differences in creep strains, such as differences in cement type or water/cement ratio. The development of creep strains with time for each sampling date is shown in chronological order in Figures 6-12 through 6-15. Due to the effects of the COVID-19 pandemic on Auburn University, there are some limited periods where data were not collected during the spring and summer of 2020.

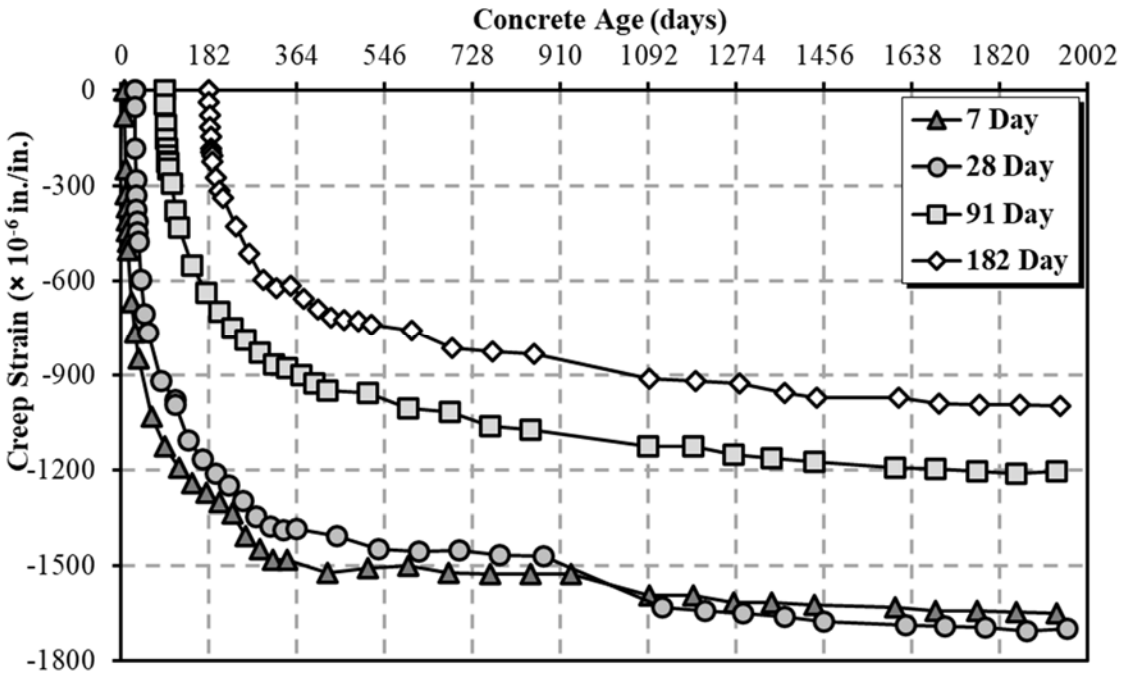

Figure 6-12: Development of creep strain with time for the 04/10/2018 sampling date

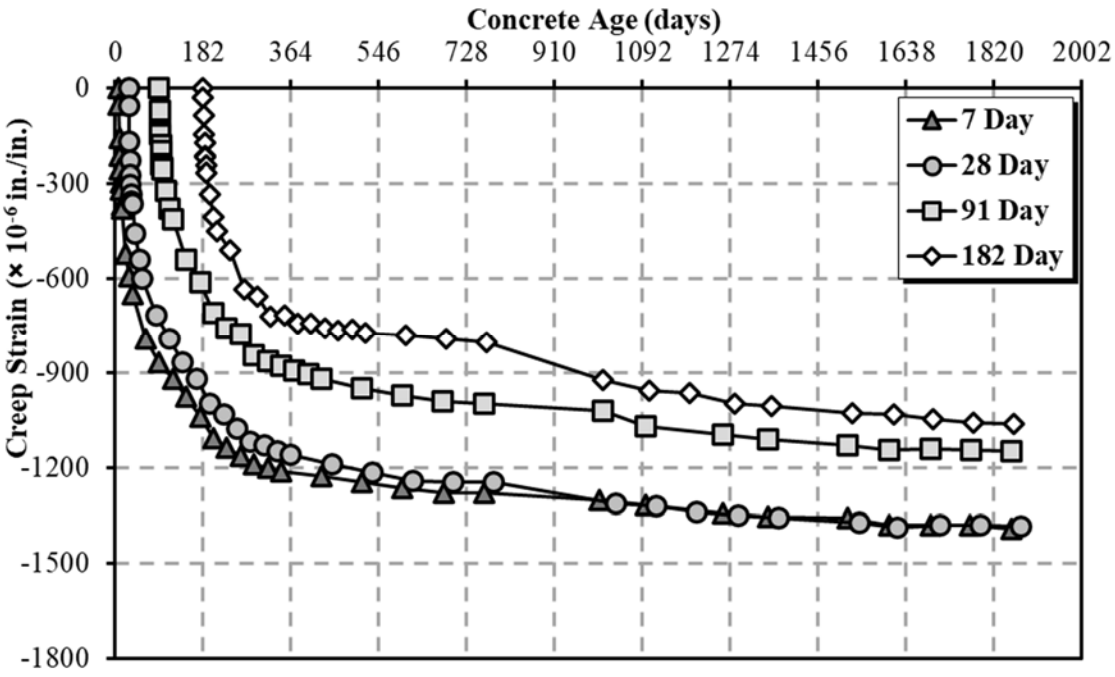

Figure 6-13: Development of creep strain with time for the 07/09/2018 sampling date

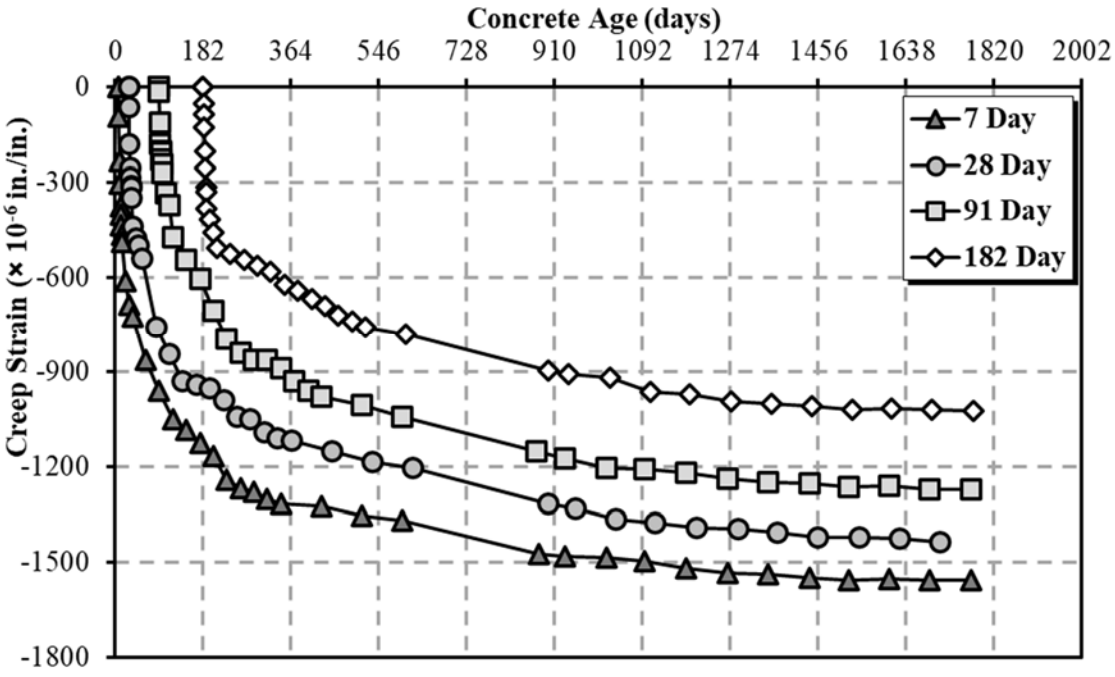

Figure 6-14: Development of creep strain with time for the 11/19/2018 sampling date

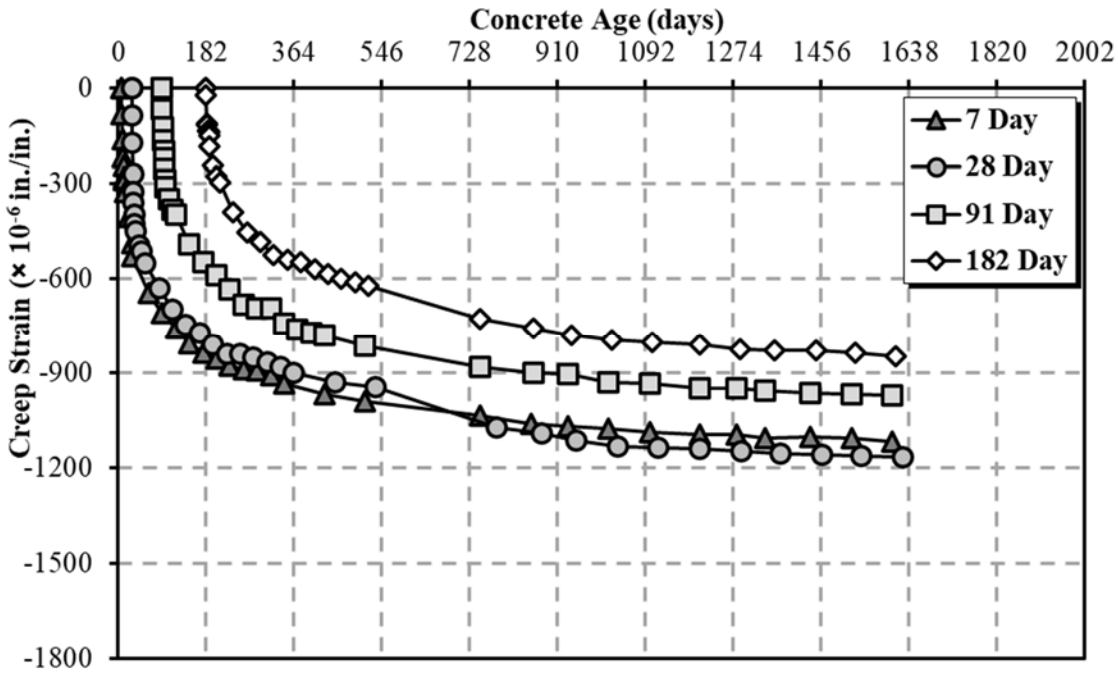

Figure 6-15: Development of creep strain with time for the 04/16/2019 sampling date

6.6.2 Compliance Results

To provide the most accurate comparison of creep values for the purposes of this research, the compliance was calculated for each creep measurement. This value normalizes the creep strain based on the applied stress, while only comparing the creep strains does not account for differences in loading for different specimens (ACI Committee 209 2008). Equation 2.1 was used to calculate all compliance values, and the average 4-year compliance values that correspond to the shrinkage strains in Table 6-7 are presented in Table 6-8.

Table 6-8: Average 4-year compliance results for all specimens

4-Year Compliance Results (×10^{-6}/psi)				
Sampling Date	**04/10/2018**	**07/09/2018**	**11/19/2018**	**04/16/2019**
7 Days	1.096	0.881	0.863	0.596
28 Days	1.026	0.775	0.738	0.555
91 Days	0.777	0.668	0.653	0.505
182 Days	0.683	0.643	0.567	0.471

For all results presented in the table above, the compliance decreased consistently as the loading age increased and the sampling dates continued with the 04/10/2018 sampling date exhibiting the greatest compliance, and the 04/16/2019 sampling date exhibiting the least. This relationship is

based in part on the concrete strength, which generally increased with loading age for each sampling date and throughout the four ALDOT approved mixture proportions for each sampling date. The development of compliance with time for each sampling date is shown in chronological order in Figures 6-16 through 6-19.

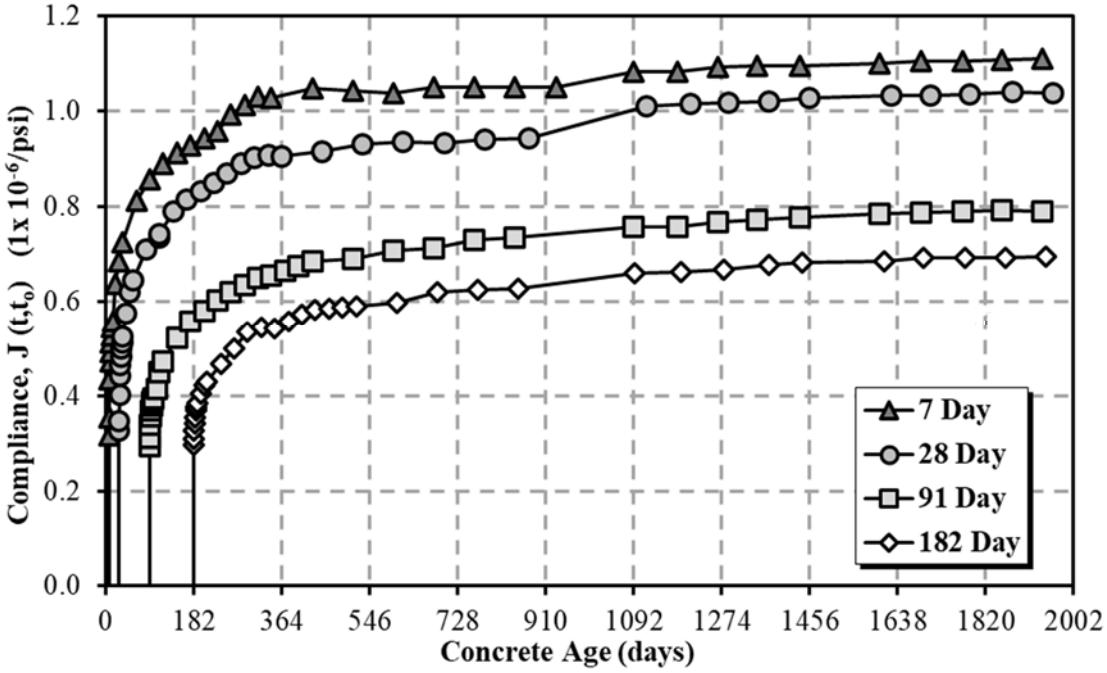

Figure 6-16: Development of compliance with time for the 04/10/2018 sampling date

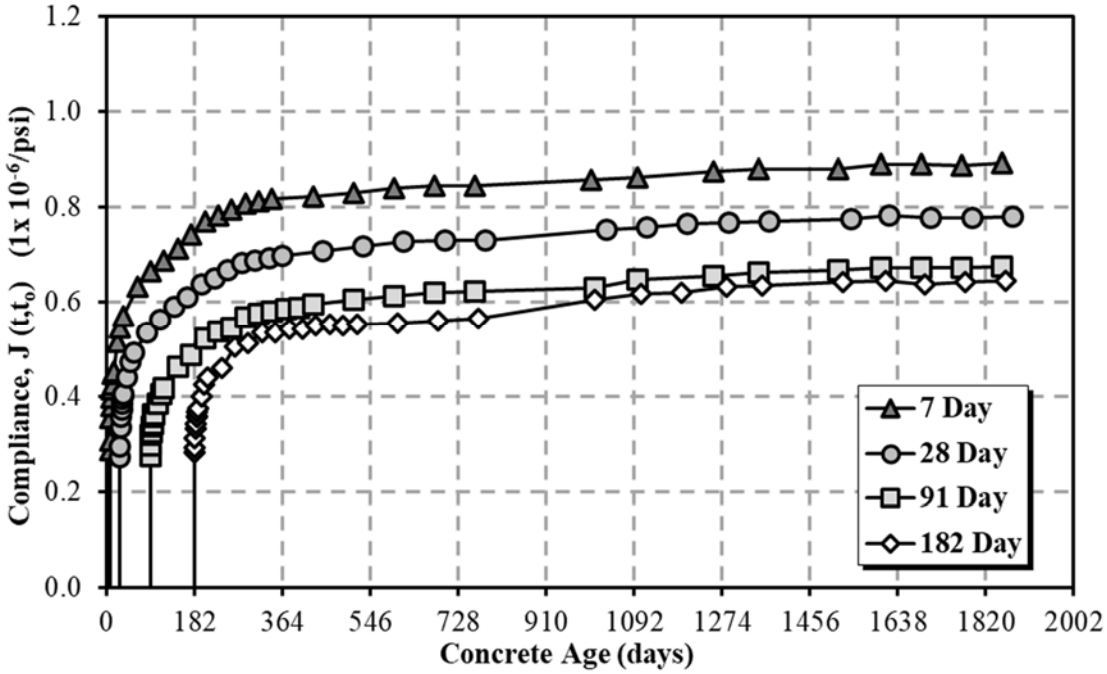

Figure 6-17: Development of compliance with time for the 07/09/2018 sampling date

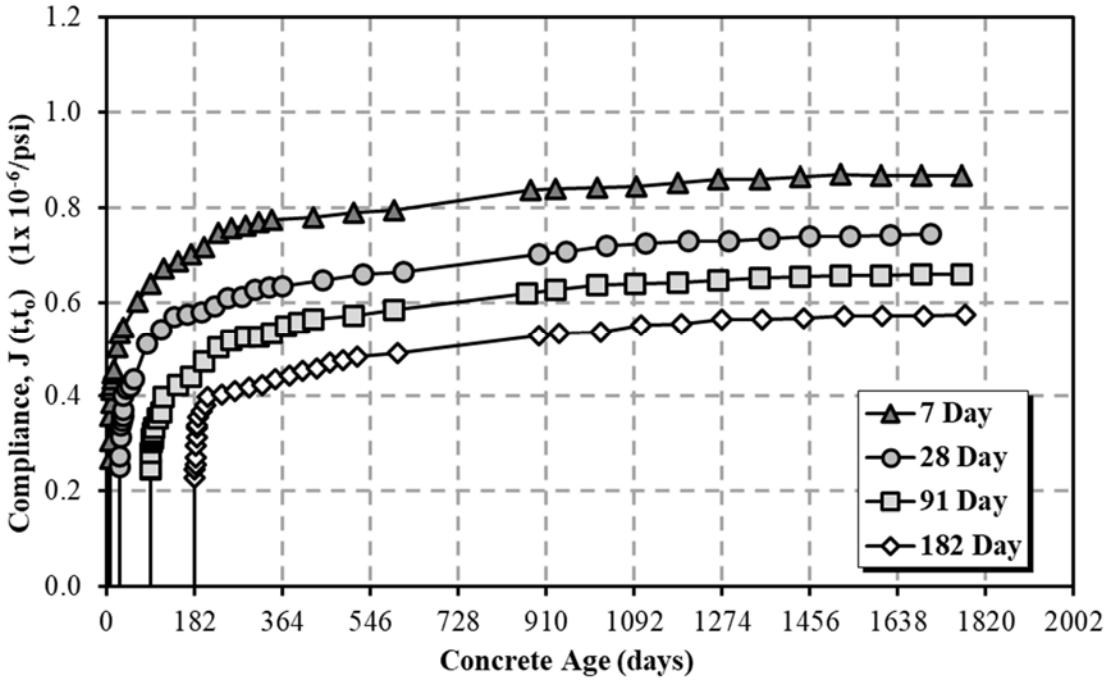

Figure 6-18: Development of compliance with time for the 11/19/2018 sampling date

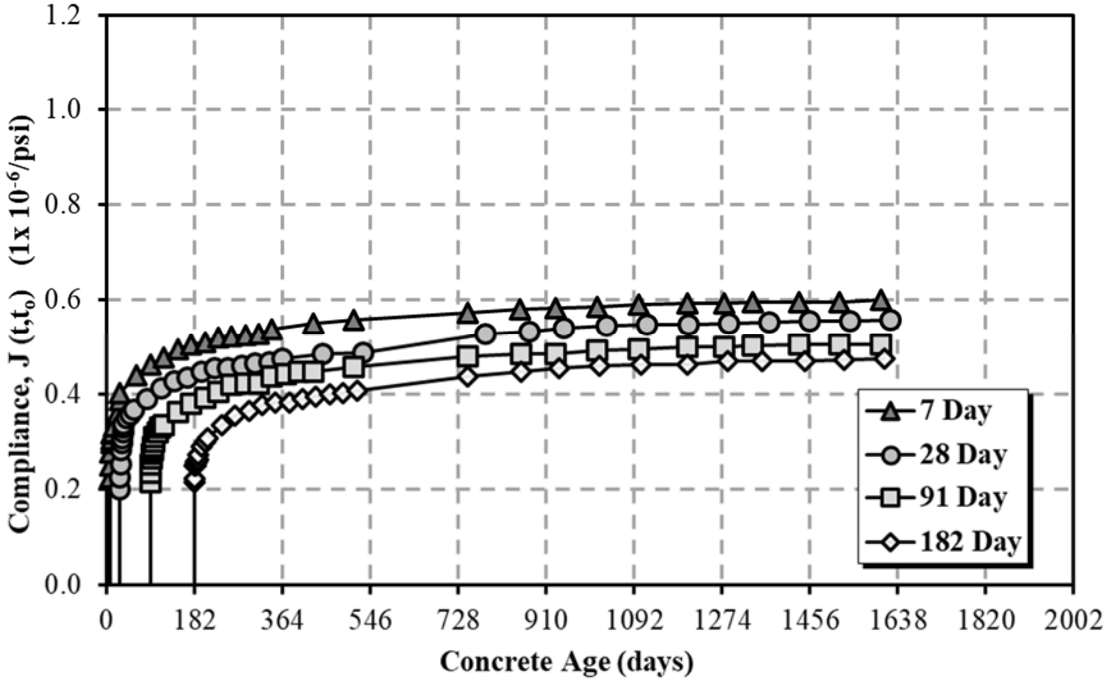

Figure 6-19: Development of compliance with time for the 04/16/2019 sampling date

6.7 SUMMARY OF RESULTS

6.7.1 Fresh Concrete Properties

After analysis of the results from the testing of fresh concrete properties for the purposes of this research, the following conclusions are made:

- The slumps of all fresh concrete mixtures fell between the required 3 to 9 inches in accordance with ALDOT specifications.
- The total air contents of all fresh concrete mixtures fell between the ALDOT requirement of 3 to 6 percent.
- The unit weights of all concrete mixtures were very similar and did not vary significantly from the theoretical unit weights of the ALDOT approved mixture proportions.
- All fresh concrete temperatures fell between the ALDOT requirement of 50°F to 95°F.

6.7.2 Hardened Concrete Properties

After analysis of the results from the testing of hardened concrete properties, excluding creep and shrinkage, the following conclusions are made:

- The 04/10/2018 sampling date produced the lowest compressive strengths, and the 04/16/2019 sampling date produced the highest compressive strengths across the samples from all creep testing loading ages.
- Like compressive strength, the 04/10/2018 sampling date produced the lowest modulus of elasticity, and the 04/16/2019 sampling date produced the highest modulus of elasticity.
- All methods used to calculate the equivalent age at loading indicate that the elevated curing regime discussed in Section 4.5.2.1 is successful at developing maturity in concrete.

6.7.3 Creep and Shrinkage Results

After analysis of the results of creep and shrinkage testing for all sampling dates, the following conclusions are made:

- In general, the 04/10/2018 and the 04/16/2019 sampling dates experienced the highest and lowest shrinkage strains, respectively, for all specimen types.
- The change in shrinkage strains across sampling dates can partially be attributed to the change in compressive strength.
- The majority of shrinkage in the cylinder specimens developed within the first year of drying, while for the prisms, the majority of shrinkage developed within the first three months. This is likely due to the differences in size and volume-to-surface-area ratio for the two types of specimens.

- The moist-cured prisms developed very similar shrinkage strains to the air-cured prisms; however, in general, the moist-cured prisms exhibited slightly higher magnitudes.
- Like the shrinkage specimens, the 04/10/2018 and the 04/16/2019 sampling dates experienced the greatest and least creep strains, respectively.
- The compliance of each creep measurement was calculated to normalize the applied stress and reduce inconsistencies in testing.
- The 04/10/2018 and the 04/16/2019 sampling dates again experienced the greatest and least compliance values, respectively.
- The main contributing factor for the differences in creep and shrinkage values between sampling dates is believed to be the systematic improvement of concrete composition and mixture proportions throughout the duration of the project.

Chapter 7

PREDICTION OF CREEP AND SHRINKAGE OF THE CONCRETE IN THE I-59/I-20 SEGMENTAL BRIDGE

7.1 INTRODUCTION

One of the main objectives of this research is to use existing prediction models to predict creep and shrinkage of the concrete test specimens and compare those predictions with the measured test values. This chapter presents the comparisons between the measured and predicted creep and shrinkage values for all test cylinders. As covered in Chapter 3, the eight prediction models studied for the purposes of this research are:

- AASHTO LRFD (2017),
- ACI 209 (2008),
- B3 (Bažant and Baweja 2000),
- B4 (Bažant 2015),
- CEB MC 1990 (CEB 1990),
- CEB MC 90-99 (CEB 1999),
- CEB MC 2010 (fib 2012), and
- GL 2000 (Gardner and Lockman 2001).

To provide the most accurate assessment of each prediction model, all comparisons between predicted and measured values for creep are based on compliance to normalize the creep strains based on applied load. Because the compliance accounts for both elastic and inelastic deformations, the modulus of elasticity is required by each model to predict compliance. For this reason, each model's elastic modulus predictions, as outlined in Chapter 3, are compared, in addition to the compliance and shrinkage values.

To graphically visualize the accuracy of each prediction model to the measured values, the measured values are plotted against the predicted values, with the line of equality at a 1:1 slope. Predictions above the line of equality are overpredictions, and those below the line of equality are underpredictions. Error bands are also displayed on each graph at ±20 percent for reference. Gardner and Lockman (2001) state, "A simple model that could predict shrinkage within 15% would be excellent, and a prediction within 20% would be adequate." They also state that for compliance, an even higher error would be acceptable because of the additional calculations involved (Gardner and Lockman 2001). A more detailed summary of compliance and shrinkage prediction with the models listed above, as well as the prediction of the shrinkage prisms, can be found in Appendix B.

It should also be noted that as discussed in Chapter 3, because of the B4 model's optional factors related to supplementary cementitious materials and chemical admixtures, it is

separated into two separate models. For compliance and shrinkage according to the B4 model, the predictions including the multipliers represent the B4 model, and those that do not include the multipliers represent the B4* model.

7.2 MODULUS OF ELASTICITY PREDICTIONS

The modulus of elasticity at each loading age is predicted for every model based on its respective method, which is defined in Chapter 3. A summary of inputs required for each model's prediction of the modulus of elasticity is presented in Table 7-1, and the predicted modulus of elasticity at each loading age for all sampling dates is presented in Table 7-2. Because the three CEB MC models predict the same values for modulus of elasticity, they are represented by only one entry in each table.

Table 7-1: Summary of inputs for each elastic modulus prediction model

Model	Input		Formulation
AASHTO LRFD	Compressive Strength	Table 5-2	Equation 3.1
	Unit Weight	Table 5-1	
ACI 209	Compressive Strength	Table 5-2	Equation 3.9
	Unit Weight	Table 5-1	
B3	Compressive Strength	Table 5-2	Equation 3.34
	28-Day Elastic Modulus	Table 5-3	
B4	Compressive Strength	Table 5-2	Equation 3.68
	28-day Elastic Modulus	Table 5-3	
CEB MC	Compressive Strength	Table 5-2	Equation 3.153
	Cement Type	Table 4-2	
	Aggregate Type	Quartzite	
GL 2000	Compressive Strength	Table 5-2	Equation 3.181

Table 7-2: Modulus of elasticity predictions for each model

Predicted Modulus of Elasticity (ksi)							
Sampling Date	**Age (Days)**	**AASHTO LRFD**	**ACI 209**	**B3**	**B4**	**CEB MC**	**GL 2000**
04/10/2018	**7**	4,260	4,070	3,990	3,920	4,590	4,210
	28	4,520	4,450	4,530	4,510	5,090	4,560
	91	4,490	4,420	4,730	4,710	5,350	4,530
	182	4,590	4,560	4,780	4,760	5,450	4,660
07/09/2018	**7**	4,210	4,130	4,160	4,100	4,720	4,390
	28	4,470	4,520	4,750	4,720	5,250	4,760
	91	4,560	4,660	4,960	4,930	5,520	4,880
	182	4,560	4,660	5,010	4,990	5,620	4,880
11/19/2018	**7**	4,720	4,660	4,240	4,190	4,900	4,660
	28	4,910	4,940	4,920	4,890	5,360	4,910
	91	4,970	5,040	5,140	5,110	5,580	5,000
	182	4,950	5,010	5,190	5,170	5,670	4,970
04/16/2019	**7**	4,860	4,920	4,530	4,460	5,000	4,940
	28	5,010	5,150	5,190	5,160	5,560	5,150
	91	5,070	5,250	5,410	5,390	5,850	5,240
	182	5,030	5,190	5,470	5,450	5,960	5,180

The graphs illustrating the comparison between the measured elastic modulus values and the predicted values for each model are shown in Figures 7-1 through 7-6. It can be seen in the graphs that the vast majority of the predictions fall in the ± 20 percent error bands, with the exception of four of the individual CEB MC predictions.

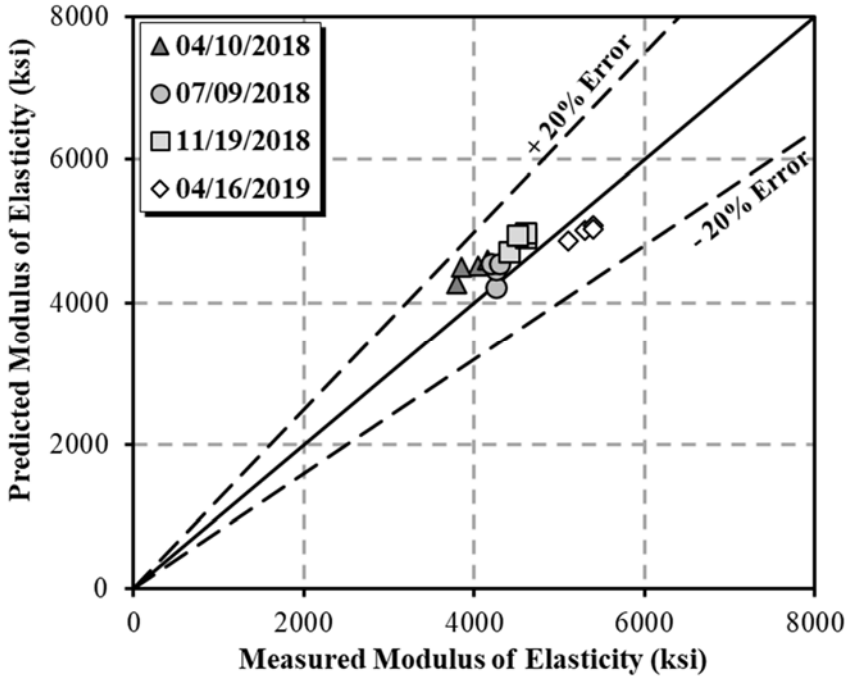

Figure 7-1: Measured versus predicted modulus of elasticity using the AASHTO LRFD Model

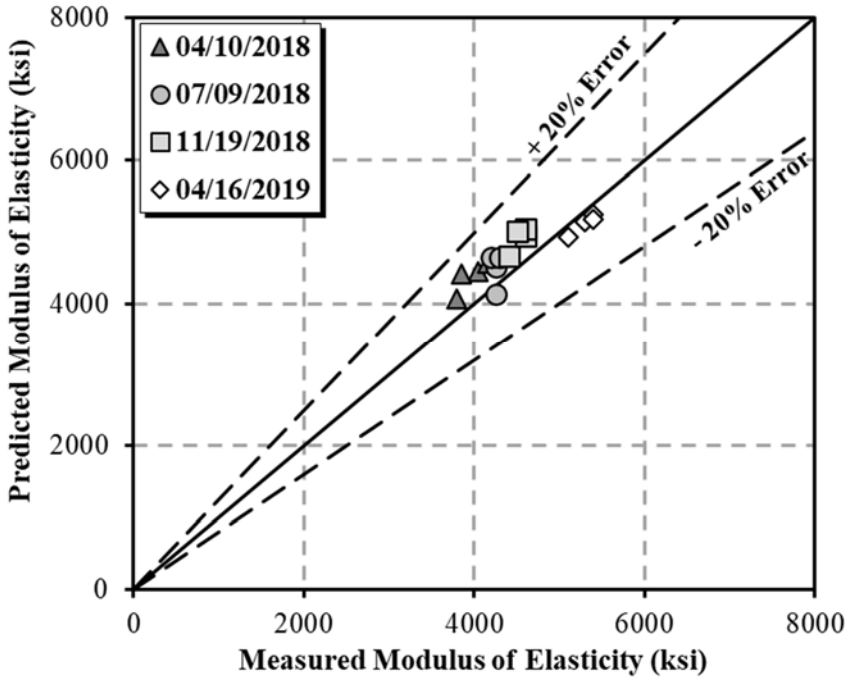

Figure 7-2: Measured versus predicted modulus of elasticity using the ACI 209 Model

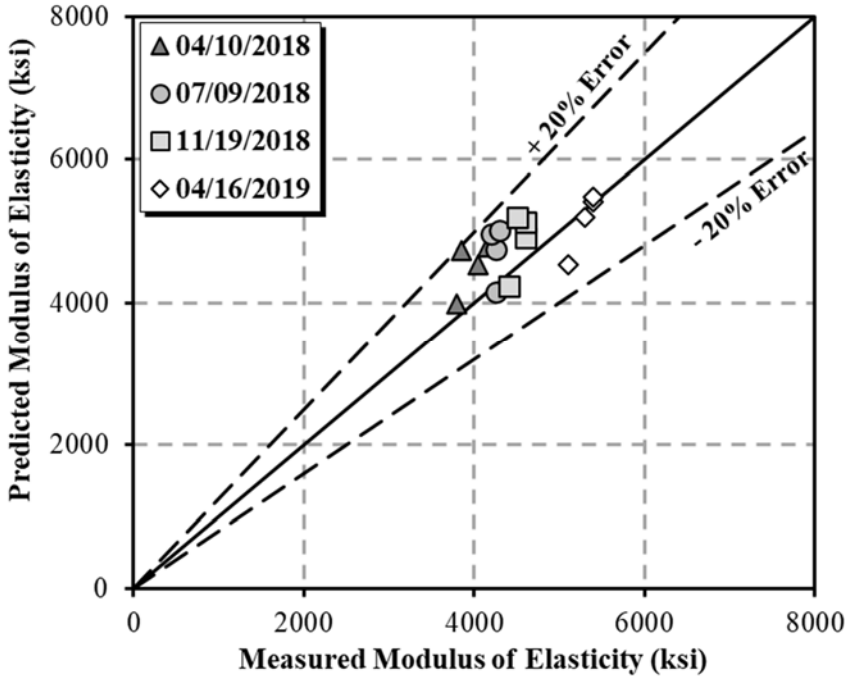

Figure 7-3: Measured versus predicted modulus of elasticity using the B3 Model

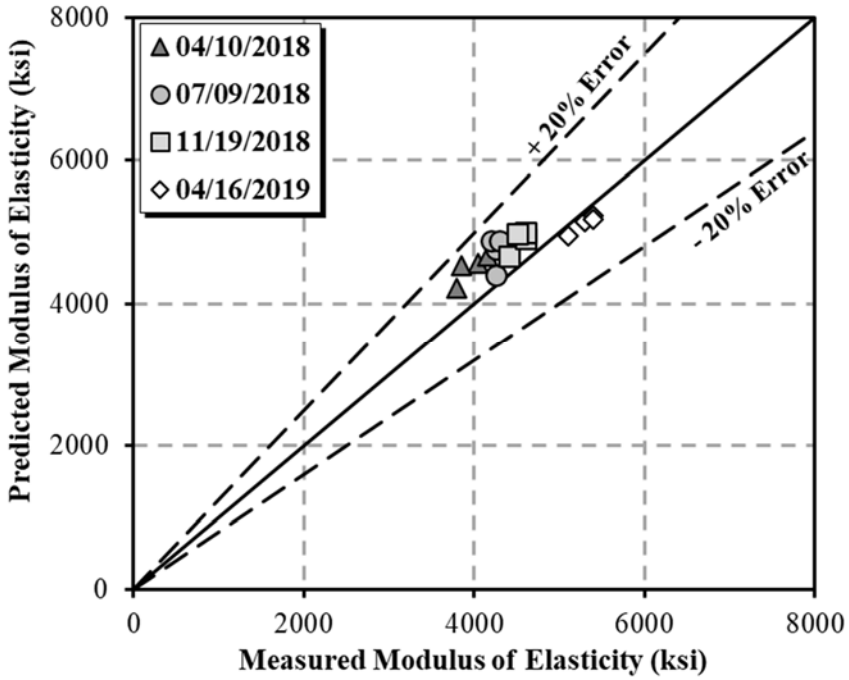

Figure 7-4: Measured versus predicted modulus of elasticity using the B4 Model

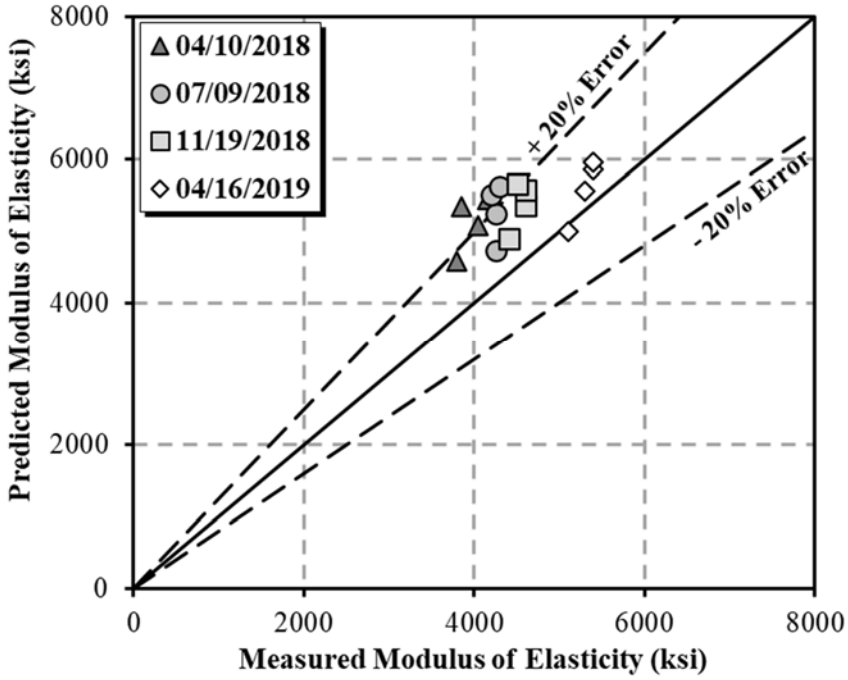

Figure 7-5: Measured versus predicted modulus of elasticity using the CEB MC Models

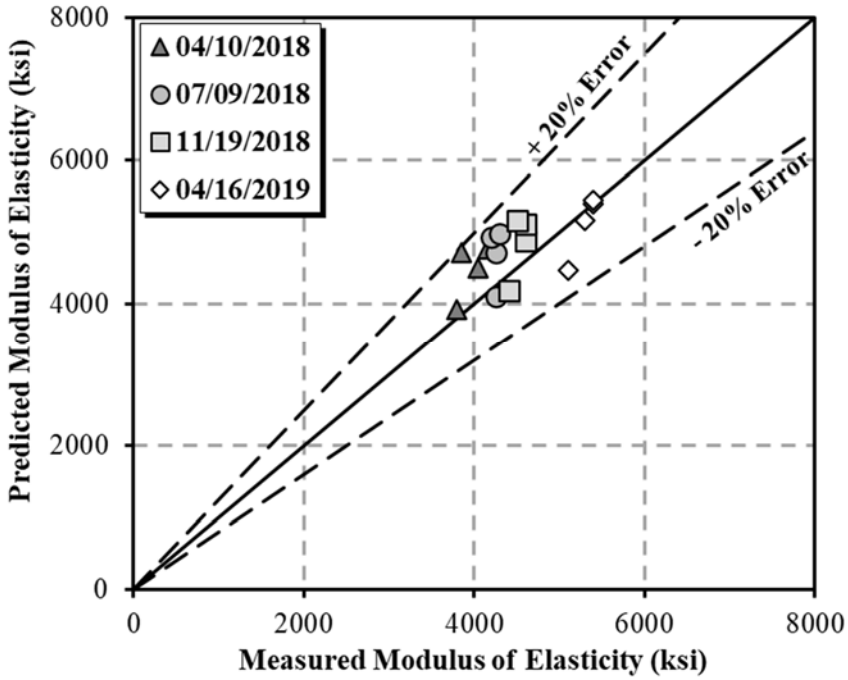

Figure 7-6: Measured versus predicted modulus of elasticity using the GL 2000 Model

7.3 AASHTO LRFD COMPLIANCE AND SHRINKAGE PREDICTIONS

The formulations for all AASHTO LRFD creep and shrinkage predictions presented in this section are defined in Section 3.2.1. The key input parameters for the concrete sampled during this project for the AASHTO LRFD creep and shrinkage prediction model are presented in Table 7-3, with justifications listed where they are necessary.

Table 7-3: Summary of AASHTO LRFD creep and shrinkage prediction inputs

Creep and Shrinkage Model Input Parameters		
Input		**Justification (if necessary)**
Volume-to-surface area ratio of cylinders	1.5 in.	Excluding cylinder ends not exposed to drying
Volume-to-surface area ratio of prisms	0.66 in.	Including all prism sides
Relative humidity	46.9%	Average measured value
Compressive strength at age of loading	Table 5-2	Determined through concrete testing
Chronological age at loading	7, 28, 91, 182 days	Used during testing
Predicted elastic modulus at age of loading	Table 6-2	AASHTO LRFD prediction
Exposure to drying before 5 days of curing	+20% shrinkage	Based on AASHTO LRFD provisions

The comparison between the measured and AASHTO LRFD predicted compliance values for all sampling dates is shown in Figure 7-7. In general, the AASHTO LRFD prediction model significantly underpredicts compliance when compared to testing results, with the majority of prediction values falling outside of the -20% error band. The predictions of the 04/10/2018 sampling date and the 04/16/2019 sampling date are the least and most accurate, respectively.

The comparison between the measured and AASHTO LRFD predicted shrinkage values for the shrinkage cylinders is shown in Figure 7-8. The AASHTO LRFD predicts shrinkage strain very accurately, with the vast majority of predicted values falling within the ±20 percent error bands.

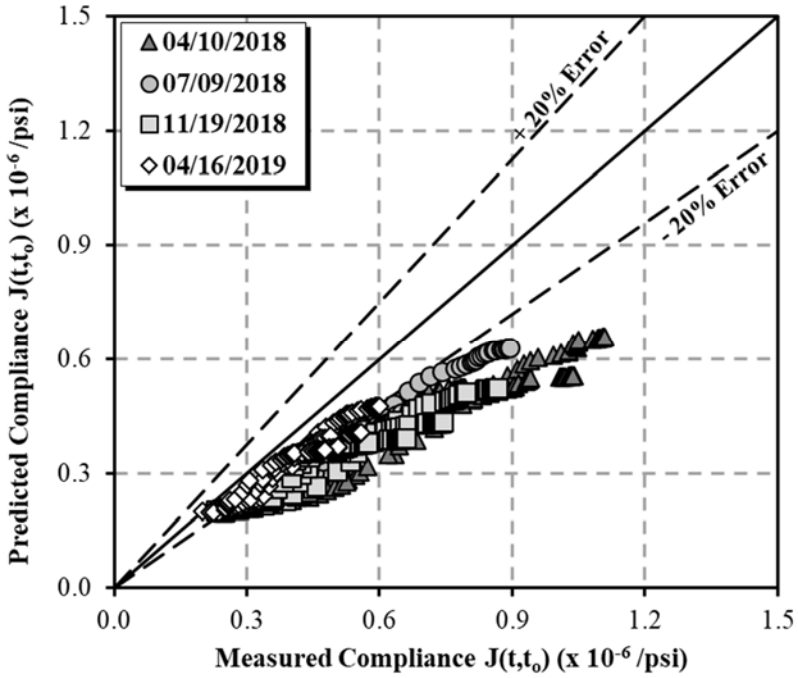

Figure 7-7: Measured versus predicted compliance using the AASHTO LRFD Model

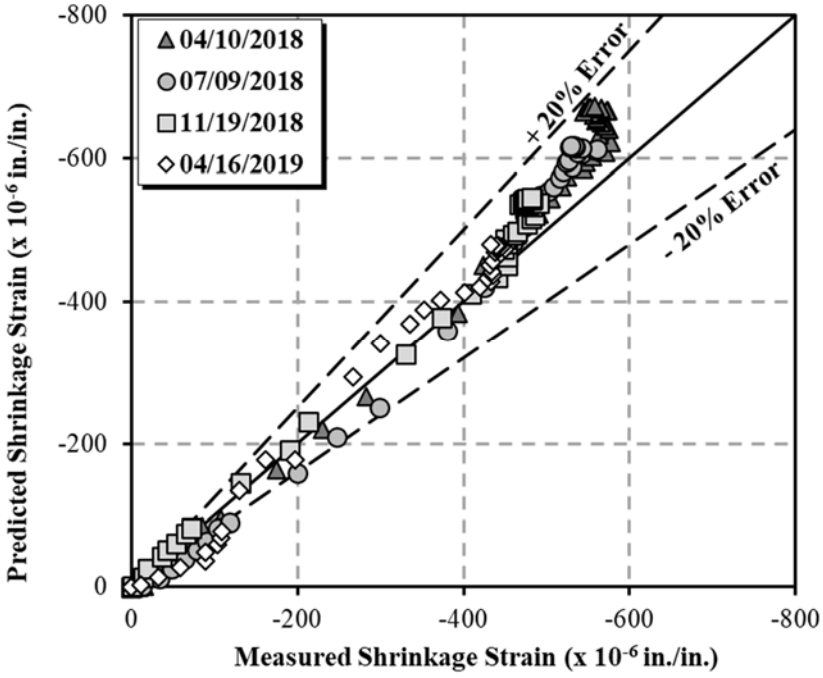

Figure 7-8: Measured versus predicted shrinkage for cylinders using the AASHTO LRFD Model

7.4 ACI 209 COMPLIANCE AND SHRINKAGE PREDICTIONS

The ACI 209 creep and shrinkage prediction models are defined in Section 3.2.2. The key input parameters for this model for the concrete sampled during this project are presented in Table 7-4. Due to uncertainties in the interpretation of the ACI 209 model, several assumptions had to be made. The first assumption was that the cement content mentioned in the model was taken as the sum of all cementitious materials for each mixture proportion, several of which contained Class F fly ash. The second assumption was that the slump was taken as the value before chemical admixtures were added.

Table 7-4: Summary of ACI 209 creep and shrinkage prediction inputs

Creep and Shrinkage Model Input Parameters		
Input		**Justification (if necessary)**
Volume-to-surface area ratio of cylinders	1.5 in.	Excluding cylinder ends not exposed to drying
Volume-to-surface area ratio of prisms	0.66 in.	Including all prism sides
Relative humidity	46.9%	Average measured value
28-Day compressive strength	Table 5-2	Determined through concrete testing
Chronological age at loading	7, 28, 91, 182 days	Used during testing
Predicted elastic modulus at age of loading	Table 6-2	ACI 209 prediction
Curing Type	Chapter 4	---
Slump	0 in.	Assumed pre-admixture slump
Cement content	Table 4-2	Assumed total cementitious material content
Air content	Table 5-1	Determined through concrete testing
Fine aggregate content	Table 4-2	From mixture proportions

The comparison between the measured and ACI 209 predicted compliance values is shown in Figure 7-9. Like AASHTO LRFD, this model significantly underpredicts compliance, with the vast majority of values falling outside the -20 percent error band. The predictions appear to improve with the sampling dates as they become more accurate from the 04/10/2018 sampling date to the 04/16/2019 sampling date.

The comparison between the measured and predicted shrinkage strains for the ACI 209 model is shown in Figure 7-10. This model generally predicts shrinkage within the ±20 percent error band for the higher strength concretes; however, some values from the 04/10/2018 and 07/09/2018 sampling dates fall outside the -20 percent band.

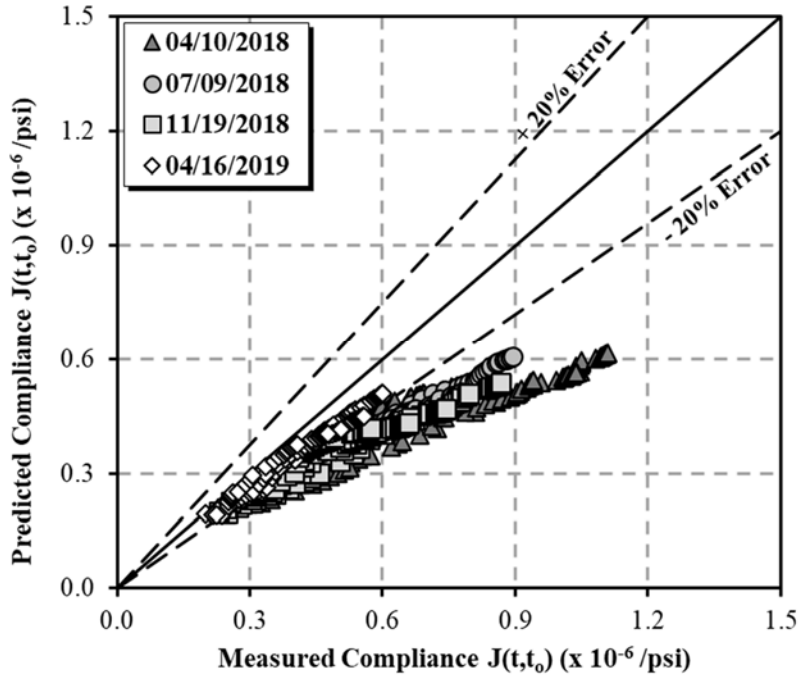

Figure 7-9: Measured versus predicted compliance using the ACI 209 Model

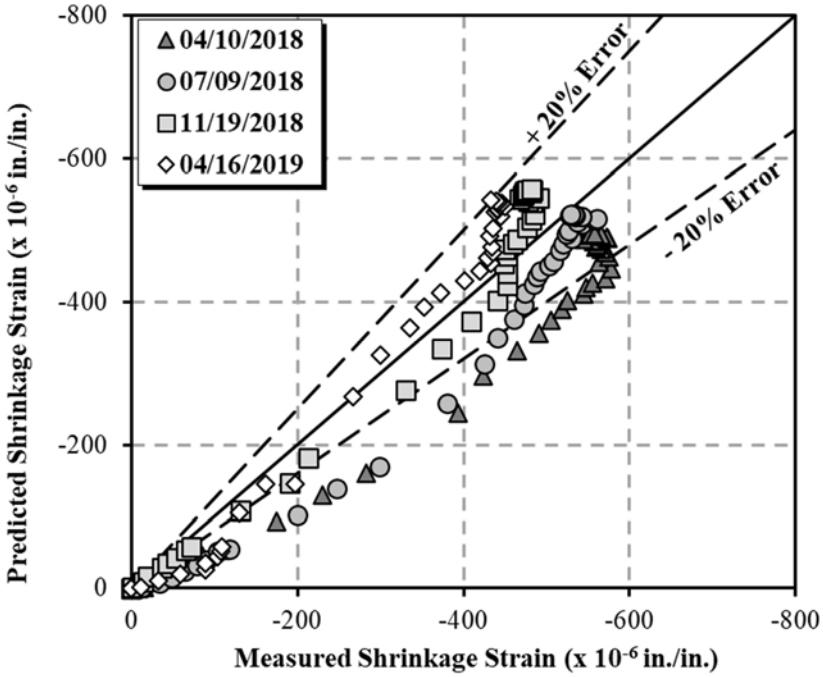

Figure 7-10: Measured versus predicted shrinkage for cylinders using the ACI 209 Model

7.5 B3 COMPLIANCE AND SHRINKAGE PREDICTIONS

The B3 creep and shrinkage prediction models are defined in Section 3.2.3. Like the ACI 209 model, the B3 input parameter for cement content is assumed to be the total cementitious material content for each mixture proportion. A summary of key input parameters for the B3 creep and shrinkage prediction model for the concrete sampled during this project is presented in Table 7-5.

Table 7-5: Summary of B3 creep and shrinkage prediction inputs

Creep and Shrinkage Model Input Parameters		
Input		**Justification (if necessary)**
Volume-to-surface area ratio of cylinders	1.5 in.	Excluding cylinder ends not exposed to drying
Volume-to-surface area ratio of prisms	0.66 in.	Including all prism sides
Relative humidity	46.9%	Average measured value
28-Day compressive strength	Table 5-2	Determined through concrete testing
Equivalent age at loading	Table 5-5	Based on B3 maturity method
Equivalent age when drying began	Table 5-6	Based on B3 maturity method
Predicted elastic modulus at age of loading	Table 6-2	B3 prediction
Curing type	Chapter 4	---
Cement type	Table 4-2	From mixture proportions
Cement content	Table 4-2	Assumed total cementitious material content
Water-cement ratio	Table 4-2	From mixture proportions
Aggregate-cement ratio	Table 4-2	From mixture proportions

The comparison between the measured compliance values and those predicted by the B3 model is shown in Figure 7-11. While the majority of values are within the 20 percent error bands, the B3 model tends to underpredict compliance at early ages for all four sampling dates. Additionally, at later ages, compliance is overpredicted for most sampling dates, but most severely for the 04/16/2019 sampling date.

The comparison between the measured shrinkage strains and B3 predicted shrinkage strains is shown in Figure 7-12. It can be seen in the figure that the B3 model significantly underpredicts shrinkage strain for all four sampling dates as no values appear to fall within the -20 percent error band.

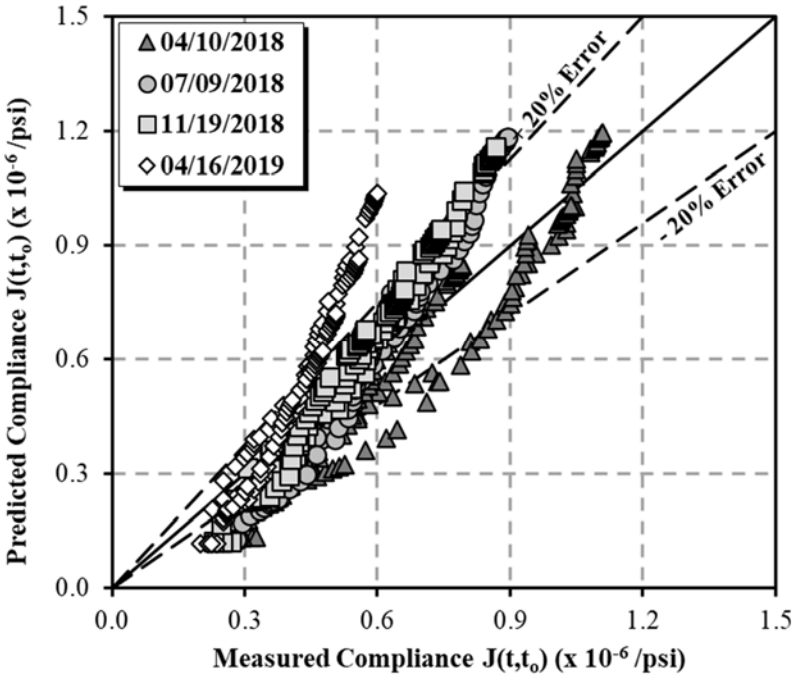

Figure 7-11: Measured versus predicted compliance using the B3 Model

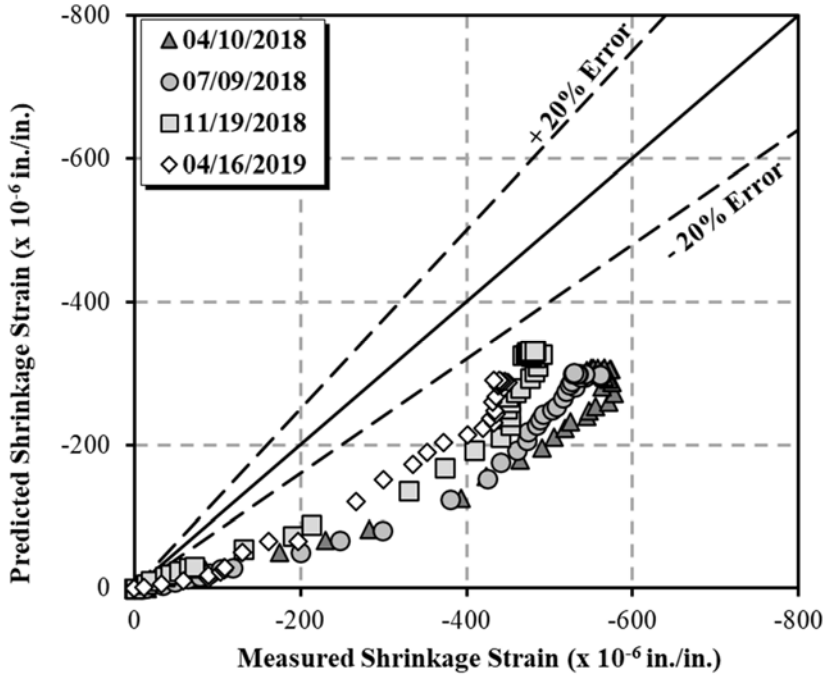

Figure 7-12: Measured versus predicted shrinkage for cylinders using the B3 Model

7.6 B4 COMPLIANCE AND SHRINKAGE PREDICTIONS

The B4 creep and shrinkage prediction models are defined in Section 3.2.4. Its formulation keeps components from the B3 model, but several changes were made, including the addition of parameters and scaling factors based on cement type, supplementary cementitious materials, and chemical admixtures. A summary of the key input parameters used for the B4 model for the concrete sampled during this project is presented in Table 7-6.

Table 7-6: Summary of B4 creep and shrinkage prediction inputs

Creep and Shrinkage Model Input Parameters		
Input		**Justification (if necessary)**
Volume-to-surface area ratio of cylinders	1.5 in.	Excluding cylinder ends not exposed to drying
Volume-to-surface area ratio of prisms	0.66 in.	Including all prism sides
Relative humidity	46.9%	Average measured value
28-Day compressive strength	Table 5-2	Determined through concrete testing
Equivalent age at loading	Table 5-5	Based on B4 maturity method
Equivalent age when drying began	Table 5-6	Based on B4 maturity method
Predicted elastic modulus at age of loading	Table 6-2	B4 prediction
Cement type	Table 4-2	From mixture proportions
Cement content	Table 4-2	Assumed total cementitious material content
Water-cement ratio	Table 4-2	From mixture proportions
Aggregate-cement ratio	Table 4-2	From mixture proportions
SCMs and admixtures	Table 4-2	From mixture proportions

The comparison between the measured compliance values and those predicted by the B4 model is shown in Figure 7-13. While a number of early-age values fall within the 20 percent error bands, the B4 model, on the whole, significantly overpredicts compliance for all sampling dates.

The comparison between measured shrinkage strains and those predicted by the B4 model is shown in Figure 7-14. In this case, the B4 model significantly underpredicts shrinkage

strains for the 04/16/2019 sampling date. It also underpredicts values for the 04/10/2018 and 07/09/2018 sampling dates, while the 11/19/2018 sampling date predictions fall within the 20 percent error band. This significant disparity in predictions for the same model is due to the parameters and scaling factors based on cement type, supplementary cementitious materials, and chemical admixtures, which were presented in Table 7-6.

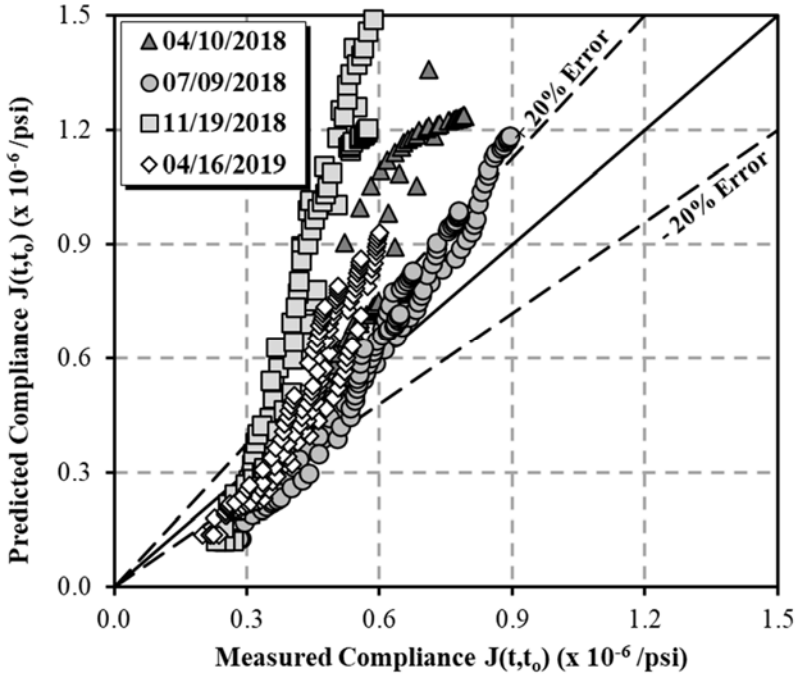

Figure 7-13: Measured versus predicted compliance using the B4 Model

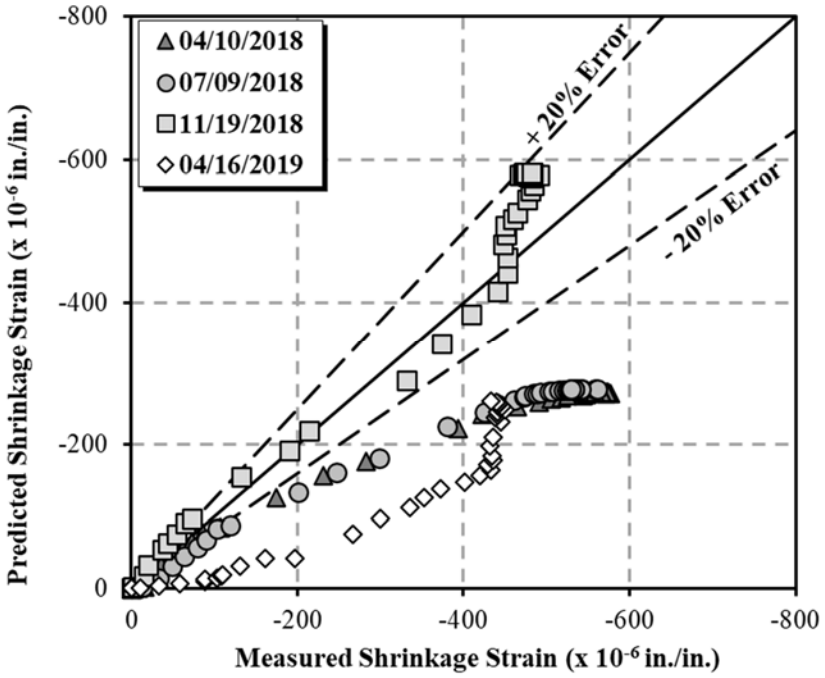

Figure 7-14: Measured versus predicted shrinkage for cylinders using the B4 Model

7.7 B4* COMPLIANCE AND SHRINKAGE PREDICTIONS

As discussed in Section 3.2.4, for this research, the B4* model is the same as the B4 model; however, it does not include the scaling factors based on supplementary cementitious materials and chemical admixtures. The comparison between the measured compliance values and those predicted by the B4* model is shown in Figure 7-15. Like the B4 model, the B4* model significantly overpredicts compliance, especially at later concrete ages. The comparison between the measured shrinkage strains and those predicted by the B4* model is shown in Figure 7-16. This model underpredicts shrinkage strain for the 04/10/2018 and 07/09/2018 sampling dates, as well as for early ages of the 11/19/2018 sampling date. However, this error is much less severe than the B4 model. The remainder of the shrinkage values fall within the 20 percent error bands.

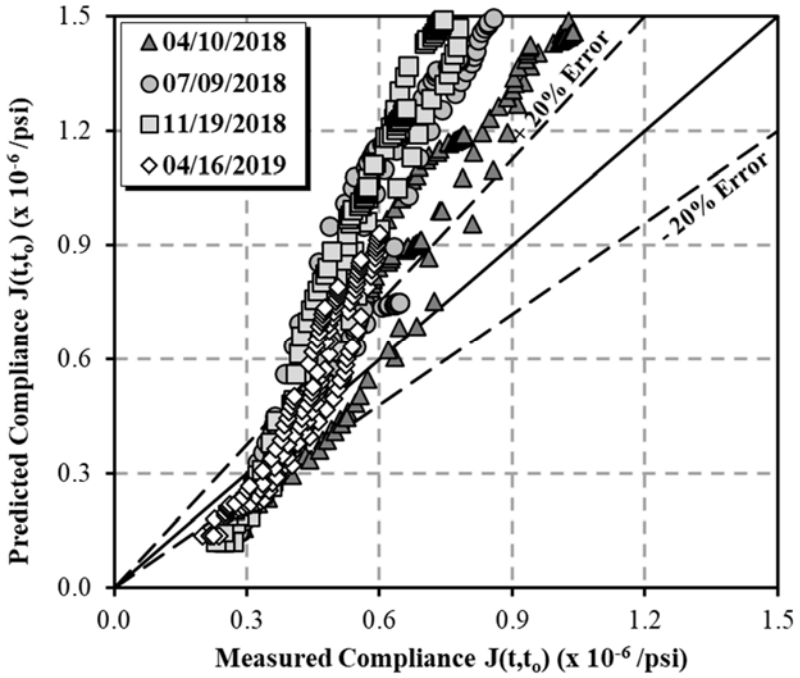

Figure 7-15: Measured versus predicted compliance using the B4* Model

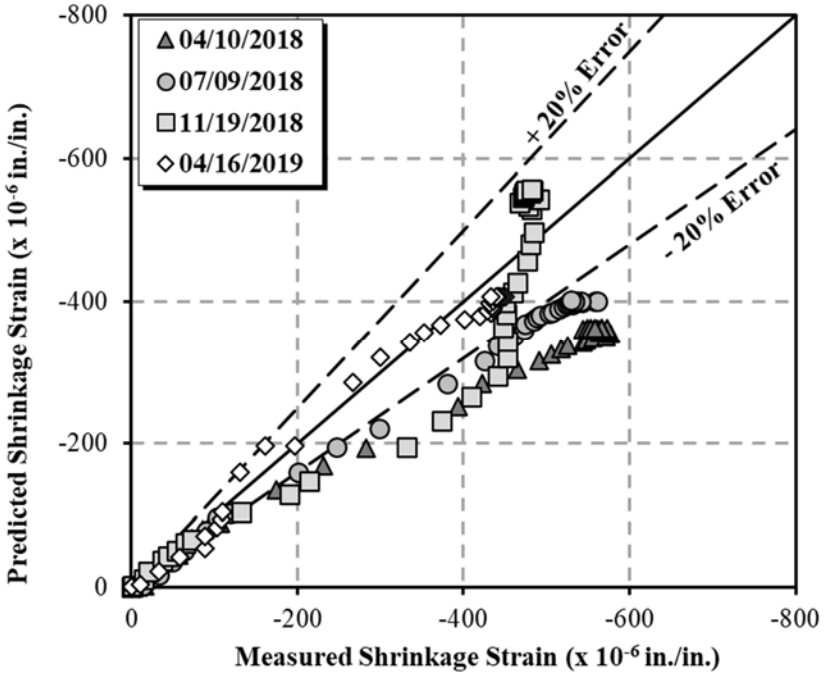

Figure 7-16: Measured versus predicted shrinkage for cylinders using the B4* Model

7.8 CEB MC 1990 Compliance and Shrinkage Predictions

The CEB MC 1990 creep and shrinkage prediction models are defined in Section 3.2.5, and a summary of key input parameters used for this model for the concrete sampled during this project is presented in Table 7-7. Because the three CEB models studied in this research are based on the CEB MC 1990 model, Table 7-7 also applies to the CEB MC 90-99 and CEB MC 2010 models.

Table 7-7: Summary of CEB creep and shrinkage prediction inputs

Creep and Shrinkage Model Input Parameters		
Input		**Justification (if necessary)**
Volume-to-surface area ratio of cylinders	1.5 in.	Excluding cylinder ends not exposed to drying
Volume-to-surface area ratio of prisms	0.66 in.	Including all prism sides
Relative humidity	46.9%	Average measured value
28-Day compressive strength	Table 5-2	Determined through concrete testing
Equivalent age at loading	Table 5-5	Based on CEB maturity method
Equivalent age when drying began	Table 5-6	Based on CEB maturity method
Predicted elastic modulus at age of loading	Table 6-2	CEB prediction
Cement type	Table 4-2	From mixture proportions

The comparison between the measured compliance values and those predicted by the CEB MC 1990 model is shown in Figure 7-17. This model predicts compliance for most of the values very well, with the vast majority falling between the ±20 percent error bands. The only predictions to fall outside the error bands are for the 04/10/2018 sampling date; however, these predictions are not far below the -20 percent error band. The comparison between measured shrinkage strains and those predicted by the CEB MC 1990 model are shown in Figure 7-18. In this case, the model consistently underpredicts shrinkage strain, with most values falling outside the -20 percent error band.

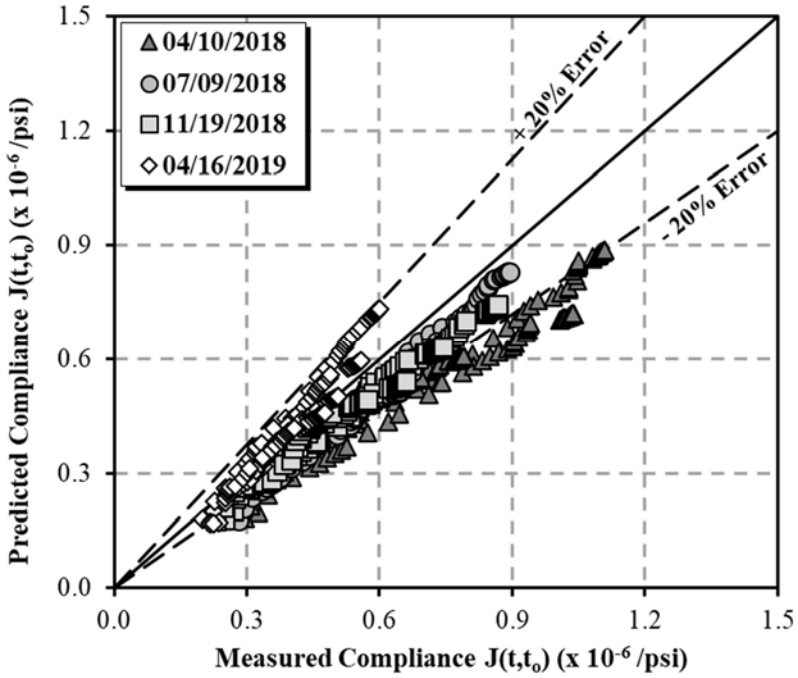

Figure 7-17: Measured versus predicted compliance using the CEB MC 1990 Model

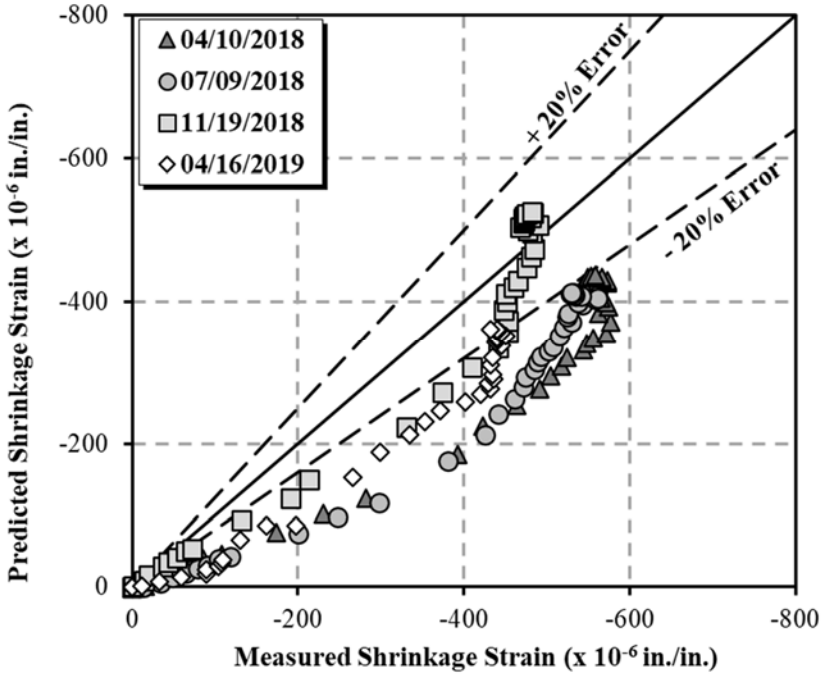

Figure 7-18: Measured versus predicted shrinkage for cylinders using the CEB MC 1990 Model

7.9 CEB MC 90-99 Compliance and Shrinkage Predictions

The CEB MC 90-99 creep and shrinkage prediction model is defined in Section 3.2.6 and is an update to the CEB MC 1990 model. The comparison between the measured compliance values

and those predicted by the CEB MC 90-99 model is shown in Figure 7-19. The majority of predictions fall within the 20 percent error bands, but they tend toward underprediction more than the CEB MC 1990 model. In addition, most of the values from the 04/10/2018 sampling fall outside the -20 percent error band; however, the predicted values have a slope that seems to follow that of the -20 percent error band. The comparison between the measured shrinkage strains and those predicted by the CEB MC 90-99 model is shown in Figure 7-20. While this model tends to underpredict shrinkage at early ages for all sampling dates, all values at later ages fall within the 20 percent error bands. In general, for shrinkage, this model is an improvement over its predecessor, the CEB MC 1990 model.

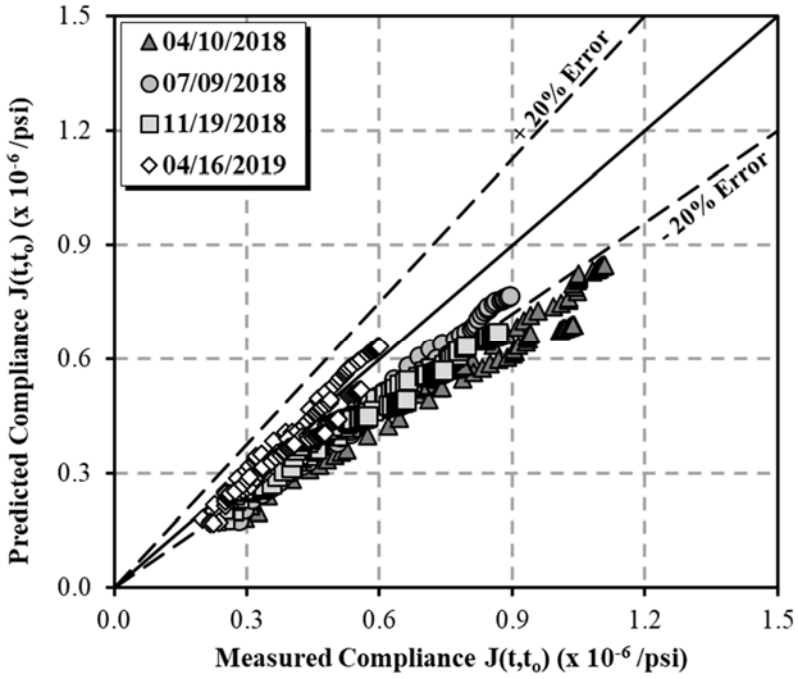

Figure 7-19: Measured versus predicted compliance using the CEB MC 90-99 Model

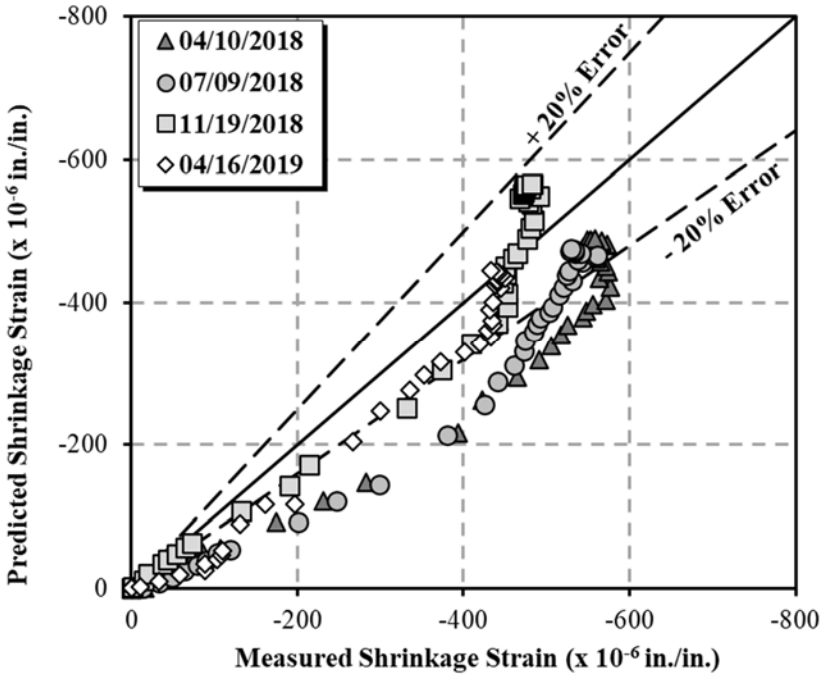

Figure 7-20: Measured versus predicted shrinkage for cylinders using the CEB MC 90-99 Model

7.10 CEB MC 2010 COMPLIANCE AND SHRINKAGE PREDICTIONS

The CEB MC 2010 creep and shrinkage prediction model is defined in Section 3.2.7. The comparison between the measured compliance values and those predicted by this model is shown in Figure 7-21. The CEB MC 2010 model underpredicts compliance more than the two earlier CEB models, with approximately half of its predictions falling outside the -20 percent error band. The comparison between the measured shrinkage strains and those predicted by the CEB MC 2010 model is shown in Figure 7-22. In this case, the model predicts the same values as the CEB MC 90-99, so the trends are the same. It tends to underpredict at early ages, while later ages provide more accurate predictions.

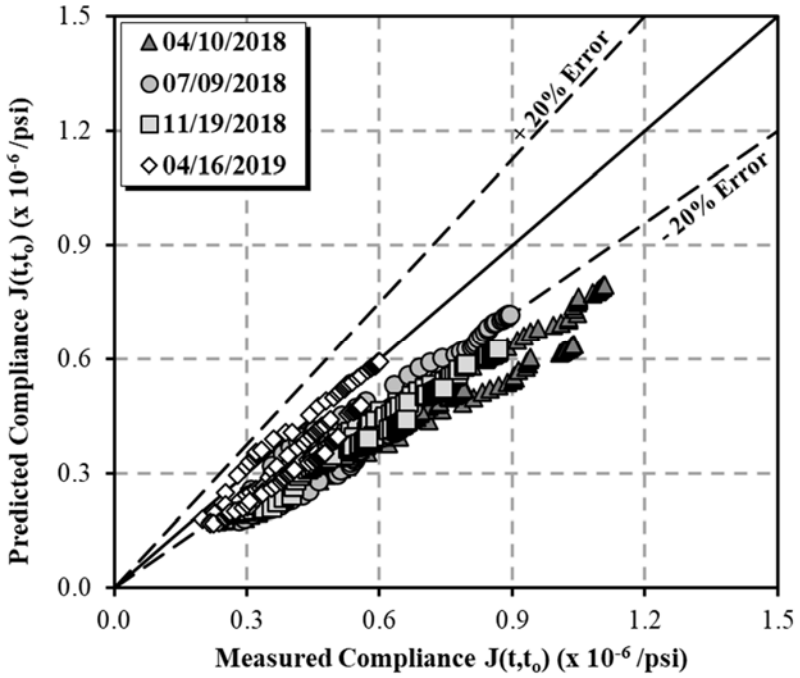

Figure 7-21: Measured versus predicted compliance using the CEB MC 2010 Model

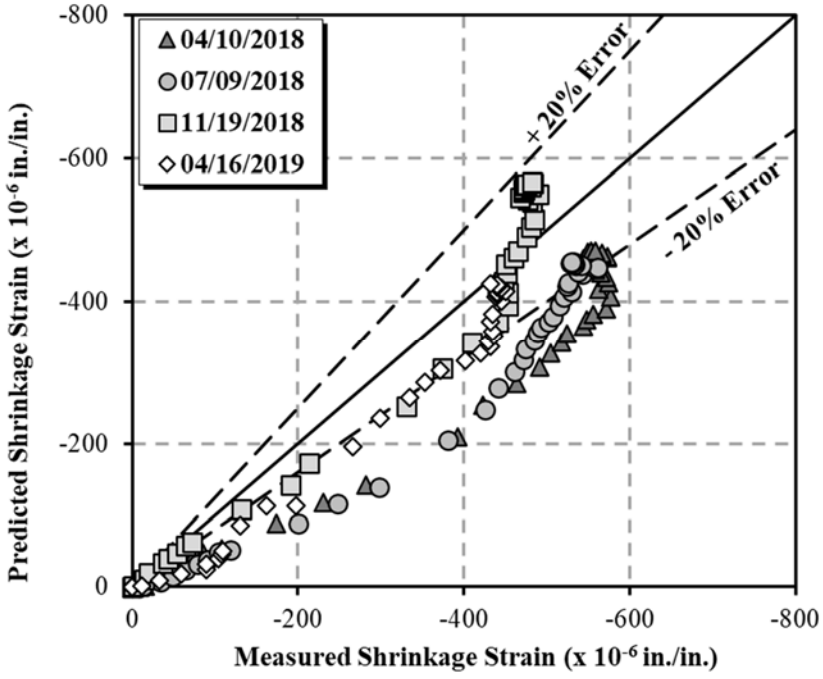

Figure 7-22: Measured versus predicted shrinkage for cylinders using the CEB MC 2010 Model

7.11 GL 2000 Compliance and Shrinkage Predictions

The GL 2000 creep and shrinkage prediction models are defined in Section 3.2.8, and a summary of key input parameters for the concrete sampled during this project is presented in Table 7-8.

Table 7-8: Summary of GL 2000 creep and shrinkage prediction inputs

Creep and Shrinkage Model Input Parameters		
Input		**Justification (if necessary)**
Volume-to-surface area ratio of cylinders	1.5 in.	Excluding cylinder ends not exposed to drying
Volume-to-surface area ratio of prisms	0.66 in.	Including all prism sides
Relative humidity	46.9%	Average measured value
28-Day compressive strength	Table 5-2	Determined through concrete testing
Predicted 28-day elastic modulus	Table 6-2	GL 2000 prediction
Equivalent age at loading	Table 5-5	Based on GL 2000 maturity method
Equivalent age when drying began	Table 5-6	Based on GL 2000 maturity method
Predicted elastic modulus at age of loading	Table 6-2	GL 2000 prediction
Cement type	Table 4-2	From mixture proportions

The comparison between the measured compliance values and those predicted by the GL 2000 model is shown in Figure 7-23. While values from the 04/10/2018 and 04/16/2019 sampling dates are underpredicted and overpredicted, respectively, this model otherwise predicts compliance reasonably well, with approximately half of the values falling very close to the line of equality. The comparison between the measured shrinkage strains and those predicted by the GL 2000 model is shown in Figure 7-24. Many of the shrinkage predictions fall within the 20 percent error bands, with early-age predictions falling outside the -20 percent error band, and later-age predictions for the 11/19/2018 sampling date falling outside the +20 percent error band.

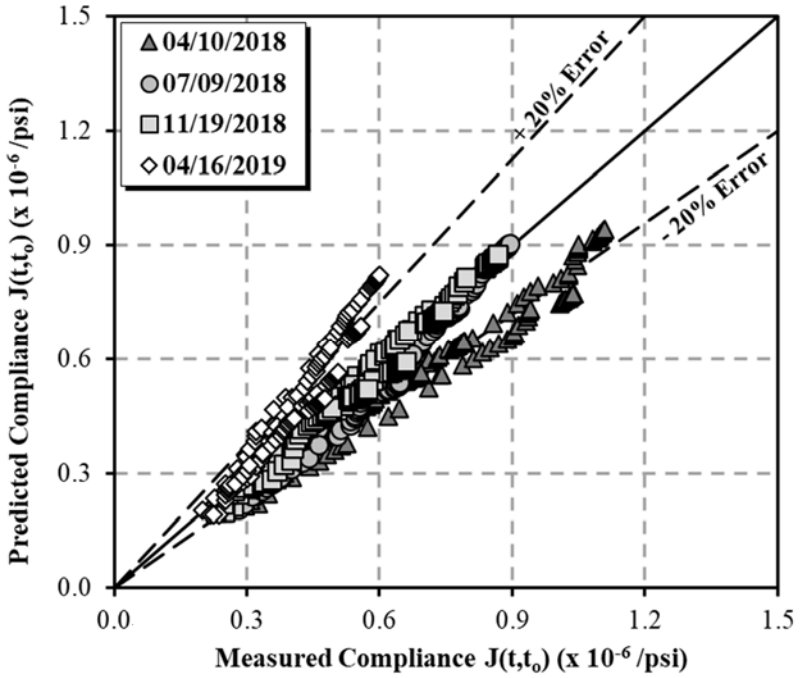

Figure 7-23: Measured versus predicted compliance using the GL 2000 Model

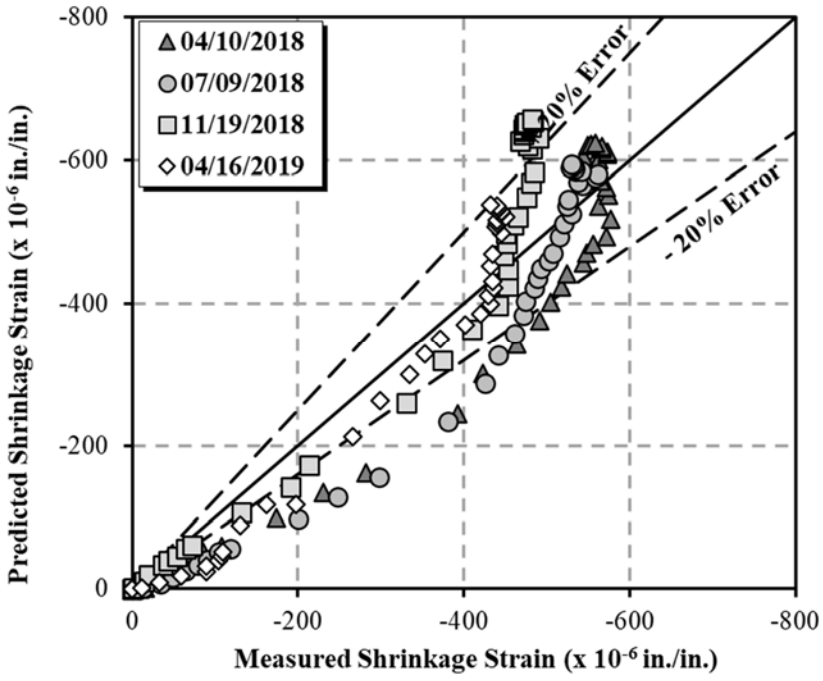

Figure 7-24: Measured versus predicted shrinkage for cylinders using the GL 2000 Model

Chapter 8

STATISTICAL ANALYSIS OF CREEP AND SHRINKAGE PREDICTION MODEL ACCURACY

8.1 INTRODUCTION

This chapter covers the statistical analysis used to compare the accuracy of the creep and shrinkage prediction models covered in this study. The primary goal of this analysis is to determine the most accurate model for predicting both creep and shrinkage in the concrete used in the I-59/I-20 segmental bridge. The following sections present the techniques used for statistical comparison, the results of the analysis, and the selection of the most accurate model based on the analysis. The most accurate model is also calibrated to improve its prediction accuracy, which is covered in Chapter 9. It should be noted that this analysis considers all prediction models included in the upcoming edition (10th) of the *AASHTO LRFD Bridge Design Specifications*. Therefore, all prediction models covered in this study are considered, with the exception of the GL 2000 model because it is not recommended for use in the 10th Edition of the *AASHTO LRFD Bridge Design Specifications* (Bayrak 2022).

8.2 STATISTICAL COMPARISON TECHNIQUES

The primary statistical measure of model accuracy used in the statistical analysis is the unbiased estimate of the standard deviation of error, S_j, which is defined in Equation 8.1 (McCuen 1985). S_j values measure accuracy similarly to the sum of square errors; however, they are normalized for the number of data points, which is necessary for this study due to the different sampling dates and loading ages of the concrete. A more accurate model has an S_j that is less the S_j of a less accurate model.

$$S_j = \sqrt{\frac{1}{n-1}\sum_{i}^{n} \Delta_i^2} \qquad \text{Equation 8.1}$$

With,

S_j = unbiased estimate of the standard deviation of error,

n = number of data points, and

Δ_i = difference between measured and predicted values.

Standard deviation of error values have the same units as the data being analyzed, so it cannot be used to compare models when accounting for both compliance and shrinkage strain because the two values have such different magnitudes. Therefore, in this study, the S_j values are normalized by assigning a rating index between 0.00 and 1.00 to each model for both compliance

and shrinkage based on its respective S_j value. The weighted average of S_j values based on the number of segments cast for each mixture proportion is first taken to determine the rating indices. The percentages of segments cast from the concrete of each sampling date are presented in Table 8-1. The model with the lowest S_j value is then given a rating index of 1.00, and the model with the highest S_j value is given a rating index of 0.00. The rating indices of the remainder of the models that fall somewhere in between are determined through linear interpolation. The average of the rating indices for compliance and shrinkage is determined for each prediction model, and ranking values of 1 through 8 are assigned, with the most accurate model having a value of 1.

Table 8-1: Rating index weights based on number of segments cast

Rating Index Weights	
04/10/2018	0.006
07/09/2018	0.183
11/19/2018	0.428
04/16/2019	0.383
Total	**1.000**

Because linear interpolation is used to assign rating indices to each prediction model, any outliers tend to skew the results so that the differences in the remaining models might not seem significant. To account for this effect, in cases where significant outliers of high S_j values occur, the interpolation is performed over two regions; one line assigns values to the outliers, and a second line with a steeper slope assigns values to the more accurate models. This process is discussed further in the following section.

8.3 STATISTICAL ANALYSIS RESULTS

8.3.1 Statistical Comparison of Compliance Prediction Models

For every model included in this analysis, all predicted compliance values for all loading ages are used to calculate a single S_j value for each sampling date. The weighted average of these values is then determined based on the percentages of segments cast from each mixture proportion, shown in Table 8-1. A summary of the calculated S_j values and the weighted average for each prediction model is presented in Table 8-2.

Table 8-2: Summary of S_j values for compliance

Model	S_j Values for Compliance ($\times 10^{-6}$ /psi)				
	04/10/2018	07/09/2018	11/19/2018	04/16/2019	Weighted Average
AASHTO LRFD	0.282	0.182	0.201	0.088	0.155
ACI 209	0.292	0.180	0.186	0.064	0.139
B3	0.108	0.129	0.125	0.193	0.152
B4	0.588	0.687	0.886	0.153	0.567
B4*	0.320	0.410	0.468	0.559	0.492
CEB MC 1990	0.176	0.079	0.077	0.057	0.070
CEB MC 90-99	0.195	0.110	0.117	0.038	0.086
CEB MC 2010	0.250	0.165	0.165	0.075	0.131

From observation of the weighted S_j averages, the CEB MC 1990 model predicts compliance most accurately, and the B4 model predicts compliance the least accurately. These weighted averages determine the rating index of each compliance prediction model. Because the B4 and B4* models have much larger S_j values than the other prediction models, they represent outliers. Therefore, interpolation used to assign rating indices to each model is done in two regions as shown in Figure 8-1. To sufficiently account for the differences between the other six models, their line of interpolation includes a range of rating indices of 0.2 to 1.0, with the least accurate of the six receiving a rating index of 0.2. The second line of interpolation including rating indices of 0.0 to 0.2 has a more gradual slope and is used for the B4 and B4* models. The rating index of each compliance prediction model is presented in Table 8-3, and the interpolation graph showing the two interpolation regions used to determine the rating indices is shown in Figure 8-1.

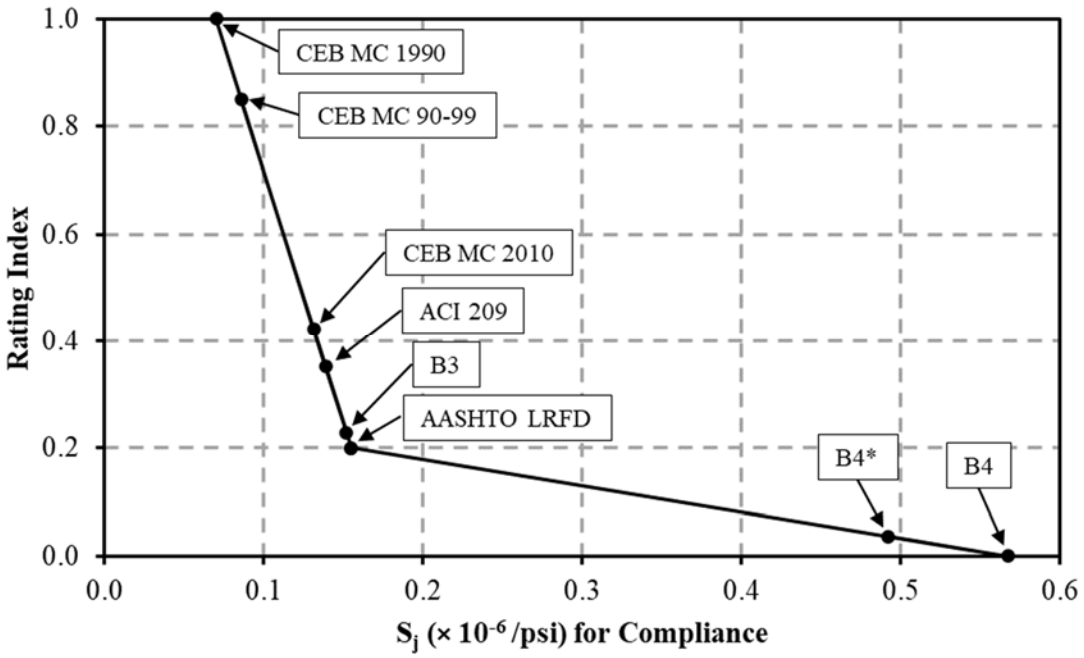

Figure 8-1: Graph used for interpolation of compliance rating indices

Table 8-3: Compliance rating indices

Model	Compliance Rating Indices		
	S_j Average (× 10^{-6} /psi)	Rating Index	Model Ranking
AASHTO LRFD	0.155	0.20	6
ACI 209	0.139	0.35	4
B3	0.152	0.23	5
B4	0.567	0.00	8
B4*	0.492	0.04	7
CEB MC 1990	0.070	1.00	1
CEB MC 90-99	0.086	0.85	2
CEB MC 2010	0.131	0.42	3

8.3.2 Statistical Comparison of Shrinkage Prediction Models

The average S_j value for each shrinkage prediction model is determined in the same way as for compliance: one value is calculated for each sampling date, and the rating index weights in Table 8-1 are used to calculate the weighted average for each model. A summary of S_j values for the shrinkage cylinders is presented in Table 8-4.

Table 8-4: Summary of S_j values for shrinkage cylinders

Model	S_j Values for Shrinkage (× 10^{-6} in./in.)				
	04/10/2018	07/09/2018	11/19/2018	04/16/2019	Weighted Average
AASHTO LRFD	66.9	53.1	40.0	29.7	38.6
ACI 209	95.4	59.9	47.6	63.0	56.0
B3	239	218	154	147	164
B4	233	200	67.5	191	140
B4*	167	107	73.9	30.8	63.9
CEB MC 1990	154	145	52.5	104	89.7
CEB MC 90-99	114	100	54.4	48.8	60.9
CEB MC 2010	126	112	54.4	58.6	66.9

From the table, it can be seen that the AASHTO LRFD model predicts shrinkage in the companion cylinders most accurately, and the B3 model predicts shrinkage the least accurately. Because the weighted averages contain no apparent outliers, linear interpolation across all the models is used to calculate rating indices for each shrinkage prediction model. The rating index for each shrinkage prediction model for the shrinkage cylinders is presented in Table 8-5, and the interpolation graph used for shrinkage is shown in Figure 8-2.

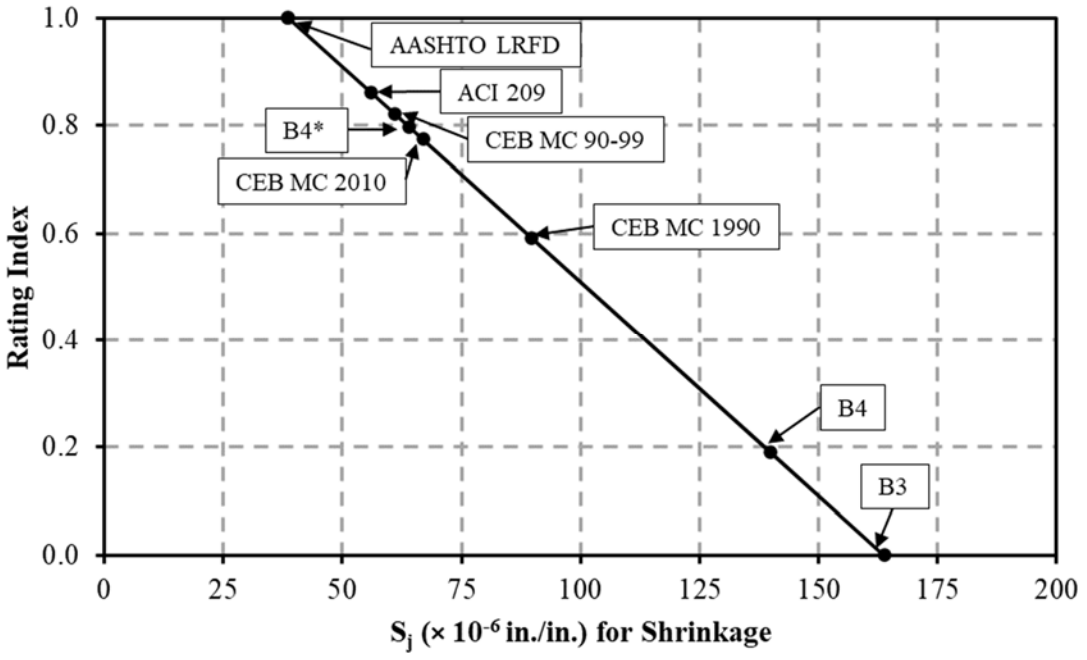

Figure 8-2: Graph used for interpolation of shrinkage rating indices

Table 8-5: Shrinkage cylinder rating indices

Model	Shrinkage Cylinder Rating Indices		
	S_j Average ($\times 10^{-6}$ in./in.)	Rating Index	Model Ranking
AASHTO LRFD	38.6	1.00	1
ACI 209	56.0	0.86	2
B3	163	0.00	8
B4	139	0.19	7
B4*	63.9	0.80	4
CEB MC 1990	89.7	0.59	6
CEB MC 90-99	60.9	0.82	3
CEB MC 2010	66.9	0.77	5

A summary of S_j values for the air-cured and moist-cured shrinkage prisms is presented in Table 8-6 and Table 8-7, respectively.

Table 8-6: Summary of S_j values for air-cured shrinkage prisms

Model	S_j Values for Shrinkage ($\times 10^{-6}$ in./in.)				
	04/10/2018	07/09/2018	11/19/2018	04/16/2019	Weighted Average
AASHTO LRFD	117	97.3	66.5	54.6	67.9
ACI 209	223	150	90.7	85.0	100
B3	331	273	189	153	191
B4	105	184	303	96.6	201
B4*	67.0	210	179	346	248
CEB MC 1990	207	169	137	90.3	125
CEB MC 90-99	119	76.0	92.7	55.8	75.6
CEB MC 2010	144	97.3	87.6	34.7	69.5

Table 8-7: Summary of S_j values for moist-cured shrinkage prisms

Model	S_j Values for Shrinkage (× 10^{-6} in./in.)				
	04/10/2018	07/09/2018	11/19/2018	04/16/2019	Weighted Average
AASHTO LRFD	189	128	153	78.3	120
ACI 209	283	168	141	51.9	113
B3	272	183	118	59.3	108
B4	142	194	247	92.0	177
B4*	111	224	123	339	224
CEB MC 1990	257	182	182	94.1	149
CEB MC 90-99	168	85.8	45.0	53.5	56.5
CEB MC 2010	192	108	43.1	34.8	52.8

From the above tables, the most accurate shrinkage prediction model for the air-cured shrinkage prisms is the AASHTO LRFD model, and the least accurate is the B4* model. For the moist-cured prisms, the most accurate model is the CEB MC 2010 model, and the least accurate is the B4* model. Table 8-8 and Table 8-9 present the rating indices for each prediction model for air-cured and moist-cured prisms, respectively.

Table 8-8: Air-cured shrinkage prism rating indices

Model	Shrinkage Prism Rating Indices		
	S_j Average (× 10^{-6} in./in.)	Rating Index	Model Ranking
AASHTO LRFD	67.9	1.00	1
ACI 209	100	0.82	4
B3	191	0.31	6
B4	201	0.26	7
B4*	248	0.00	8
CEB MC 1990	125	0.68	5
CEB MC 90-99	75.6	0.96	3
CEB MC 2010	69.5	0.99	2

Table 8-9: Moist-cured shrinkage prism rating indices

Model	Shrinkage Prism Rating Indices		
	S_j Average ($\times 10^{-6}$ in./in.)	**Rating Index**	**Model Ranking**
AASHTO LRFD	120.3	0.61	5
ACI 209	112.8	0.65	4
B3	108.5	0.67	3
B4	177.2	0.27	7
B4*	224.2	0.00	8
CEB MC 1990	149.1	0.44	6
CEB MC 90-99	56.5	0.98	2
CEB MC 2010	52.8	1.00	1

8.4 MODEL SELECTION

The rating indices assigned to each compliance and shrinkage prediction model are used to normalize the S_j values of compliance and shrinkage so that a composite, single value may be determined. Because it is unclear exactly what percentage of total inelastic deformation is caused by creep and shrinkage individually, weights of 50%:50%, 40%:60%, and 60%:40% were given to the creep and shrinkage strain, respectively, when calculating the composite rating index. Each of these composite values for each prediction model is presented in Table 8-10, and the model rankings for each composite value are presented in Table 8-11. To denote what weights are assigned for each average, the abbreviations “CR” and “SH” are used for creep and shrinkage, respectively. For example, and entry of “CR:SH = 60:40” denotes a weight assigned to creep of 60 percent and a weight assigned to shrinkage of 40 percent when calculating the composite value.

It should also be noted that the selection of the most accurate model does not account for the drying shrinkage prisms. Because the shrinkage cylinders have the same shape and size as the creep cylinders, only the shrinkage results collected for the cylinders are used to identify the most accurate model. Additionally, the cylinders have a higher volume-to-surface area ratio, which is closer to that of the bridge segments.

Table 8-10: Composite rating indices for compliance and shrinkage cylinders

Model	Composite Rating Indices				
	Compliance Rating Index	Shrinkage Rating Index	CR:SH = 50:50	CR:SH = 60:40	CR:SH = 40:60
AASHTO LRFD	0.20	1.00	0.60	0.52	0.68
ACI 209	0.35	0.86	0.61	0.56	0.66
B3	0.23	0.00	0.11	0.14	0.09
B4	0.00	0.19	0.10	0.08	0.11
B4*	0.04	0.80	0.42	0.34	0.49
CEB MC 1990	1.00	0.59	0.80	0.84	0.76
CEB MC 90-99	0.85	0.82	0.84	0.84	0.83
CEB MC 2010	0.42	0.77	0.60	0.56	0.63

Table 8-11: Model rankings for combination of compliance and shrinkage

Model	Model Rankings		
	CR:SH = 50:50	CR:SH = 60:40	CR:SH = 40:60
AASHTO LRFD	4	5	3
ACI 209	3	4	4
B3	7	7	8
B4	8	8	7
B4*	6	6	6
CEB MC 1990	2	2	2
CEB MC 90-99	1	1	1
CEB MC 2010	5	3	5

Based on the statistical analysis, for a combination of compliance and shrinkage, the most accurate prediction model is the CEB MC 90-99 model. For all assigned weights, the CEB MC 90-99 model has the top ranking. The second most accurate model is the CEB MC 1990 model. The least accurate models of the eight in the analysis are the B3 and the B4 models. Because the CEB MC 90-99 model is the most accurate to predict creep and shrinkage, and it is a recommended model in the 10th Edition of the *AASHTO LRFD Bridge Design Specifications*, it is the model selected for calibration.

Chapter 9

CREEP AND SHRINKAGE PREDICTION MODEL CALIBRATION

9.1 INTRODUCTION

An objective of this research project is to calibrate the most accurate creep and shrinkage prediction model for the Birmingham I-59/I-20 segmental bridge. As discussed in Chapter 8, the CEB MC 90-99 model was determined to be the most accurate model, and its calibration is covered in Section 9.2. Additionally, because of its use in the *Bridge Designer II* software, the CEB MC 1990 model was also calibrated and is presented in Section 9.3.

9.2 CEB MC 90-99 CALIBRATION

The first step of model calibration was to perform a sensitivity analysis of the various coefficients from the equations that make up the model to determine the best coefficients to calibrate. These coefficients were then changed to minimize the S_j values for each sampling date. The same coefficients were used for each sampling date; however, they were calibrated separately, so the values vary between sampling dates. Due to the similarities between the CEB MC 90-99 and CEB MC 1990 compliance prediction models, the selected compliance coefficients were the same, so their symbols in the following sections are the same, with the exception of a subscript used to differentiate between models.

9.2.1 CEB MC 90-99 Sensitivity Analysis

This section presents the results of the sensitivity analysis performed on various coefficients from the CEB MC 90-99 creep and shrinkage prediction model. The sensitivity analysis was performed by changing many parameters and components of this model by 25 percent and graphically determining the parameters that would have the most significant impact on model accuracy. Parameters that were not altered were those that were unique to the I-59/I-20 segmental bridge, such as the relative humidity or volume-to-surface factors.

9.2.1.1 CEB MC 90-99 Compliance Sensitivity Analysis

An important step in accurately predicting compliance is to correctly predict the elastic response of the concrete. To accomplish this, the CEB MC 90-99 modulus of elasticity was first calibrated before the error in the time-dependent part of the compliance was considered. It was determined through the analysis that a single parameter, μ_{99}, could replace E_{co} in Equation 9.1 and be changed to predict the elastic modulus more accurately, as given by Equation 9.2. In the original

CEB MC 90-99 model, an E_{co} value of 21,500 MPa is used. The effect of varying μ_{99} by ±25% on the CEB MC 90-99 28-day elastic modulus predictions is shown in Figure 9-1.

$$E_{ci} = \alpha_E \cdot E_{co} \left[\frac{f_{cm}}{f_{cmo}} \right]^{1/3} \quad \text{Equation 9.1}$$

$$E_{ci} = \alpha_E \cdot \mu_{99} \left[\frac{f_{cm}}{f_{cmo}} \right]^{1/3} \quad \text{Equation 9.2}$$

With,

μ_{99} = empirical parameter being calibrated (MPa).

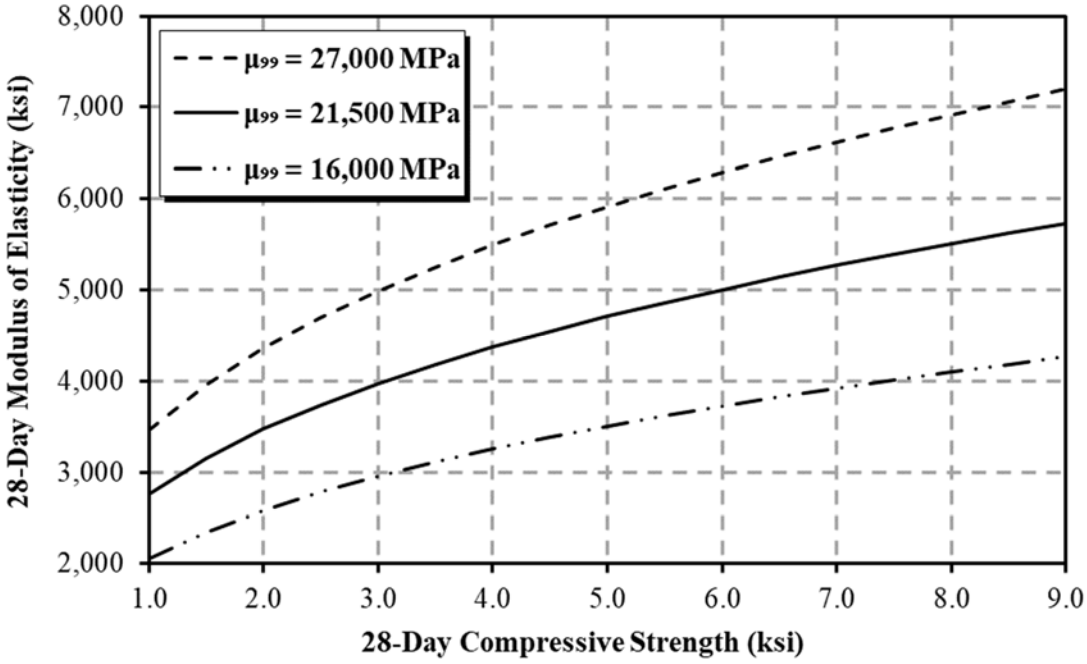

Figure 9-1: Sensitivity of CEB MC 90-99 elastic modulus with varied μ_{99}

The next step of compliance calibration was performed on the strength component of the notional creep coefficient given by Equation 9.3. It was determined that the parameter, ρ_{99}, shown in Equation 9.4, could be calibrated for a more accurate compliance prediction. As shown in Equation 9.3, the original CEB MC 90-99 model uses a ρ_{99} value of 5.3. The effect of varying ρ_{99} on compliance predictions is shown in Figure 9-2.

$$\beta(f_{cm}) = \frac{5.3}{(f_{cm}/f_{cmo})^{0.5}} \quad \text{Equation 9.3}$$

$$\beta(f_{cm}) = \frac{\rho_{99}}{(f_{cm}/f_{cmo})^{0.5}} \quad \text{Equation 9.4}$$

With,

ρ_{99} = empirical parameter being calibrated (unitless).

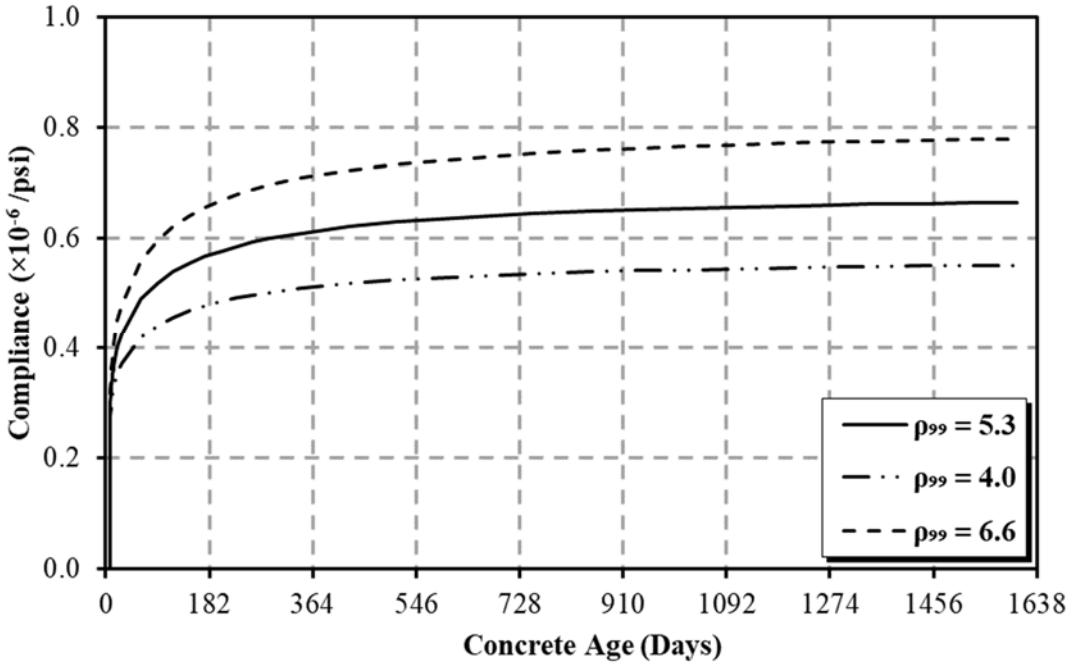

Figure 9-2: Sensitivity of CEB MC 90-99 compliance with varied ρ_{99}

The final change to the CEB MC 90-99 compliance model was made by replacing the exponent in Equation 9.5 with the empirical parameter, λ_{99}, shown in Equation 9.6. As shown in Equation 9.5, the original CEB MC 90-99 model uses a λ_{99} value of 0.2. The effect of varying λ_{99} on compliance predictions is shown in Figure 9-3.

$$\beta(t_o) = \frac{1}{0.1 + (t_o / t_1)^{0.2}} \qquad \text{Equation 9.5}$$

$$\beta(t_o) = \frac{1}{0.1 + (t_o / t_1)^{\lambda_{99}}} \qquad \text{Equation 9.6}$$

With,

λ_{99} = empirical parameter being calibrated (unitless).

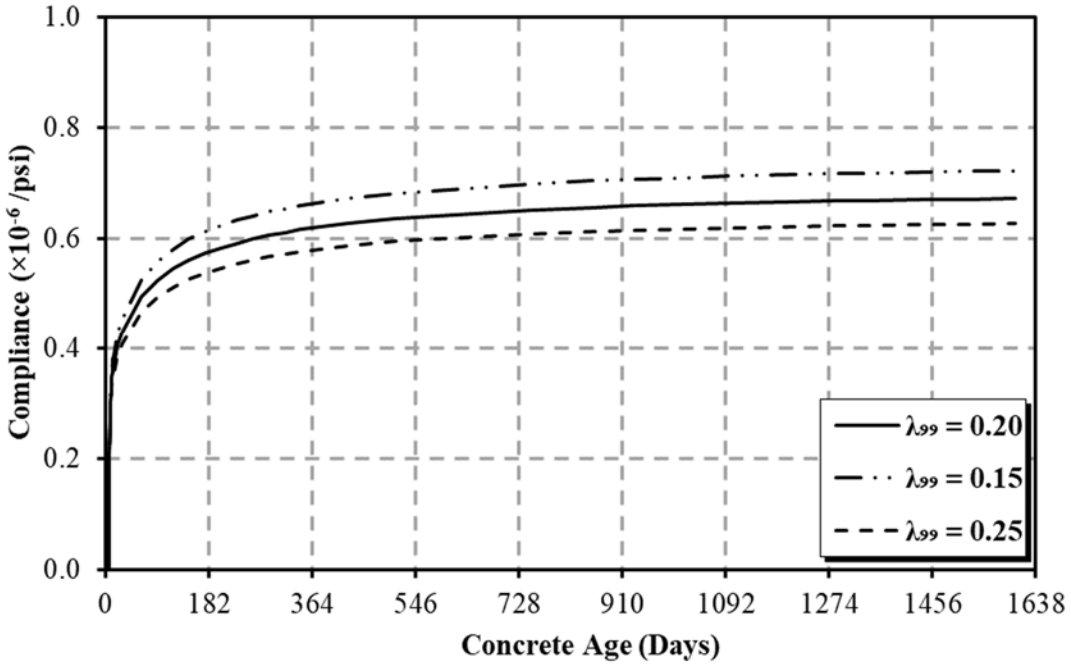

Figure 9-3: Sensitivity of CEB MC 90-99 compliance with varied λ_{99}

9.2.1.2 CEB MC 90-99 Shrinkage Sensitivity Analysis

The first two changes to the CEB MC 90-99 shrinkage prediction model were made to the time-dependent factor of drying shrinkage, given by Equation 9.7. It was determined that adding coefficients, τ and ω, as shown in Equation 9.8, whose values could be changed, would lead to more accurate shrinkage predictions. The effects of varying τ and ω on shrinkage predictions are shown in Figures 9-4 and 9-5, respectively.

$$\beta_{ds}(t-t_s) = \left[\frac{(t-t_s)/t_1}{350(h/h_o)^2 + (t-t_s)/t_1}\right]^{0.5} \qquad \text{Equation 9.7}$$

$$\beta_{ds}(t-t_s) = \tau\left[\frac{(t-t_s)/t_1}{350(h/h_o)^2 + \omega(t-t_s)/t_1}\right]^{0.5} \qquad \text{Equation 9.8}$$

With,

τ = empirical parameter being calibrated (unitless) and

ω = empirical parameter being calibrated (unitless).

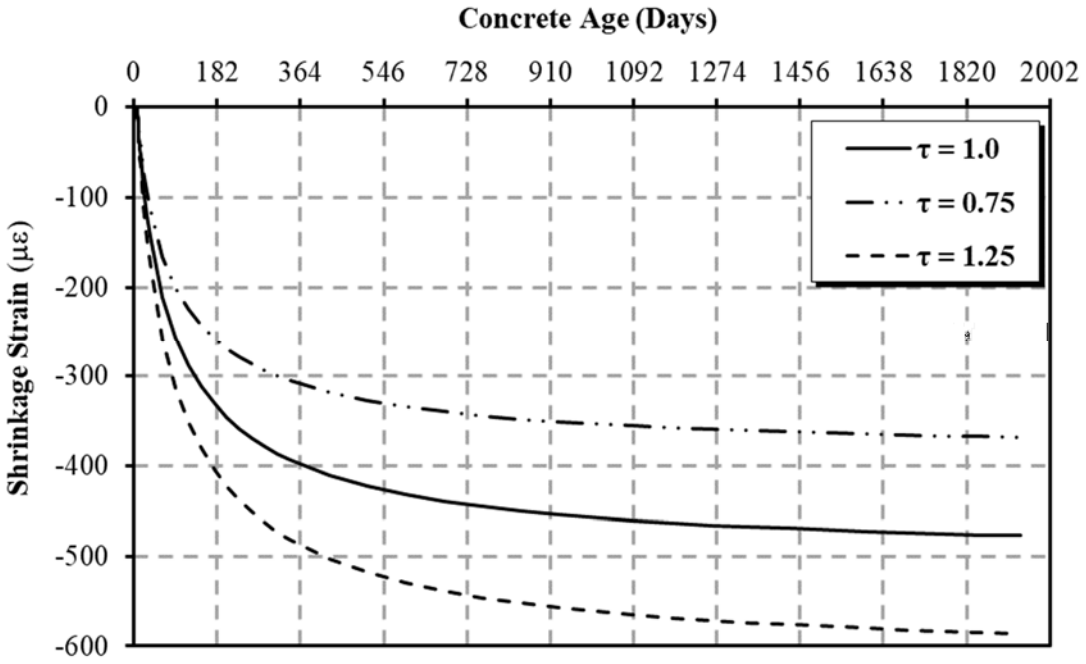

Figure 9-4: Sensitivity of CEB MC 90-99 shrinkage with varied τ

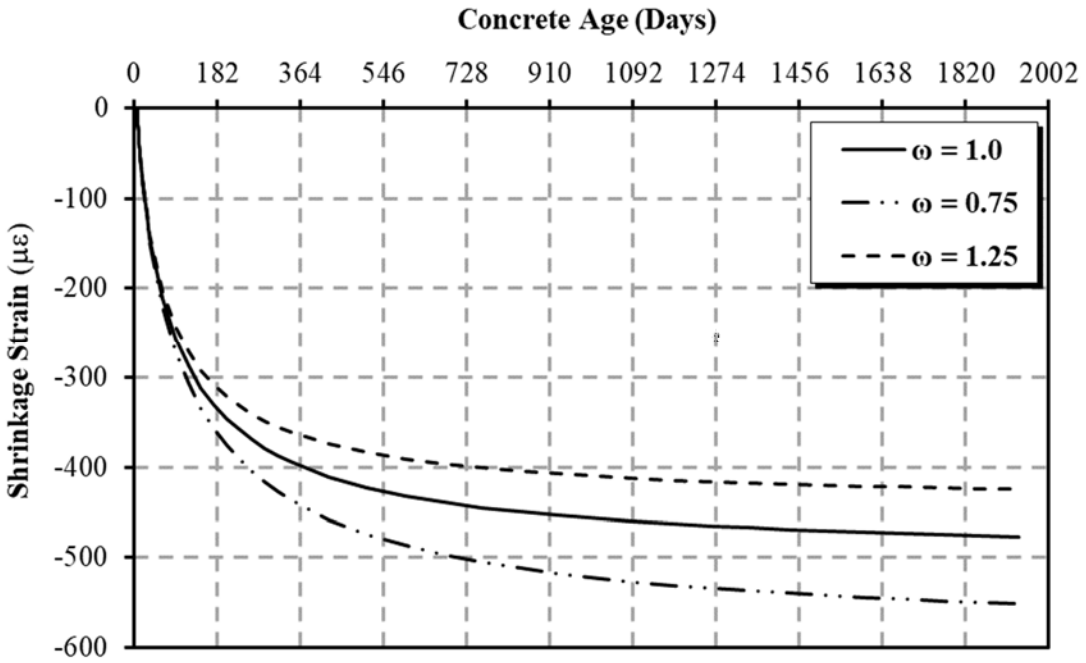

Figure 9-5: Sensitivity of CEB MC 90-99 shrinkage with varied ω

The final change to the CEB MC 90-99 shrinkage prediction model was made by replacing the exponent in the notional Autogenous shrinkage coefficient, shown in Equation 9.9, with the empirical parameter, θ, shown in Equation 9.10. As shown in Equation 9.9, the original CEB MC

90-99 model uses a θ value of 2.5. The effect of varying θ on shrinkage predictions is shown in Figure 9-6.

$$\varepsilon_{caso}(f_{cm}) = -\alpha_{as}\left(\frac{f_{cm}/f_{cmo}}{6+f_{cm}/f_{cmo}}\right)^{2.5}\cdot 10^{-6} \qquad \text{Equation 9.9}$$

$$\varepsilon_{caso}(f_{cm}) = -\alpha_{as}\left(\frac{f_{cm}/f_{cmo}}{6+f_{cm}/f_{cmo}}\right)^{\theta}\cdot 10^{-6} \qquad \text{Equation 9.10}$$

With,

θ = empirical parameter being calibrated (unitless).

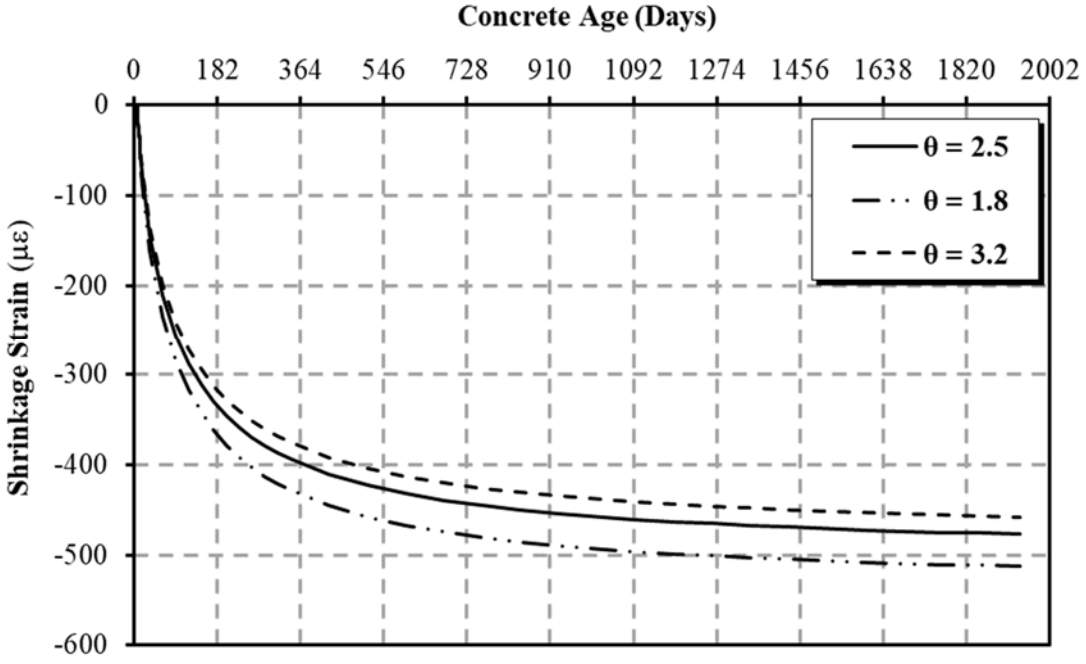

Figure 9-6: Sensitivity of CEB MC 90-99 shrinkage with varied θ

9.2.1.3 Number of Calibration Factors

Multiple parameters beyond those presented in this section were considered for the CEB MC 90-99 model calibration. It was observed that as the number of calibration factors increases, the effect that each additional factor has on the prediction improvement decreases. The goal of this calibration was to provide the most accurate predictions by calibrating variables that have a significant effect on the prediction accuracy, without making any insignificant changes to the model. Figure 9-7 and Figure 9-8 show the S_j values for each sampling date and all data collected as the number of calibration factors increases for compliance and shrinkage, respectively. These plots were created by calibrating the entire model with a different number of parameters between one and five. The parameters that were chosen had the most significant impact in the sensitivity analysis in descending order. For compliance, the slope begins to plateau after three calibration

factors. For shrinkage it is less clear, but because of the small relative difference between three and four, three CEB MC 90-99 calibration factors were used for both compliance and shrinkage.

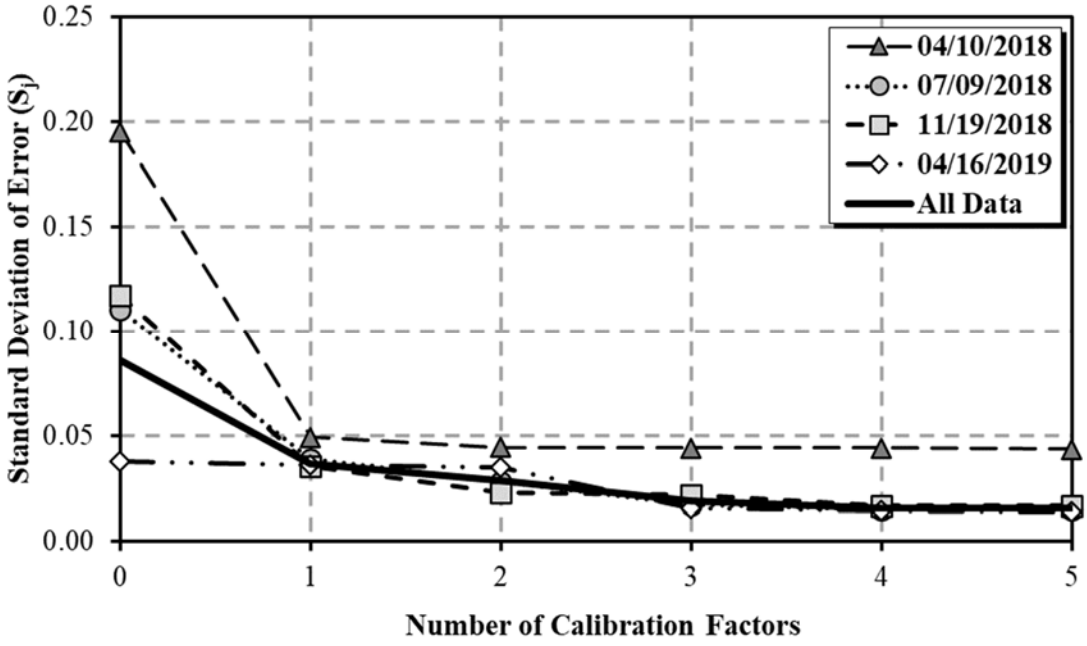

Figure 9-7: CEB MC 90-99 S_j versus number of calibration factors for compliance

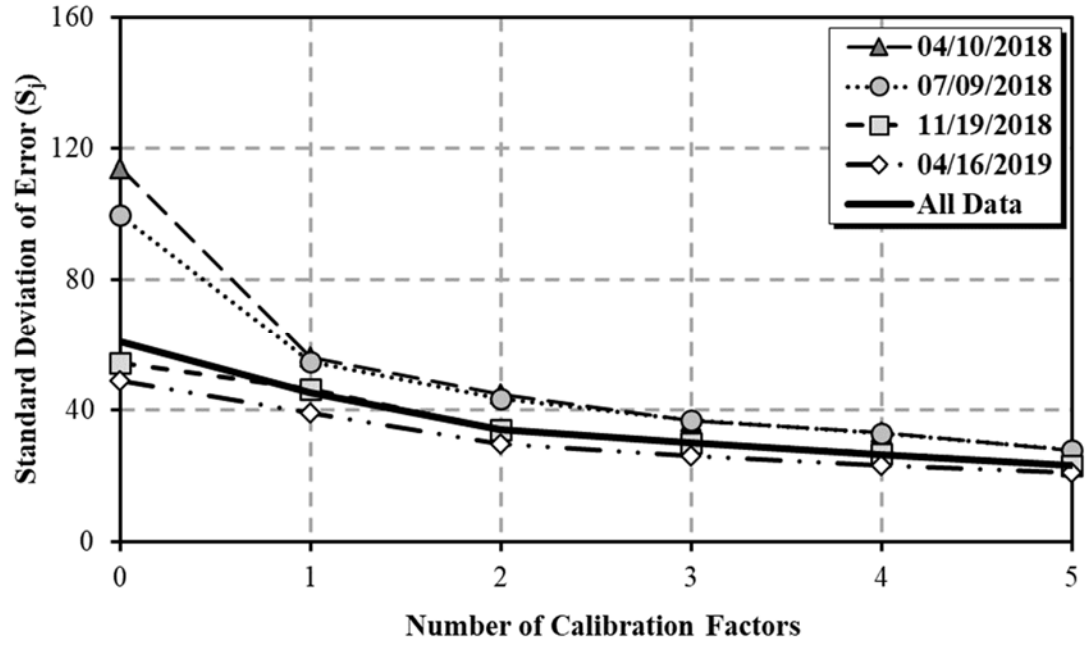

Figure 9-8: CEB MC 90-99 S_j versus number of calibration factors for shrinkage

9.2.2 CEB MC 90-99 Calibration Results

Each empirical parameter discussed in the previous sections was calibrated for each sampling date to minimize its respective *Sj* value and to improve the overall prediction accuracy. The calibrated empirical parameters for the CEB MC 90-99 prediction model are presented in Table 9-1.

Table 9-1: CEB MC 90-99 original and calibrated empirical parameters

Empirical Parameter	Original CEB MC 90-99 Model	04/10/2018	07/09/2018	11/19/2018	04/16/2019
μ_{99} (MPa)	21,500	16,500	17,000	18,000	20,500
ρ_{99} (unitless)	5.3	5.7	4.2	6.0	3.7
λ_{99} (unitless)	0.20	0.21	0.15	0.21	0.10
τ (unitless)	1.0	1.4	1.4	1.0	1.1
ω (unitless)	1.0	1.5	1.5	1.5	1.5
θ (unitless)	2.5	1.5	1.5	1.5	1.5

The calibrated empirical parameters in Table 9-1 were determined to be the most accurate for each sampling date by minimizing the S_j values using the Solver function on Microsoft Excel.

9.2.2.1 Calibrated CEB MC 90-99 Modulus of Elasticity

The calibrated CEB MC 90-99 modulus of elasticity for each sampling date is presented in the 28-day modulus of elasticity given by Equations 9.11 through 9.14.

04/10/2018 Sampling Date:

$$E_{ci} = \alpha_E \cdot 16{,}500 \left[\frac{f_{cm}}{f_{cmo}} \right]^{1/3} \qquad \text{Equation 9.11}$$

07/09/2018 Sampling Date:

$$E_{ci} = \alpha_E \cdot 17{,}000 \left[\frac{f_{cm}}{f_{cmo}} \right]^{1/3} \qquad \text{Equation 9.12}$$

11/19/2018 Sampling Date:

$$E_{ci} = \alpha_E \cdot 18{,}000 \left[\frac{f_{cm}}{f_{cmo}} \right]^{1/3} \qquad \text{Equation 9.13}$$

04/16/2019 Sampling Date:

$$E_{ci} = \alpha_E \cdot 20{,}500 \left[\frac{f_{cm}}{f_{cmo}} \right]^{1/3} \qquad \text{Equation 9.14}$$

A comparison of both the original and calibrated CEB MC 90-99 modulus of elasticity to the measured values is presented in Table 9-2. It is clear from this comparison that the calibration provided significant improvement for all sampling dates, with the weighted average percent error

improving from -14.7% to 0.4%, which was calculated with the weights presented in Table 8-1. Additionally, the comparisons between the measured elastic modulus values and those predicted by both the original and calibrated CEB MC 90-99 models are shown in Figure 9-9 and Figure 9-10, respectively.

Table 9-2: Comparison of original and calibrated CEB MC 90-99 modulus of elasticity to measured values

Loading Age (Days)	Measured Elastic Modulus (ksi)	Original Predicted Elastic Modulus (ksi)	Error (%)	Calibrated Predicted Elastic Modulus (ksi)	Error (%)
04/10/2018					
7	3800	4588	-20.7%	3521	7.3%
28	4050	5087	-25.6%	3904	3.6%
91	3850	5348	-38.9%	4105	-6.6%
182	4150	5449	-31.3%	4182	-0.8%
07/09/2018					
7	4250	4723	-11.1%	3735	12.1%
28	4250	5246	-23.4%	4148	2.4%
91	4200	5518	-31.4%	4363	-3.9%
182	4300	5622	-30.8%	4446	-3.4%
11/19/2018					
7	4400	4898	-11.3%	4101	6.8%
28	4600	5358	-16.5%	4486	2.5%
91	4600	5583	-21.4%	4674	-1.6%
182	4500	5668	-26.0%	4745	-5.4%
04/16/2019					
7	5100	5003	1.9%	4770	6.5%
28	5300	5565	-5.0%	5306	-0.1%
91	5400	5854	-8.4%	5581	-3.4%
182	5400	5965	-10.5%	5687	-5.3%
Average Percent Error		-14.7%		0.4%	

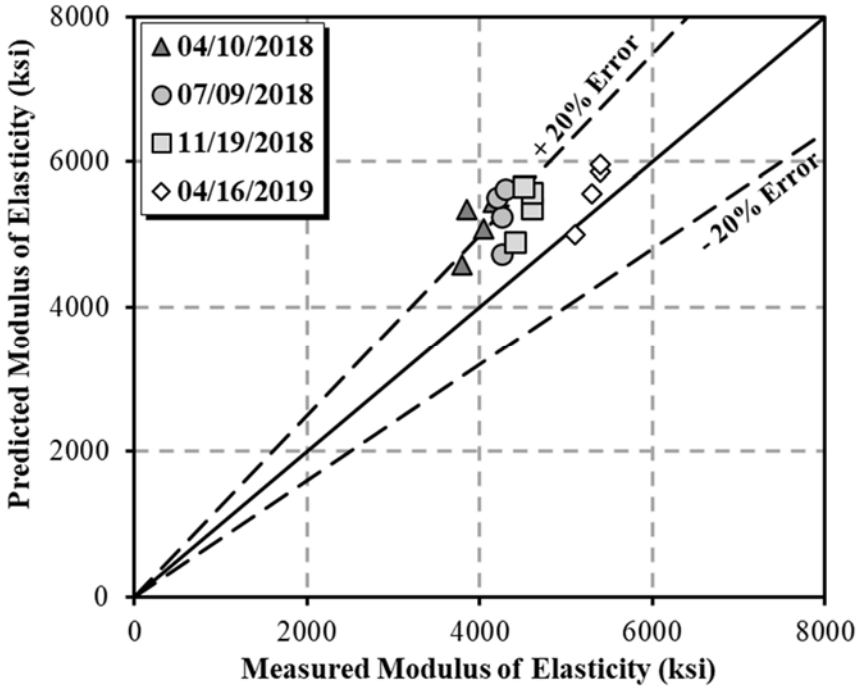

Figure 9-9: Measured versus predicted elastic modulus using the original CEB MC 90-99 model

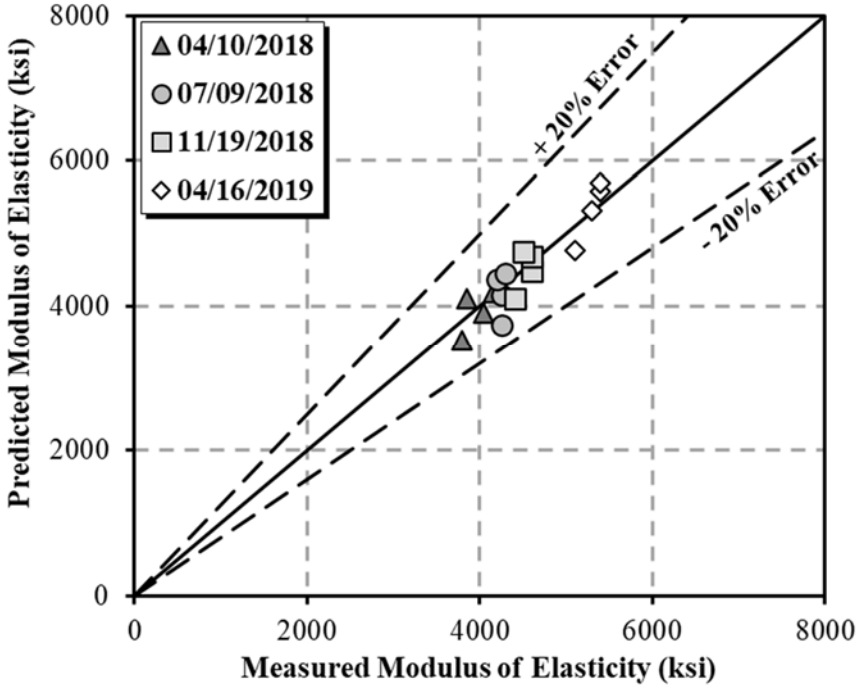

Figure 9-10: Measured versus predicted elastic modulus using the calibrated CEB MC 90-99 model

9.2.2.2 Calibrated CEB MC 90-99 Compliance

The S_j value for compliance for each sampling date was minimized by changing the empirical parameters, ρ_{99} and λ_{99}. The changes made to the CEB MC 90-99 model to the parameter, ρ_{99}, are presented in Equations 9.15 through 9.18. The changes made through the parameter, λ_{99}, are presented in Equations 9.19 through 9.22.

04/10/2018 Sampling Date:

$$\beta(f_{cm}) = \frac{5.7}{(f_{cm}/f_{cmo})^{0.5}} \qquad \text{Equation 9.15}$$

07/09/2018 Sampling Date:

$$\beta(f_{cm}) = \frac{4.2}{(f_{cm}/f_{cmo})^{0.5}} \qquad \text{Equation 9.16}$$

11/19/2018 Sampling Date:

$$\beta(f_{cm}) = \frac{6.0}{(f_{cm}/f_{cmo})^{0.5}} \qquad \text{Equation 9.17}$$

04/16/2019 Sampling Date:

$$\beta(f_{cm}) = \frac{3.7}{(f_{cm}/f_{cmo})^{0.5}} \qquad \text{Equation 9.18}$$

04/10/2018 Sampling Date:

$$\beta(t_o) = \frac{1}{0.1 + (t_o/t_1)^{0.21}} \qquad \text{Equation 9.19}$$

07/09/2018 Sampling Date:

$$\beta(t_o) = \frac{1}{0.1 + (t_o/t_1)^{0.15}} \qquad \text{Equation 9.20}$$

11/19/2018 Sampling Date:

$$\beta(t_o) = \frac{1}{0.1 + (t_o/t_1)^{0.21}} \qquad \text{Equation 9.21}$$

04/16/2019 Sampling Date:

$$\beta(t_o) = \frac{1}{0.1 + (t_o/t_1)^{0.10}} \qquad \text{Equation 9.22}$$

A comparison of the S_j values for the original CEB MC 90-99 compliance prediction model to those of the calibrated model is presented in Table 9-3. The calibration improved the compliance predictions for all sampling dates by over 50 percent, with an average improvement of 78 percent. The comparisons between the measured compliance values and those predicted by both the original and calibrated CEB MC 90-99 models are shown in Figure 9-11 and Figure 9-12, respectively. Unlike the original CEB MC 90-99 model, the vast majority of values fall within the 20 percent error bands, with many values falling much closer to the line of equality.

Table 9-3: Comparison of S_j values for compliance predictions for original and calibrated CEB MC 90-99 model

Sampling Date	**Original CEB MC 90-99 Model** S_j ($\times 10^{-6}$/psi)	**Calibrated CEB MC 90-99 Model** S_j ($\times 10^{-6}$/psi)	**Reduction in S_j** (%)
04/10/2018	0.195	0.044	77%
07/09/2018	0.110	0.017	84%
11/19/2018	0.117	0.023	81%
04/16/2019	0.038	0.016	58%
All Data	**0.086**	**0.019**	**78%**

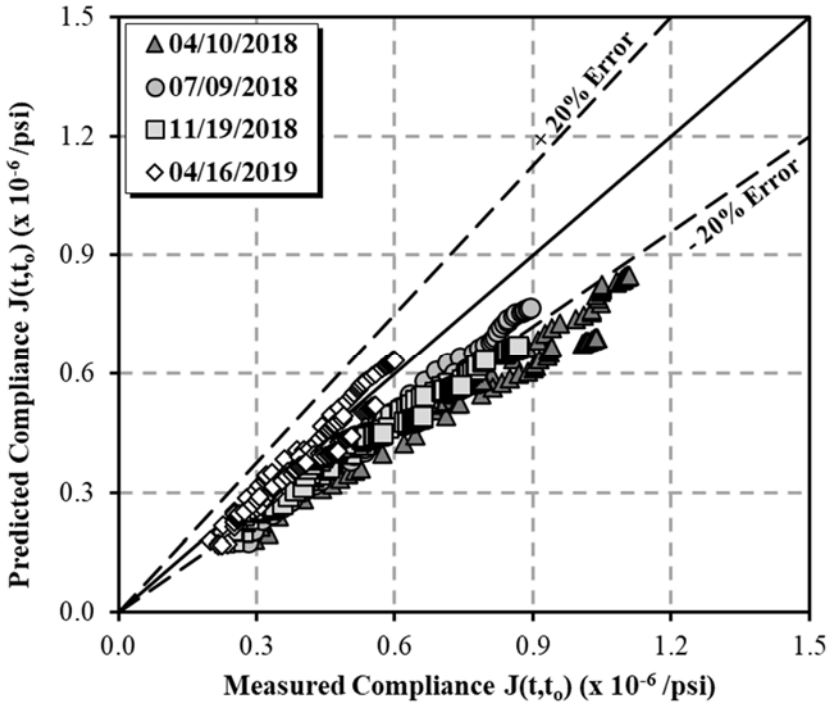

Figure 9-11: Measured versus predicted compliance using the original CEB MC 90-99 model

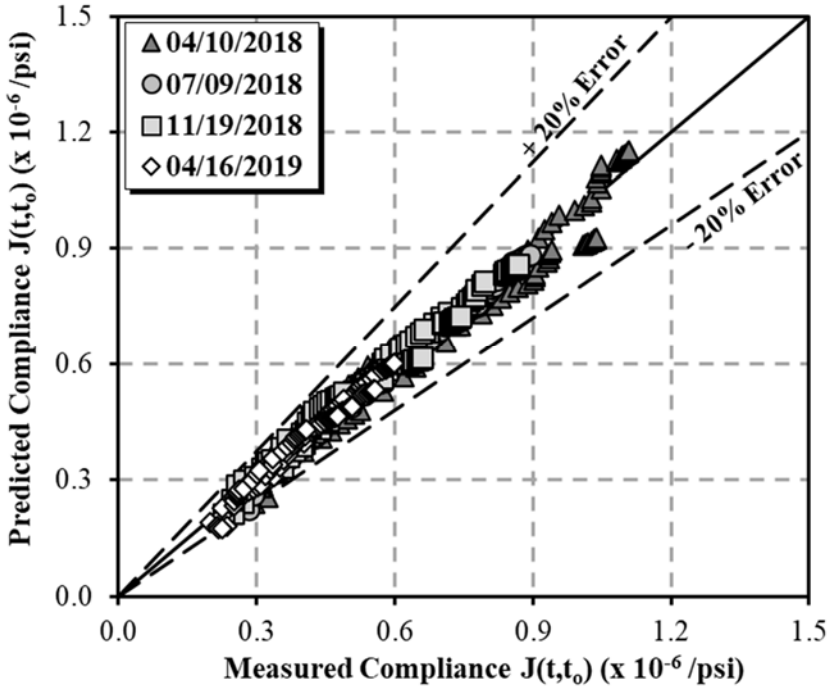

Figure 9-12: Measured versus predicted compliance using the calibrated CEB MC 90-99 model

9.2.2.3 Calibrated CEB MC 90-99 Shrinkage

The S_j value for shrinkage for each sampling date was minimized by changing the three empirical parameters discussed in Section 9.2.1.2. The changes made to the parameters, τ and ω, are

presented in Equations 9.23 through 9.26, and the changes made to the parameter, θ, for all sampling dates are presented in Equation 9.27.

04/10/2018 Sampling Date:

$$\beta_{ds}(t-t_s) = 1.4\left[\frac{(t-t_s)/t_1}{350(h/h_o)^2 + 1.5(t-t_s)/t_1}\right]^{0.5} \quad \text{Equation 9.23}$$

07/09/2018 Sampling Date:

$$\beta_{ds}(t-t_s) = 1.4\left[\frac{(t-t_s)/t_1}{350(h/h_o)^2 + 1.5(t-t_s)/t_1}\right]^{0.5} \quad \text{Equation 9.24}$$

11/19/2018 Sampling Date:

$$\beta_{ds}(t-t_s) = 1.0\left[\frac{(t-t_s)/t_1}{350(h/h_o)^2 + 1.5(t-t_s)/t_1}\right]^{0.5} \quad \text{Equation 9.25}$$

04/16/2019 Sampling Date:

$$\beta_{ds}(t-t_s) = 1.1\left[\frac{(t-t_s)/t_1}{350(h/h_o)^2 + 1.5(t-t_s)/t_1}\right]^{0.5} \quad \text{Equation 9.26}$$

All Sampling Dates:

$$\varepsilon_{caso}(f_{cm}) = -\alpha_{as}\left(\frac{f_{cm}/f_{cmo}}{6 + f_{cm}/f_{cmo}}\right)^{1.5} \cdot 10^{-6} \quad \text{Equation 9.27}$$

A comparison of the S_j values for the original CEB MC 90-99 shrinkage prediction model to those of the calibrated model is presented in Table 9-4. The calibration improved the predictions for all sampling dates by more than 40 percent, with an average improvement of 50 percent. The comparisons between the measured shrinkage strains and those predicted by both the original and calibrated CEB MC 90-99 models are shown in Figure 9-13 and Figure 9-14, respectively, in which only a small percentage of values fall outside the 20 percent error bands.

Table 9-4: Comparison of S_j values for shrinkage predictions for original and calibrated CEB MC 90-99 model

Sampling Date	**Original CEB MC 90-99 Model** S_j ($\times 10^{-6}$ in./in.)	**Calibrated CEB MC 90-99 Model** S_j ($\times 10^{-6}$ in./in.)	**Reduction in S_j** (%)
04/10/2018	114	37	67%
07/09/2018	100	37	62%
11/19/2018	53.6	30.4	43%
04/16/2019	48.1	26.2	46%
All Data	**60.3**	**30.1**	**50%**

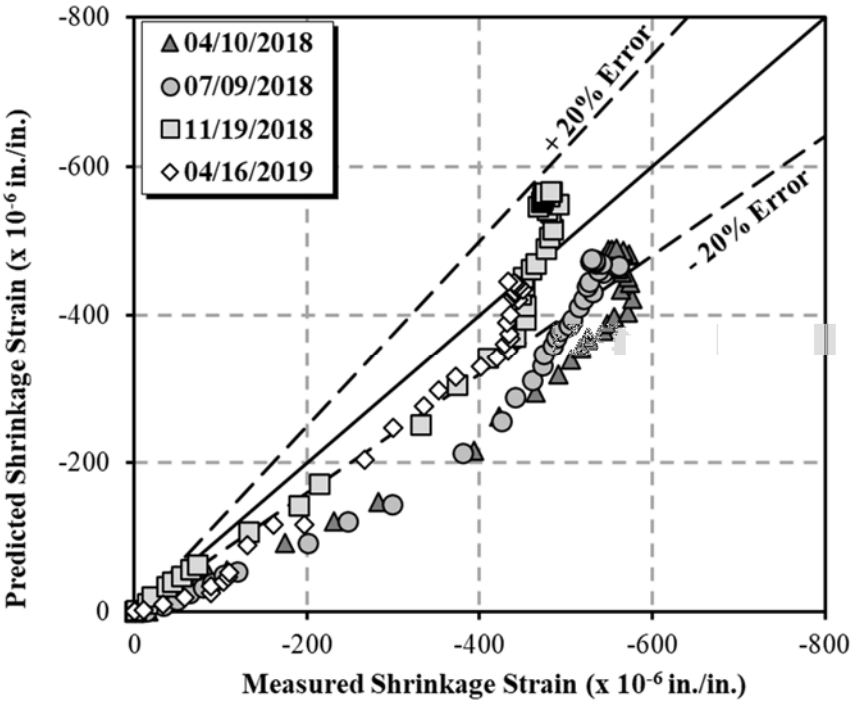

Figure 9-13: Measured versus predicted shrinkage using the original CEB MC 90-99 model

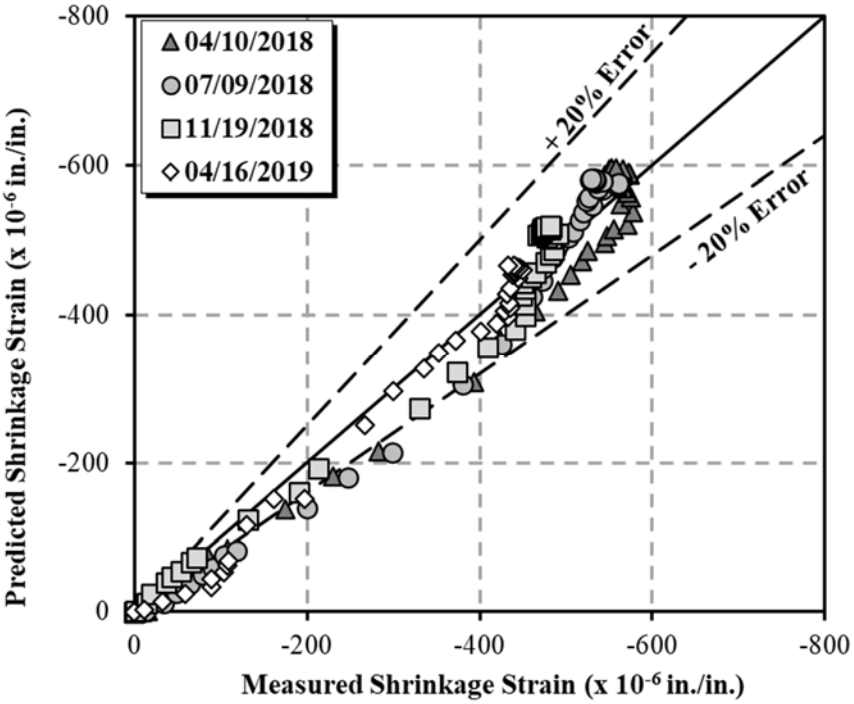

Figure 9-14: Measured versus predicted shrinkage using the calibrated CEB MC 90-99 model

9.3 CEB MC 1990 CALIBRATION

Because of its use in the *Bridge Designer II* software, the CEB MC 1990 prediction model was calibrated in the same way as the CEB MC 90-99 model to best predict creep and shrinkage for the concrete in the Birmingham I-59/I-20 segmental bridge. This section outlines the calibration of the CEB MC 1990 prediction model.

9.3.1 CEB MC 1990 Sensitivity Analysis

This section presents the results of the sensitivity analysis performed on various coefficients from the CEB MC 1990 creep and shrinkage prediction model.

9.3.1.1 CEB MC 1990 Compliance Sensitivity Analysis

As mentioned in Section 9.2, the empirical parameters in the CEB MC 1990 compliance prediction model that were chosen for calibration correspond to the same parameters in the CEB MC 90-99 model due to similarities between the two. The first change was made to the CEB MC 1990 28-day elastic modulus equation, by replacing E_{co} with μ_{90}. The original and modified 28-day elastic modulus is presented in Equations 9.28 and 9.29, respectively. In the original CEB MC 1990 model, an E_{co} value of 21,500 MPa is used. The effect of changing μ_{90} on the predicted 28-day elastic modulus is shown in Figure 9-15. Because the same elastic modulus values are predicted for the CEB MC 1990 and CEB MC 90-99 models when quartzite aggregates are used, the effect of changing μ_{90} is the same as for the CEB MC 90-99 model.

$$E_{ci} = E_{co}[f_{cm}/10]^{1/3} \qquad \text{Equation 9.28}$$

$$E_{ci} = \mu_{90}[f_{cm}/10]^{1/3} \qquad \text{Equation 9.29}$$

With,

μ_{90} = empirical parameter being calibrated (MPa).

Like the CEB MC 90-99 model, the second change to the CEB MC 1990 compliance prediction model was made by calibrating the empirical parameter, ρ_{90}, in the strength component of the notional creep coefficient, shown in Equations 9.30 and 9.31. As shown in Equation 9.30, the original CEB MC 1990 model uses a ρ_{90} value of 5.3. The effect of varying ρ_{90} on compliance predictions is shown in Figure 9-16.

$$\beta(f_{cm}) = \frac{5.3}{(f_{cm}/10)^{0.5}} \qquad \text{Equation 9.30}$$

$$\beta(f_{cm}) = \frac{\rho_{90}}{(f_{cm}/10)^{0.5}} \qquad \text{Equation 9.31}$$

With,

ρ_{90} = empirical parameter being calibrated (unitless).

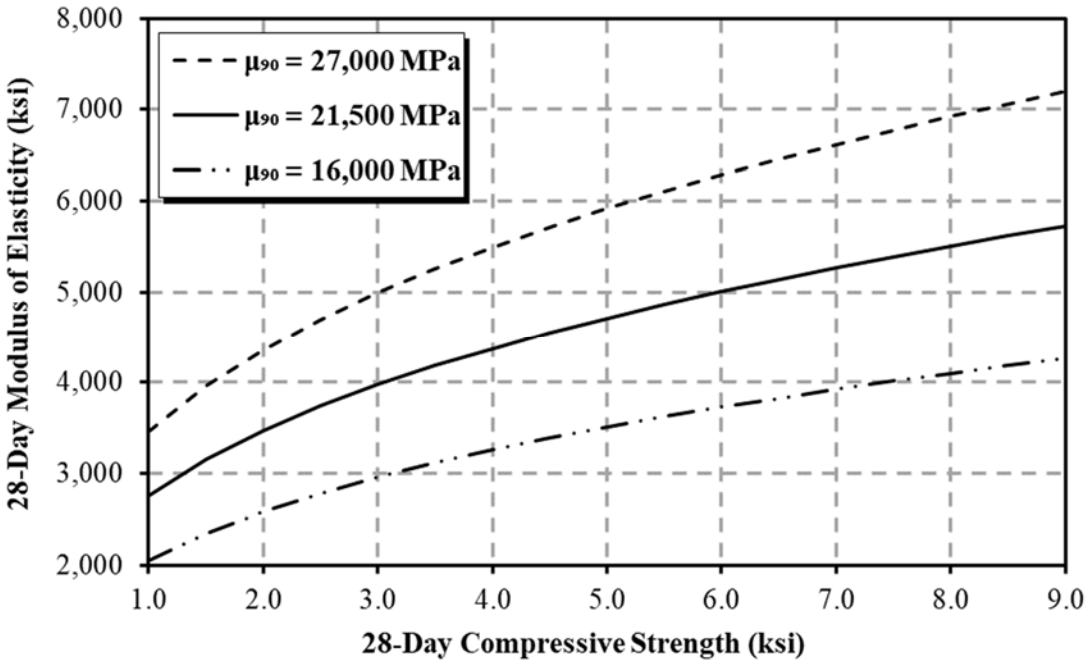

Figure 9-15: Sensitivity of CEB MC 1990 elastic modulus with varied μ_{90}

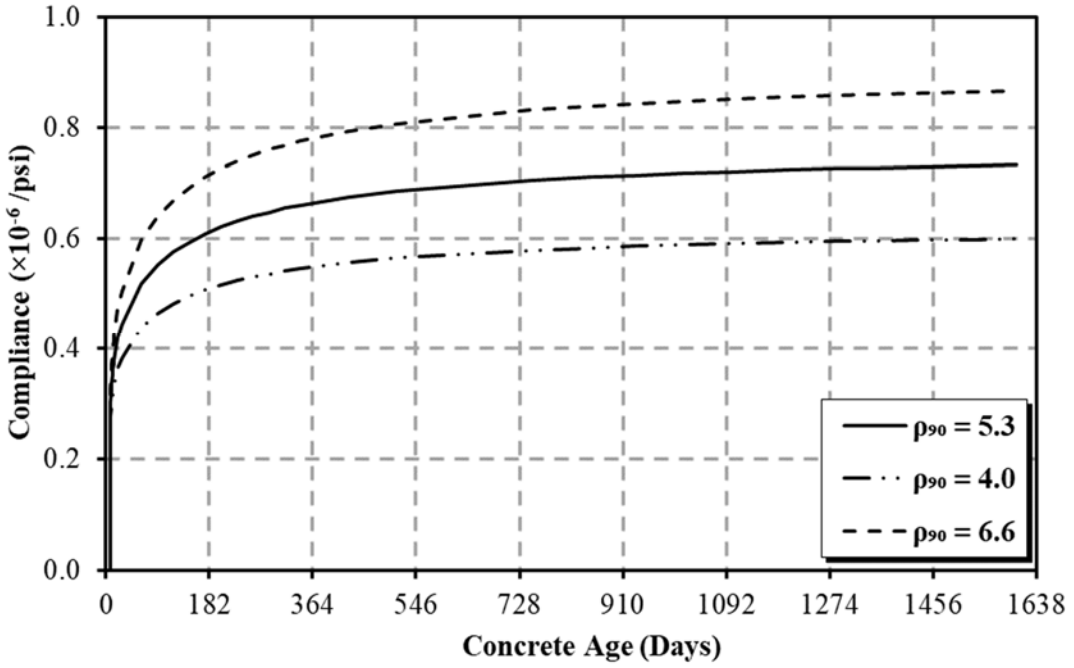

Figure 9-16: Sensitivity of CEB MC 1990 compliance with varied ρ_{90}

The final change to the CEB MC 1990 compliance prediction model was made by replacing the exponent in Equation 9.32 with the empirical parameter, λ_{90}, shown in Equation 9.33. As shown

in Equation 9.32, the original CEB MC 1990 model uses a λ_{90} value of 0.2. The effect of varying λ_{90} on compliance predictions is shown in Figure 9-17.

$$\beta(t_0) = \frac{1}{0.1 + (t_0)^{0.2}} \qquad \text{Equation 9.32}$$

$$\beta(t_0) = \frac{1}{0.1 + (t_0)^{\lambda_{90}}} \qquad \text{Equation 9.33}$$

With,

λ_{90} = empirical parameter being calibrated (unitless).

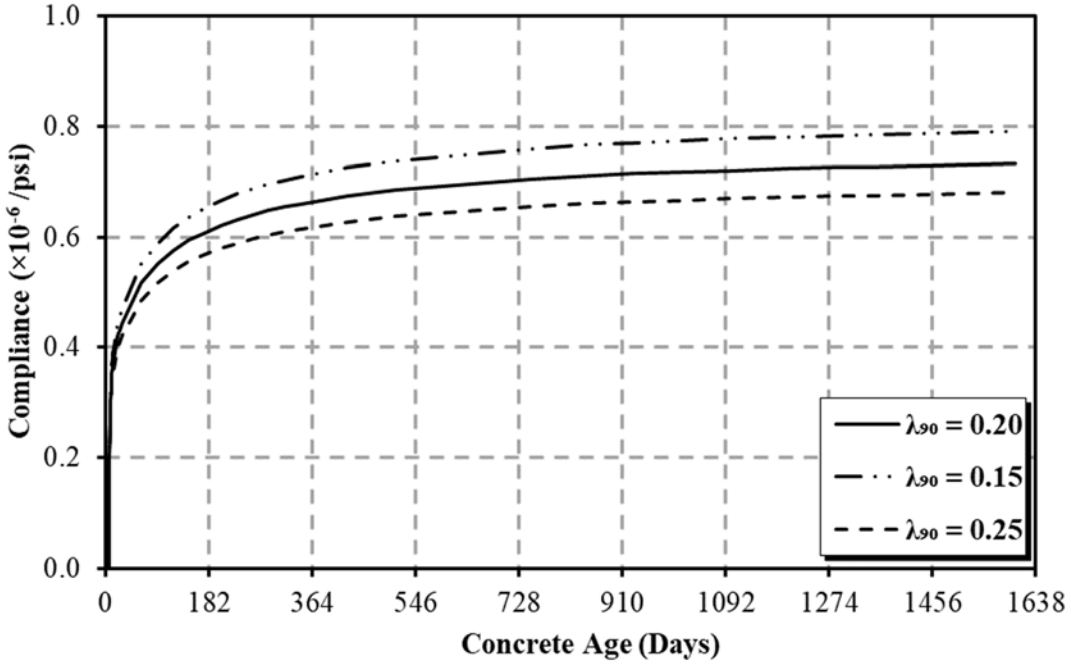

Figure 9-17: Sensitivity of CEB MC 1990 compliance with varied λ_{90}

9.3.1.2 CEB MC 1990 Shrinkage Sensitivity Analysis

The first two changes to the CEB MC 1990 shrinkage prediction model were made by adding coefficient, ψ, and replacing the exponent with the empirical parameter, η, in the time function of the shrinkage prediction, shown in Equations 9.34 and 9.35, respectively. The effects of varying ψ and η on shrinkage predictions are shown in Figure 9-18 and 9-19, respectively.

$$\beta_s(t - t_s) = \left[\frac{(t - t_s)}{350(h/100)^2 + (t - t_s)}\right]^{0.5} \qquad \text{Equation 9.34}$$

$$\beta_s(t - t_s) = \psi\left[\frac{(t - t_s)}{350(h/100)^2 + (t - t_s)}\right]^{\eta} \qquad \text{Equation 9.35}$$

With,

ψ = empirical parameter being calibrated (unitless) and

η = empirical parameter being calibrated (unitless).

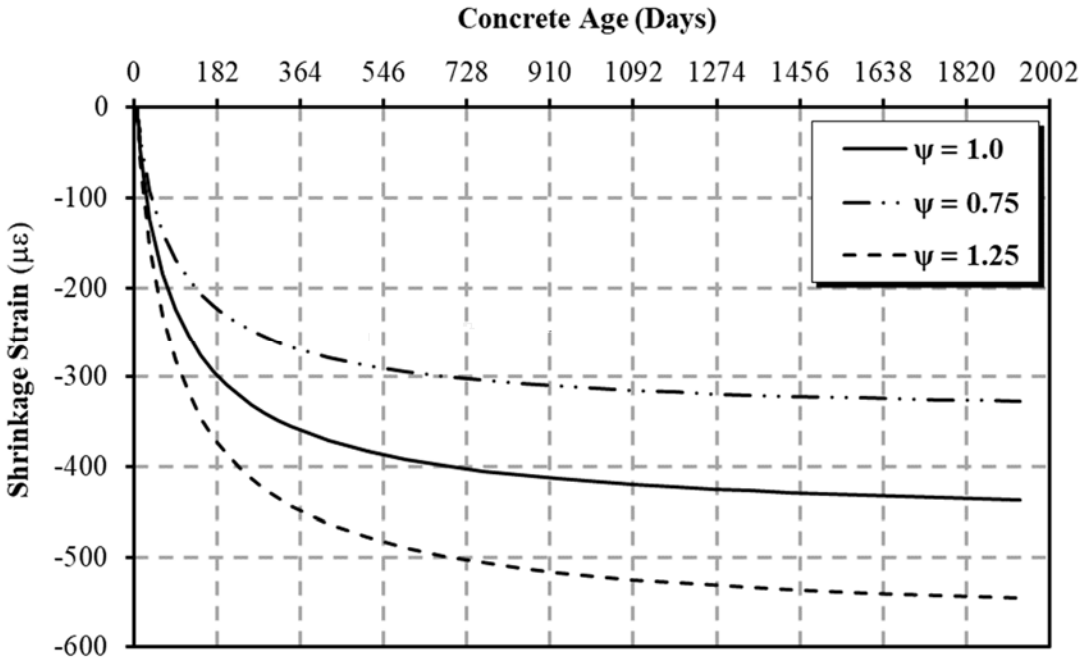

Figure 9-18: Sensitivity of CEB MC 1990 shrinkage with varied *ψ*

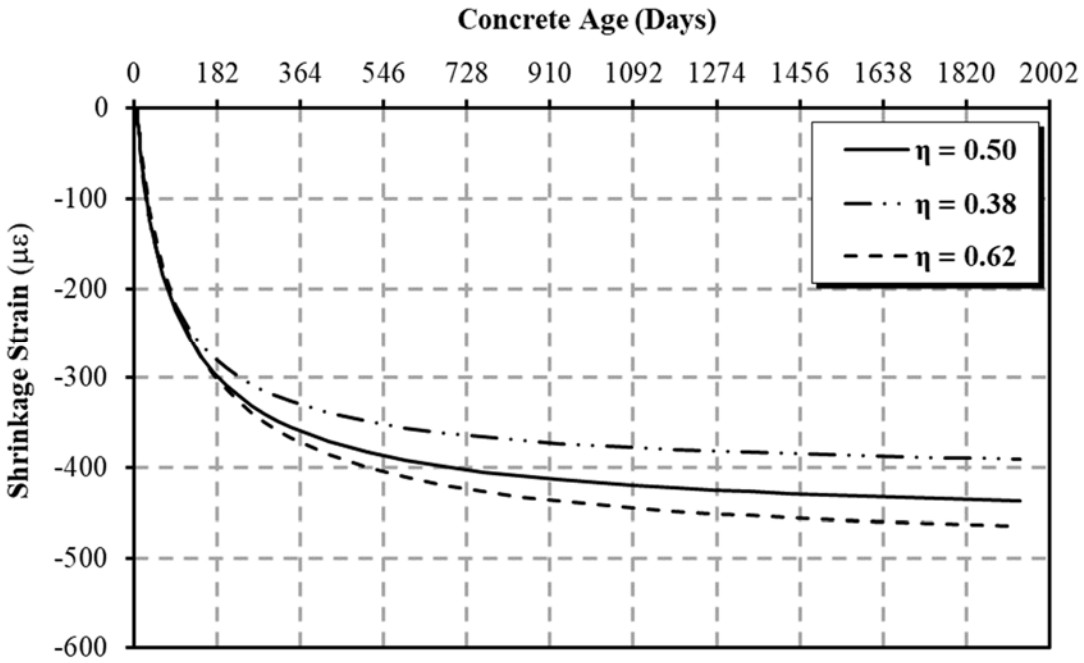

Figure 9-19: Sensitivity of CEB MC 1990 shrinkage with varied *η*

The final change to the CEB MC 1990 shrinkage prediction model was made by calibrating the empirical parameter, *v*, in the strength factor of the shrinkage prediction, shown in Equations 9.36 and 9.37. As shown in Equation 9.36, the original CEB MC 1990 model uses a *v* value of 160. The effect of varying *v* on shrinkage predictions is shown in Figure 9-20.

$$\varepsilon_s(f_{cm}) = \left[160 + 10\beta_{sc}(9 - f_{cm}/10)\right] \times 10^{-6} \quad \text{Equation 9.36}$$

$$\varepsilon_s(f_{cm}) = \left[v + 10\beta_{sc}(9 - f_{cm}/10)\right] \times 10^{-6} \quad \text{Equation 9.37}$$

With,

v = empirical parameter being calibrated (unitless).

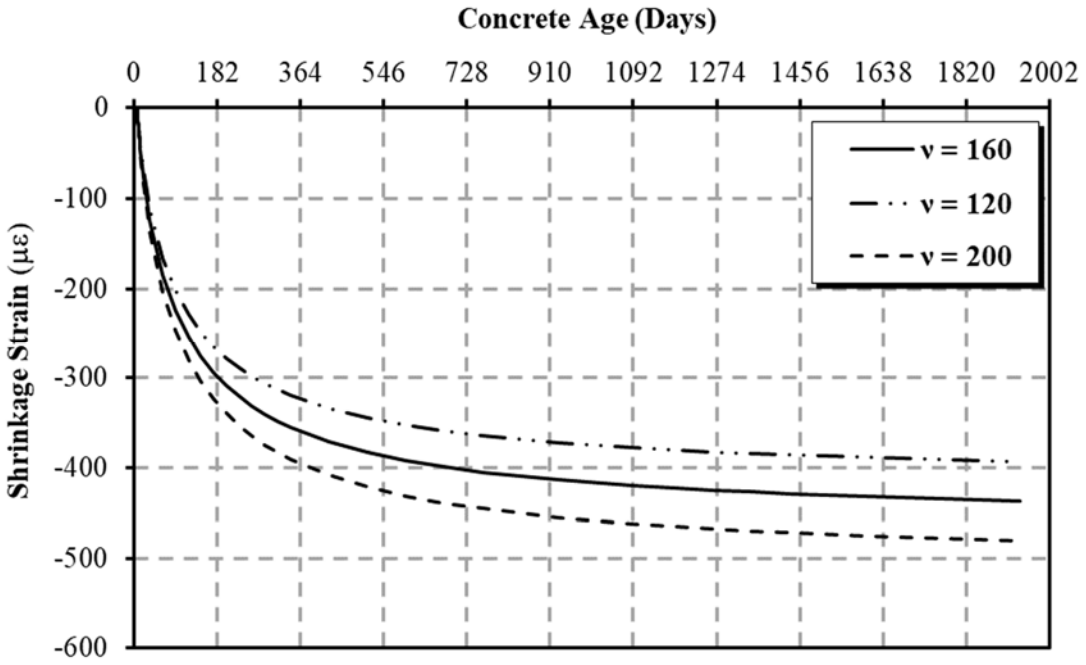

Figure 9-20: Sensitivity of CEB MC 1990 shrinkage with varied v

9.3.1.3 Number of Calibration Factors

As with the CEB MC 90-99 model, several other calibration factors were considered beyond the three selected for each of the CEB MC 1990 models. The graphs showing the change in S_j values with the number of calibration factors are shown in Figure 9-21 and Figure 9-22 for compliance and shrinkage, respectively. Like the CEB MC 90-99 model, the S_j for compliance appears to plateau after three calibration factors. This plateau is less clear for the shrinkage graph; however, because of the small changes between three and four calibration factors, and for consistency between models, three calibration factors were selected for both shrinkage and compliance.

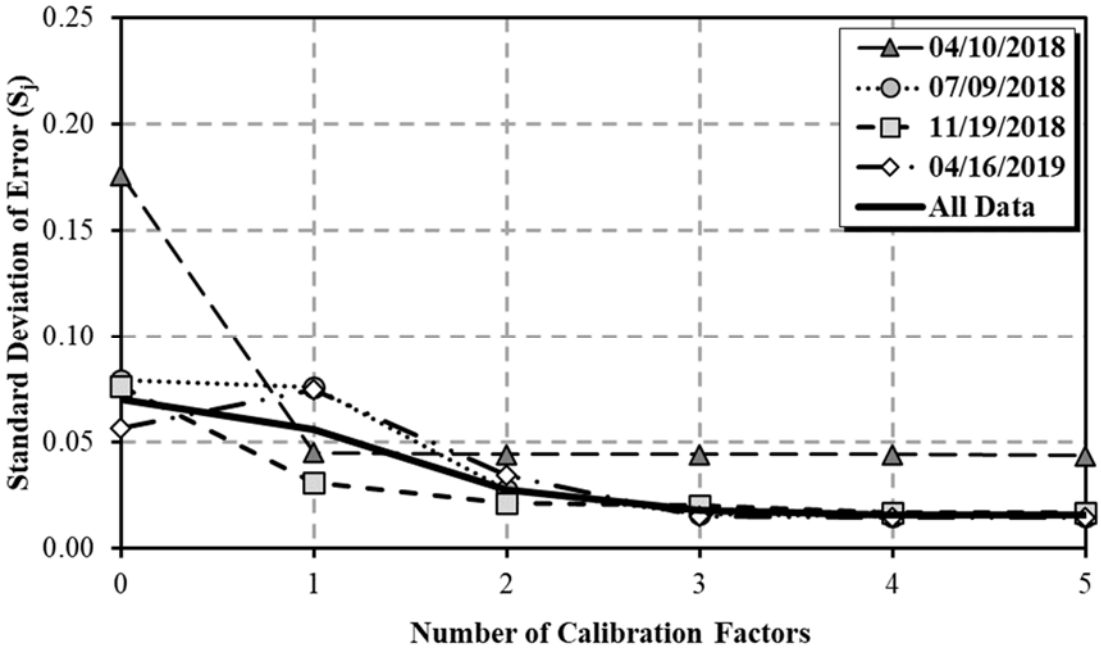

Figure 9-21: CEB MC 1990 S_j versus number of calibration factors for compliance

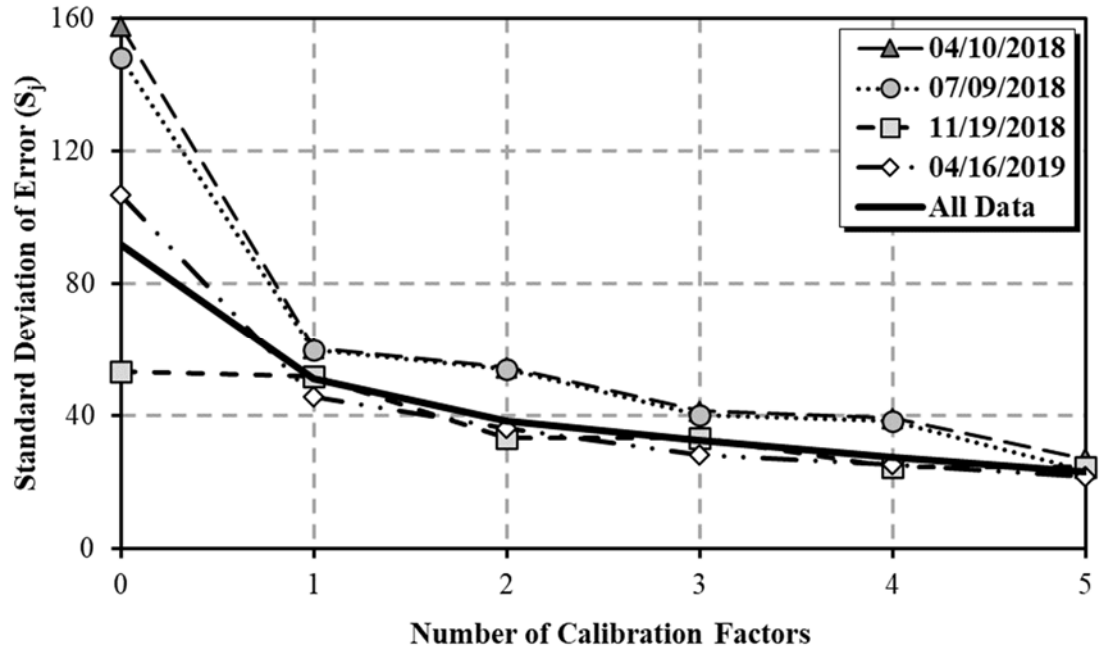

Figure 9-22: CEB MC 1990 S_j versus number of calibration factors for shrinkage

9.3.2 CEB MC 1990 Calibration Results

Each empirical parameter defined in the previous sections was calibrated to achieve the most accurate compliance and shrinkage predictions for the CEB MC 1990 model. The calibrated empirical parameters for this model are presented in Table 9-5.

Table 9-5: CEB MC 1990 original and calibrated empirical parameters

Empirical Parameter	Original CEB MC 1990 Model	04/10/2018	07/09/2018	11/19/2018	04/16/2019
μ_{90} (MPa)	21,500	16,500	17,000	18,000	20,500
ρ_{90} (unitless)	5.3	5.4	3.8	5.2	3.0
λ_{90} (unitless)	0.20	0.21	0.15	0.21	0.10
ψ (unitless)	1.0	1.5	1.5	1.3	1.5
η (unitless)	0.50	0.30	0.29	0.25	0.25
v (unitless)	160	240	240	190	240

9.3.2.1 Calibrated CEB MC 1990 Modulus of Elasticity

The calibrated CEB MC 1990 modulus of elasticity for each sampling date is presented in the 28-day modulus of elasticity given by Equations 9.38 through 9.41.

04/10/2018 Sampling Date:

$$E_{ci} = 16{,}500[f_{cm}/10]^{1/3} \qquad \text{Equation 9.38}$$

07/09/2018 Sampling Date:

$$E_{ci} = 17{,}000[f_{cm}/10]^{1/3} \qquad \text{Equation 9.39}$$

11/19/2018 Sampling Date:

$$E_{ci} = 18{,}000[f_{cm}/10]^{1/3} \qquad \text{Equation 9.40}$$

04/16/2019 Sampling Date:

$$E_{ci} = 20{,}500[f_{cm}/10]^{1/3} \qquad \text{Equation 9.41}$$

Because the CEB MC 1990 model predicts the same elastic modulus as the CEB MC 90-99 model for concretes with quartzite aggregate, the results of the elastic modulus calibration is the same for the two models, so the results for the CEB MC 1990 elastic modulus calibration are presented in Table 9-2 and Figure 9-10.

9.3.2.2 Calibrated CEB MC 1990 Compliance

The improvements made to the CEB MC 1990 compliance prediction model by changing ρ_{90} are presented in Equations 9.42 through 9.45, and the improvements made by changing λ_{90} are presented in Equations 9.46 through 9.49.

04/10/2018 Sampling Date:

$$\beta(f_{cm}) = \frac{5.4}{(f_{cm}/10)^{0.5}} \qquad \text{Equation 9.42}$$

07/09/2018 Sampling Date:

$$\beta(f_{cm}) = \frac{3.8}{(f_{cm}/10)^{0.5}} \qquad \text{Equation 9.43}$$

11/19/2018 Sampling Date:

$$\beta(f_{cm}) = \frac{5.2}{(f_{cm}/10)^{0.5}} \qquad \text{Equation 9.44}$$

04/16/2019 Sampling Date:

$$\beta(f_{cm}) = \frac{3.0}{(f_{cm}/10)^{0.5}} \qquad \text{Equation 9.45}$$

04/10/2018 Sampling Date:

$$\beta(t_0) = \frac{1}{0.1 + (t_0)^{0.21}} \qquad \text{Equation 9.46}$$

07/09/2018 Sampling Date:

$$\beta(t_0) = \frac{1}{0.1 + (t_0)^{0.15}} \qquad \text{Equation 9.47}$$

11/19/2018 Sampling Date:

$$\beta(t_0) = \frac{1}{0.1 + (t_0)^{0.21}} \qquad \text{Equation 9.48}$$

04/16/2019 Sampling Date:

$$\beta(t_0) = \frac{1}{0.1 + (t_0)^{0.10}} \qquad \text{Equation 9.49}$$

A comparison of the S_j values for the original CEB MC 1990 compliance prediction model and those predicted by the calibrated model is presented in Table 9-6. The calibrated model provides an improvement of over 70 percent for all sampling dates, with an average improvement of 74 percent. The comparisons between measured compliance values and those predicted by both the original and calibrated CEB MC 1990 models are shown in Figure 9-23 and Figure 9-24, respectively. After calibration, nearly all compliance predictions fall within the 20 percent error bands.

Table 9-6: Comparison of S_j values for compliance predictions for original and calibrated CEB MC 1990 model

Sampling Date	**Original CEB MC 1990 Model** S_j ($\times 10^{-6}$/psi)	**Calibrated CEB MC 1990 Model** S_j ($\times 10^{-6}$/psi)	**Reduction in S_j** (%)
04/10/2018	0.176	0.044	75%
07/09/2018	0.079	0.016	79%
11/19/2018	0.077	0.021	73%
04/16/2019	0.057	0.015	73%
All Data	**0.070**	**0.018**	**74%**

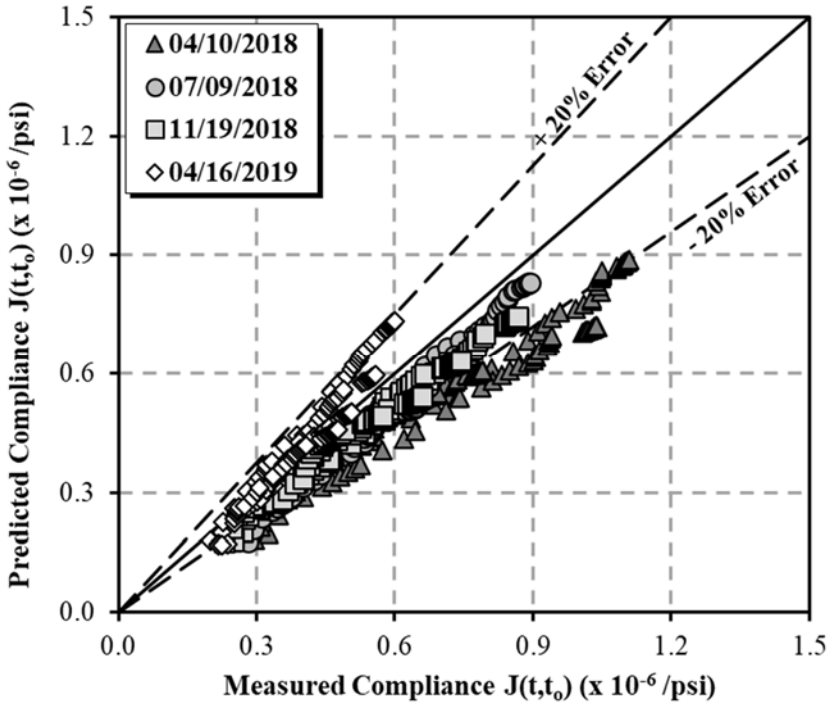

Figure 9-23: Measured versus predicted compliance using the original CEB MC 1990 model

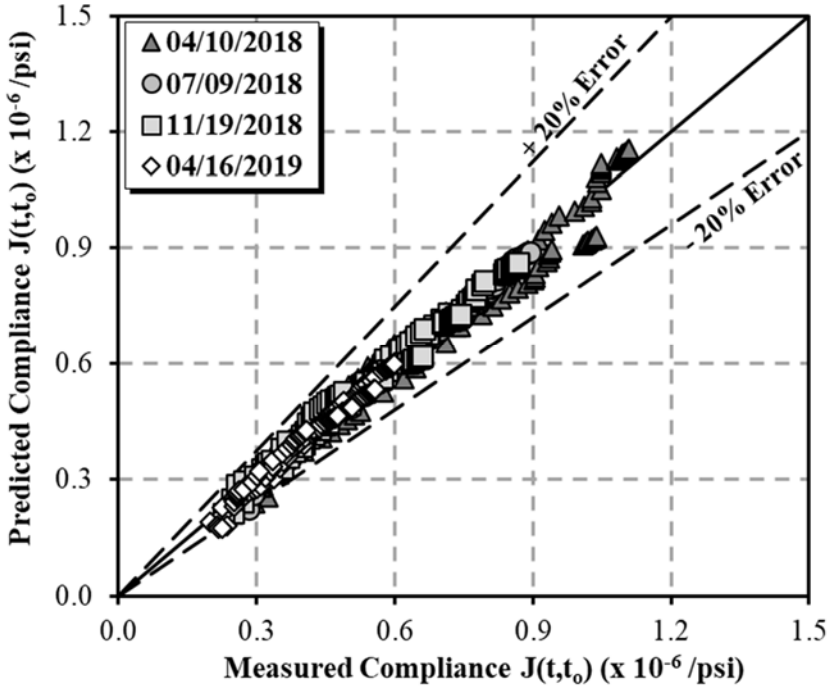

Figure 9-24: Measured versus predicted compliance using the calibrated CEB MC 1990 model

9.3.2.3 Calibrated CEB MC 1990 Shrinkage

The improvements made to the CEB MC 1990 shrinkage prediction model by changing ψ and η are presented in Equations 9.50 through 9.53, and the improvements made by changing v are presented in Equations 9.54 through 9.57.

04/10/2018 Sampling Date:

$$\beta_s(t-t_s) = 1.5\left[\frac{(t-t_s)}{350(h/100)^2 + (t-t_s)}\right]^{0.30} \quad \text{Equation 9.50}$$

07/09/2018 Sampling Date:

$$\beta_s(t-t_s) = 1.5\left[\frac{(t-t_s)}{350(h/100)^2 + (t-t_s)}\right]^{0.29} \quad \text{Equation 9.51}$$

11/19/2018 Sampling Date:

$$\beta_s(t-t_s) = 1.3\left[\frac{(t-t_s)}{350(h/100)^2 + (t-t_s)}\right]^{0.25} \quad \text{Equation 9.52}$$

04/16/2019 Sampling Date:

$$\beta_s(t-t_s) = 1.5\left[\frac{(t-t_s)}{350(h/100)^2 + (t-t_s)}\right]^{0.25} \quad \text{Equation 9.53}$$

04/10/2018 Sampling Date:

$$\varepsilon_s(f_{cm}) = \left[240 + 10\beta_{sc}(9 - f_{cm}/10)\right] \times 10^{-6} \quad \text{Equation 9.54}$$

07/09/2018 Sampling Date:

$$\varepsilon_s(f_{cm}) = \left[240 + 10\beta_{sc}(9 - f_{cm}/10)\right] \times 10^{-6} \quad \text{Equation 9.55}$$

11/19/2018 Sampling Date:

$$\varepsilon_s(f_{cm}) = \left[190 + 10\beta_{sc}(9 - f_{cm}/10)\right] \times 10^{-6} \quad \text{Equation 9.56}$$

04/16/2019 Sampling Date:

$$\varepsilon_s(f_{cm}) = \left[240 + 10\beta_{sc}(9 - f_{cm}/10)\right] \times 10^{-6} \quad \text{Equation 9.57}$$

A comparison of the S_j values for the original CEB MC 1990 shrinkage prediction model and those predicted by the calibrated model is presented in Table 9-7. The calibration provided an improvement of at least 36 percent for all sampling dates, with three of the four sampling dates improving over 70 percent, and an average improvement of 63 percent was obtained. The comparisons between measured shrinkage strains and those predicted by both the original and calibrated CEB MC 1990 models are shown in Figure 9-25 and Figure 9-26, respectively. After calibration, only a small number of shrinkage predictions fall outside the 20 percent error band.

Table 9-7: Comparison of S_j values for shrinkage predictions for original and calibrated CEB MC 1990 model

Sampling Date	**Original CEB MC 1990 Model** S_j (× 10^{-6} in./in.)	**Calibrated CEB MC 1990 Model** S_j (× 10^{-6} in./in.)	**Reduction in S_j** (%)
04/10/2018	154	41.8	73%
07/09/2018	145	40.3	72%
11/19/2018	52.5	33.7	36%
04/16/2019	104	28.7	72%
All Data	**89.7**	**33.0**	**63%**

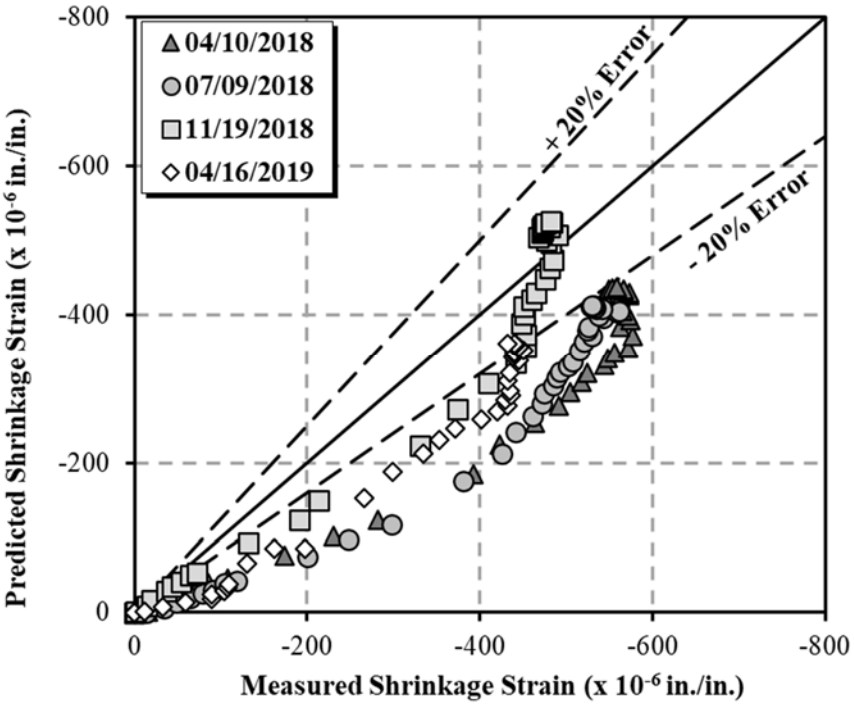

Figure 9-25: Measured versus predicted shrinkage using the original CEB MC 1990 model

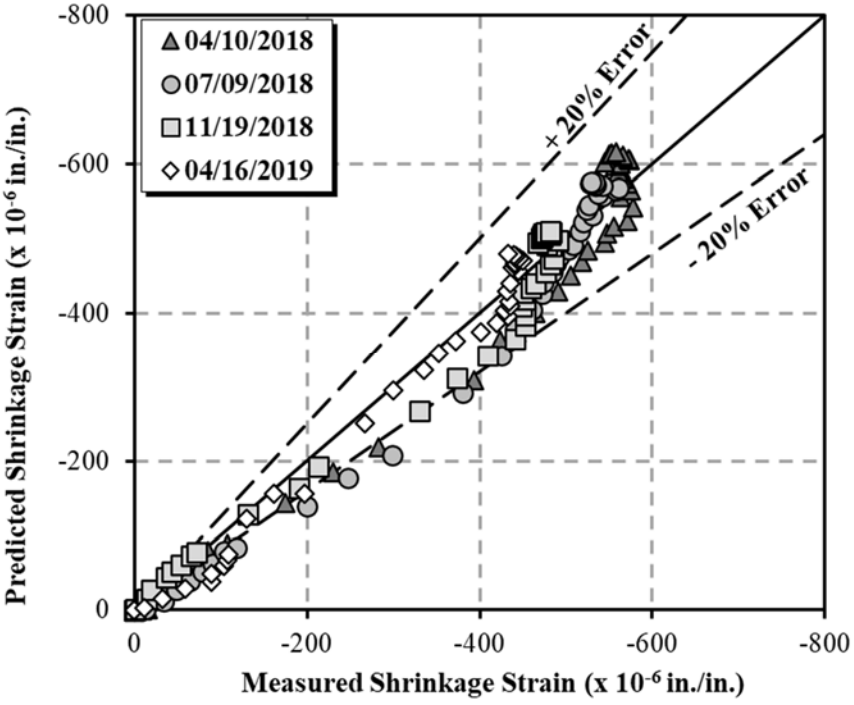

Figure 9-26: Measured versus predicted shrinkage using the calibrated CEB MC 1990 model

Chapter 10

SUMMARY, CONCLUSIONS, AND RECOMMENDATIONS

10.1 SUMMARY OF WORK PERFORMED

The primary objective of this research project is to accurately predict creep and shrinkage of the concrete used in the I-59/I-20 segmental bridge in Birmingham, Alabama. The first stage of experimental work was the collection of concrete specimens from the jobsite. The specimens were then tested for various concrete properties including compressive strength, modulus of elasticity, creep, and shrinkage. The data acquired through creep and shrinkage testing were used to determine the most accurate of several commonly used creep and shrinkage prediction models and to calibrate the most accurate model to improve predictions.

10.1.1 Specimen Collection

Concrete specimens were collected on four sampling dates throughout the duration of construction: April 10, 2018, July 9, 2018, November 19, 2018, and April 16, 2019. Altogether, 96 – 6 in.×12 in. cylinders and 24 – 3 in.×3 in.×11.25 in. rectangular prisms were collected, divided equally across the four sampling dates. Four ALDOT approved mixture proportions were used in the construction of the I-59/I-20 segmental bridge, and each sampling date represents one of the four mixture proportions. All specimens were cured alongside their corresponding bridge segments and were then transported to Auburn University for testing in the concrete materials laboratory.

10.1.2 Testing of Concrete Specimens

All fresh concrete testing was performed by technicians on the jobsite before the concrete was transported to the laboratory. Before creep and shrinkage testing began, concrete samples were tested for both compressive strength and modulus of elasticity in accordance with the requirements in AASHTO T22 (2017) and ASTM C469 (2014), respectively. Creep testing was performed in accordance with ASTM C512 (2015) by loading the specimens to 40 percent of their compressive strength at four loading ages: 7, 28, 91, and 182 days. Shrinkage testing of the concrete prisms was performed in accordance with AASHTO T160 (2017). The average total duration of creep and shrinkage data collection was approximately five years.

10.1.3 Modeling and Calibrating Compliance and Shrinkage

The following eight commonly used creep and shrinkage prediction models were used to model creep and shrinkage in the test specimens:

- AASHTO LRFD (2020),
- ACI 209 (2008),
- B3 (Bažant and Baweja 2000),
- B4 (Bažant 2015),
- CEB MC 1990 (CEB 1990),
- CEB MC 90-99 (CEB 1999),
- CEB MC 2010 (fib 2012), and
- GL 2000 (Gardner and Lockman 2001).

All eight prediction models use various components of the concrete's mixture proportions, fresh properties, hardened properties, and environmental properties to predict compliance and shrinkage. All measured data were compared to those predicted by each model, and a statistical analysis was performed to determine the model that most accurately predicts creep and shrinkage. The most accurate model was then calibrated to more accurately predict creep and shrinkage in the I-59/I-20 segmental bridge. Due to its use in the *Bridge Designer II* software, the CEB MC 1990 model was also calibrated.

10.2 CONCLUSIONS

Based on the testing performed in this research project, the following conclusions are made concerning the fresh and hardened properties of the concrete collected from the construction of the I-59/I-20 segmental bridge:

- All concrete mixtures studied in this research met the fresh property requirements specified by ALDOT.
- Both the compressive strength and the modulus of elasticity increased as the project continued, with the 04/10/2018 and the 04/16/2019 sampling dates exhibiting the lowest and highest values for both properties, respectively.
- The 04/10/2018 sampling date had the lowest compressive strength and experienced the highest drying shrinkage and compliance of the four sampling dates.
- The 04/16/2019 sampling date had the highest compressive strength and experienced the lowest drying shrinkage and compliance of the four sampling dates.
- In the shrinkage prisms, the 04/10/2018 and the 04/16/2019 sampling dates experienced the highest and lowest shrinkage, respectively, with similar magnitudes observed for the different curing regimes.

After compliance and shrinkage modeling was completed with the eight prediction models, the following conclusions can be made concerning the prediction models:

- The CEB MC 1990 and the CEB MC 90-99 prediction models most accurately predict creep in the concrete studied in this project.
- The B4 prediction model least accurately predicts compliance.
- The AASHTO LRFD and ACI 209 models most accurately predict shrinkage in the cylindrical specimens.
- The B3 and B4 models least accurately predict shrinkage in the cylindrical specimens.
- The CEB MC 90-99 model most accurately predicts both compliance and shrinkage, followed by the CEB MC 1990 model.
- Due to its relative accuracy, the CEB MC 90-99 model was calibrated along with the CEB MC 1990 model.
- Calibration provided significant improvements to the predictions of both the CEB MC 90-99 model and the CEB MC 1990 model.

10.3 RECOMMENDATIONS

The following recommendations concerning the use of compliance and shrinkage prediction models to predict compliance and shrinkage in the I-59/I-20 segmental bridge are offered:

- In the Birmingham I-59/I-20 segmental bridge, the calibrated CEB MC 90-99 model as defined in Section 9.2 should be used to predict compliance and shrinkage of the concrete sampled during this project.
- In cases where the CEB MC 1990 model is used in the *Bridge Designer II* software, the calibrated CEB MC 1990 model as defined in Section 9.3 may also be used for the I-59/I-20 segmental bridge.

REFERENCES

AASHTO. 2020. *AASHTO LRFD Bridge Design Specifications.* 9th ed. Washington D.C.: American Association of State Highway and Transportation Officials.

AASHTO T22. 2017. “Standard Test Method for Compressive Strength of Cylindrical Concrete Specimens.” Standard Specifications for Transportation Materials and Methods of Sampling and Testing. Washington D.C.: American Association of State Highway and Transportation Officials.

AASHTO T23. 2018. “Standard Method of Test for Making and Curing Concrete Test Specimens in the Field.” Standard Specifications for Transportation Materials and Methods of Sampling and Testing. Washington D.C: American Association of State Highway and Transportation Officials.

AASHTO T119. 2018. “Standard Method of Test for Slump of Hydraulic Cement Concrete.” Standard Specifications for Transportation Materials and Methods of Sampling and Testing. Washington D.C.: American Association of State Highway and Transportation Officials.

AASHTO T121. 2019. “Standard Method of Test for Density (Unit Weight), Yield, and Air Content (Gravimetric) of Concrete.” Standard Specifications for Transportation Materials and Methods of Sampling and Testing. Washington D.C.: American Association of State Highway and Transportation Officials.

AASHTO T160. 2017. “Standard Method of Test for Length Change of Hardened Hydraulic Cement Mortar and Concrete.” Standard Specifications for Transportation Materials and Methods of Sampling and Testing. Washington D.C: American Association of State Highway and Transportation Officials.

AASHTO T309. 2015. “Standard Method of Test for Temperature of Freshly Mixed Portland Cement Concrete.” Standard Specifications for Transportation Materials and Methods of Sampling and Testing. Washington D.C.: American Association of State Highway and Transportation Officials.

ACI Committee 209. 1992. *Prediction of Creep, Shrinkage, and Temperature Effects in Concrete Structures* (ACI 209R-92). Farmington Hills, MI: American Concrete Institute.

ACI Committee 209. 2008. *Guide for Modeling and Calculating Shrinkage and Creep in Hardened Concrete* (ACI 209.2R-08). Farmington Hills, MI: American Concrete Institute.

ALDOT 501. 2012. Structural Portland Cement Concrete. *Standard Specifications for Highway Construction*. Montgomery, AL. Alabama Department of Transportation.

Al-Manaseer, A., and Prado, A. 2015. Statistical Comparisons of Creep and Shrinkage Prediction Models Using RILEM and NU-ITI Databases. *ACI Materials Journal* 112, no. 1: 125–136 and 1–4.

Al-Omaishi, N. 2001. *Prestress Losses in High Strength Pretensioned Concrete Bridge Girders*. Ph.D. Dissertation. University of Nebraska-Lincoln.

ASBI. 2019. *Construction Practices Handbook for Concrete Segmental and Cable-Supported Bridges*. 3rd ed. Buda, TX.

ASTM C469. 2014. “Standard Test Method for Static Modulus of Elasticity and Poisson’s Ratio of Concrete in Compression.” West Conshohocken, Pennsylvania: ASTM International.

ASTM C512. 2015. “Standard Test Method for Creep of Concrete in Compression.” West Conshohocken, PA: ASTM International.

ASTM C1074. 2019. *Standard Practice for Estimating Concrete Strength by the Maturity Method*. ASTM International. West Coshohocken, PA.

Bayrak, O. 2022. “Details on Two Upcoming Changes to the AASHTO LRFD Bridge Design Specifications: Creep and Shrinkage Estimates and Regions Requiring Minimum Transverse Reinforcement.” *ASPIRE*, 44–45.

Bažant, Z. P. 2015. RILEM draft recommendation: TC-242-MDC multi-decade creep and shrinkage of concrete: Material model and structural analysis. *RILEM Technical Committee: Materials and Structures* 48: 753–770.

Bažant, Z. P., and Baweja, S. 2000. Creep and Shrinkage Prediction Model for Analysis and Design of Concrete Structures: Model B3. *Symposium Paper* 194: 1–84.

Bažant, Z. P., M. H. Hubler, and Q. Yu. 2011. “Pervasiveness of Excessive Segmental Bridge Deflections: Wake-Up Call for Creep.” *ACI Structural Journal* 108 (6): 766–774.

Branson, D. E., and M. L. Christiason. 1971. “Time Dependent Concrete Properties Related to Design-Strength and Elastic Properties, Creep, and Shrinkage.” *Symposium Paper* 27: 257–78.

Byard, B. E., A. K. Schindler, and R. W. Barnes. 2012. “Early-Age Autogenous Effects in Internally Cured Concrete and Mortar.” *ACI Symposium* 290: 1–18.

CEB. 1990. *CEB-FIP Model Code 1990*. Lausanne, Switzerland: Comité Euro-International du Béton.

CEB. 1999. Structural Concrete: Textbook on Behaviour, Design and Performance. Updated Knowledge of the CEB/FIP Model Code 1990. Vol. 1. Fib Bulletin 1. Lausanne, Switzerland: Federation Internationale du Beton.

Collins, M. P., and Mitchell, D. 1991. *Prestressed Concrete Structures*. Englewood Cliffs, NJ: Prentice Hall.

fib. 2012. *fib Model Code 2012: Final Draft*. Lausanne, Switzerland: Fédération Internationale du Béton.

Gabaldón, L. B. F., M. ASCE, J. F. R. Pérez, and J. K. Paredes. 2020. “Moment Redistribution in Segmental Cantilever Bridges: Simplified Approach.” *ASCE Technical Note* 25 (3).

Gardner, N. J., and Lockman, M. J. 2001. Design Provisions for Drying Shrinkage and Creep of Normal-Strength Concrete. *ACI Materials Journal* 98, no. 2: 159–167.

Goel, R., Kumar, R., and Paul, D. K. 2007. Comparative Study of Various Creep and Shrinkage Prediction Models for Concrete. *Journal of Materials in Civil Engineering* 19, no. 3: 249–260.

Greene, G. G., and Graybeal, B. A. 2013. *Lightweight Concrete: Mechanical Properties* (FHWA-HRT-13-062). Federal Highway Administration.

Hedegaard, B. D. 2020. "Multi-Decade, Multi-Scale Modeling of Aging Basic Creep of Concrete." *ACI Materials Journal* 117 (6): 17–27.

Holt, E. 2001. "Early Age Autogenous Shrinkage of Concrete." Seattle, WA: The University of Washington in Seattle.

Huo, X. S., Al-Omaishi, N., and Tadros, M. K. 2001. Creep, Shrinkage, and Modulus of Elasticity of High-Performance Concrete. *ACI Materials Journal*. 98, no. 6: 440–449.

Jensen, O. M., and P. F. Hansen. 1996. "Autogenous Deformation and Change of the Relative Humidity in Silica Fume-Modified Cement Paste." *ACI Materials Journal* 93 (6).

Kamatchi, P., K. B. Rao, B. Dhayalini, S. Saibabu, S. Parivallal, K. Ravisankar, and N. R. Iyer. 2014. "Long-Term Prestress Loss and Camber of Box-Girder Bridge." *ACI Structural Journal* 111 (6): 1297–1306.

Kavanaugh, B. 2008. *Creep Behavior of Self-Consolidating Concrete*. M.S. Thesis. Auburn, AL: Auburn University.

Keske, S. D. 2014. *Use of Self-Consolidating Concrete in Precast, Prestressed Girders*. Ph.D. Dissertation. Auburn, AL: Auburn University.

L'Hermite, R. G. 1960. "Volume Changes of Concrete." Fourth International Symposium on the Chemistry of Cement. Washington D.C.

Mante, D. M. 2016. *Improving Camber Predictions for Precast, Prestressed Concrete Bridge Girders*. Ph.D. Dissertation. Auburn, AL: Auburn University.

McCuen, R. H. 1985. *Statistical Methods for Engineers.* Lebanon, IN. Prentice Hall, Inc.:439.

Mehta, P. Kumar, and Paulo J. M. Monteiro. 2014. *Concrete: Microstructure, Properties, and Materials*. Fourth. McGraw Hill Education.

Neville, A. M. 2011. *Properties of Concrete*. 5th ed. Longman, England: Pearson.

Raphael, W., E. Zgheib, and A. Chateauneuf. 2018. "Experimental Investigations and Sensitivity Analysis to Explaing the Large Creep of Concrete Deformations in the Bridge of Cheviré." *Case Studies in Construction Materials* 9.

Rizkalla, S., Mirmiran, A., Zia, P., and Russell, H. 2007. *Application of the LRFD Bridge Design Specifications to High-Strength Structural Concrete: Flexure and Compression Provisions* (No. 595). Washington D.C.: National Cooperative Highway Research Program.

Schindler, A. K., Barnes, R. W., Kamgang, J. K., and Kavanaugh, B. 2017. Compliance of Self-Consolidating Concrete for Prestressed Applications. *ACI Materials Journal* 114, no. 2: 273–283.

Suksawang, N., Nassif, H., and Mohammed, A. 2005. Creep and Shrinkage of High-Performance/High-Strength Concrete. *ACI Special Publication* SP-228: 1397–1415.

Tadros, M. K., Al-Omaishi, N., Seguirant, S. J., and Gallt, J. G. 2003. *Prestress Losses in Pretensioned High-Strength Concrete Bridge Girders* (No. 496). Washington D. C.: National Cooperative Highway Research Program.

Wang, S., C. C. Fu, and F. ASCE. 2014. “Simplification of Creep and Shrinkage Analysis of Segmental Bridges.” *ASCE Technical Note* 20 (8): B6014001-1–5.

Ye, C., L. J. Butler, M. Z. E. B. Elshafie, and C. R. Middleton. 2020. “Evaluating Prestress Losses in a Prestressed Concrete Girder Railway Bridge Using Distributed and Discrete Fibre Optic Sensors.” *Construction and Building Materials* 247: 1–18.

Appendix A

RAW CREEP AND SHRINKAGE DATA

This appendix presents all raw data collected through creep and shrinkage testing throughout the duration of this research project. The following significant time intervals are denoted in the tables in this appendix: one day, one week, one month, one year, and each of the following years.

Table A-1 (Part 1): Raw data for 04/10/2018 samples loaded at 7 days

Sampling Date			04/10/2018	
Loading Age			7 Days	
Compressive Strength (psi)			5,100	
Modulus of Elasticity (ksi)			3,800	
Target Applied Load (kips)			57.7	
Concrete Age After Loading (Days)	**Total Strain (με)**	**Shrinkage Strain (με)**	**Strain due to Load (με)**	**Creep Strain (με)**
Pre-Load	0	0	0	0
Post-Load	-664	-8	-656	0
2-6 Hours	-752	-16	-736	-80
1	-925	-24	-901	-245
2	-1016	-36	-980	-325
3	-1078	-57	-1021	-365
4	-1126	-62	-1063	-407
5	-1170	-72	-1097	-442
6	-1218	-86	-1133	-477
7	-1265	-107	-1158	-502
14	-1497	-174	-1322	-667
21	-1652	-230	-1422	-766
28	-1787	-282	-1505	-849
56	-2080	-393	-1687	-1031
84	-2204	-423	-1780	-1125
112	-2311	-464	-1847	-1191
140	-2387	-491	-1897	-1241
168	-2432	-505	-1926	-1271
196	-2476	-518	-1958	-1303
224	-2517	-525	-1992	-1337
251	-2607	-544	-2062	-1407
280	-2650	-547	-2102	-1447
308	-2694	-556	-2138	-1483
336	-2708	-571	-2137	-1482
420	-2757	-577	-2179	-1524

Table A-1 (Part 2): Raw data for 04/10/2018 samples loaded at 7 days (continued)

Concrete Age After Loading (Days)	Total Strain (με)	Shrinkage Strain (με)	Strain due to Load (με)	Creep Strain (με)
504	-2729	-563	-2165	-1510
588	-2731	-575	-2156	-1500
672	-2752	-572	-2180	-1525
756	-2746	-565	-2181	-1525
840	-2741	-559	-2182	-1527
924	-2742	-560	-2181	-1526
1086	-2806	-556	-2250	-1594
1176	-2814	-563	-2251	-1596
1260	-2816	-544	-2272	-1616
1340	-2848	-573	-2274	-1619
1428	-2852	-573	-2279	-1623
1595	-2853	-566	-2287	-1631
1679	-2864	-566	-2297	-1642
1765	-2848	-550	-2298	-1642
1847	-2857	-553	-2304	-1648
1931	-2866	-559	-2308	-1652

Table A-2 (Part 1): Raw data for 04/10/2018 samples loaded at 28 days

Sampling Date			04/10/2018	
Loading Age			28 Days	
Compressive Strength (psi)			6,100	
Modulus of Elasticity (ksi)			4,050	
Target Applied Load (kips)			69.0	
Concrete Age After Loading (Days)	**Total Strain (με)**	**Shrinkage Strain (με)**	**Strain due to Load (με)**	**Creep Strain (με)**
Pre-Load	0	0	0	0
Post-Load	-778	0	-778	0
2-6 Hours	-839	-9	-830	-52
1	-978	-16	-962	-183
2	-1076	-18	-1058	-279
3	-1125	-16	-1109	-330
4	-1187	-33	-1154	-376
5	-1235	-45	-1191	-412
6	-1277	-52	-1226	-447
7	-1320	-64	-1256	-477
14	-1475	-103	-1373	-594
21	-1602	-120	-1482	-703
28	-1686	-144	-1542	-764
56	-1891	-193	-1698	-919
84	-2054	-281	-1773	-994
112	-2196	-310	-1886	-1107
140	-2260	-314	-1945	-1167
168	-2303	-313	-1990	-1211
196	-2345	-316	-2029	-1251
224	-2417	-341	-2076	-1297
252	-2464	-337	-2127	-1348
280	-2500	-346	-2154	-1376
308	-2527	-361	-2165	-1387
336	-2537	-373	-2164	-1385
420	-2552	-367	-2185	-1406

Table A-2 (Part 2): Raw data for 04/10/2018 samples loaded at 28 days (continued)

Concrete Age After Loading (Days)	Total Strain (με)	Shrinkage Strain(με)	Strain due to Load (με)	Creep Strain (με)
504	-2595	-370	-2225	-1446
588	-2601	-365	-2236	-1457
672	-2606	-377	-2229	-1451
756	-2613	-369	-2245	-1466
847	-2630	-381	-2249	-1471
1092	-2739	-327	-2412	-1633
1182	-2763	-340	-2422	-1644
1260	-2753	-325	-2429	-1650
1345	-2809	-370	-2439	-1661
1427	-2809	-355	-2454	-1676
1597	-2799	-333	-2466	-1688
1679	-2794	-325	-2469	-1690
1761	-2800	-328	-2472	-1694
1848	-2811	-327	-2484	-1706
1931	-2811	-332	-2480	-1701

Table A-3 (Part 1): Raw data for 04/10/2018 samples loaded at 91 days

Sampling Date			04/10/2018	
Loading Age			91 Days	
Compressive Strength (psi)			6,000	
Modulus of Elasticity (ksi)			3,850	
Target Applied Load (kips)			67.9	
Concrete Age After Loading (Days)	**Total Strain (με)**	**Shrinkage Strain (με)**	**Strain due to Load (με)**	**Creep Strain (με)**
Pre-Load	0	0	0	0
Post-Load	-714	0	-714	0
2-6 Hours	-756	1	-758	-44
1	-836	-13	-823	-109
2	-885	-18	-868	-154
3	-913	-18	-895	-181
4	-940	-22	-918	-204
5	-960	-23	-936	-223
6	-976	-34	-942	-228
7	-993	-34	-959	-245
14	-1069	-62	-1007	-293
21	-1167	-74	-1093	-379
28	-1224	-82	-1143	-429
56	-1370	-104	-1266	-552
84	-1447	-96	-1351	-638
112	-1506	-96	-1410	-697
140	-1564	-100	-1463	-750
167	-1622	-120	-1502	-789
196	-1665	-123	-1542	-829
224	-1711	-132	-1579	-866
252	-1739	-147	-1592	-879
281	-1774	-159	-1615	-901
308	-1791	-152	-1638	-925
336	-1814	-153	-1661	-947
420	-1826	-155	-1672	-958

Table A-3 (Part 2): Raw data for 04/10/2018 samples loaded at 91 days (continued)

Concrete Age After Loading (Days)	Total Strain (με)	Shrinkage Strain (με)	Strain due to Load (με)	Creep Strain (με)
504	-1868	-150	-1718	-1004
588	-1877	-147	-1730	-1017
672	-1915	-141	-1774	-1060
756	-1921	-135	-1787	-1073
1000	-1976	-136	-1841	-1127
1092	-1984	-144	-1839	-1126
1176	-1984	-120	-1864	-1150
1256	-2027	-149	-1878	-1165
1344	-2036	-148	-1888	-1174
1511	-2047	-142	-1905	-1192
1595	-2052	-142	-1910	-1196
1681	-2042	-125	-1917	-1204
1763	-2052	-129	-1924	-1210
1847	-2052	-134	-1918	-1205

Table A-4 (Part 1): Raw data for 04/10/2018 samples loaded at 182 days

Sampling Date			04/10/2018	
Loading Age			182 Days	
Compressive Strength (psi)			6,400	
Modulus of Elasticity (ksi)			4,150	
Target Applied Load (kips)			72.4	
Concrete Age After Loading (Days)	**Total Strain (με)**	**Shrinkage Strain (με)**	**Strain due to Load (με)**	**Creep Strain (με)**
Pre-Load	0	0	0	0
Post-Load	-744	0	-743	0
2-6 Hours	-777	1	-778	-35
1	-823	-2	-821	-78
2	-855	2	-857	-114
3	-894	-4	-890	-147
4	-943	-17	-926	-182
5	-956	-18	-938	-195
6	-966	-18	-948	-205
7	-982	-15	-967	-223
14	-1031	-14	-1017	-274
21	-1070	-14	-1056	-313
28	-1097	-18	-1078	-335
56	-1210	-38	-1172	-429
83	-1296	-40	-1256	-513
112	-1382	-41	-1341	-598
140	-1418	-54	-1364	-621
168	-1422	-64	-1358	-614
196	-1464	-66	-1398	-655
224	-1505	-70	-1434	-691
252	-1529	-71	-1459	-715
280	-1535	-66	-1468	-725
308	-1543	-72	-1471	-728
336	-1547	-66	-1481	-738
420	-1568	-66	-1501	-758

Table A-4 (Part 2): Raw data for 04/10/2018 samples loaded at 182 days (continued)

Concrete Age After Loading (Days)	Total Strain (με)	Shrinkage Strain (με)	Strain due to Load (με)	Creep Strain (με)
504	-1619	-62	-1557	-813
588	-1630	-62	-1567	-824
672	-1634	-58	-1576	-833
911	-1706	-50	-1656	-913
1008	-1723	-62	-1661	-918
1098	-1712	-41	-1671	-928
1191	-1791	-90	-1701	-958
1259	-1783	-68	-1715	-971
1428	-1776	-61	-1716	-972
1511	-1784	-49	-1735	-992
1596	-1780	-43	-1737	-994
1679	-1789	-53	-1736	-993
1763	-1792	-50	-1741	-998

Table A-5 (Part 1): Raw data for 07/09/2018 samples loaded at 7 days

Sampling Date			07/09/2018	
Loading Age			7 Days	
Compressive Strength (psi)			5,600	
Modulus of Elasticity (ksi)			4,250	
Target Applied Load (kips)			63.3	
Concrete Age After Loading (Days)	**Total Strain (με)**	**Shrinkage Strain (με)**	**Strain due to Load (με)**	**Creep Strain (με)**
Pre-Load	0	0	0	0
Post-Load	-661	-8	-653	0
2-6 Hours	-716	-13	-703	-51
1	-845	-34	-811	-158
2	-915	-49	-866	-214
3	-972	-64	-908	-255
4	-1027	-79	-947	-294
5	-1063	-91	-972	-319
6	-1123	-103	-1019	-367
7	-1150	-119	-1031	-378
14	-1373	-200	-1173	-520
21	-1493	-247	-1246	-593
28	-1598	-298	-1300	-647
56	-1826	-380	-1445	-793
84	-1945	-425	-1521	-868
112	-2013	-441	-1572	-919
140	-2090	-461	-1629	-976
168	-2165	-472	-1693	-1040
196	-2232	-474	-1758	-1105
224	-2272	-485	-1788	-1135
252	-2305	-488	-1817	-1164
280	-2335	-492	-1842	-1190
308	-2357	-502	-1855	-1202
336	-2373	-507	-1865	-1213
420	-2393	-515	-1878	-1225

Table A-5 (Part 2): Raw data for 07/09/2018 samples loaded at 7 days (continued)

Concrete Age After Loading (Days)	Total Strain (με)	Shrinkage Strain (με)	Strain due to Load (με)	Creep Strain (με)
504	-2418	-520	-1898	-1245
588	-2446	-530	-1916	-1263
672	-2455	-524	-1931	-1278
756	-2458	-526	-1932	-1279
996	-2512	-556	-1956	-1303
1092	-2506	-537	-1969	-1316
1250	-2555	-558	-1996	-1344
1344	-2569	-561	-2008	-1356
1509	-2554	-542	-2012	-1360
1596	-2567	-534	-2033	-1380
1681	-2562	-528	-2034	-1381
1764	-2565	-533	-2032	-1379
1848	-2573	-529	-2043	-1391

Table A-6 (Part 1): Raw data for 07/09/2018 samples loaded at 28 days

Sampling Date			07/09/2018	
Loading Age			28 Days	
Compressive Strength (psi)			6,700	
Modulus of Elasticity (ksi)			4,250	
Target Applied Load (kips)			75.8	
Concrete Age After Loading (Days)	**Total Strain (με)**	**Shrinkage Strain (με)**	**Strain due to Load (με)**	**Creep Strain (με)**
Pre-Load	0	0	0	0
Post-Load	-749	-3	-746	0
2-6 Hours	-810	-6	-804	-57
1	-930	-15	-916	-169
2	-994	-20	-974	-228
3	-1045	-25	-1020	-274
4	-1078	-27	-1051	-305
5	-1111	-33	-1078	-332
6	-1140	-39	-1101	-355
7	-1162	-54	-1108	-362
14	-1290	-88	-1202	-456
21	-1398	-111	-1287	-541
28	-1469	-124	-1345	-599
56	-1612	-149	-1463	-716
84	-1733	-194	-1539	-793
112	-1829	-217	-1612	-866
140	-1884	-218	-1665	-919
168	-1974	-230	-1744	-998
196	-2017	-240	-1777	-1030
224	-2065	-244	-1821	-1075
252	-2113	-248	-1865	-1119
280	-2133	-258	-1875	-1129
308	-2158	-263	-1895	-1149
336	-2175	-269	-1907	-1160
420	-2210	-276	-1934	-1188

Table A-6 (Part 2): Raw data for 07/09/2018 samples loaded at 28 days (continued)

Concrete Age After Loading (Days)	Total Strain (με)	Shrinkage Strain (με)	Strain due to Load (με)	Creep Strain (με)
504	-2238	-276	-1962	-1216
588	-2267	-280	-1988	-1241
672	-2276	-283	-1993	-1246
756	-2279	-286	-1993	-1247
1008	-2354	-296	-2058	-1312
1092	-2370	-303	-2067	-1321
1176	-2365	-278	-2087	-1341
1262	-2430	-332	-2097	-1351
1345	-2429	-324	-2105	-1359
1514	-2410	-290	-2120	-1374
1592	-2428	-292	-2136	-1389
1680	-2410	-283	-2126	-1380
1764	-2411	-284	-2127	-1381
1848	-2414	-284	-2130	-1384

Table A-7 (Part 1): Raw data for 07/09/2018 samples loaded at 91 days

Sampling Date			07/09/2018	
Loading Age			91 Days	
Compressive Strength (psi)			7,100	
Modulus of Elasticity (ksi)			4,200	
Target Applied Load (kips)			80.3	
Concrete Age After Loading (Days)	**Total Strain (με)**	**Shrinkage Strain (με)**	**Strain due to Load (με)**	**Creep Strain (με)**
Pre-Load	0	0	0	0
Post-Load	-784	0	-784	0
2-6 Hours	-854	-1	-853	-69
1	-920	-2	-918	-134
2	-931	-1	-930	-146
3	-967	-2	-965	-181
4	-989	-7	-982	-199
5	-1035	-12	-1022	-238
6	-1049	-13	-1036	-252
7	-1053	-13	-1040	-256
14	-1116	-11	-1105	-322
21	-1176	-13	-1163	-379
28	-1213	-16	-1197	-413
56	-1359	-36	-1323	-539
84	-1442	-47	-1395	-611
112	-1543	-49	-1494	-710
140	-1603	-60	-1543	-759
168	-1624	-63	-1561	-777
196	-1695	-67	-1627	-844
224	-1723	-78	-1645	-861
252	-1745	-82	-1662	-879
280	-1766	-88	-1677	-893
308	-1780	-93	-1687	-903
336	-1794	-91	-1703	-919
420	-1827	-95	-1732	-948

Table A-7 (Part 2): Raw data for 07/09/2018 samples loaded at 91 days (continued)

Concrete Age After Loading (Days)	Total Strain (με)	Shrinkage Strain (με)	Strain due to Load (με)	Creep Strain (με)
504	-1860	-105	-1755	-971
588	-1873	-99	-1774	-990
672	-1883	-101	-1782	-998
919	-1935	-132	-1803	-1019
1008	-1966	-112	-1854	-1070
1166	-2014	-133	-1880	-1097
1260	-2032	-136	-1895	-1111
1425	-2032	-117	-1915	-1131
1512	-2037	-109	-1928	-1144
1597	-2028	-103	-1925	-1142
1680	-2037	-108	-1929	-1145
1764	-2037	-104	-1933	-1149

Table A-8 (Part 1): Raw data for 07/09/2018 samples loaded at 182 days

Sampling Date			07/09/2018	
Loading Age			182 Days	
Compressive Strength (psi)			7,100	
Modulus of Elasticity (ksi)			4,300	
Target Applied Load (kips)			80.3	
Concrete Age After Loading (Days)	**Total Strain (με)**	**Shrinkage Strain (με)**	**Strain due to Load (με)**	**Creep Strain (με)**
Pre-Load	0	0	0	0
Post-Load	-804	0	-804	0
2-6 Hours	-835	0	-835	-31
1	-889	0	-889	-85
2	-949	-1	-948	-144
3	-977	-2	-975	-171
4	-1019	-2	-1017	-213
5	-1025	-4	-1021	-217
6	-1052	-4	-1048	-244
7	-1074	-4	-1070	-266
14	-1145	-6	-1139	-335
21	-1220	-10	-1210	-406
28	-1268	-14	-1254	-450
56	-1331	-18	-1313	-509
84	-1463	-24	-1438	-635
112	-1487	-28	-1459	-655
140	-1557	-33	-1524	-720
168	-1558	-36	-1522	-718
196	-1586	-39	-1547	-744
223	-1588	-40	-1547	-744
252	-1604	-41	-1563	-759
280	-1611	-41	-1570	-767
308	-1610	-44	-1566	-762
336	-1622	-45	-1576	-772
420	-1634	-52	-1582	-778

Table A-8 (Part 2): Raw data for 07/09/2018 samples loaded at 182 days (continued)

Concrete Age After Loading (Days)	Total Strain (με)	Shrinkage Strain (με)	Strain due to Load (με)	Creep Strain (με)
504	-1643	-49	-1594	-790
588	-1660	-52	-1608	-804
828	-1808	-82	-1726	-922
924	-1825	-66	-1759	-955
1008	-1822	-53	-1769	-965
1101	-1897	-94	-1803	-999
1176	-1906	-98	-1808	-1004
1344	-1888	-55	-1833	-1029
1431	-1895	-58	-1837	-1033
1512	-1899	-48	-1850	-1047
1596	-1911	-50	-1861	-1057
1680	-1912	-45	-1867	-1063

Table A-9 (Part 1): Raw data for 11/19/2018 samples loaded at 7 days

Sampling Date			11/19/2018	
Loading Age			7 Days	
Compressive Strength (psi)			6,400	
Modulus of Elasticity (ksi)			4,400	
Target Applied Load (kips)			72.4	
Concrete Age After Loading (Days)	**Total Strain (με)**	**Shrinkage Strain (με)**	**Strain due to Load (με)**	**Creep Strain (με)**
Pre-Load	0	0	0	0
Post-Load	-703	0	-703	0
2-6 Hours	-799	-1	-798	-95
1	-951	-15	-936	-233
2	-1027	-20	-1008	-305
3	-1113	-37	-1077	-374
4	-1146	-44	-1103	-400
5	-1193	-54	-1139	-436
6	-1235	-65	-1169	-467
7	-1261	-72	-1189	-486
14	-1445	-132	-1313	-610
21	-1579	-191	-1388	-685
28	-1640	-214	-1426	-723
56	-1896	-331	-1565	-862
84	-2038	-374	-1664	-961
112	-2162	-410	-1752	-1049
140	-2228	-441	-1787	-1084
168	-2282	-453	-1829	-1126
196	-2323	-453	-1870	-1167
224	-2392	-448	-1944	-1241
252	-2423	-452	-1971	-1268
280	-2432	-450	-1982	-1279
308	-2464	-460	-2005	-1302
336	-2484	-465	-2020	-1317
420	-2503	-476	-2027	-1324

Table A-9 (Part 2): Raw data for 11/19/2018 samples loaded at 7 days (continued)

Concrete Age After Loading (Days)	Total Strain (με)	Shrinkage Strain (με)	Strain due to Load (με)	Creep Strain (με)
504	-2538	-481	-2057	-1354
588	-2557	-485	-2072	-1369
870	-2662	-482	-2179	-1476
924	-2664	-477	-2186	-1483
1010	-2658	-467	-2190	-1488
1089	-2690	-490	-2200	-1497
1176	-2693	-472	-2221	-1519
1260	-2709	-473	-2236	-1533
1345	-2713	-472	-2241	-1538
1430	-2732	-481	-2251	-1548
1513	-2735	-473	-2262	-1559
1596	-2733	-476	-2257	-1555
1680	-2743	-483	-2260	-1557
1765	-2743	-482	-2261	-1558

Table A-10 (Part 1): Raw data for 11/19/2018 samples loaded at 28 days

Sampling Date			11/19/2018	
Loading Age			28 Days	
Compressive Strength (psi)			7,200	
Modulus of Elasticity (ksi)			4,600	
Target Applied Load (kips)			81.4	
Concrete Age After Loading (Days)	**Total Strain (με)**	**Shrinkage Strain (με)**	**Strain due to Load (με)**	**Creep Strain (με)**
Pre-Load	0	0	0	0
Post-Load	-730	0	-730	0
2-6 Hours	-798	-1	-797	-62
1	-918	-1	-916	-181
2	-995	-4	-992	-256
3	-1026	-5	-1021	-285
4	-1057	-12	-1045	-309
5	-1066	-15	-1051	-316
6	-1107	-22	-1085	-350
7	-1197	-23	-1174	-439
14	-1249	-37	-1213	-477
21	-1289	-57	-1233	-497
28	-1414	-140	-1274	-538
56	-1676	-183	-1493	-757
84	-1800	-219	-1581	-846
112	-1905	-240	-1664	-929
140	-1929	-253	-1676	-940
168	-1943	-256	-1687	-952
196	-1985	-257	-1728	-992
224	-2041	-261	-1780	-1044
252	-2046	-259	-1787	-1052
280	-2097	-269	-1828	-1093
308	-2120	-275	-1845	-1110
336	-2131	-279	-1852	-1116
420	-2172	-286	-1886	-1150

Table A-10 (Part 2): Raw data for 11/19/2018 samples loaded at 28 days (continued)

Concrete Age After Loading (Days)	Total Strain (με)	Shrinkage Strain (με)	Strain due to Load (με)	Creep Strain (με)
504	-2212	-291	-1921	-1185
588	-2234	-294	-1939	-1204
868	-2349	-296	-2052	-1317
924	-2365	-298	-2066	-1331
1008	-2383	-283	-2101	-1365
1089	-2410	-298	-2112	-1377
1177	-2417	-288	-2129	-1394
1261	-2416	-284	-2132	-1396
1344	-2426	-285	-2141	-1406
1428	-2440	-283	-2157	-1421
1512	-2445	-288	-2157	-1422
1596	-2450	-288	-2163	-1427
1680	-2456	-284	-2172	-1436

Table A-11 (Part 1): Raw data for 11/19/2018 samples loaded at 91 days

Sampling Date			11/19/2018	
Loading Age			91 Days	
Compressive Strength (psi)			7,500	
Modulus of Elasticity (ksi)			4,600	
Target Applied Load (kips)			84.8	
Concrete Age After Loading (Days)	**Total Strain (με)**	**Shrinkage Strain (με)**	**Strain due to Load (με)**	**Creep Strain (με)**
Pre-Load	0	0	0	0
Post-Load	-755	0	-755	0
2-6 Hours	-770	-2	-768	-13
1	-867	-1	-865	-110
2	-939	-3	-936	-181
3	-966	-8	-958	-203
4	-970	-9	-961	-206
5	-993	-11	-982	-227
6	-1021	-22	-999	-244
7	-1051	-25	-1026	-271
14	-1121	-33	-1087	-332
21	-1162	-34	-1127	-372
28	-1264	-36	-1228	-473
56	-1368	-67	-1300	-545
84	-1438	-79	-1359	-604
111	-1538	-79	-1459	-704
140	-1624	-74	-1550	-795
168	-1674	-78	-1595	-840
196	-1693	-76	-1616	-861
224	-1704	-86	-1618	-863
252	-1734	-91	-1643	-888
280	-1787	-102	-1685	-930
308	-1818	-104	-1714	-959
336	-1838	-103	-1736	-981
420	-1868	-107	-1761	-1006

Table A-11 (Part 2): Raw data for 11/19/2018 samples loaded at 91 days (continued)

Concrete Age After Loading (Days)	Total Strain (με)	Shrinkage Strain (με)	Strain due to Load (με)	Creep Strain (με)
504	-1909	-111	-1798	-1043
781	-2015	-109	-1906	-1151
840	-2034	-104	-1930	-1175
926	-2052	-94	-1958	-1203
1005	-2079	-117	-1962	-1207
1092	-2072	-98	-1974	-1219
1176	-2092	-99	-1992	-1237
1261	-2104	-99	-2005	-1250
1346	-2117	-107	-2010	-1255
1429	-2119	-100	-2019	-1264
1512	-2119	-102	-2017	-1262
1596	-2137	-109	-2027	-1272
1681	-2135	-107	-2028	-1273

Table A-12 (Part 1): Raw data for 11/19/2018 samples loaded at 182 days

Sampling Date			11/19/2018	
Loading Age			182 Days	
Compressive Strength (psi)			7,400	
Modulus of Elasticity (ksi)			4,500	
Target Applied Load (kips)			83.7	
Concrete Age After Loading (Days)	**Total Strain (με)**	**Shrinkage Strain (με)**	**Strain due to Load (με)**	**Creep Strain (με)**
Pre-Load	0	0	0	0
Post-Load	-681	0	-681	0
2-6 Hours	-734	0	-734	-52
1	-767	0	-767	-86
2	-809	-1	-808	-127
4	-883	-1	-883	-201
4	-942	-4	-938	-256
5	-999	-4	-995	-314
6	-1017	-7	-1010	-328
7	-1069	-7	-1063	-381
15	-1116	-17	-1099	-417
21	-1160	-21	-1139	-457
28	-1222	-33	-1189	-508
56	-1241	-36	-1206	-524
84	-1265	-40	-1224	-543
112	-1288	-43	-1245	-563
140	-1307	-46	-1261	-580
168	-1350	-47	-1303	-621
196	-1372	-49	-1323	-642
224	-1398	-49	-1349	-667
252	-1419	-49	-1370	-689
280	-1453	-51	-1402	-720
308	-1471	-51	-1420	-738
336	-1491	-52	-1438	-757
420	-1518	-56	-1462	-780

Table A-12 (Part 2): Raw data for 11/19/2018 samples loaded at 182 days (continued)

Concrete Age After Loading (Days)	Total Strain (με)	Shrinkage Strain (με)	Strain due to Load (με)	Creep Strain (με)
714	-1636	-58	-1578	-897
756	-1643	-54	-1589	-907
842	-1651	-49	-1602	-921
925	-1727	-82	-1646	-964
1008	-1699	-45	-1654	-973
1092	-1723	-45	-1677	-996
1176	-1725	-43	-1682	-1001
1261	-1741	-51	-1689	-1008
1344	-1745	-44	-1701	-1019
1425	-1750	-50	-1700	-1018
1509	-1753	-53	-1700	-1019
1596	-1760	-53	-1707	-1026

Table A-13 (Part 1): Raw data for 04/16/2019 samples loaded at 7 days

Sampling Date			04/16/2019	
Loading Age			7 Days	
Compressive Strength (psi)			7,300	
Modulus of Elasticity (ksi)			5,100	
Target Applied Load (kips)			82.6	
Concrete Age After Loading (Days)	**Total Strain (με)**	**Shrinkage Strain (με)**	**Strain due to Load (με)**	**Creep Strain (με)**
Pre-Load	0	0	0	0
Post-Load	-670	0	-670	0
2-6 Hours	-762	-11	-751	-80
1	-863	-33	-830	-160
2	-946	-59	-887	-217
3	-1002	-89	-913	-243
4	-1039	-89	-949	-279
5	-1061	-103	-957	-287
6	-1064	-108	-956	-286
7	-1104	-109	-995	-325
14	-1206	-131	-1076	-406
21	-1319	-161	-1158	-488
21	-1398	-198	-1200	-530
55	-1583	-267	-1316	-646
84	-1678	-300	-1378	-708
112	-1762	-335	-1427	-757
140	-1830	-353	-1477	-807
168	-1879	-372	-1507	-837
196	-1925	-401	-1524	-854
224	-1968	-420	-1549	-879
252	-1992	-432	-1559	-889
280	-1993	-429	-1564	-894
308	-2014	-436	-1578	-907
336	-2037	-435	-1602	-932
420	-2070	-432	-1638	-968

Table A-13 (Part 2): Raw data for 04/16/2019 samples loaded at 7 days (continued)

Concrete Age After Loading (Days)	Total Strain (με)	Shrinkage Strain (με)	Strain due to Load (με)	Creep Strain (με)
504	-2097	-435	-1662	-992
741	-2151	-445	-1705	-1035
848	-2169	-438	-1731	-1061
924	-2178	-440	-1738	-1068
1008	-2188	-440	-1748	-1078
1094	-2208	-450	-1758	-1088
1196	-2208	-444	-1764	-1094
1273	-2213	-446	-1767	-1097
1332	-2216	-440	-1776	-1106
1427	-2216	-442	-1774	-1104
1511	-2216	-440	-1777	-1107
1596	-2219	-432	-1786	-1116

Table A-14 (Part 1): Raw data for 04/16/2019 samples loaded at 28 days

Sampling Date			04/16/2019	
Loading Age			28 Days	
Compressive Strength (psi)			8,000	
Modulus of Elasticity (ksi)			5,300	
Target Applied Load (kips)			90.5	
Concrete Age After Loading (Days)	**Total Strain (με)**	**Shrinkage Strain (με)**	**Strain due to Load (με)**	**Creep Strain (με)**
Pre-Load	0	0	0	0
Post-Load	-652	0	-652	0
2-6 Hours	-740	-2	-738	-86
1	-830	-7	-823	-171
2	-931	-8	-923	-271
3	-988	-10	-978	-326
4	-1026	-15	-1011	-359
5	-1069	-19	-1050	-398
6	-1104	-25	-1079	-427
7	-1142	-39	-1103	-451
14	-1208	-60	-1148	-496
21	-1272	-105	-1167	-515
27	-1356	-153	-1202	-550
56	-1472	-192	-1280	-628
84	-1578	-227	-1351	-699
112	-1669	-269	-1400	-748
140	-1737	-310	-1426	-774
168	-1782	-320	-1461	-809
196	-1827	-336	-1491	-839
224	-1840	-349	-1492	-840
252	-1850	-346	-1503	-851
280	-1869	-349	-1520	-868
308	-1884	-351	-1533	-881
336	-1904	-352	-1552	-900
420	-1932	-348	-1584	-932

Table A-14 (Part 2): Raw data for 04/16/2019 samples loaded at 28 days (continued)

Concrete Age After Loading (Days)	Total Strain (με)	Shrinkage Strain (με)	Strain due to Load (με)	Creep Strain (με)
504	-1948	-351	-1597	-945
756	-2099	-373	-1726	-1074
848	-2091	-349	-1742	-1090
920	-2132	-367	-1765	-1113
1007	-2136	-353	-1783	-1131
1091	-2139	-350	-1789	-1137
1176	-2153	-361	-1792	-1140
1261	-2152	-353	-1799	-1147
1344	-2163	-354	-1809	-1157
1429	-2167	-355	-1812	-1160
1511	-2170	-357	-1813	-1161
1596	-2173	-354	-1819	-1167

Table A-15 (Part 1): Raw data for 04/16/2019 samples loaded at 91 days

Sampling Date			04/16/2019	
Loading Age			91 Days	
Compressive Strength (psi)			8,300	
Modulus of Elasticity (ksi)			5,400	
Target Applied Load (kips)			93.9	
Concrete Age After Loading (Days)	**Total Strain (με)**	**Shrinkage Strain (με)**	**Strain due to Load (με)**	**Creep Strain (με)**
Pre-Load	0	0	0	0
Post-Load	-721	0	-721	0
2-6 Hours	-787	0	-787	-66
1	-855	-9	-846	-125
2	-899	-14	-885	-164
3	-935	-17	-918	-197
4	-962	-21	-942	-221
5	-999	-24	-975	-254
6	-1037	-29	-1008	-287
7	-1069	-36	-1034	-313
14	-1122	-54	-1069	-348
21	-1173	-70	-1103	-383
28	-1206	-86	-1120	-399
56	-1334	-120	-1214	-493
84	-1409	-139	-1270	-549
112	-1480	-169	-1311	-591
140	-1542	-187	-1355	-634
168	-1604	-200	-1404	-683
196	-1612	-196	-1416	-695
224	-1618	-203	-1415	-694
252	-1664	-202	-1462	-741
280	-1683	-200	-1483	-762
308	-1692	-199	-1493	-772
336	-1699	-199	-1499	-778
420	-1736	-202	-1534	-813

Table A-15 (Part 2): Raw data for 04/16/2019 samples loaded at 91 days (continued)

Concrete Age After Loading (Days)	Total Strain (με)	Shrinkage Strain (με)	Strain due to Load (με)	Creep Strain (με)
657	-1812	-210	-1602	-881
768	-1828	-206	-1622	-901
840	-1833	-208	-1625	-904
924	-1858	-208	-1650	-929
1010	-1873	-217	-1655	-934
1112	-1881	-211	-1670	-949
1189	-1883	-214	-1669	-948
1248	-1887	-208	-1679	-958
1343	-1895	-209	-1686	-965
1427	-1895	-207	-1688	-967
1512	-1891	-200	-1691	-971

Table A-16 (Part 1): Raw data for 04/16/2019 samples loaded at 182 days

Sampling Date			04/16/2019	
Loading Age			182 Days	
Compressive Strength (psi)			8,100	
Modulus of Elasticity (ksi)			5,400	
Target Applied Load (kips)			91.6	
Concrete Age After Loading (Days)	**Total Strain (με)**	**Shrinkage Strain (με)**	**Strain due to Load (με)**	**Creep Strain (με)**
Pre-Load	0	0	0	0
Post-Load	-710	0	-710	0
2-6 Hours	-732	0	-732	-23
1	-822	0	-822	-112
2	-827	-3	-824	-115
3	-850	-5	-845	-136
4	-849	-6	-844	-134
5	-854	-5	-849	-140
6	-861	-3	-858	-149
7	-897	-3	-894	-184
14	-958	-5	-953	-244
21	-992	-6	-987	-277
28	-1012	-8	-1004	-295
56	-1115	-16	-1099	-390
84	-1184	-22	-1162	-453
112	-1218	-25	-1193	-484
140	-1267	-32	-1235	-525
168	-1279	-28	-1251	-542
196	-1287	-31	-1256	-546
224	-1308	-28	-1280	-570
252	-1324	-31	-1293	-584
280	-1338	-28	-1309	-600
308	-1352	-30	-1322	-612
336	-1364	-31	-1333	-623
566	-1477	-42	-1435	-726

Table A-16 (Part 2): Raw data for 04/16/2019 samples loaded at 182 days (continued)

Concrete Age After Loading (Days)	Total Strain (με)	Shrinkage Strain (με)	Strain due to Load (με)	Creep Strain (με)
677	-1500	-34	-1466	-756
756	-1531	-40	-1491	-781
839	-1532	-29	-1504	-794
924	-1556	-41	-1514	-805
1021	-1559	-40	-1519	-809
1105	-1582	-45	-1537	-827
1176	-1573	-34	-1539	-829
1263	-1577	-37	-1540	-831
1345	-1580	-34	-1546	-837
1428	-1586	-28	-1558	-848

Table A-17 (Part 1): Raw data for 04/10/2018 shrinkage prisms

Air-Cured Prisms		Moist-Cured Prisms	
Concrete Age After Drying Began (Days)	**Shrinkage Strain (με)**	**Concrete Age After Drying Began (Days)**	**Shrinkage Strain (με)**
0	0	0	0
2-6 Hours	-77	2-6 Hours	-53
1	-130	1	-152
2	-168	2	-225
3	-222	3	-270
4	-252	4	-300
5	-283	5	-342
6	-295	6	-375
7	-318	7	-398
14	-495	14	-525
21	-568	21	-583
28	-597	28	-622
56	-668	56	-693
84	-683	84	-715
112	-723	112	-758
140	-728	140	-778
168	-745	168	-783
196	-742	196	-778
224	-720	224	-778
252	-743	250	-822
280	-787	280	-813
308	-755	308	-810
337	-730	420	-785
420	-720	504	-807
504	-727	588	-833
588	-742	671	-828
672	-767	756	-828
756	-745	840	-808
840	-743	1091	-838
1098	-778	1175	-817

Table A-17 (Part 2): Raw data for 04/10/2018 shrinkage prisms (continued)

Air-Cured Prisms		Moist-Cured Prisms	
Concrete Age After Drying Began (Days)	**Shrinkage Strain (με)**	**Concrete Age After Drying Began (Days)**	**Shrinkage Strain (με)**
1176	-763	1259	-825
1266	-758	1338	-843
1345	-783	1426	-855
1426	-792	1594	-813
1511	-763	1678	-857
1601	-787	1764	-838
1682	-795	1853	-837
1766	-787	1932	-837
1848	-798	---	---
1923	-802	---	---

Table A-18 (Part 1): Raw data for 07/09/2018 shrinkage prisms

Air-Cured Prisms		Moist-Cured Prisms	
Concrete Age After Drying Began (Days)	**Shrinkage Strain (με)**	**Concrete Age After Drying Began (Days)**	**Shrinkage Strain (με)**
0	0	0	0
2-6 Hours	-10	2-6 Hours	-25
1	-55	1	-62
2	-112	2	-142
3	-143	3	-175
4	-195	4	-220
5	-212	5	-258
6	-238	6	-278
7	-258	7	-302
14	-390	14	-425
21	-497	21	-520
28	-550	28	-553
56	-618	56	-620
84	-650	84	-657
112	-672	112	-675
139	-673	141	-687
167	-700	167	-700
196	-707	196	-725
224	-687	224	-702
252	-720	252	-707
281	-670	280	-693
308	-668	308	-670
336	-667	336	-678
420	-657	414	-680
504	-710	504	-748
587	-692	588	-687
671	-692	672	-725
755	-672	756	-673
1008	-688	1002	-725
1092	-687	1022	-718

Table A-18 (Part 2): Raw data for 07/09/2018 shrinkage prisms (continued)

Air-Cured Prisms		Moist-Cured Prisms	
Concrete Age After Drying Began (Days)	**Shrinkage Strain (με)**	**Concrete Age After Drying Began (Days)**	**Shrinkage Strain (με)**
1176	-683	1092	-703
1255	-713	1182	-693
1343	-718	1249	-730
1511	-700	1275	-743
1595	-718	1343	-727
1681	-687	1512	-710
1770	-690	1595	-715
1849	-693	1680	-697
---	---	1763	-695
---	---	1847	-693

Table A-19 (Part 1): Raw data for 11/19/2018 shrinkage prisms

Air-Cured Prisms		Moist-Cured Prisms	
Concrete Age After Drying Began (Days)	**Shrinkage Strain (με)**	**Concrete Age After Drying Began (Days)**	**Shrinkage Strain (με)**
0	0	0	0
2-6 Hours	-30	2-6 Hours	-22
1	-40	1	-95
2	-82	3	-157
3	-128	3	-197
4	-143	4	-213
5	-153	5	-258
6	-188	6	-268
7	-227	8	-308
14	-345	14	-390
21	-395	21	-472
28	-467	27	-513
56	-578	56	-580
84	-577	84	-617
114	-578	112	-660
140	-582	141	-637
168	-612	168	-647
196	-607	196	-647
252	-590	252	-640
280	-612	280	-670
308	-612	308	-640
336	-620	336	-668
420	-643	420	-695
504	-620	504	-670
588	-630	588	-685
876	-668	869	-730
925	-663	924	-743
1009	-672	1009	-700
1093	-688	1088	-730
1178	-668	1175	-703

Table A-19 (Part 2): Raw data for 11/19/2018 shrinkage prisms (continued)

Air-Cured Prisms		Moist-Cured Prisms	
Concrete Age After Drying Began (Days)	**Shrinkage Strain (με)**	**Concrete Age After Drying Began (Days)**	**Shrinkage Strain (με)**
1259	-667	1259	-717
1351	-652	1344	-703
1434	-690	1429	-730
1513	-657	1512	-712
1602	-648	1597	-697
1686	-640	1683	-697
1764	-657	1764	-693

Table A-20 (Part 1): Raw data for 04/16/2019 shrinkage prisms

Air-Cured Prisms		Moist-Cured Prisms	
Concrete Age After Drying Began (Days)	**Shrinkage Strain (με)**	**Concrete Age After Drying Began (Days)**	**Shrinkage Strain (με)**
0	0	0	0
2-6 Hours	-2	2-6 Hours	-8
1	-42	1	-63
2	-62	2	-75
3	-97	3	-100
4	-125	4	-122
5	-130	5	-158
6	-163	6	-175
7	-170	7	-202
14	-278	14	-272
21	-320	21	-338
28	-360	28	-387
56	-443	56	-430
112	-482	112	-497
140	-497	140	-513
168	-527	168	-530
196	-532	196	-552
224	-555	224	-540
252	-545	280	-565
280	-543	308	-542
308	-532	336	-550
336	-543	420	-562
420	-548	504	-540
504	-538	720	-578
728	-562	755	-568
763	-560	850	-570
858	-567	922	-557
926	-582	1006	-572
1008	-607	1092	-575
1091	-585	1195	-562

Table A-20 (Part 2): Raw data for 04/16/2019 shrinkage prisms (continued)

Air-Cured Prisms		Moist-Cured Prisms	
Concrete Age After Drying Began (Days)	**Shrinkage Strain (με)**	**Concrete Age After Drying Began (Days)**	**Shrinkage Strain (με)**
1202	-557	1266	-602
1261	-587	1331	-597
1338	-565	1426	-575
1428	-560	1510	-562
1514	-552	1595	-537
1596	-545	---	---

Appendix B

DETAILED RESULTS FROM PREDICTION MODELS

This appendix presents the detailed results from all compliance and shrinkage prediction models covered in this research project, including the calibrated CEB MC 90-99 model and the calibrated CEB MC 1990 model. All figures in this appendix show the development of the measured compliance and shrinkage values with time along with their corresponding predicted values.

B.1 AASHTO LRFD PREDICTION MODEL

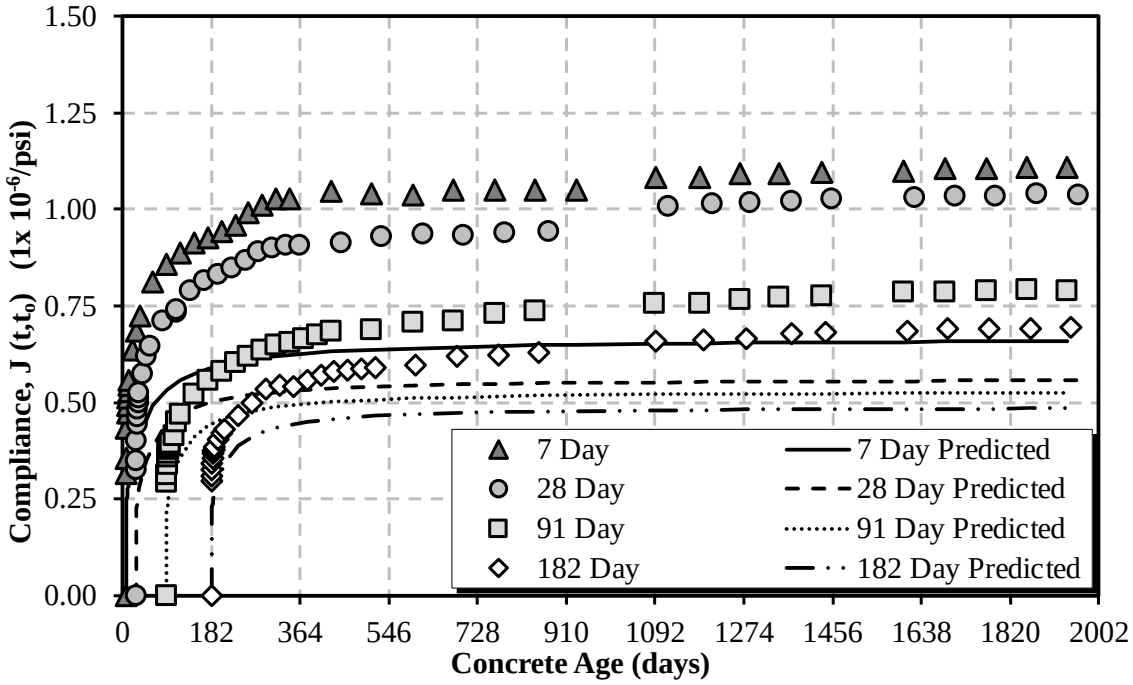

Figure B-1: AASHTO LRFD compliance for the 04/10/2018 sampling date

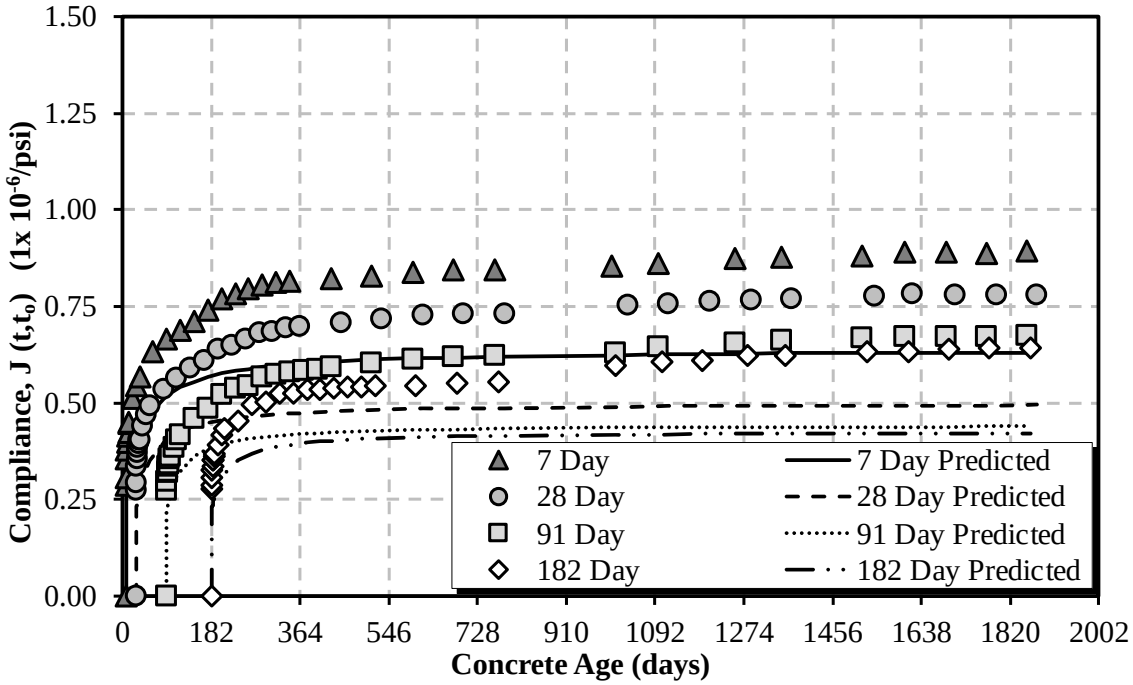

Figure B-2: AASHTO LRFD compliance for the 07/09/2018 sampling date

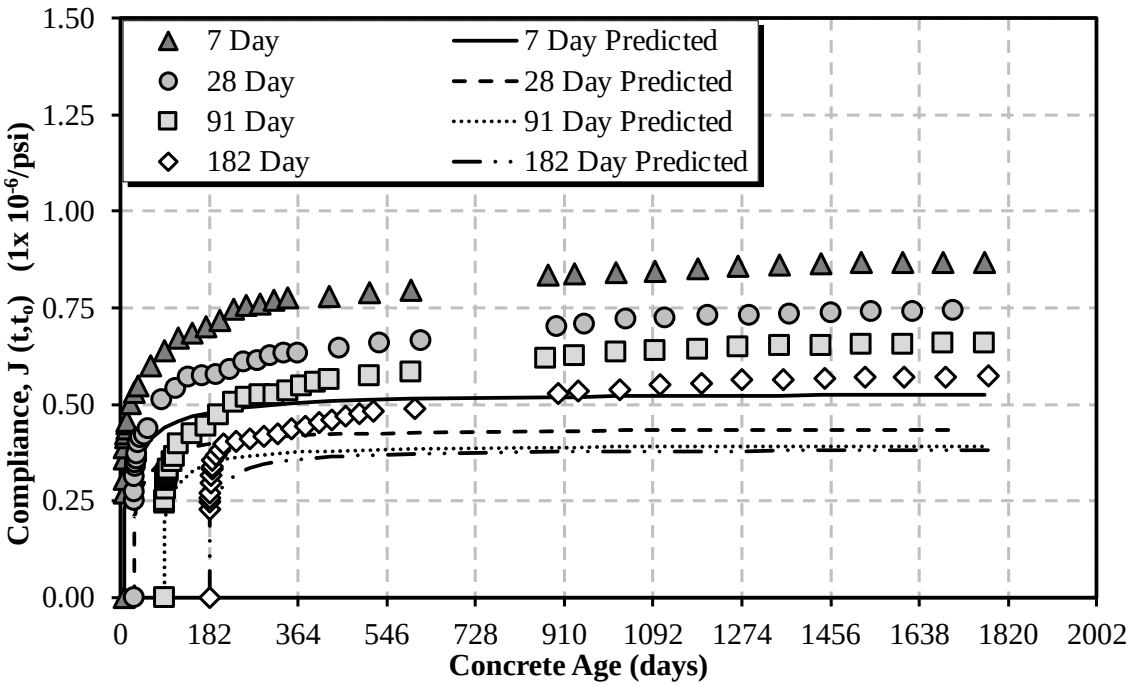

Figure B-3: AASHTO LRFD compliance for the 11/19/2018 sampling date

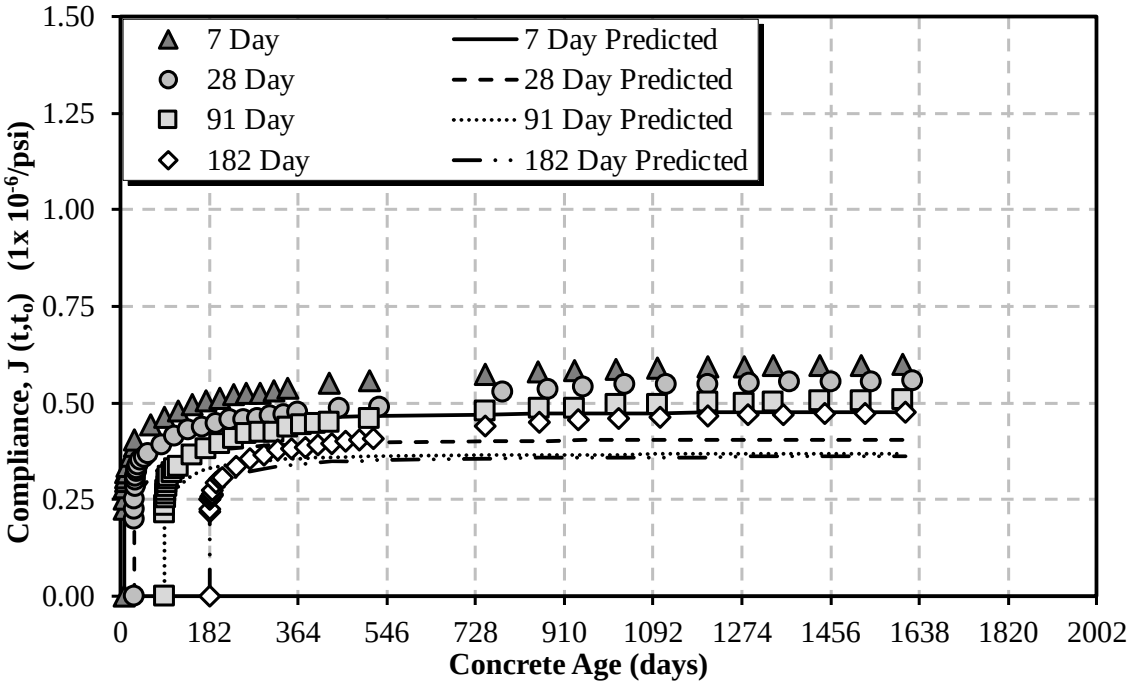

Figure B-4: AASHTO LRFD compliance for the 04/16/2019 sampling date

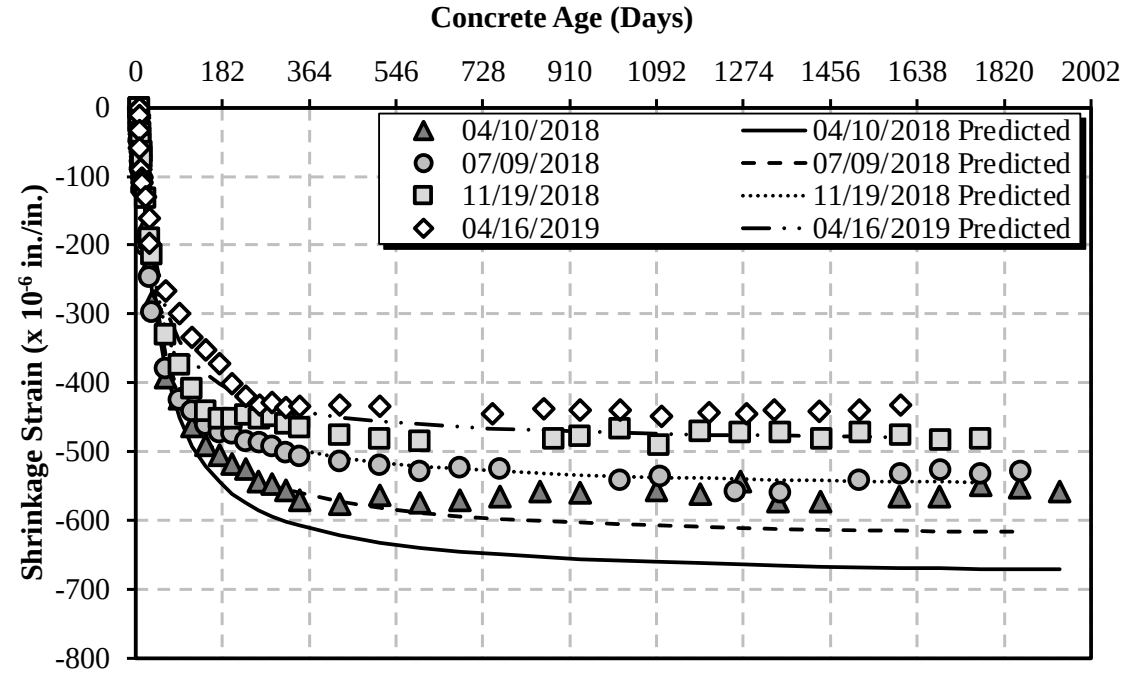

Figure B-5: AASHTO LRFD shrinkage for cylindrical specimens

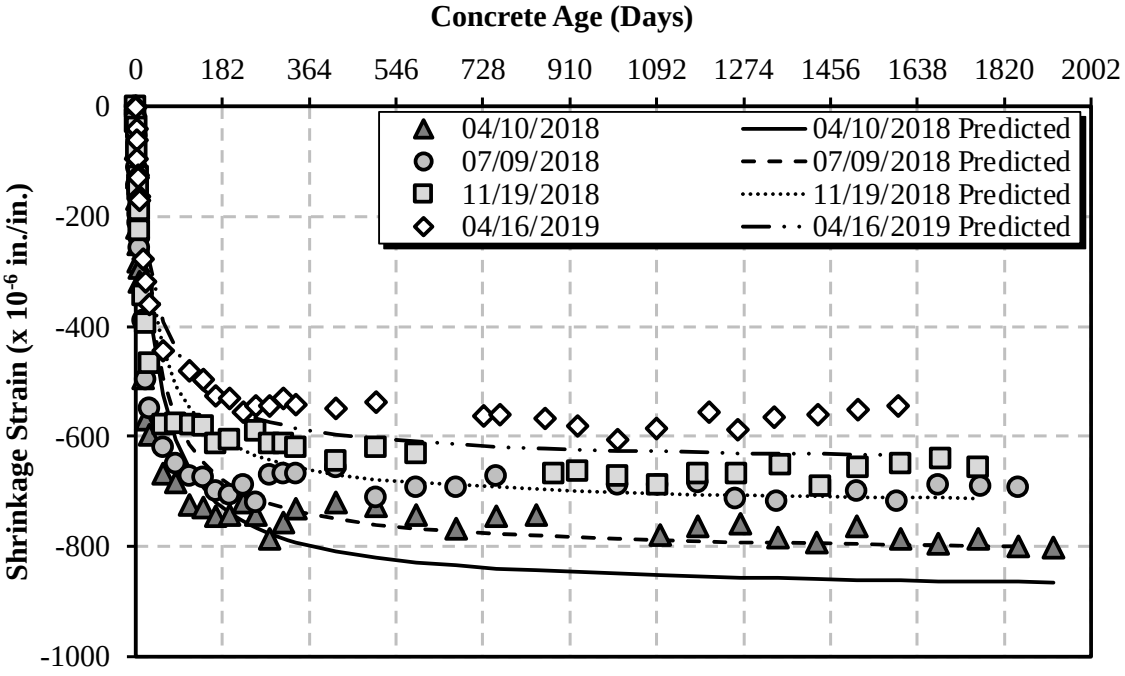

Figure B-6: AASHTO LRFD shrinkage for air-cured prisms

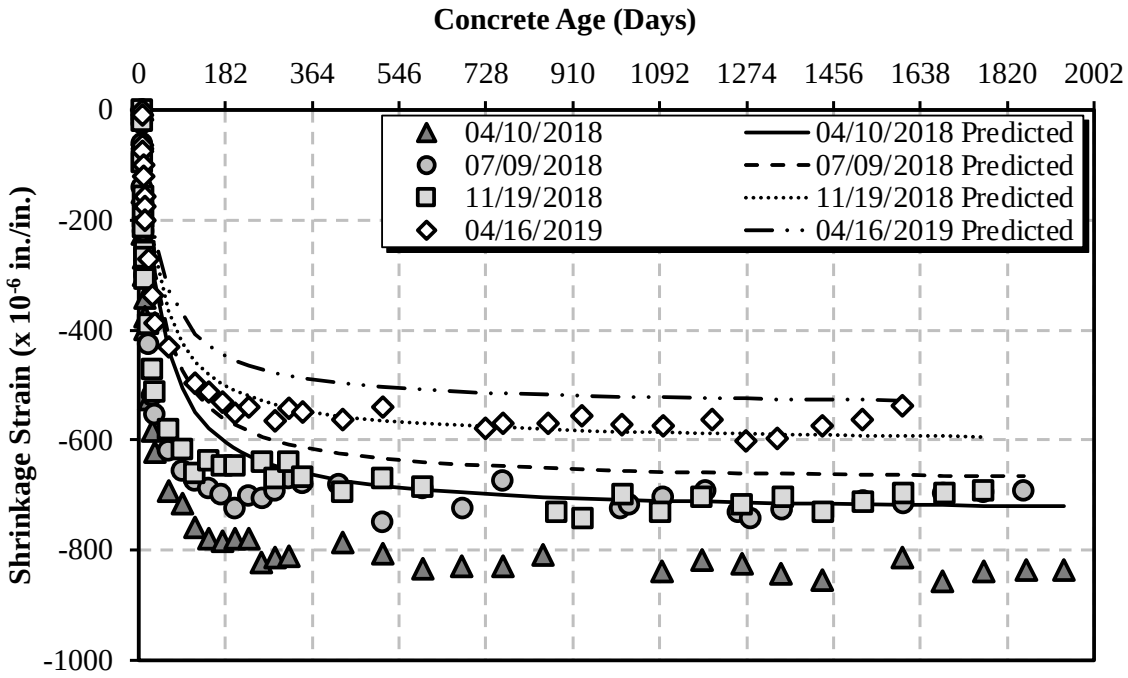

Figure B-7: AASHTO LRFD shrinkage for moist-cured prisms

B.2 ACI 209 PREDICTION MODEL

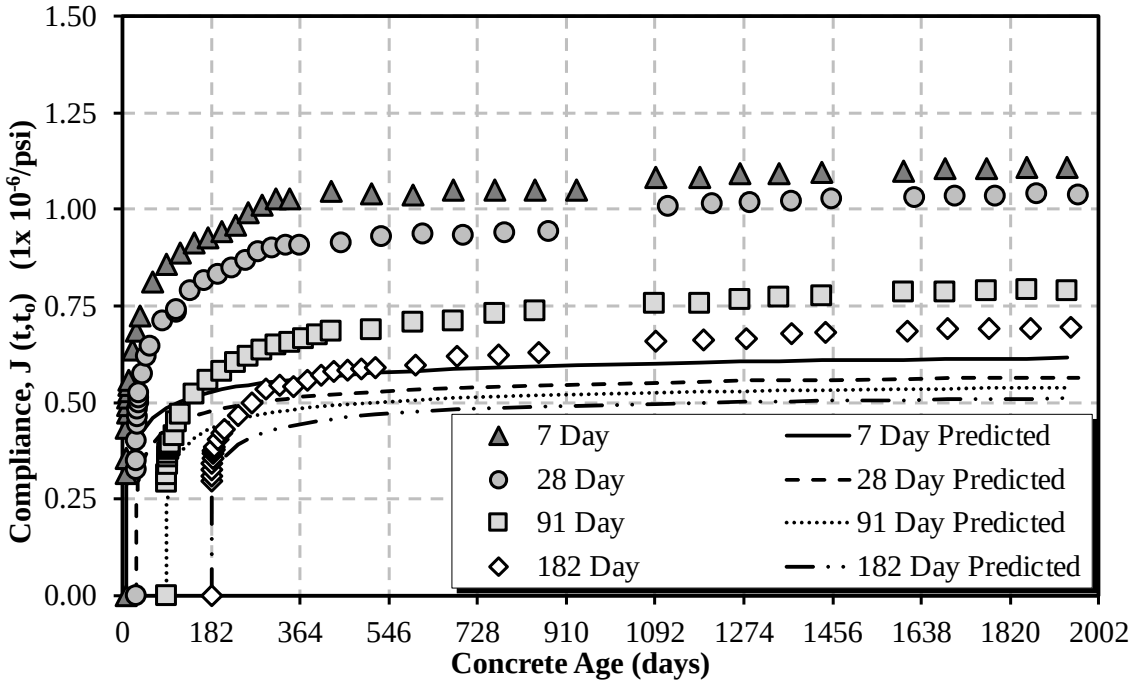

Figure B-8: ACI 209 compliance for the 04/10/2018 sampling date

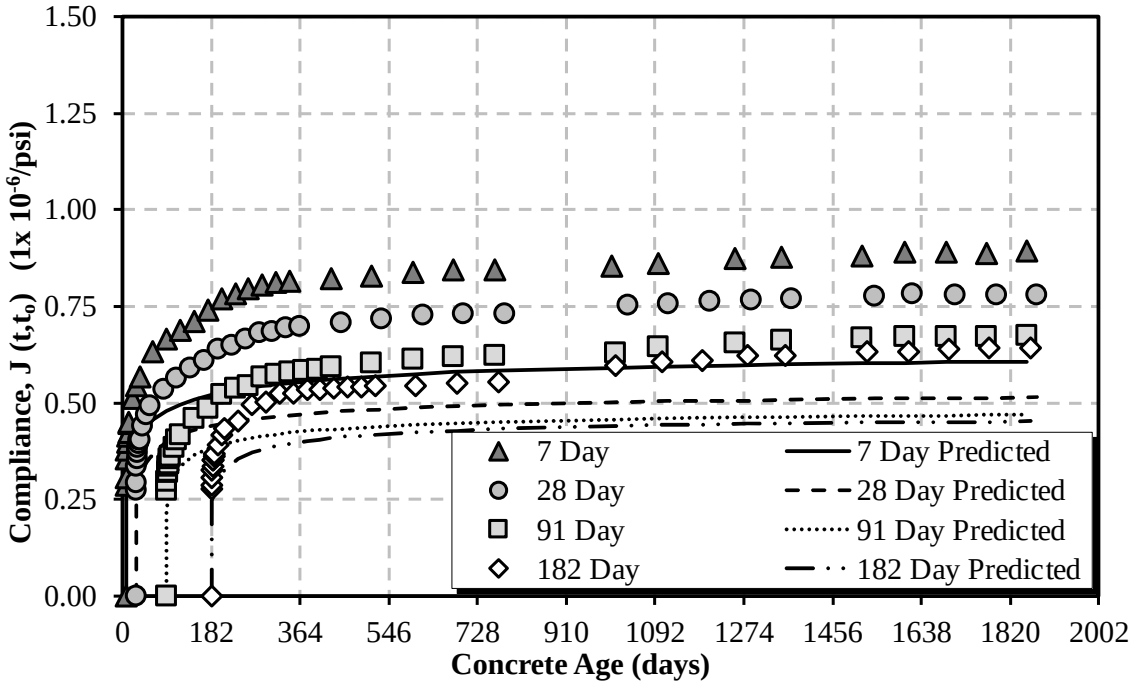

Figure B-9: ACI 209 compliance for the 07/09/2018 sampling date

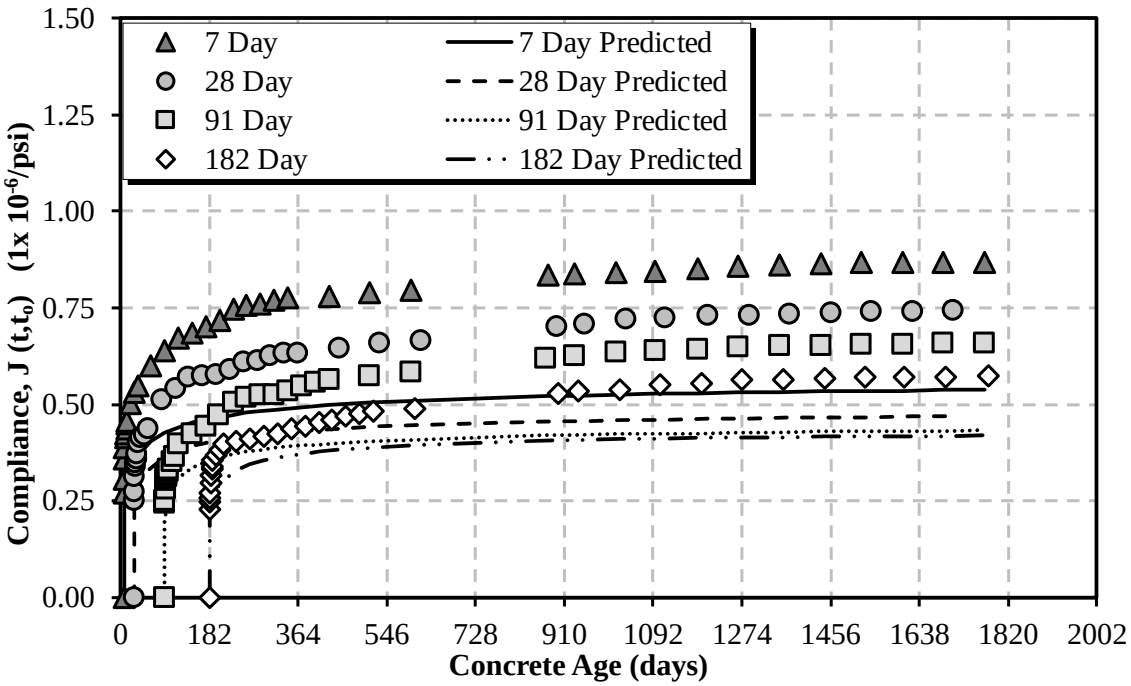

Figure B-10: ACI 209 compliance for the 11/19/2018 sampling date

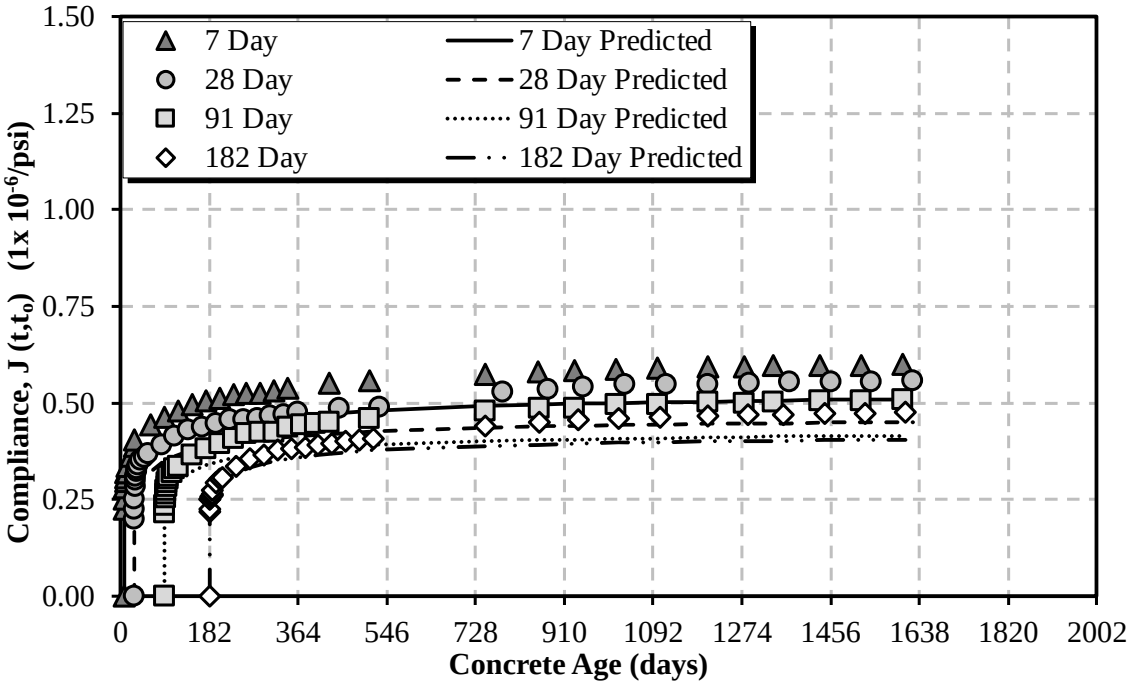

Figure B-11: ACI 209 compliance for the 04/16/2019 sampling date

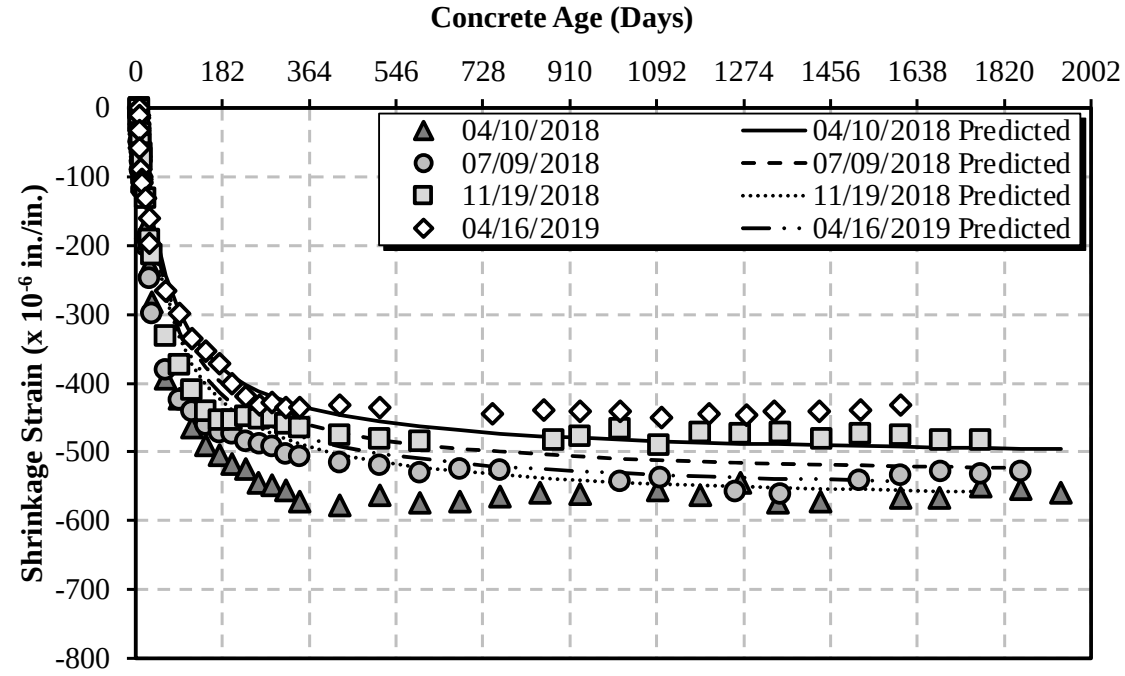

Figure B-12: ACI 209 shrinkage for cylindrical specimens

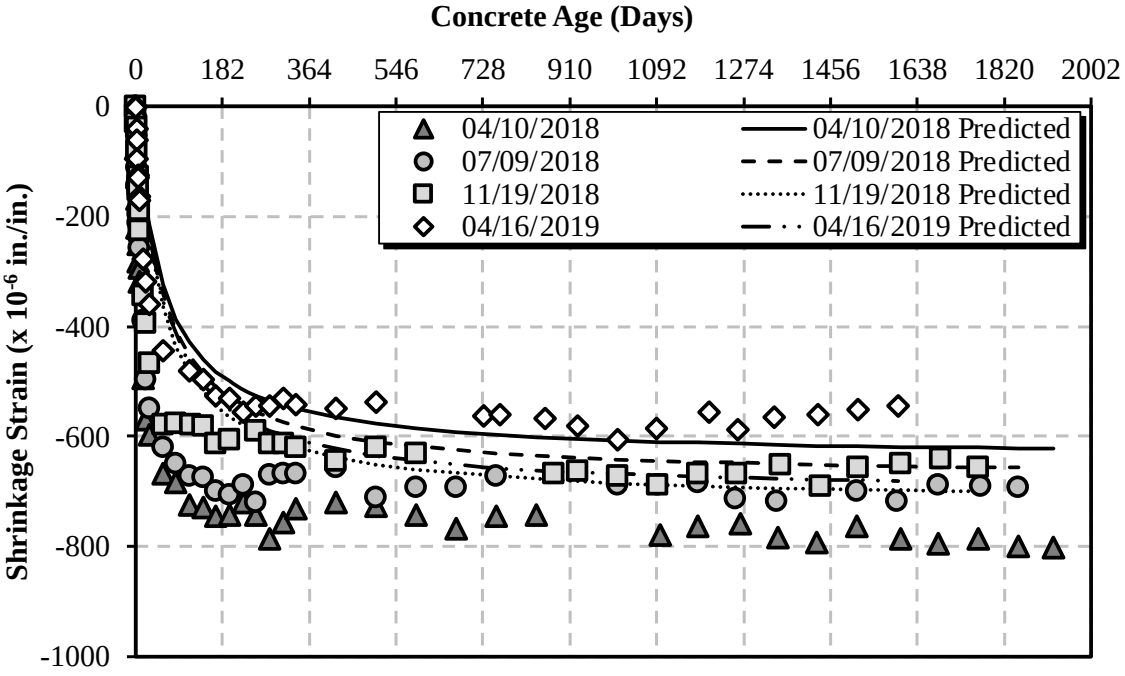

Figure B-13: ACI 209 shrinkage for air-cured prisms

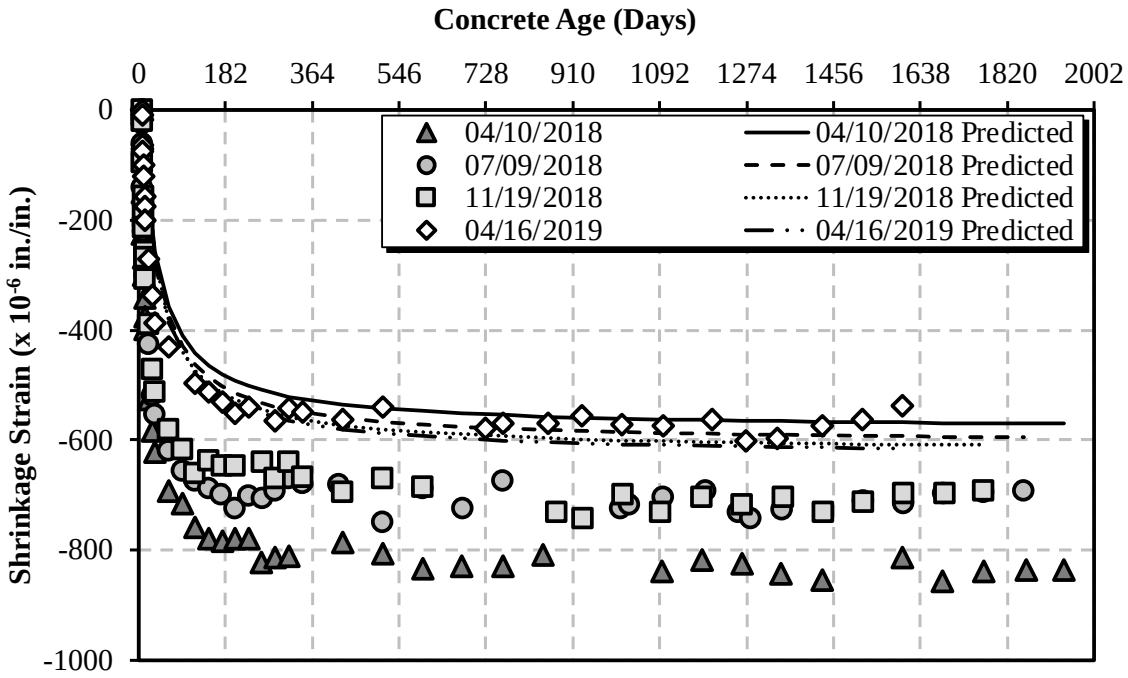

Figure B-14: ACI 209 shrinkage for moist-cured prisms

B.3 B3 PREDICTION MODEL

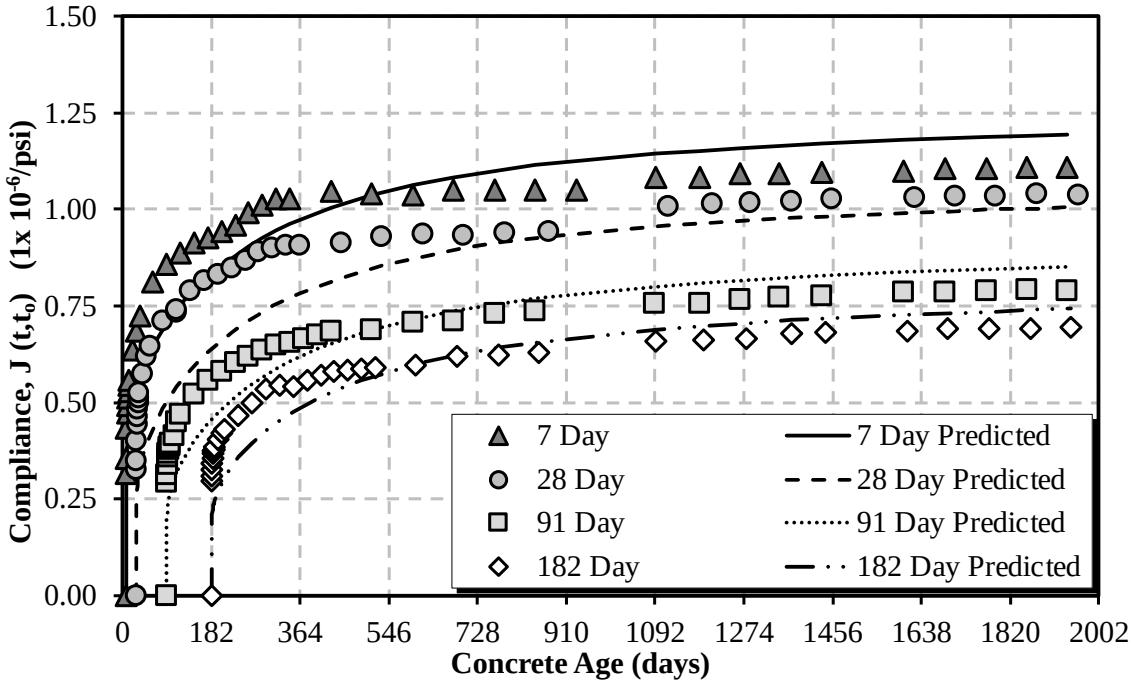

Figure B-15: B3 compliance for the 04/10/2018 sampling date

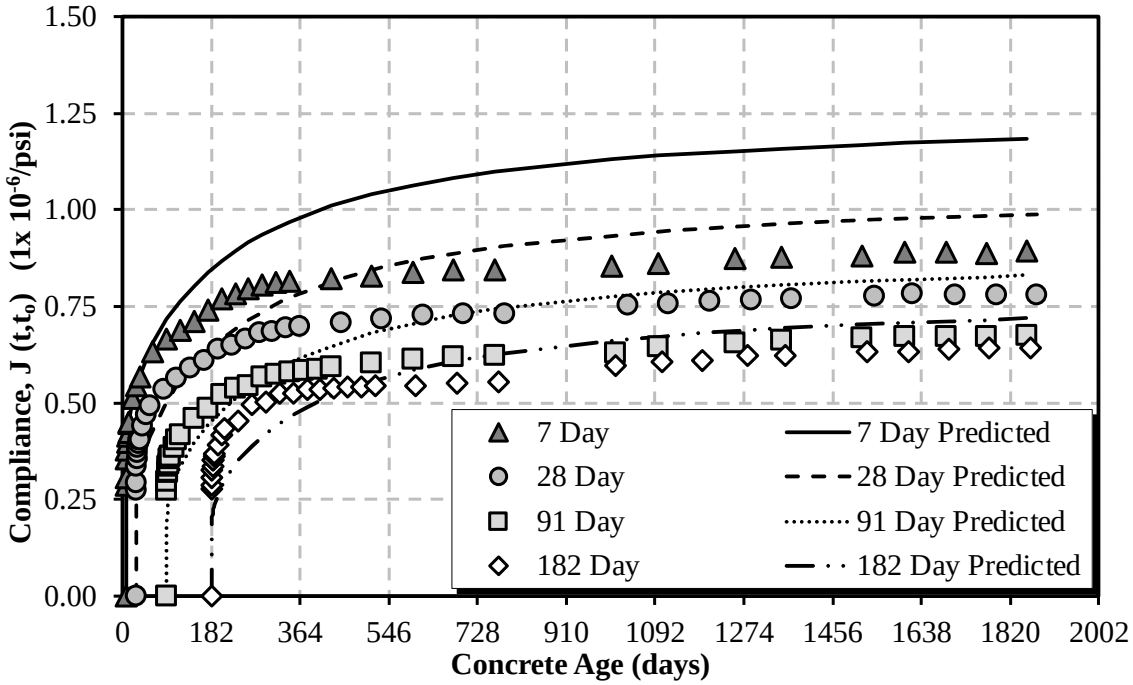

Figure B-16: B3 compliance for the 07/09/2018 sampling date

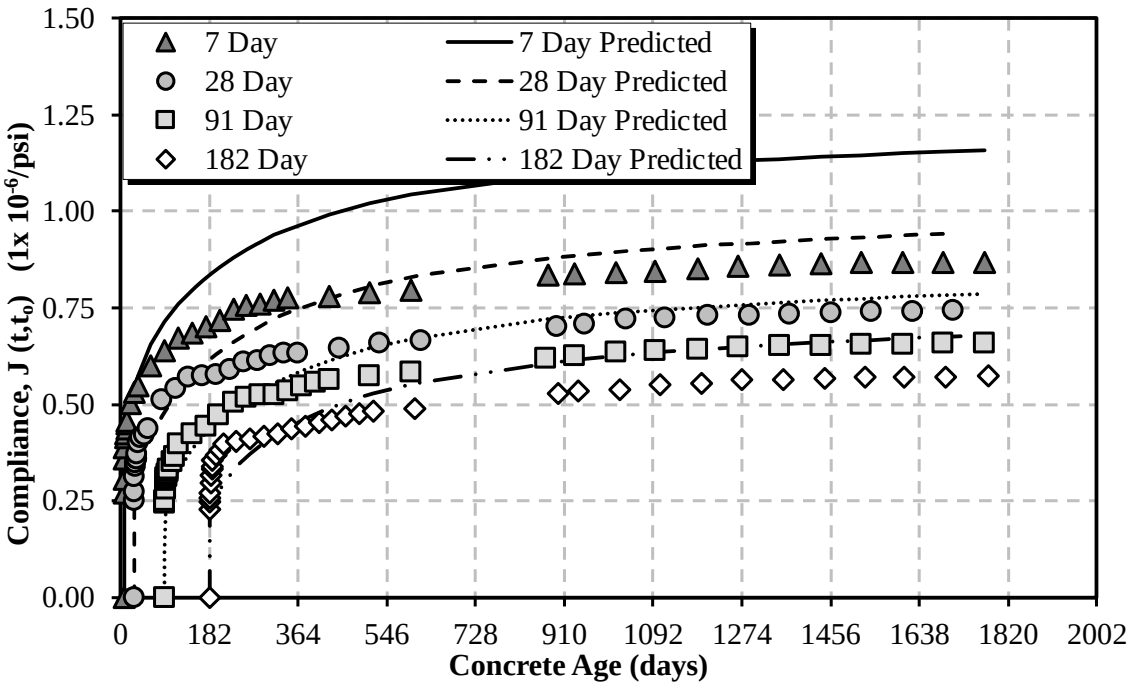

Figure B-17: B3 compliance for the 11/19/2018 sampling date

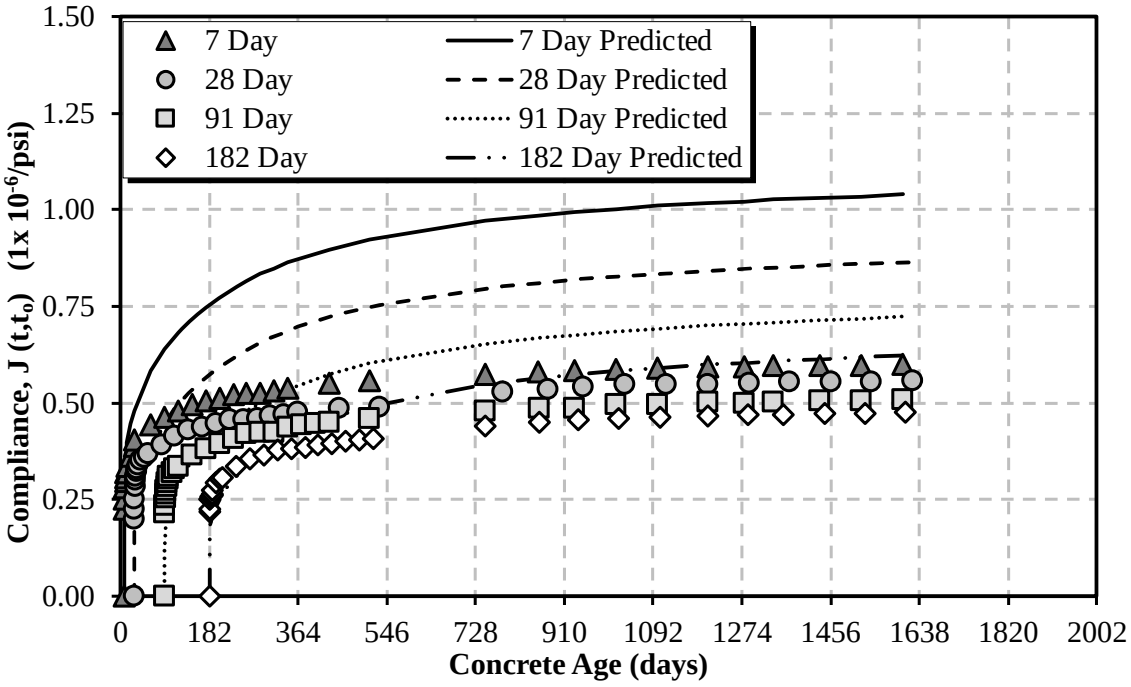

Figure B-18: B3 compliance for the 04/16/2019 sampling date

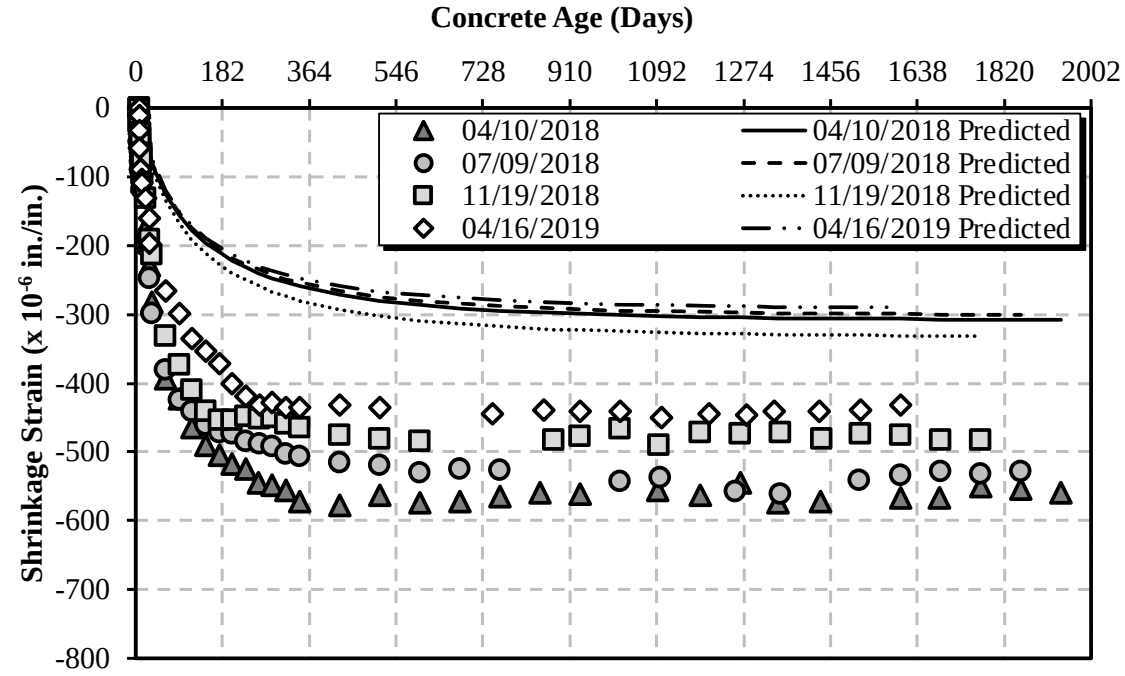

Figure B-19: B3 shrinkage for cylindrical specimens

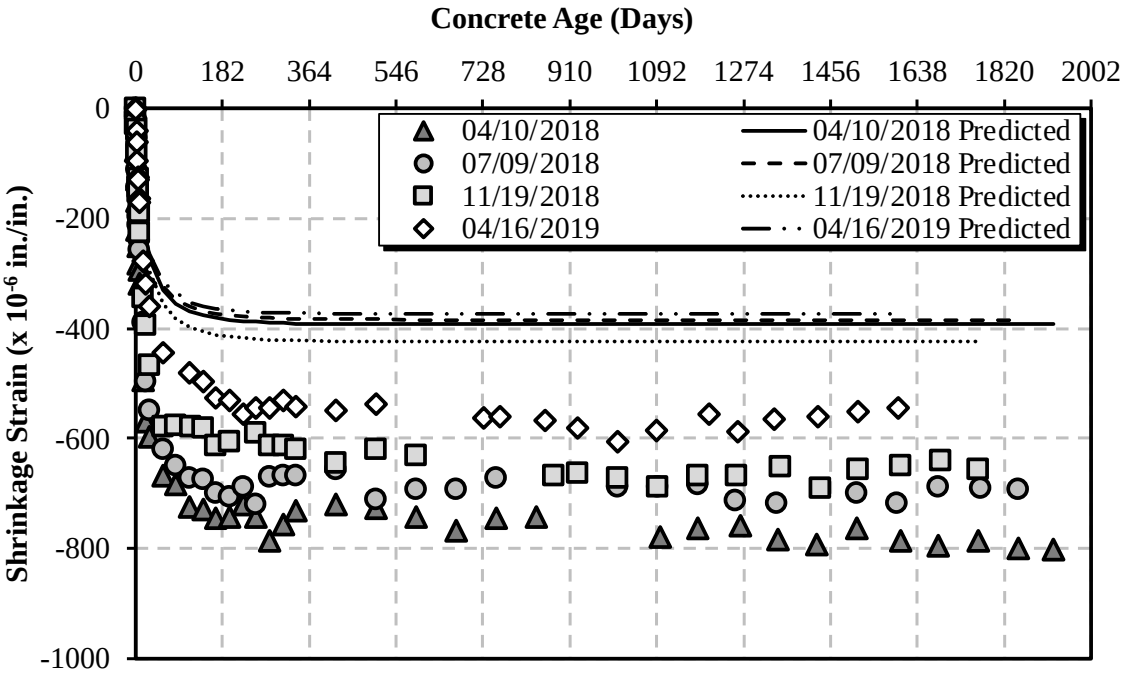

Figure B-20: B3 shrinkage for air-cured prisms

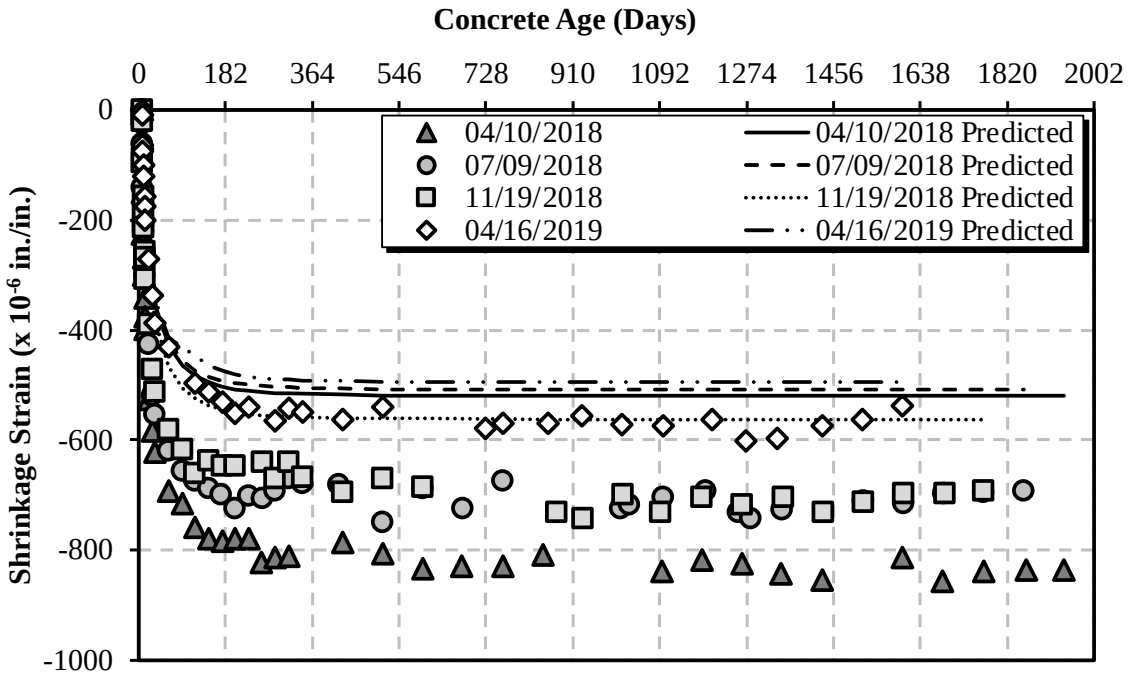

Figure B-21: B3 shrinkage for moist-cured prisms

B.4 B4 PREDICTION MODEL

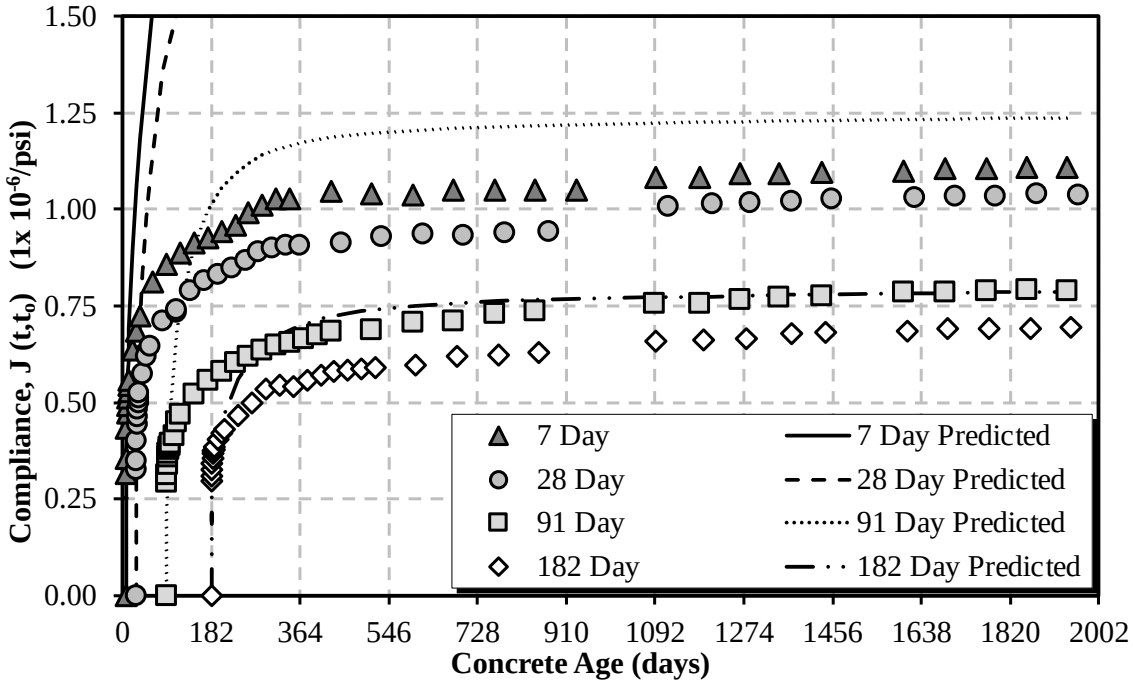

Figure B-22: B4 compliance for the 04/10/2018 sampling date

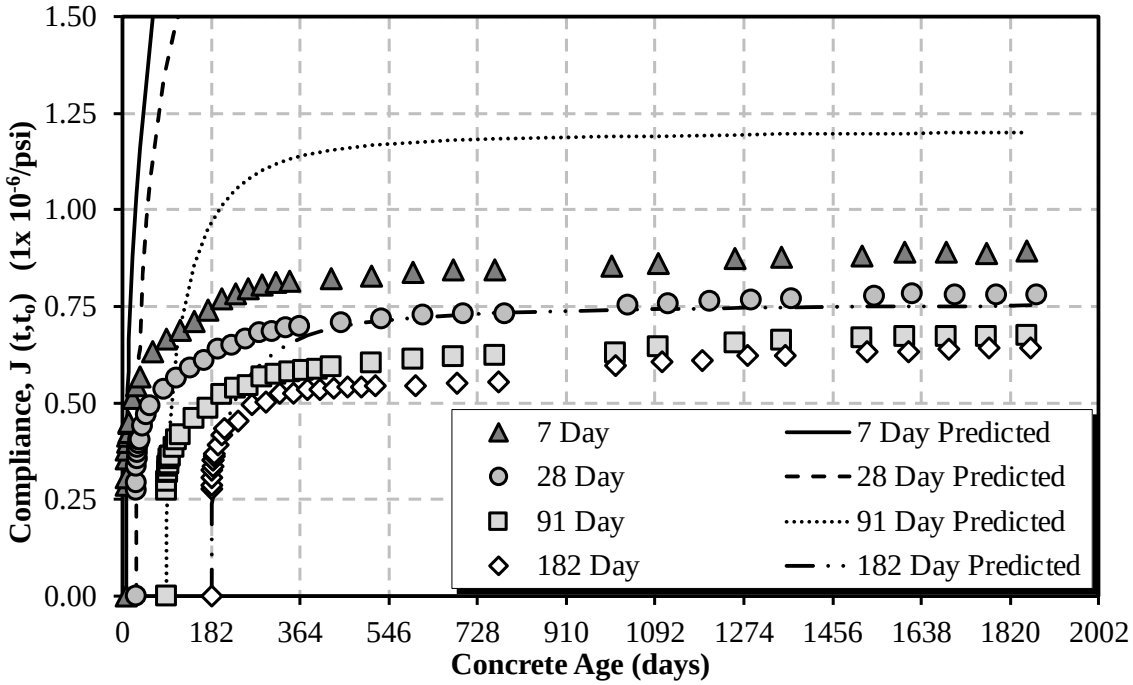

Figure B-23: B4 compliance for the 07/09/2018 sampling date

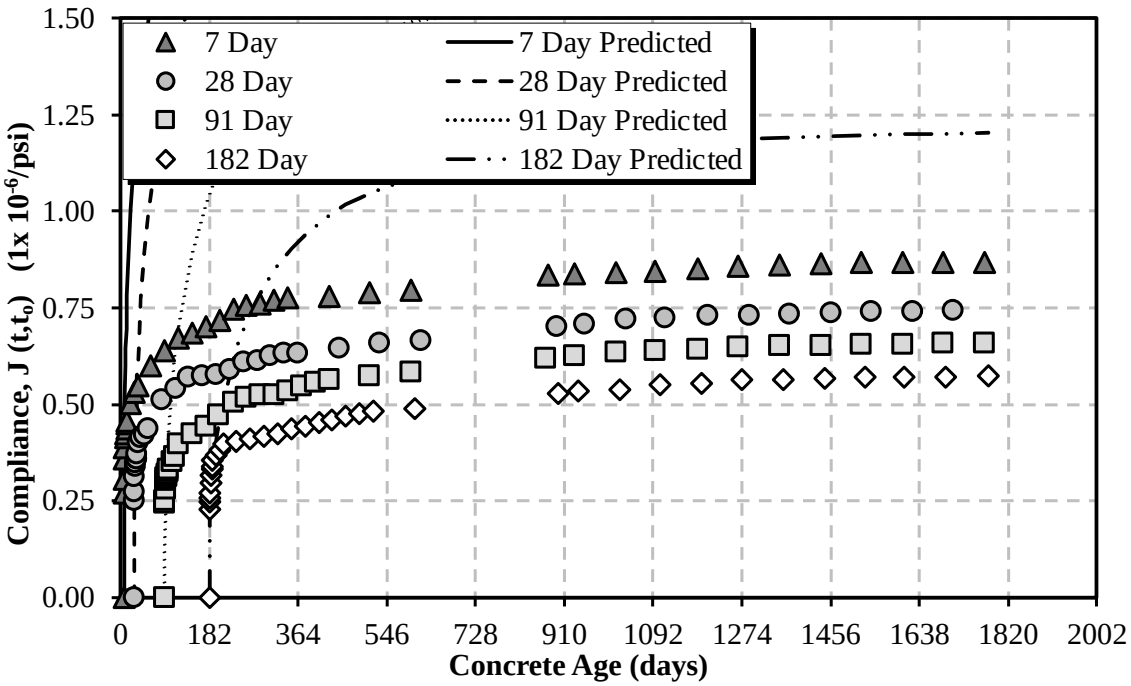

Figure B-24: B4 compliance for the 11/19/2018 sampling date

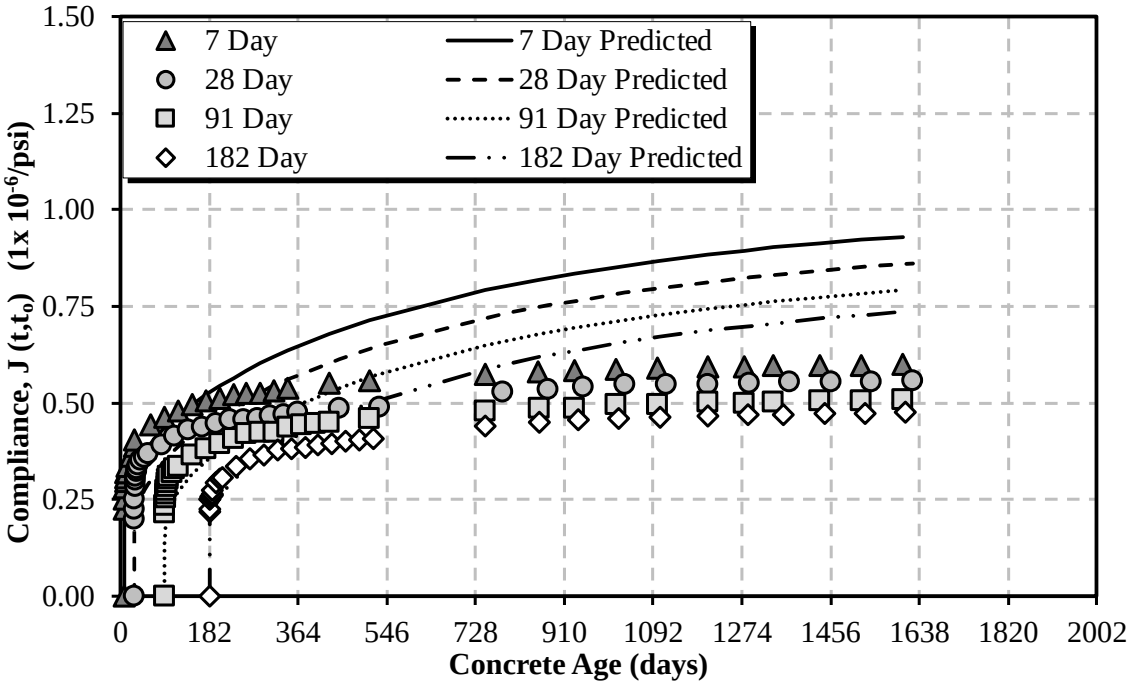

Figure B-25: B4 compliance for the 04/16/2019 sampling date

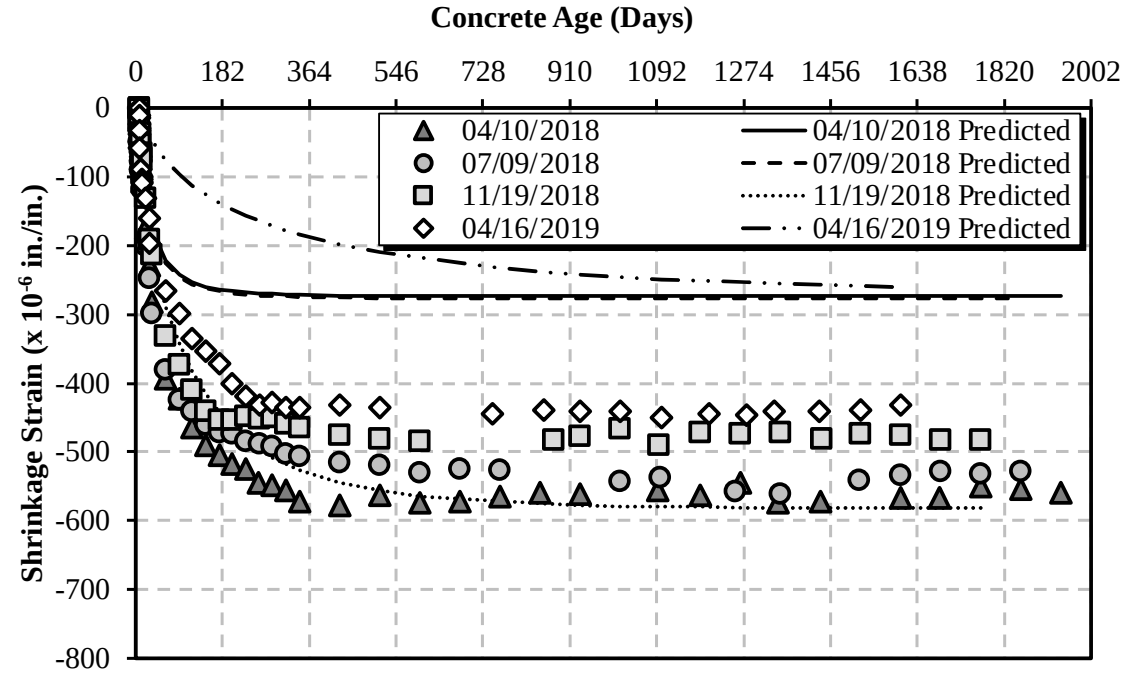

Figure B-26: B4 shrinkage for cylindrical specimens

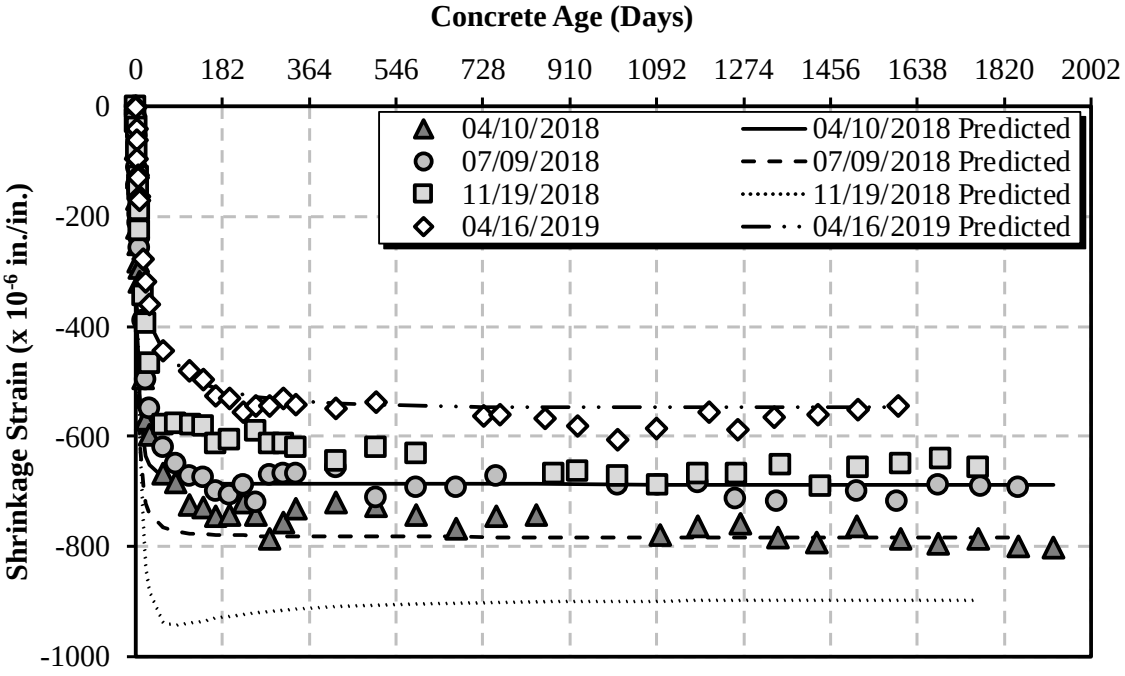

Figure B-27: B4 shrinkage for air-cured prisms

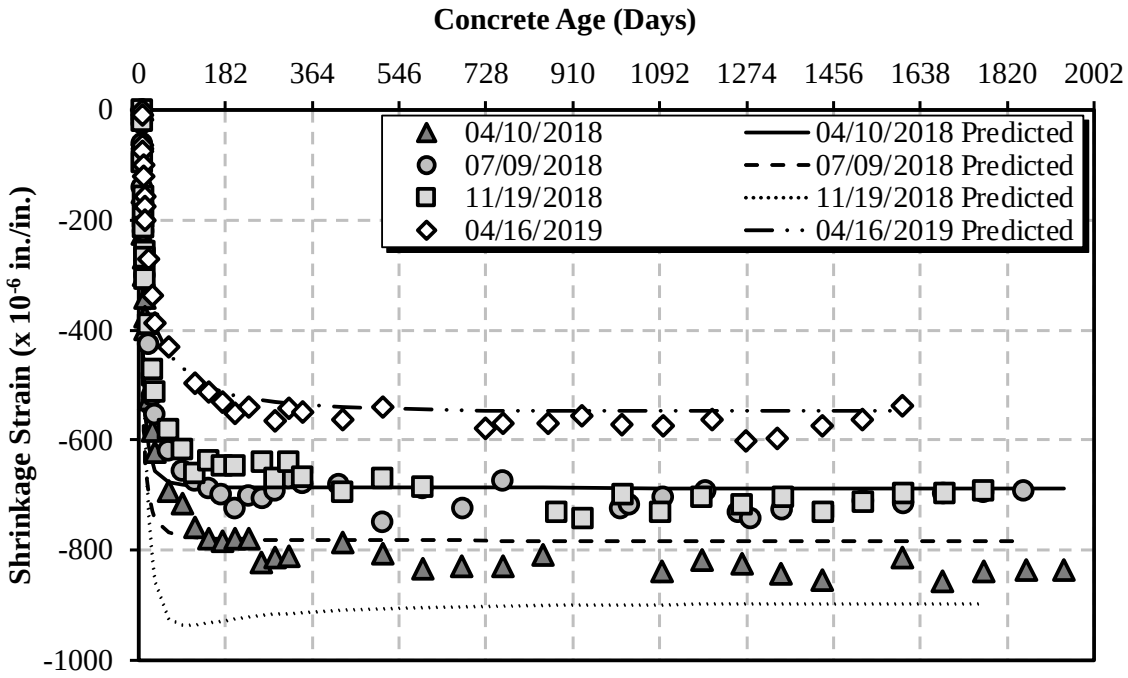

Figure B-28: B4 shrinkage for moist-cured prisms

B.5 B4* PREDICTION MODEL

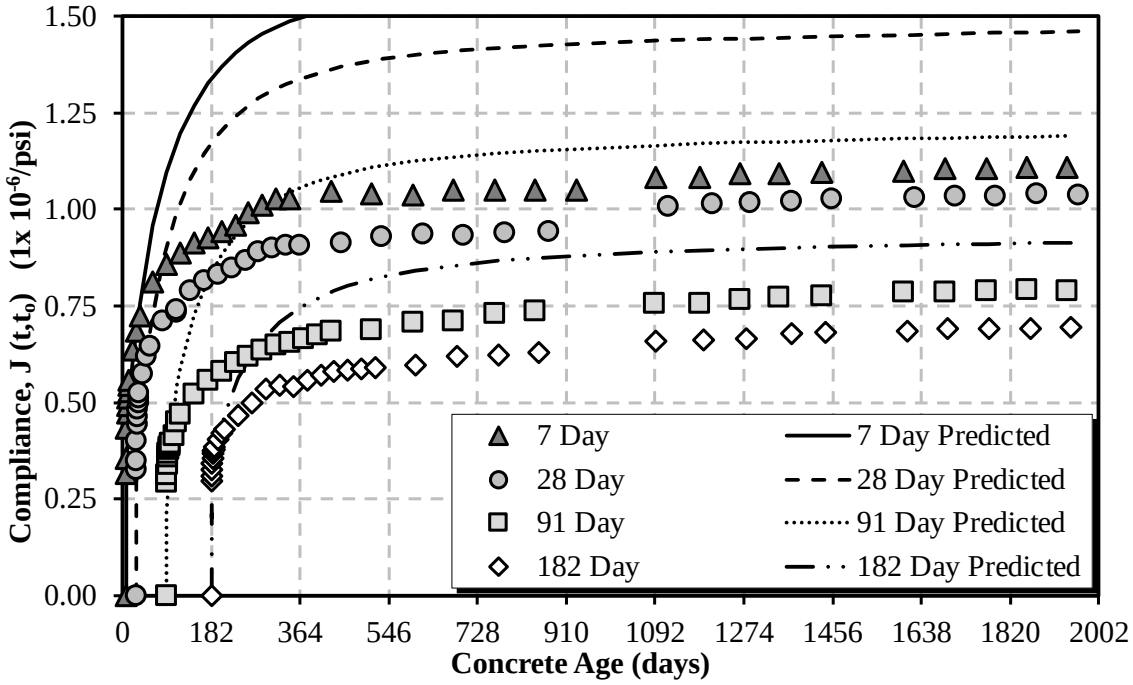

Figure B-29: B4* compliance for the 04/10/2018 sampling date

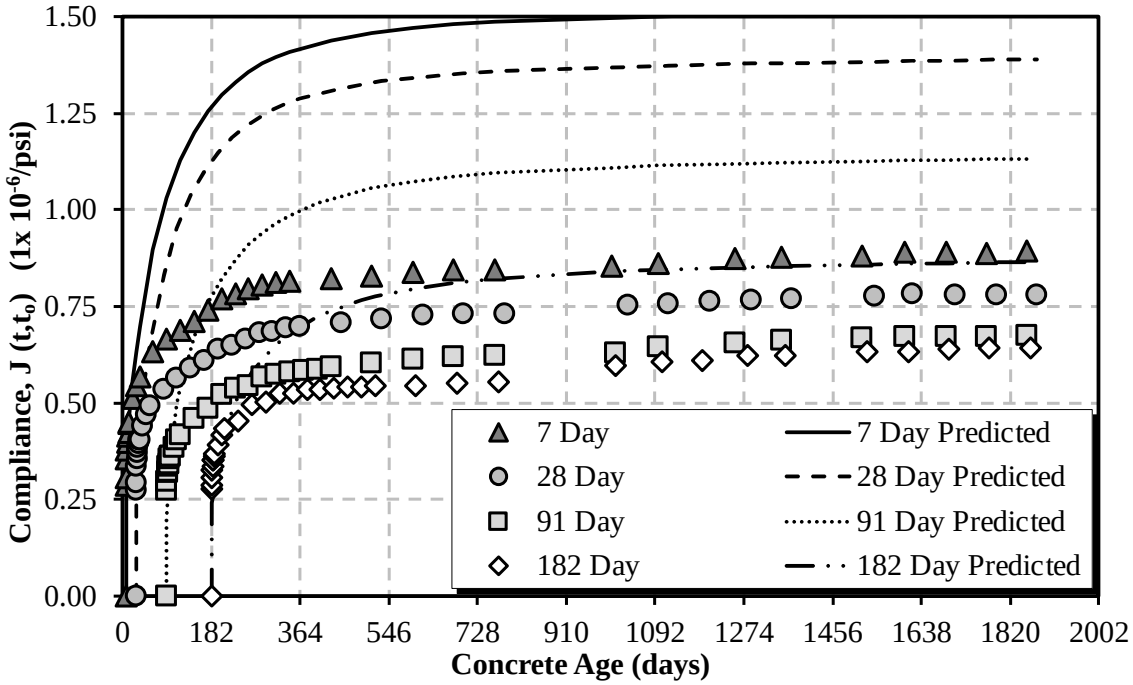

Figure B-30: B4* compliance for the 07/09/2018 sampling date

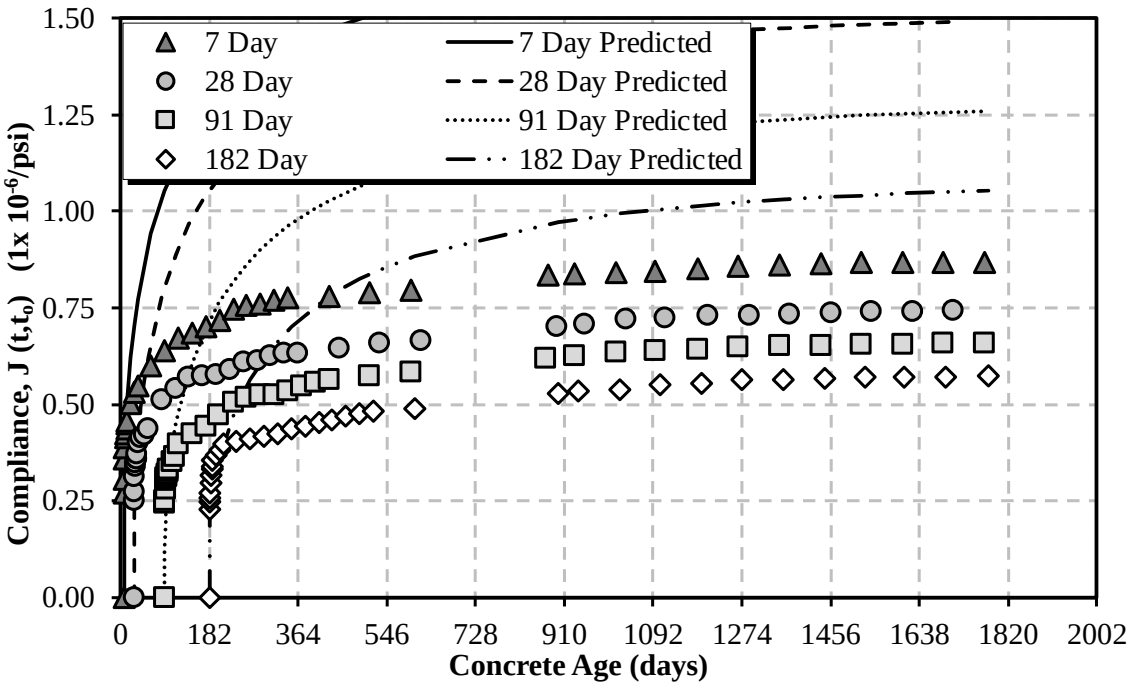

Figure B-31: B4* compliance for the 11/19/2018 sampling date

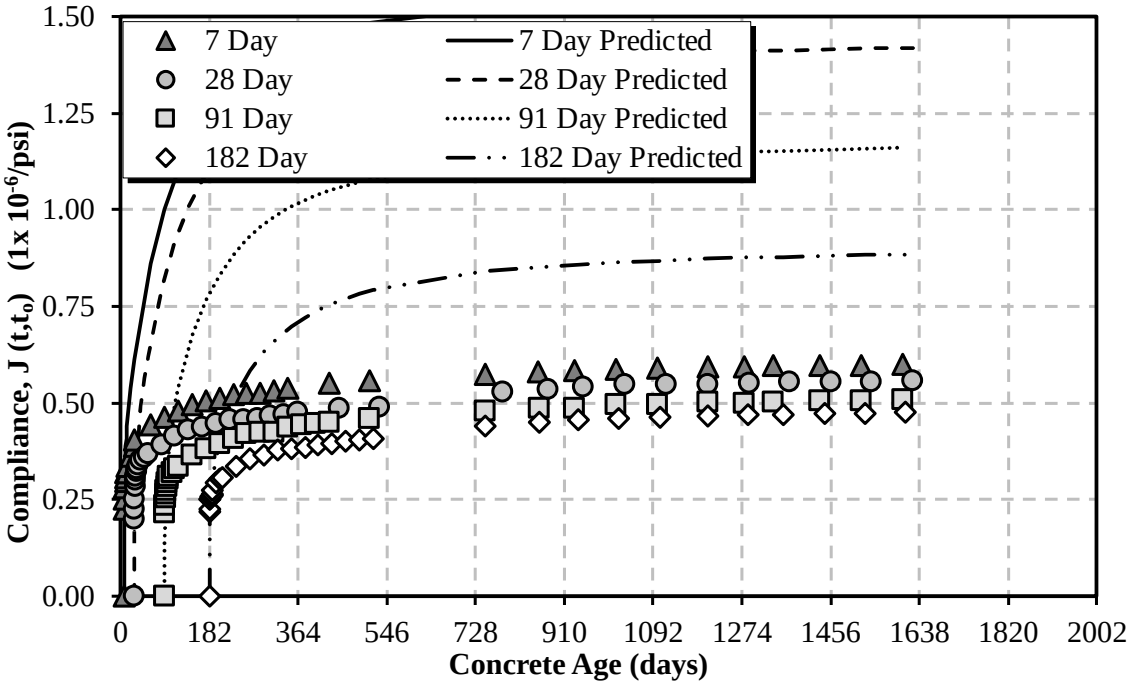

Figure B-32: B4* compliance for the 04/16/2019 sampling date

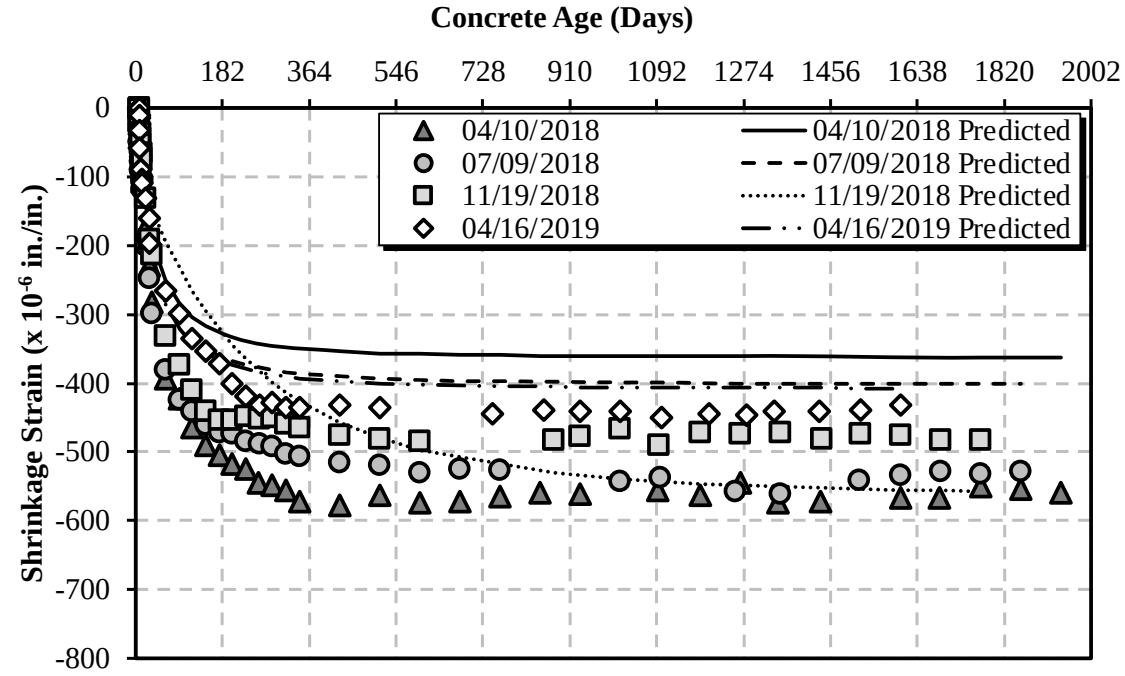

Figure B-33: B4* shrinkage for cylindrical specimens

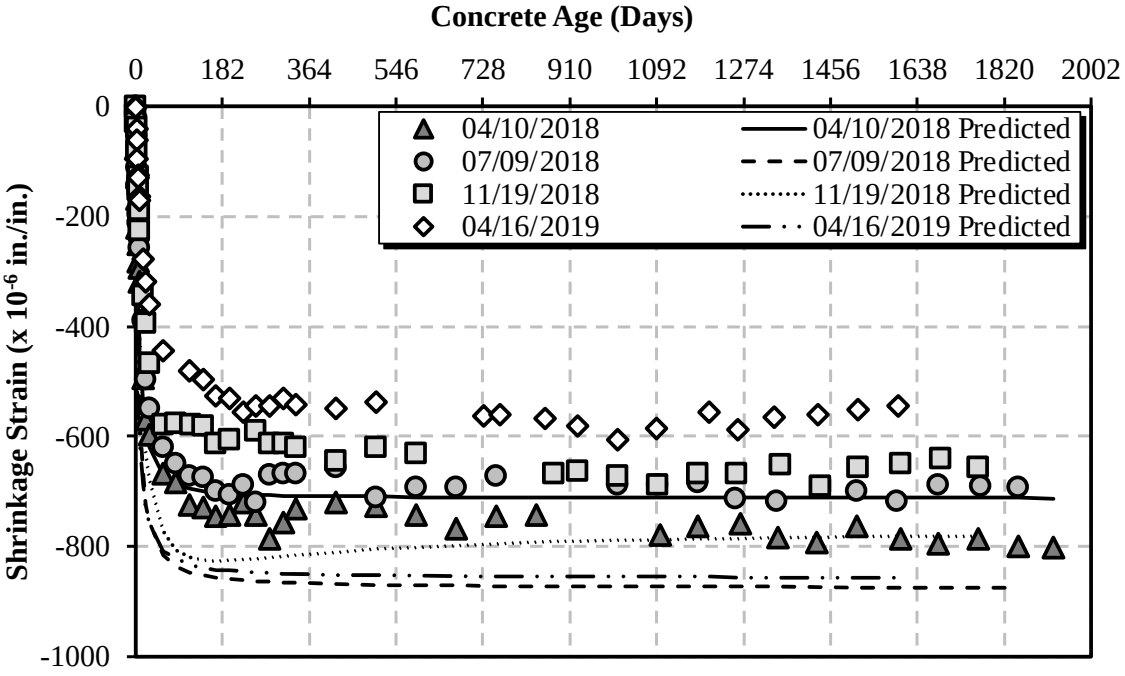

Figure B-34: B4* shrinkage for air-cured prisms

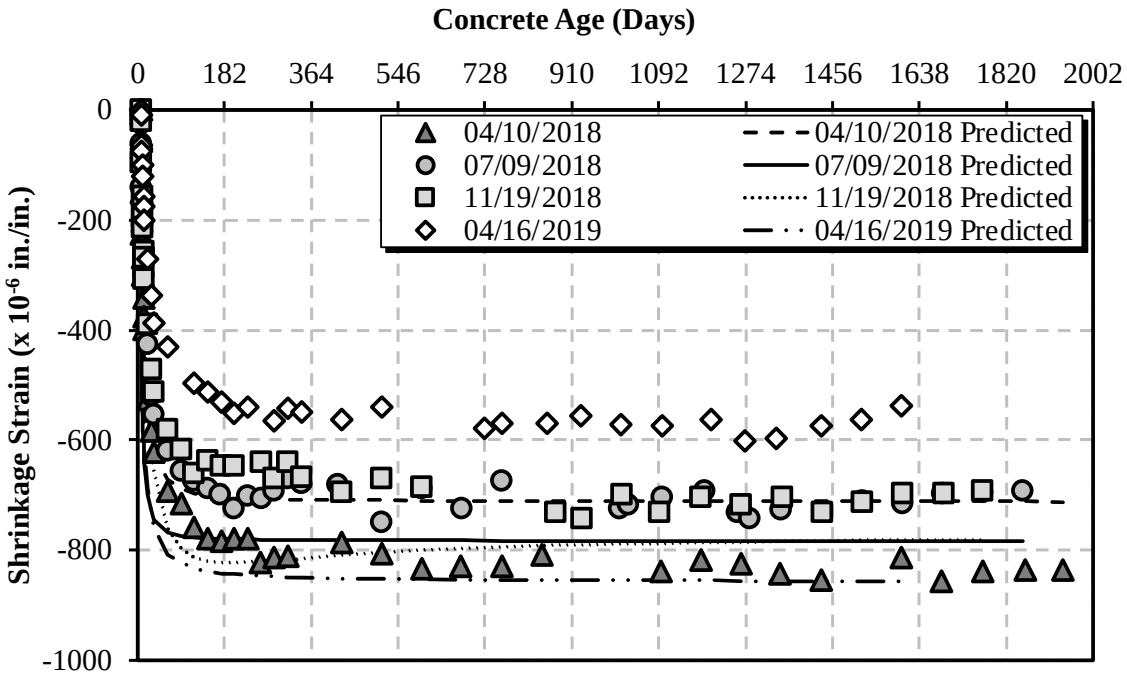

Figure B-35: B4* shrinkage for moist-cured prisms

B.6 CEB MC 1990 PREDICTION MODEL

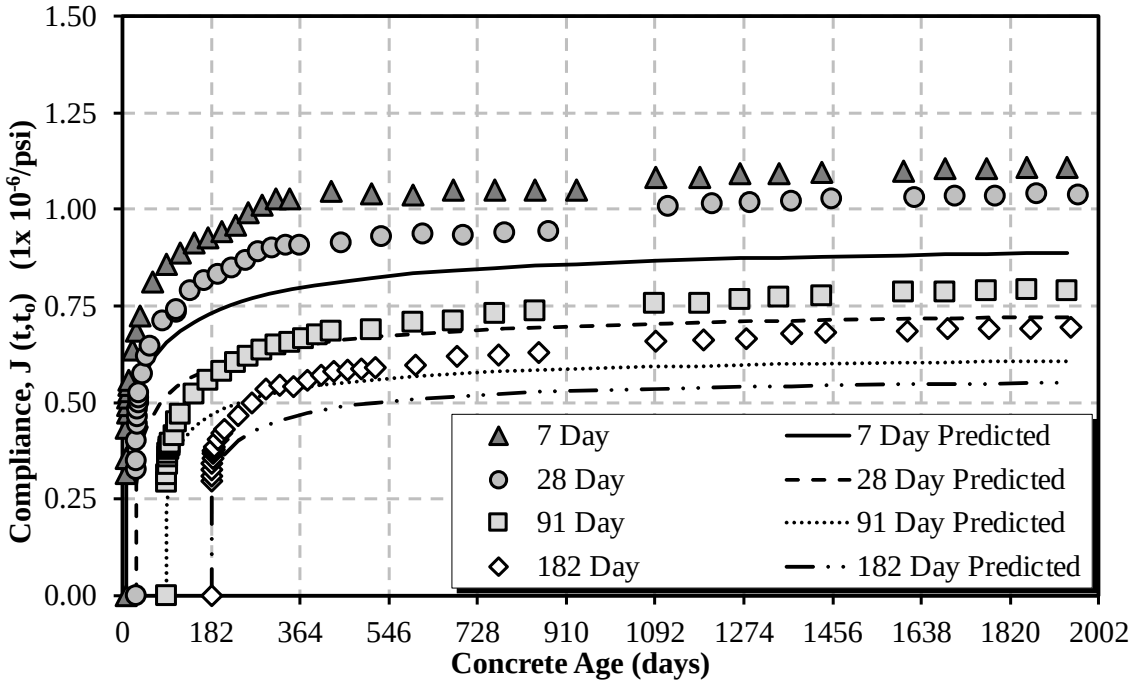

Figure B-36: CEB MC 1990 compliance for the 04/10/2018 sampling date

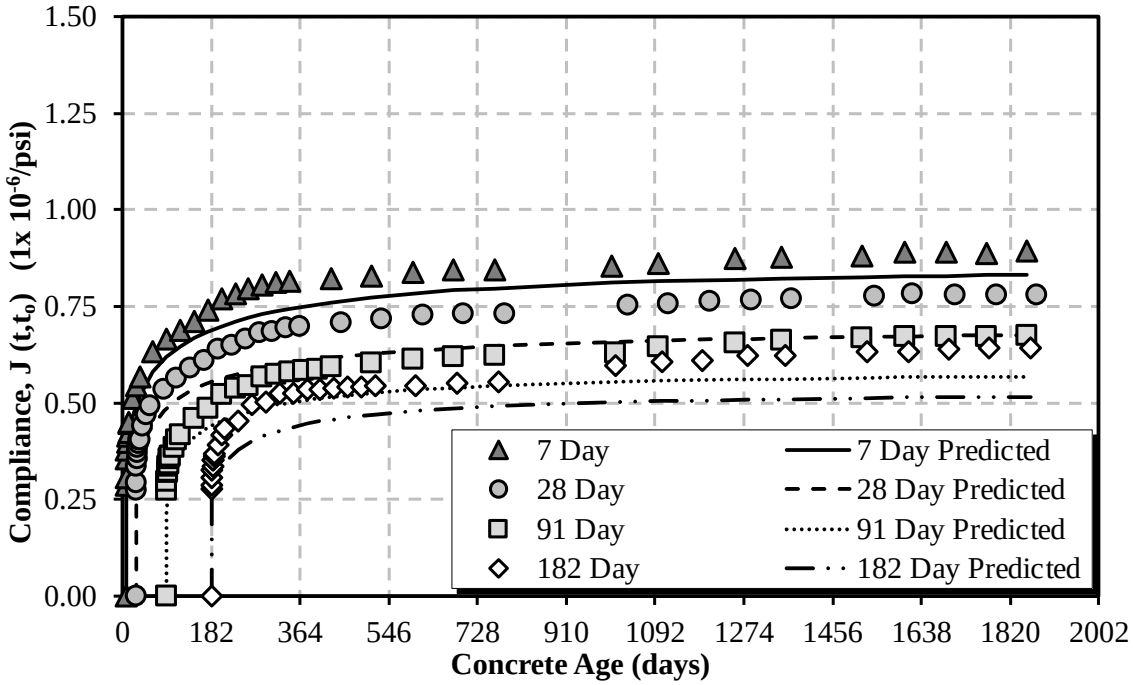

Figure B-37: CEB MC 1990 compliance for the 07/09/2018 sampling date

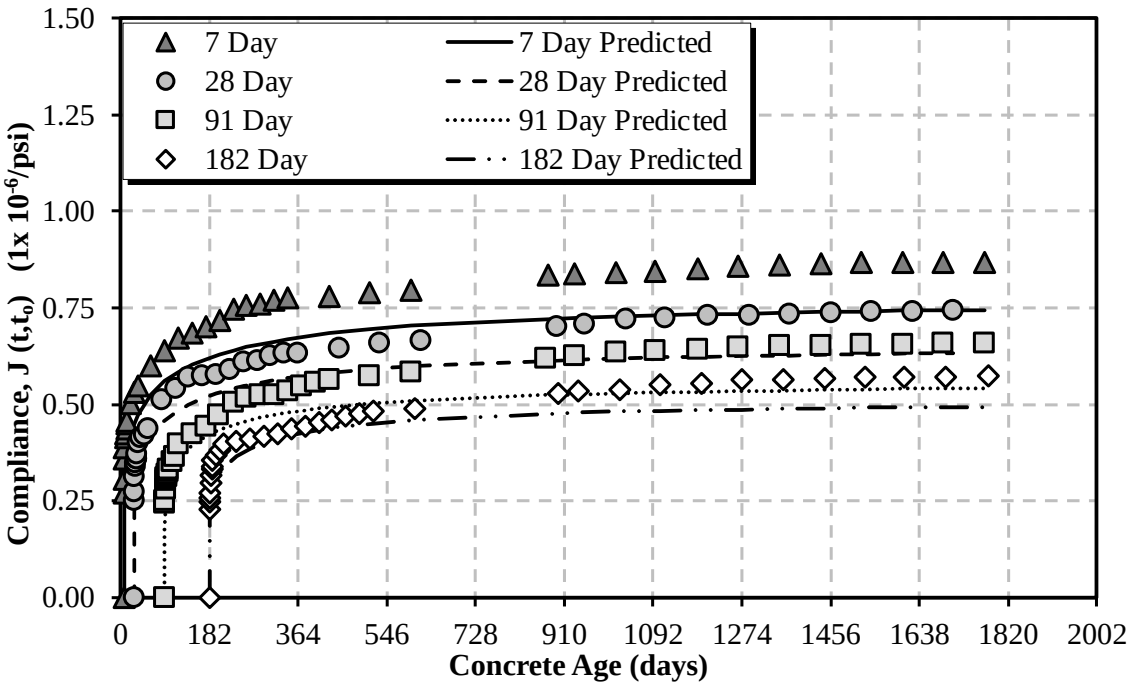

Figure B-38: CEB MC 1990 compliance for the 11/19/2018 sampling date

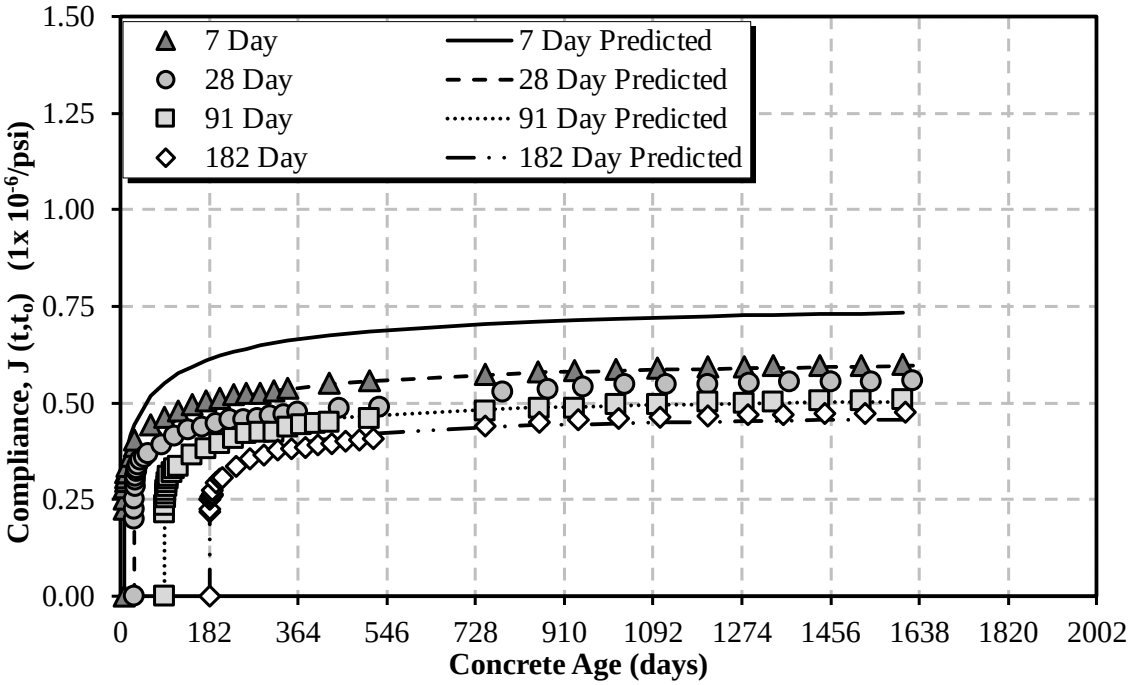

Figure B-39: CEB MC 1990 compliance for the 04/16/2019 sampling date

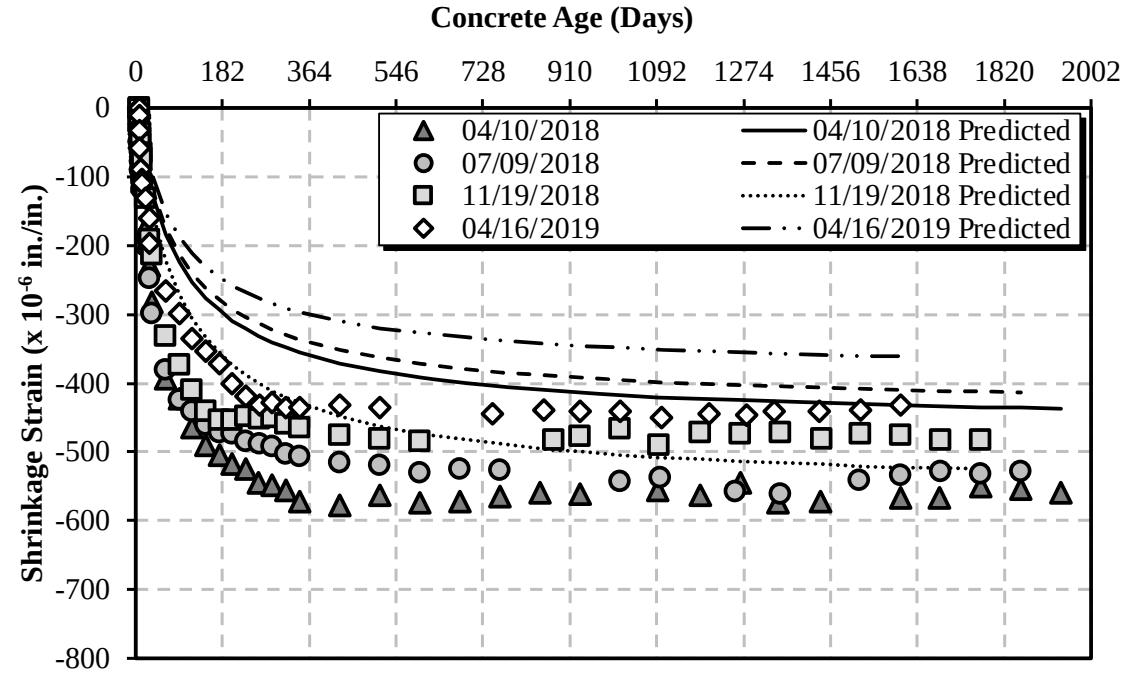

Figure B-40: CEB MC 1990 shrinkage for cylindrical specimens

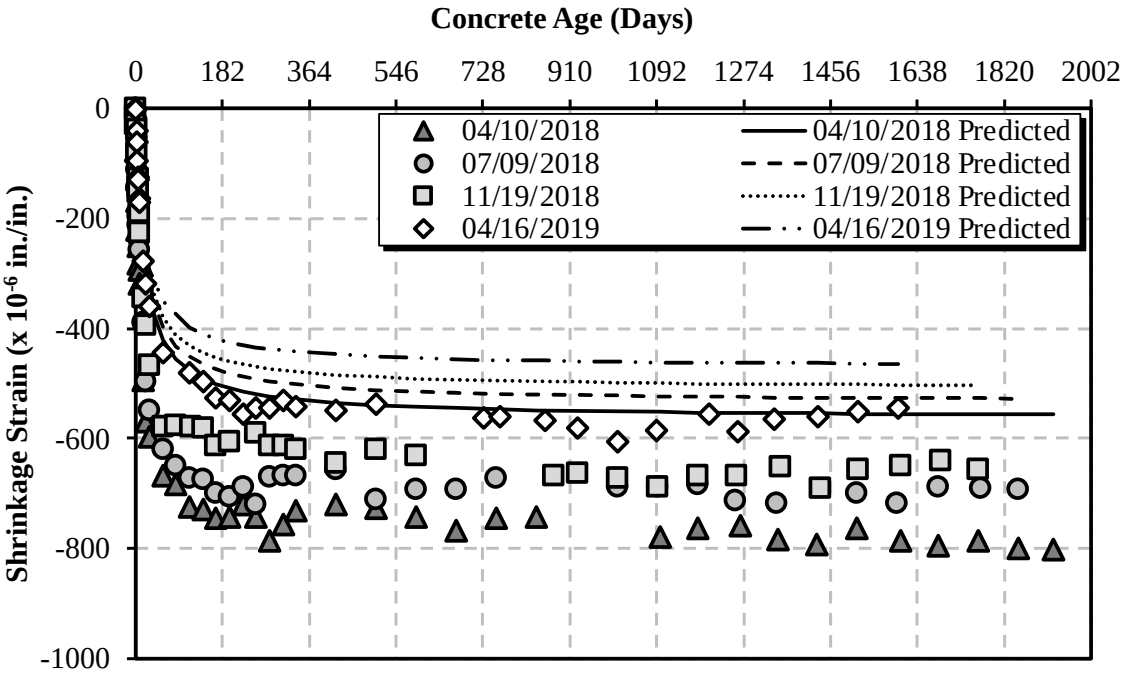

Figure B-41: CEB MC 1990 shrinkage for air-cured prisms

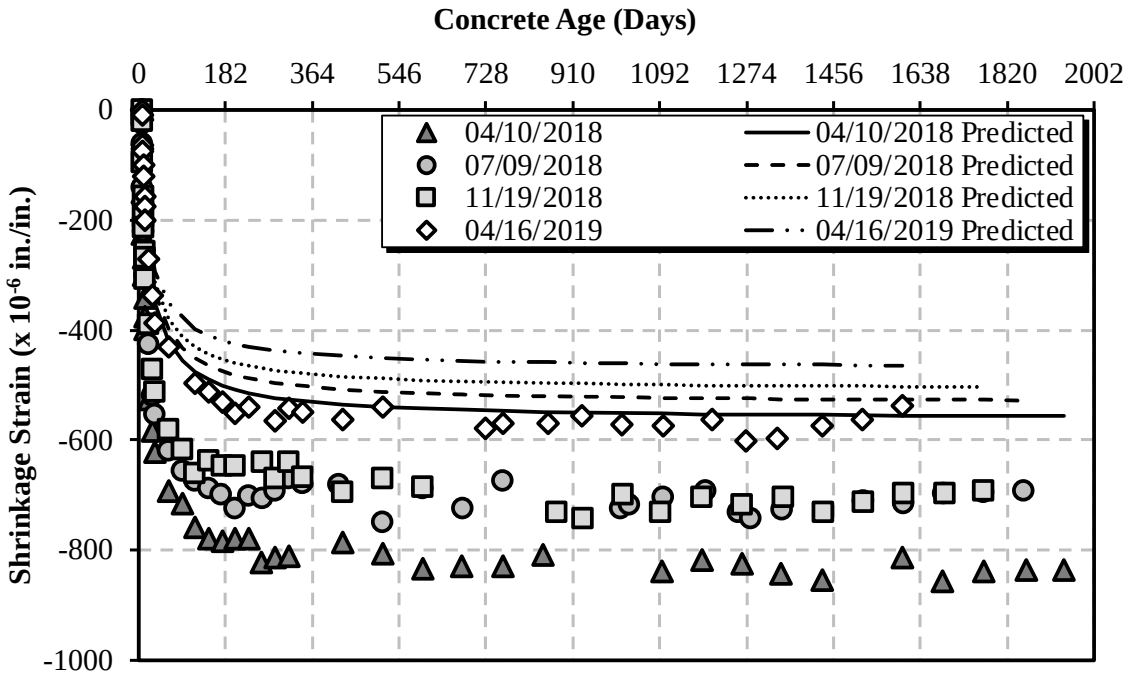

Figure B-42: CEB MC 1990 shrinkage for moist-cured prisms

B.7 CEB MC 90-99 PREDICTION MODEL

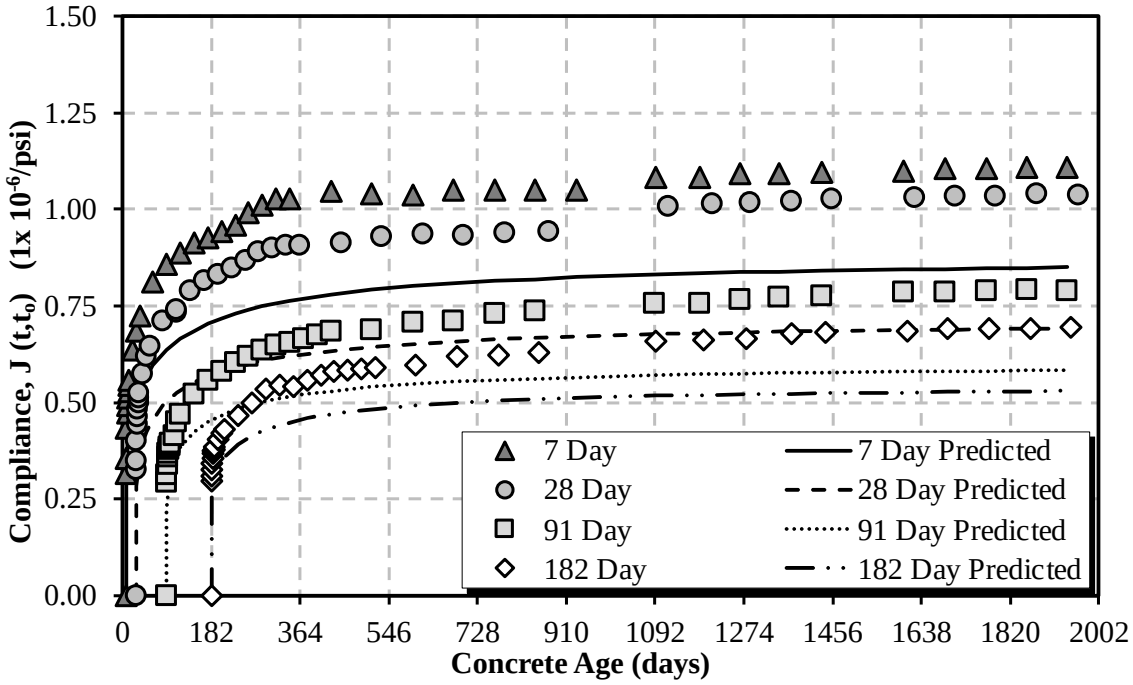

Figure B-43: CEB MC 90-99 compliance for the 04/10/2018 sampling date

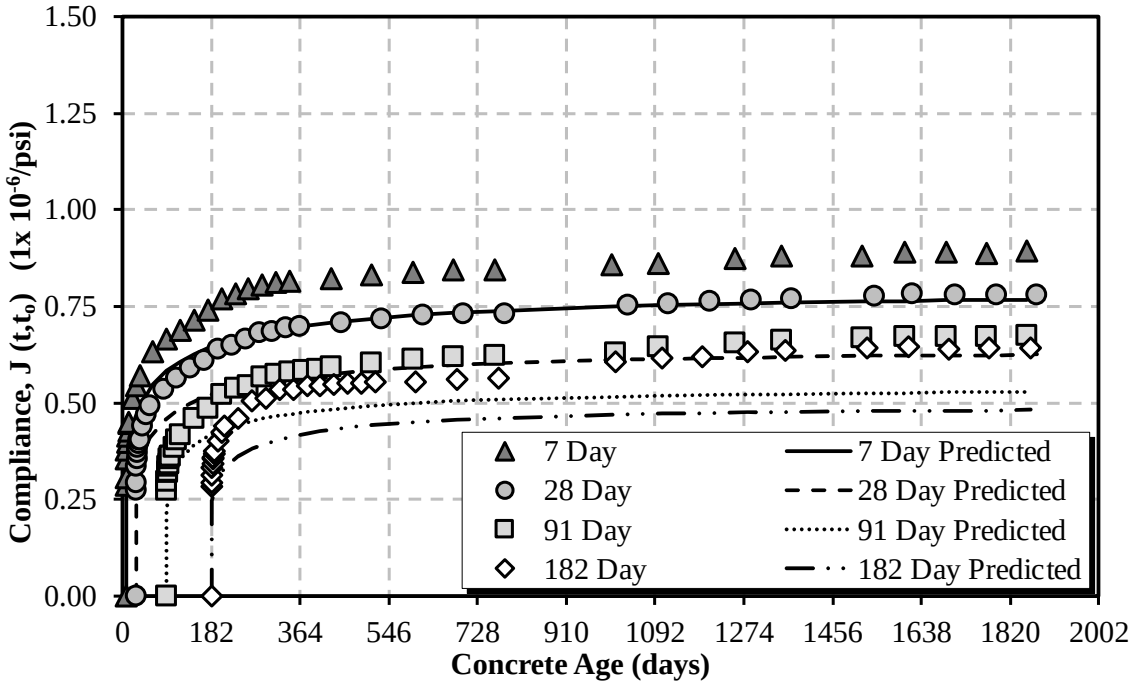

Figure B-44: CEB MC 90-99 compliance for the 07/09/2018 sampling date

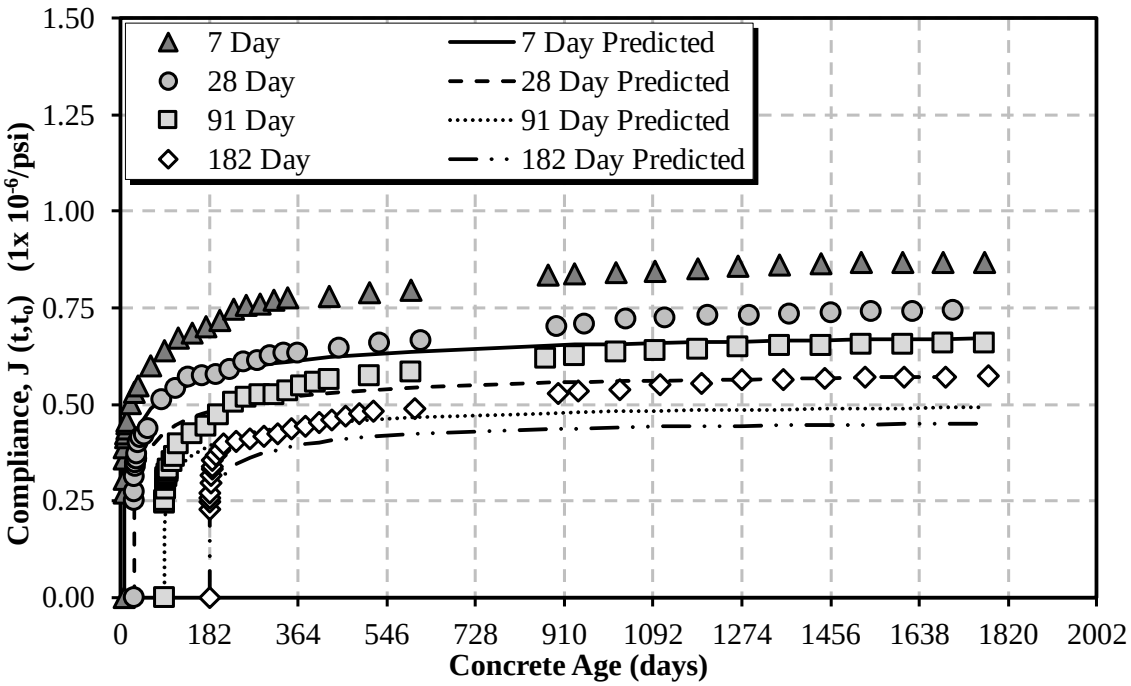

Figure B-45: CEB MC 90-99 compliance for the 11/19/2018 sampling date

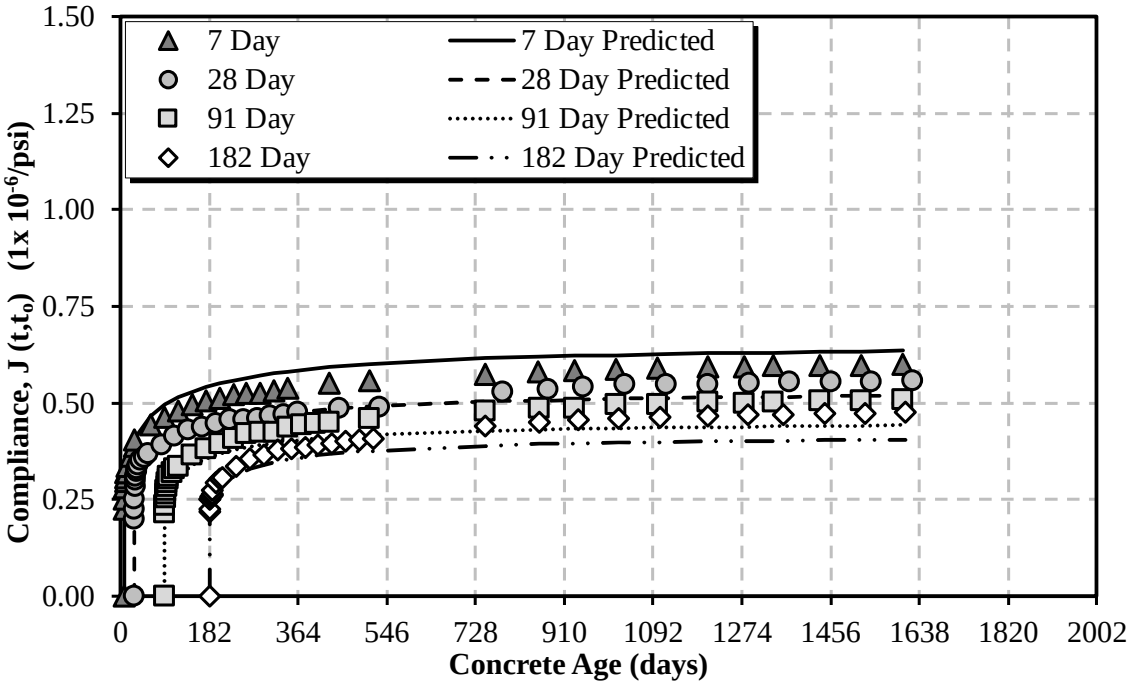

Figure B-46: CEB MC 90-99 compliance for the 04/16/2019 sampling date

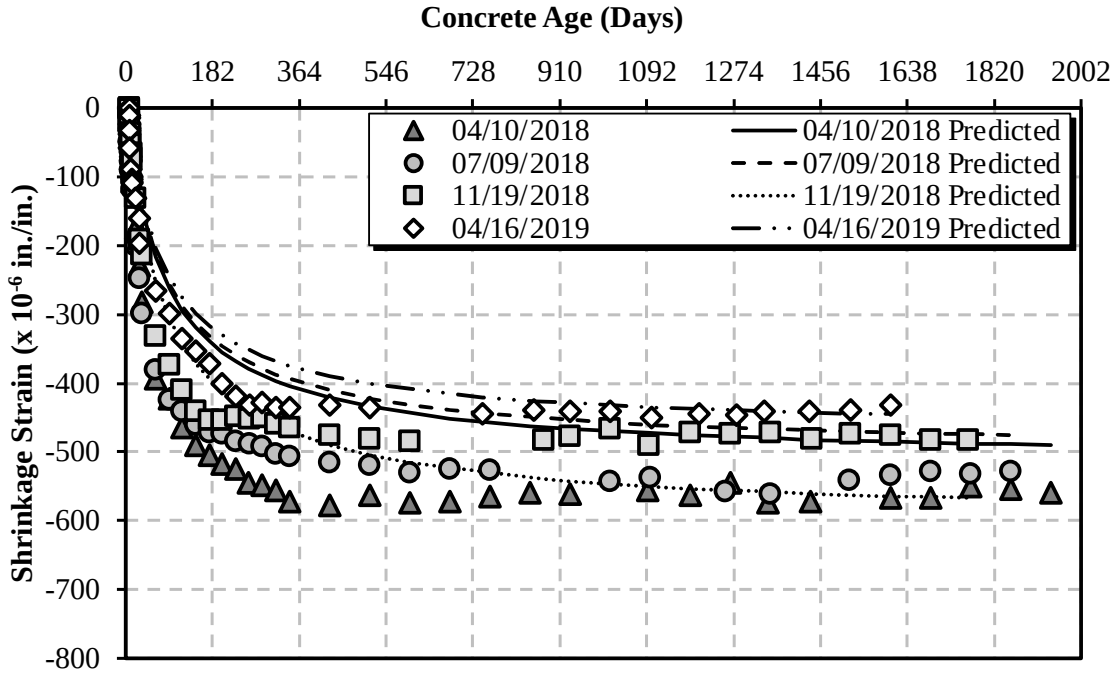

Figure B-47: CEB MC 90-99 shrinkage for cylindrical specimens

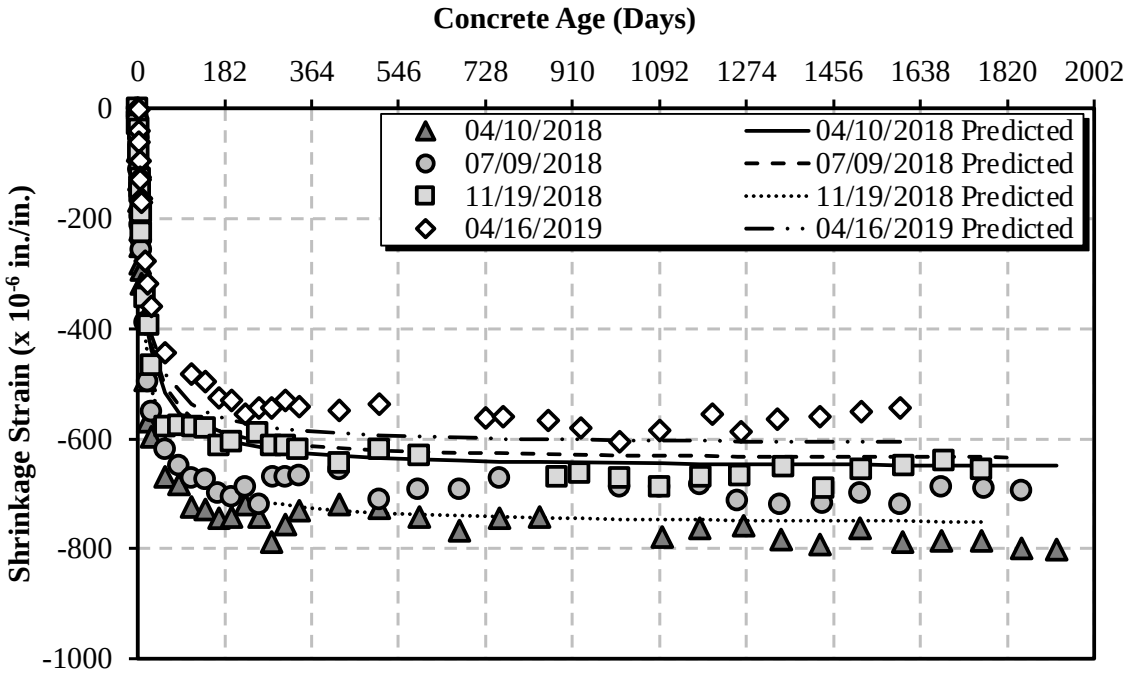

Figure B-48: CEB MC 90-99 shrinkage for air-cured prisms

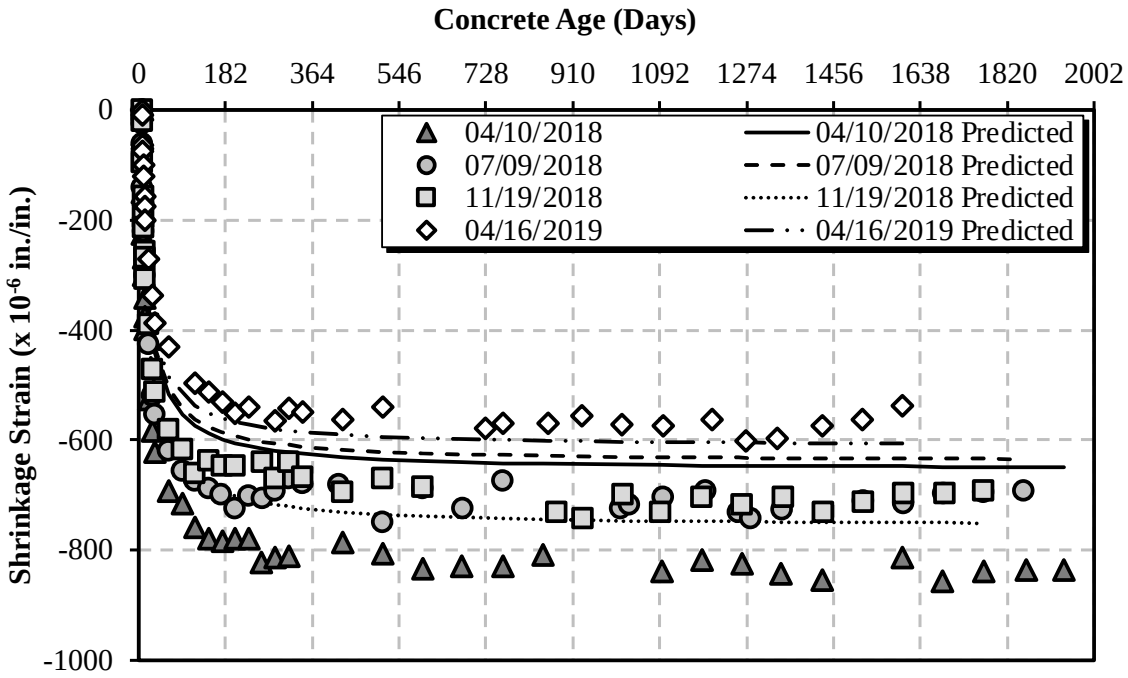

Figure B-49: CEB MC 90-99 shrinkage for moist-cured prisms

B.8 CEB MC 2010 PREDICTION MODEL

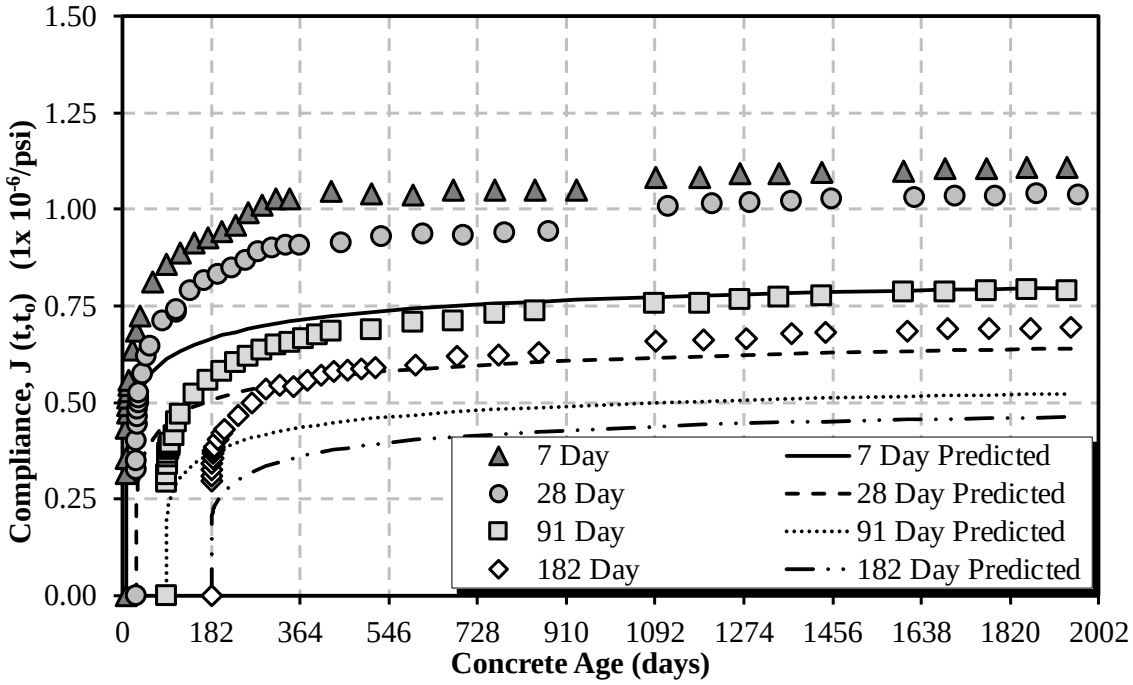

Figure B-50: CEB MC 2010 compliance for the 04/10/2018 sampling date

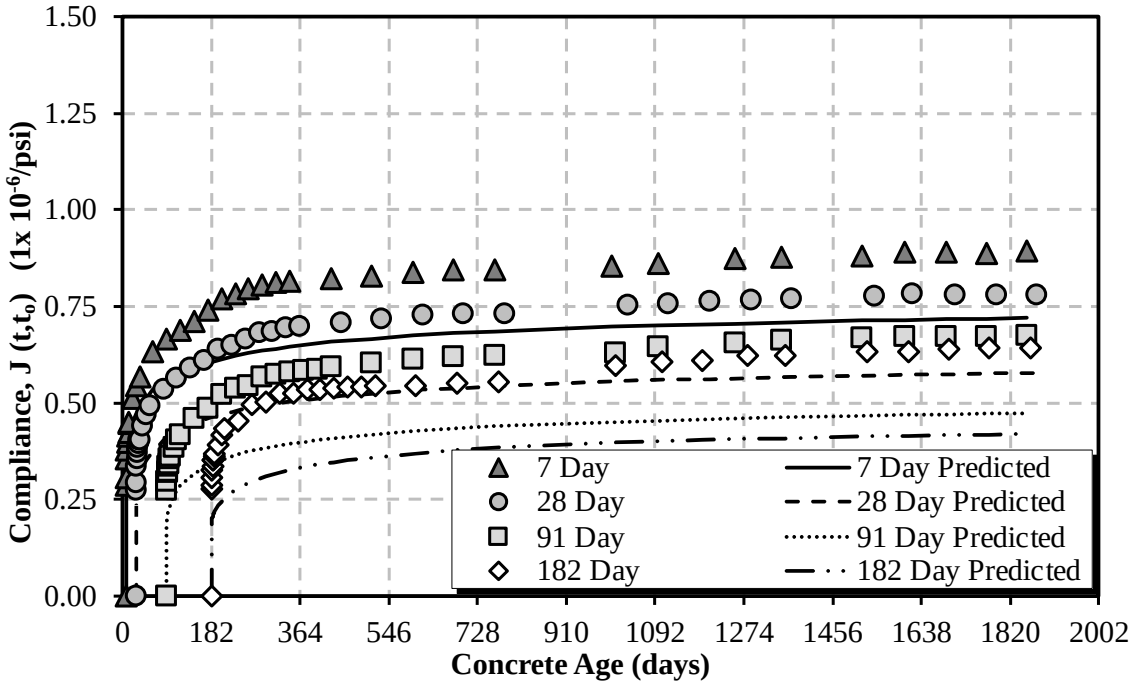

Figure B-51: CEB MC 2010 compliance for the 07/09/2018 sampling date

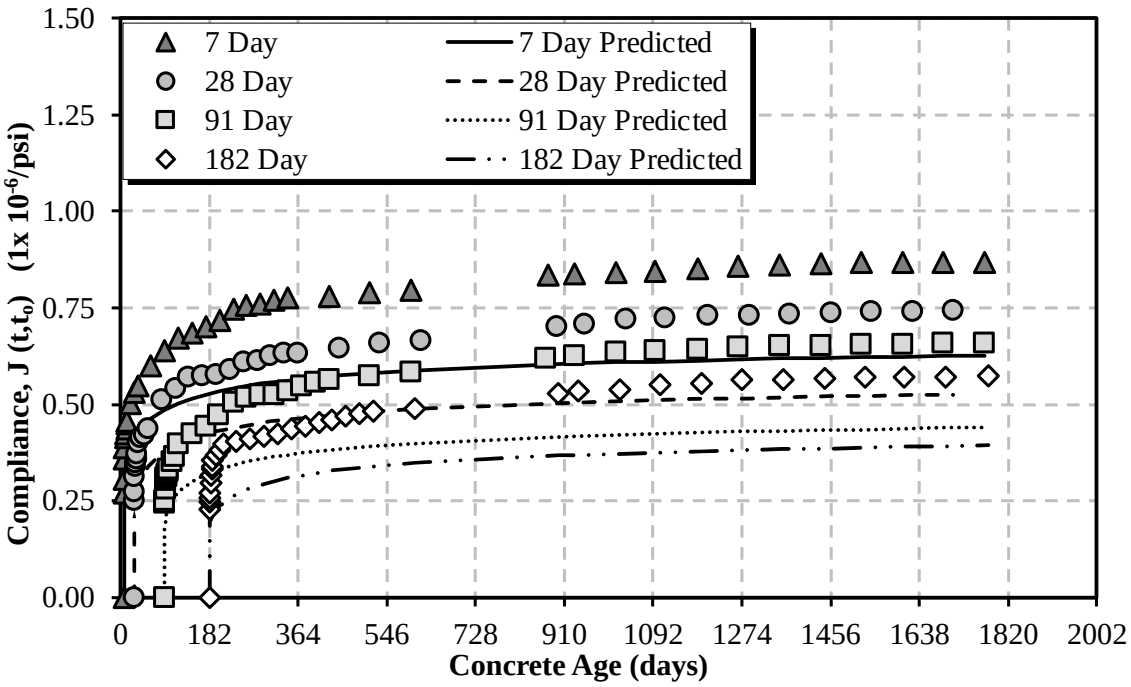

Figure B-52: CEB MC 2010 compliance for the 11/19/2018 sampling date

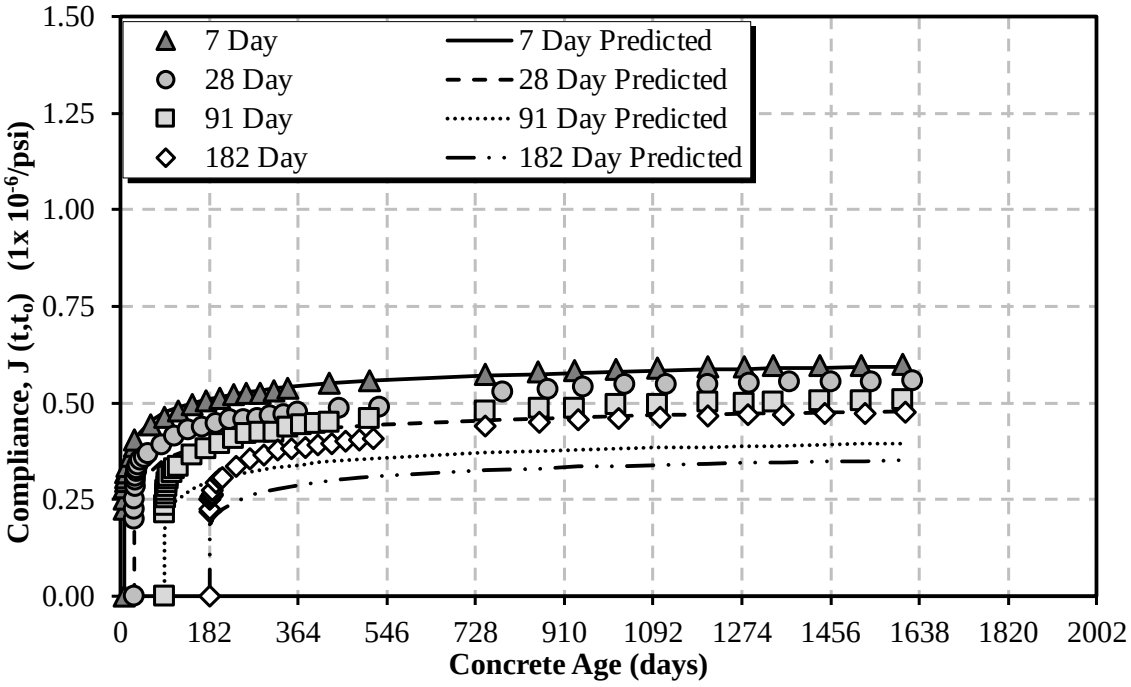

Figure B-53: CEB MC 2010 compliance for the 04/16/2019 sampling date

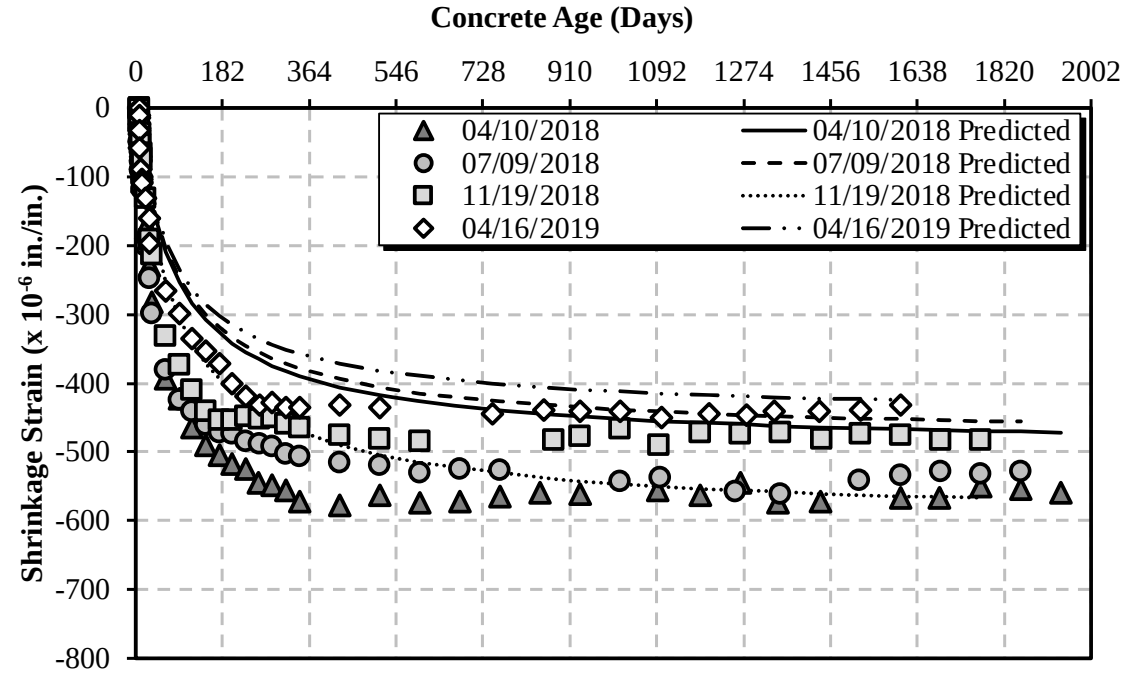

Figure B-54: CEB MC 2010 shrinkage for cylindrical specimens

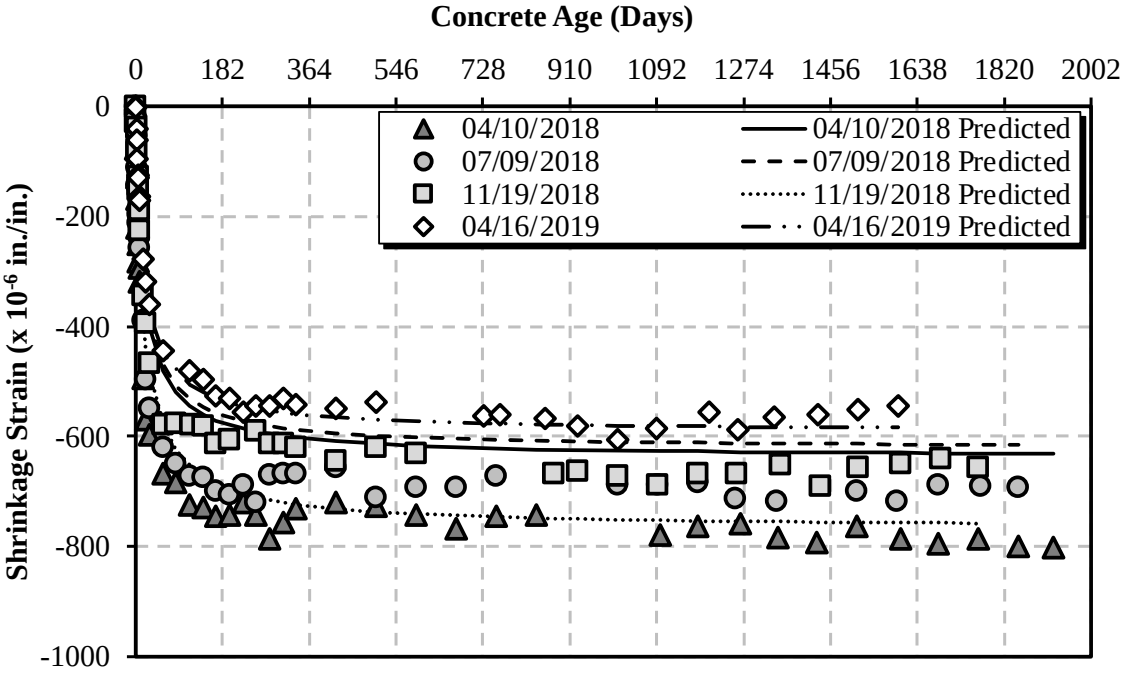

Figure B-55: CEB MC 2010 shrinkage for air-cured prisms

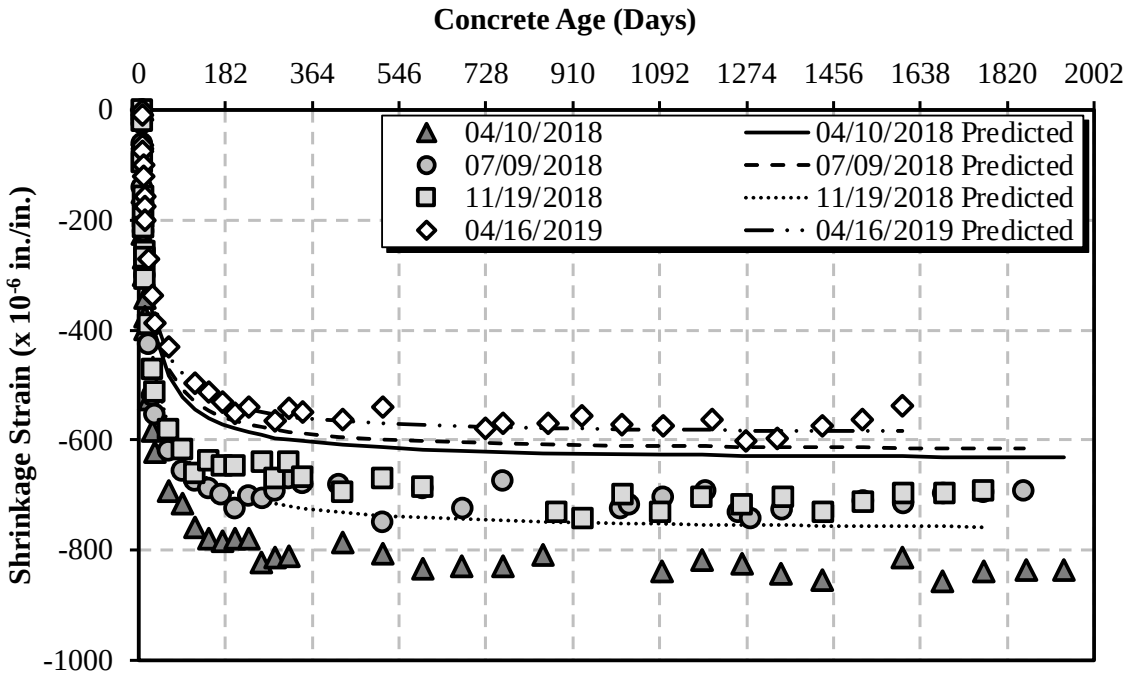

Figure B-56: CEB MC 2010 shrinkage for moist-cured prisms

B.9 GL 2000 PREDICTION MODEL

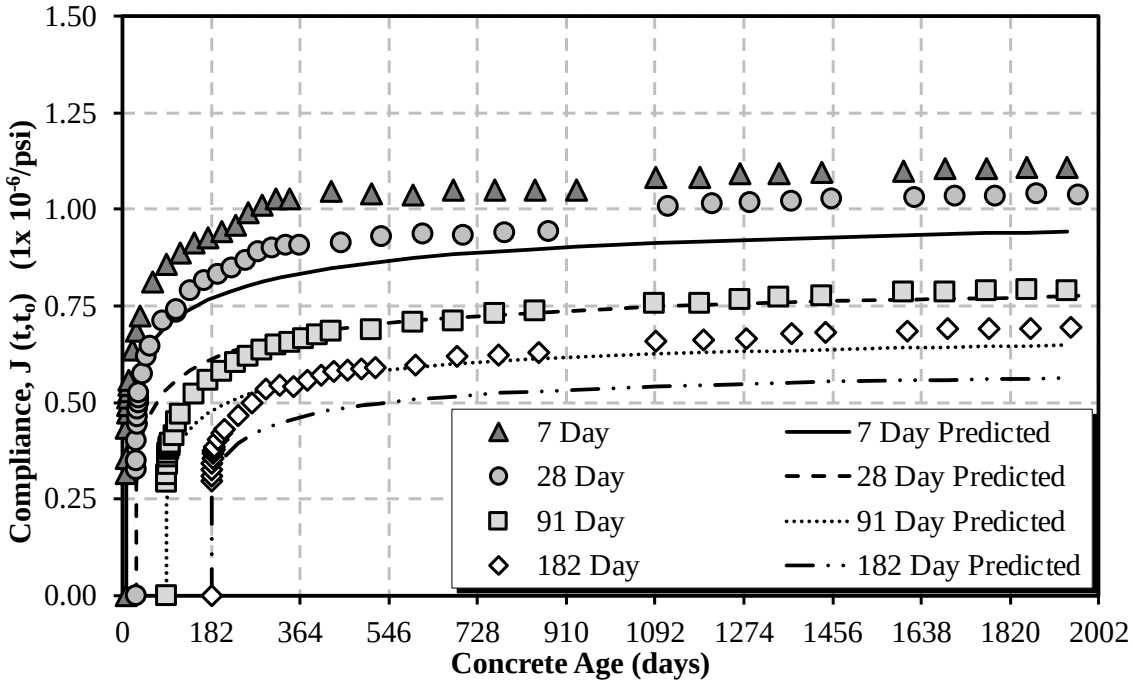

Figure B-57: GL 2000 compliance for the 04/10/2018 sampling date

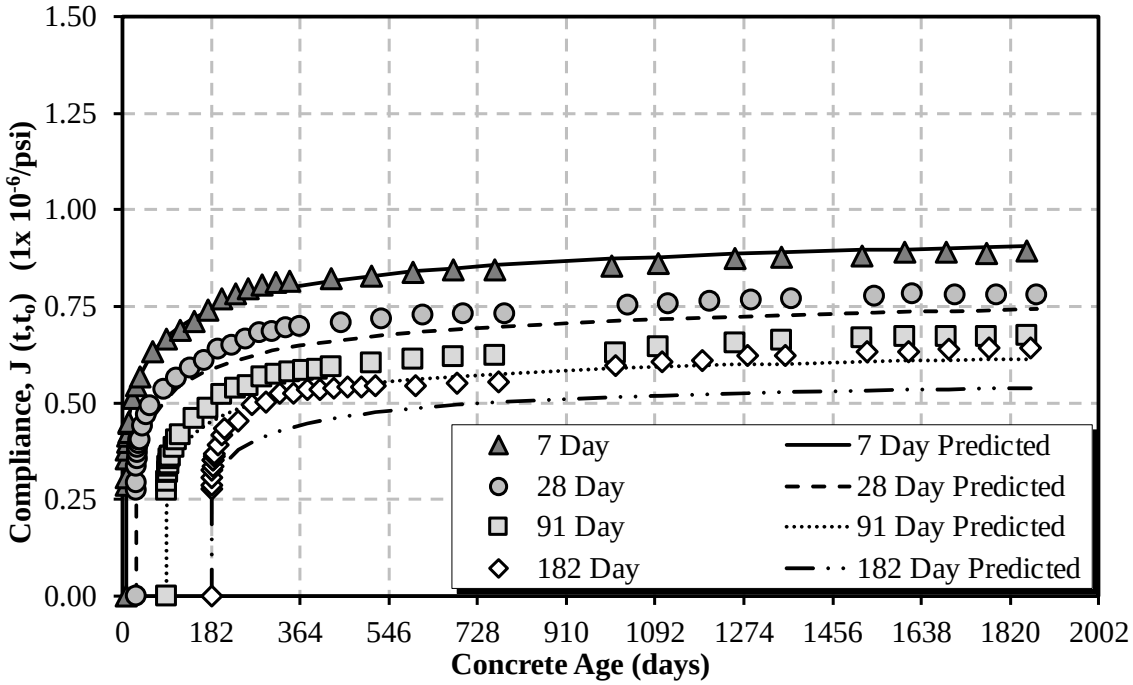

Figure B-58: GL 2000 compliance for the 07/09/2018 sampling date

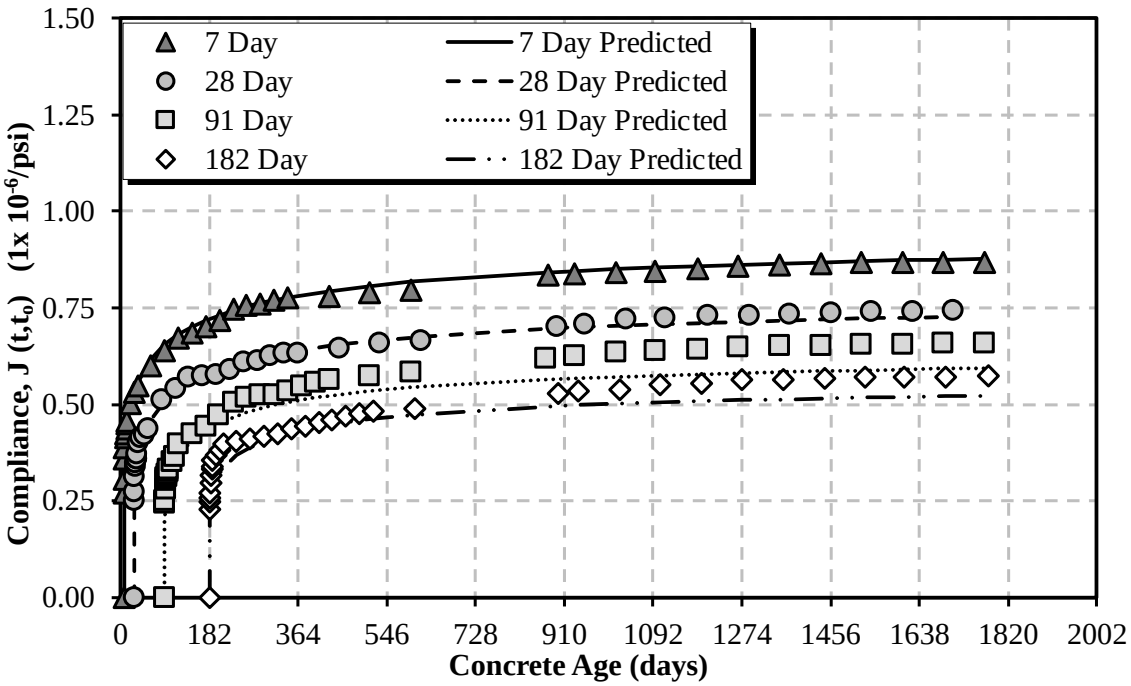

Figure B-59: GL 2000 compliance for the 11/19/2018 sampling date

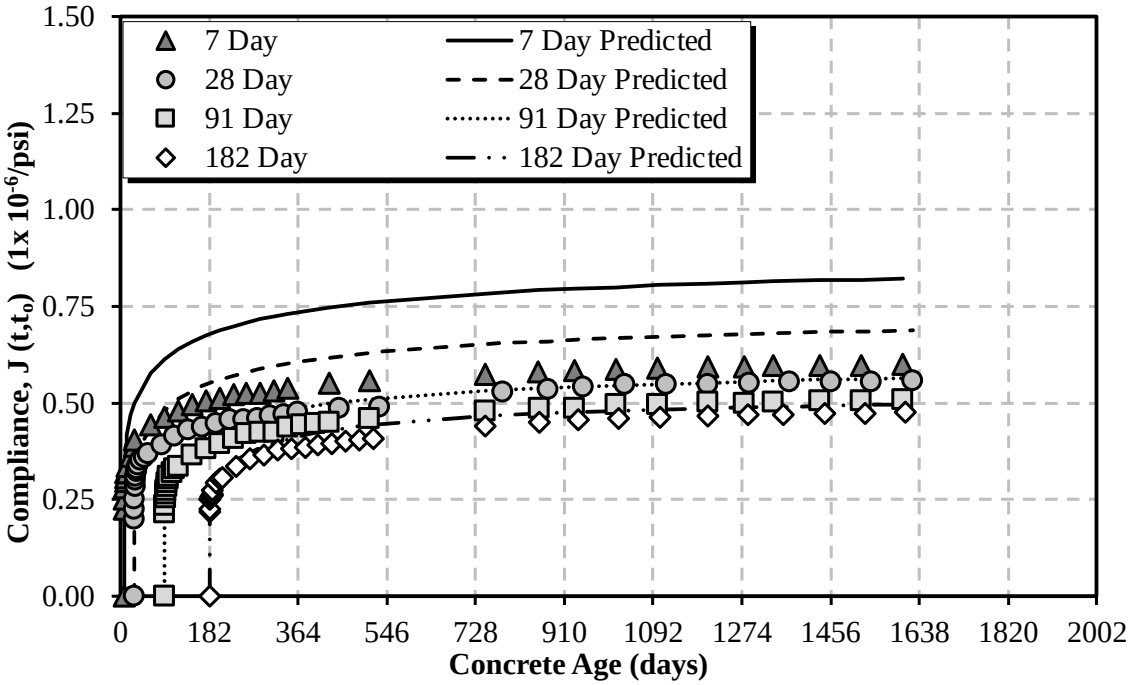

Figure B-60: GL 2000 compliance for the 04/16/2019 sampling date

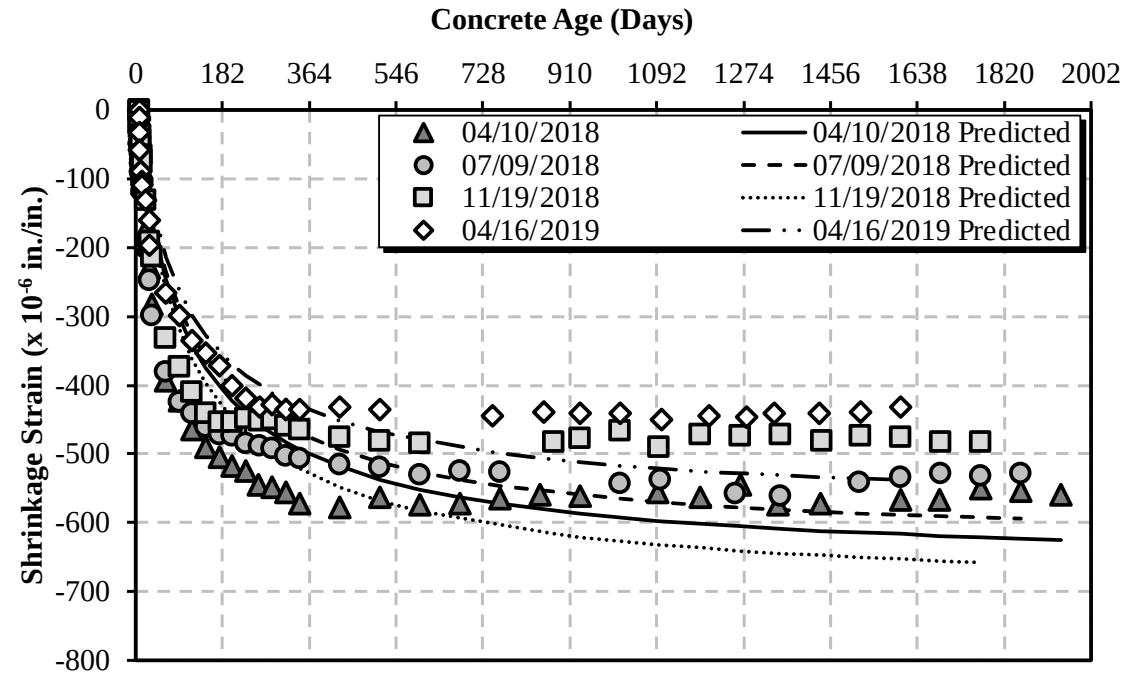

Figure B-61: GL 2000 shrinkage for cylindrical specimens

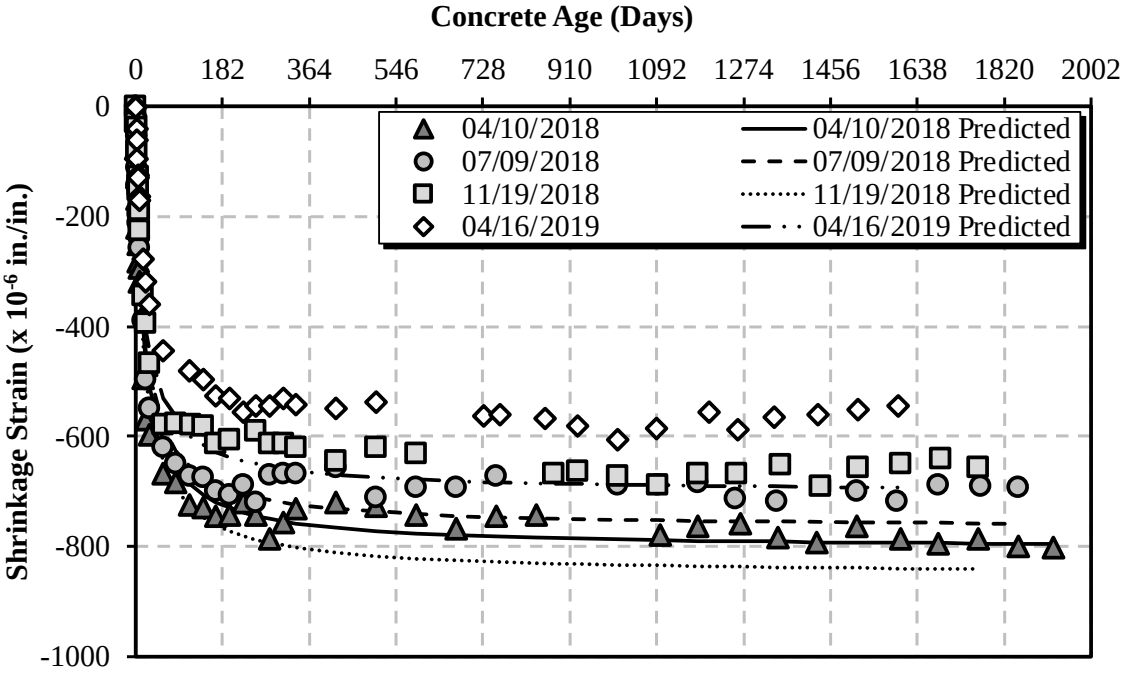

Figure B-62: GL 2000 shrinkage for air-cured prisms

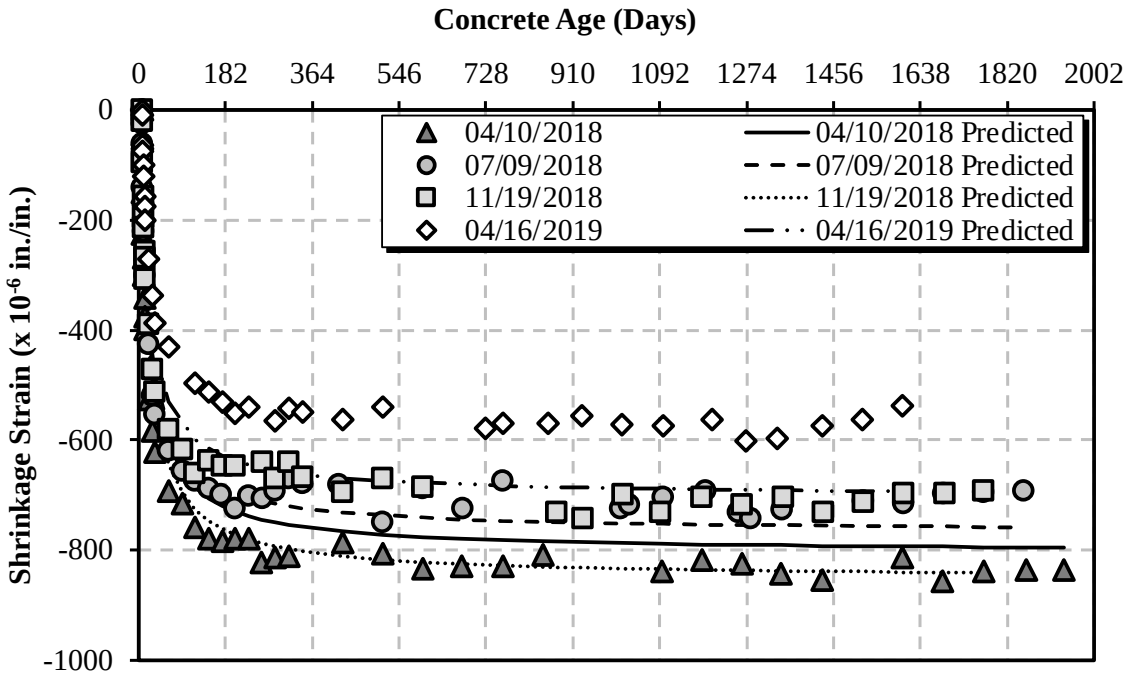

Figure B-63: GL 2000 shrinkage for moist-cured prisms

B.10 CALIBRATED CEB MC 90-99 PREDICTION MODEL

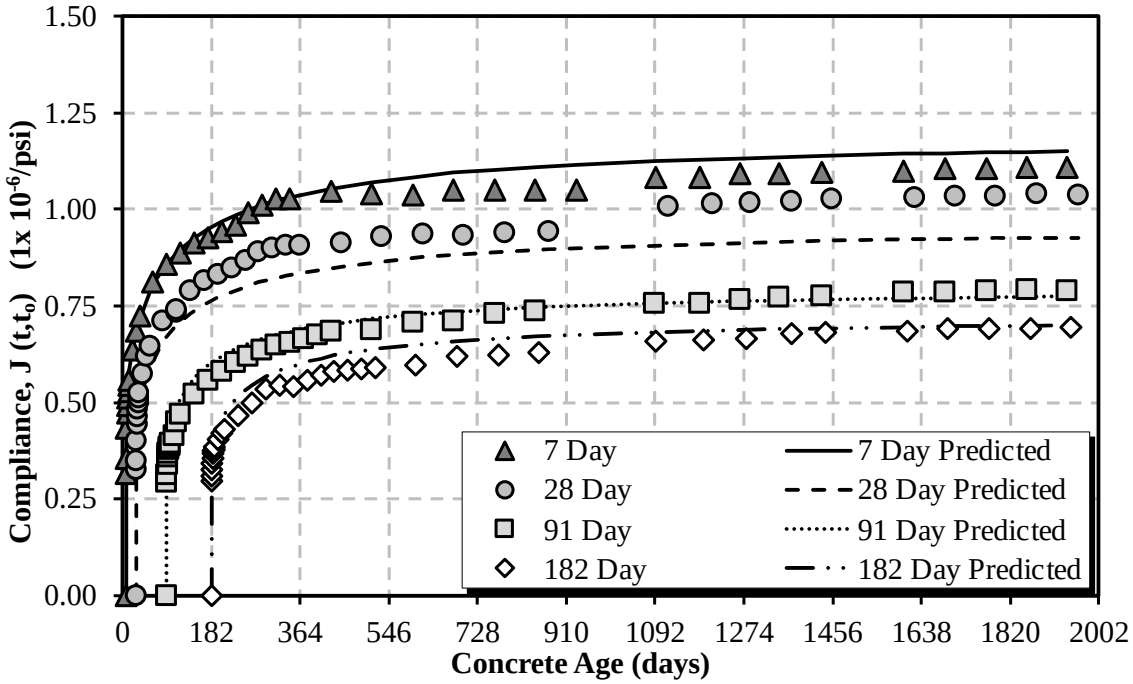

Figure B-64: Calibrated CEB MC 90-99 compliance for the 04/10/2018 sampling date

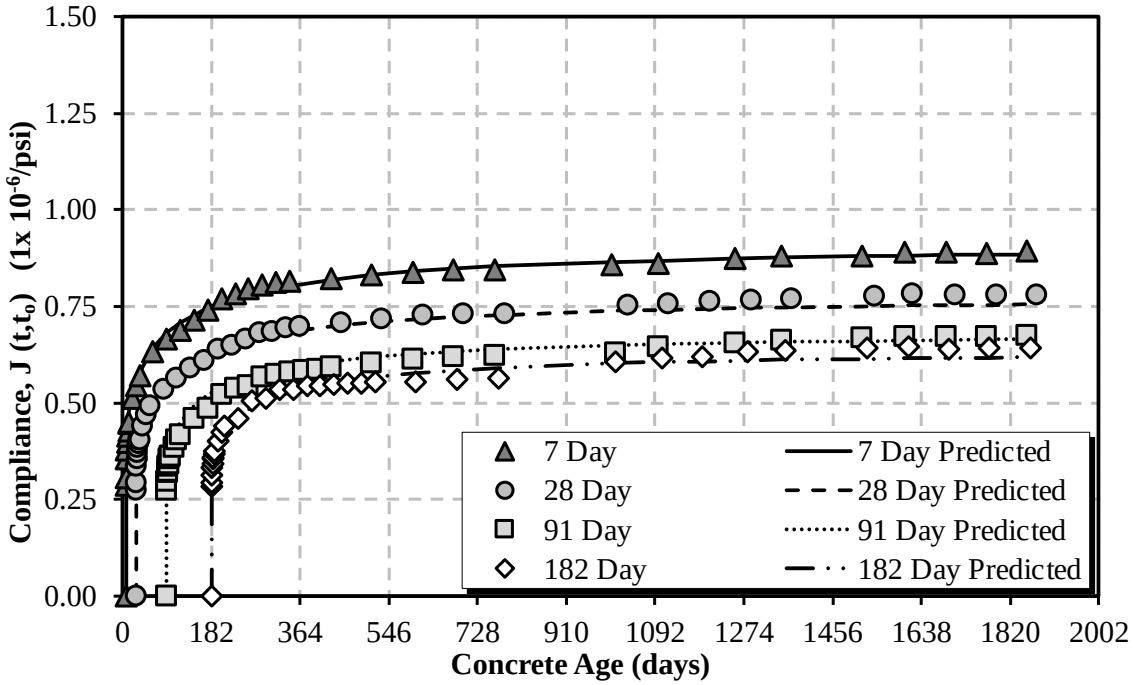

Figure B-65: Calibrated CEB MC 90-99 compliance for the 07/09/2018 sampling date

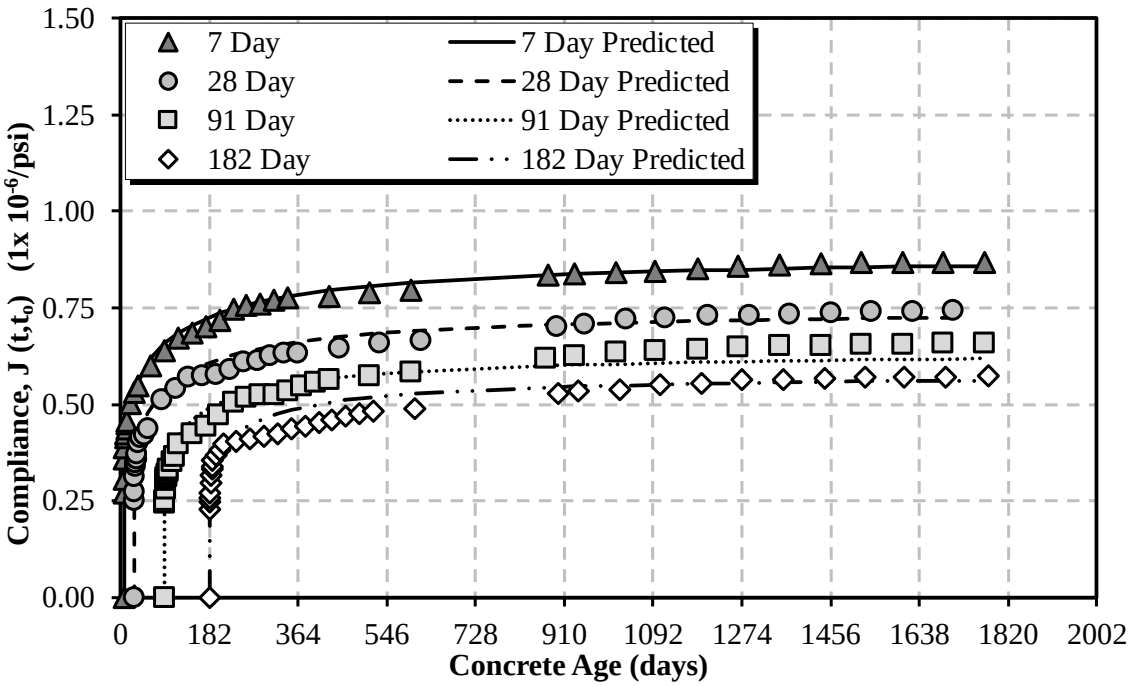

Figure B-66: Calibrated CEB MC 90-99 compliance for the 11/19/2018 sampling date

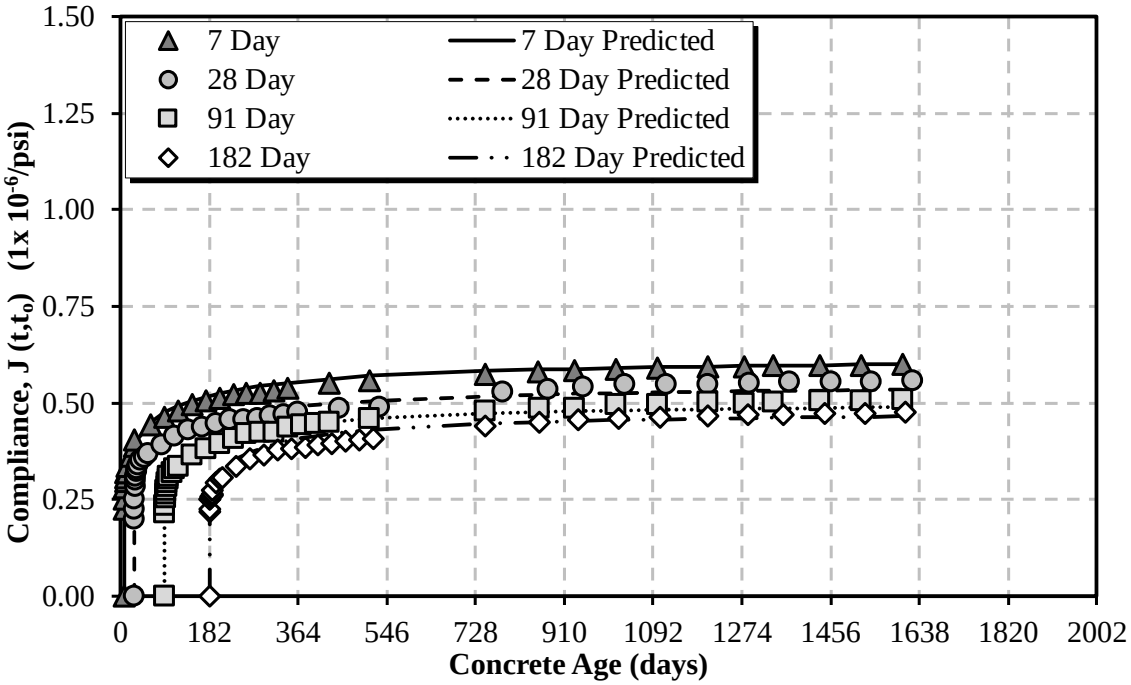

Figure B-67: Calibrated CEB MC 90-99 compliance for the 04/16/2019 sampling date

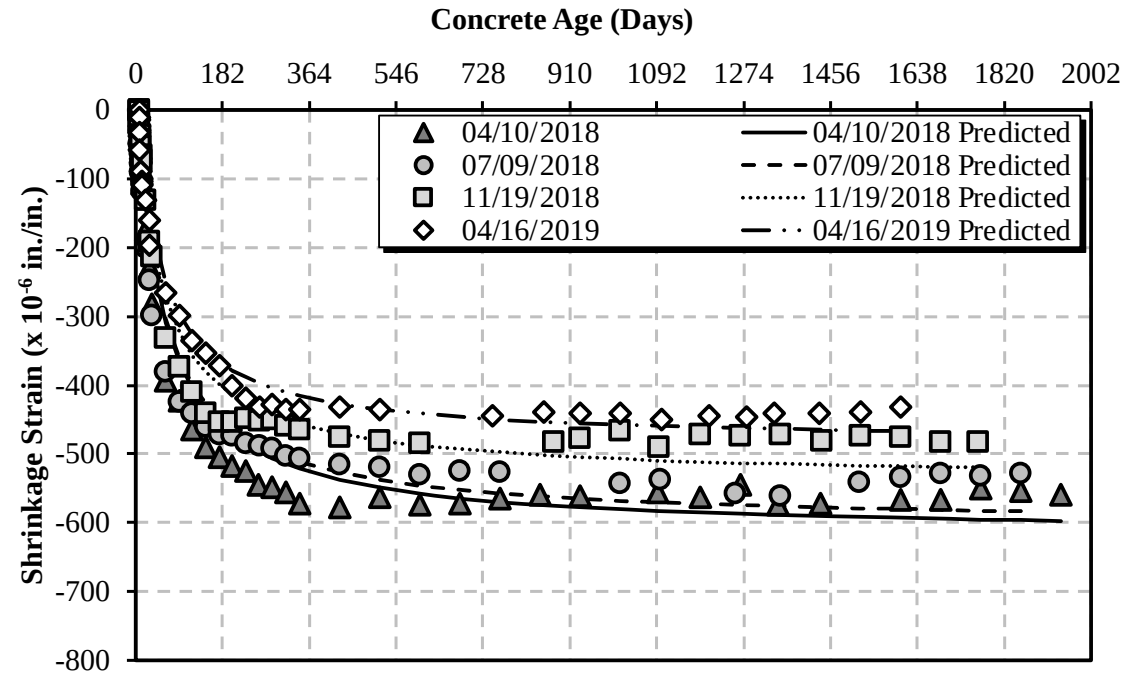

Figure B-68: Calibrated CEB MC 90-99 shrinkage for cylindrical specimens

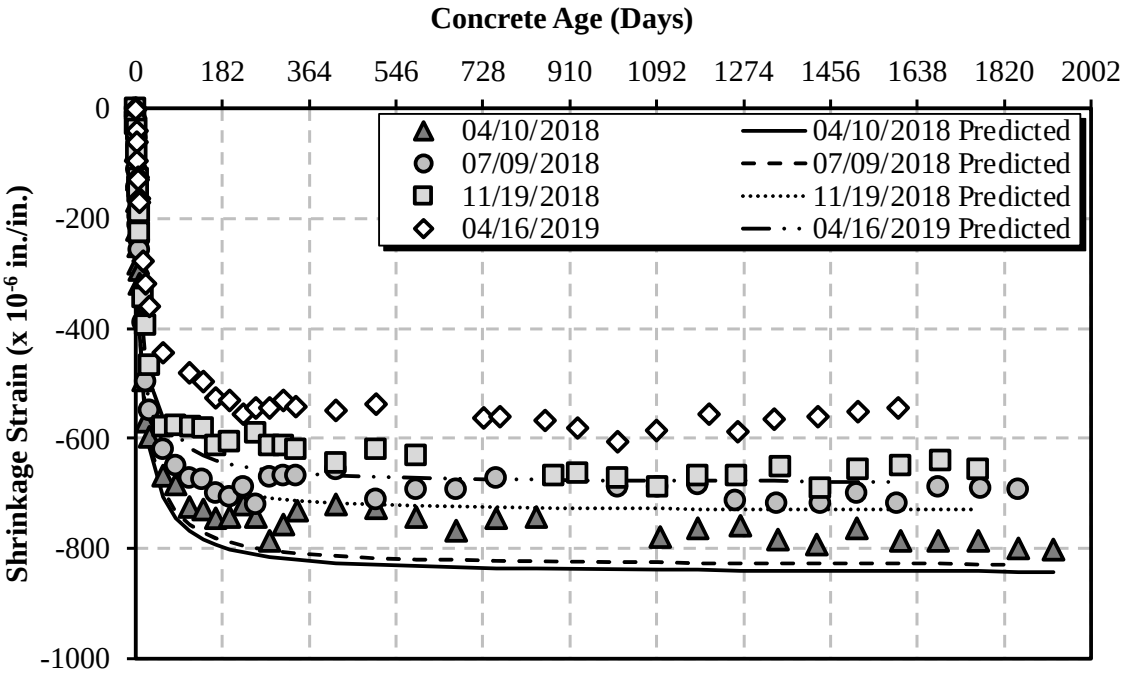

Figure B-69: Calibrated CEB MC 90-99 shrinkage for air-cured prisms

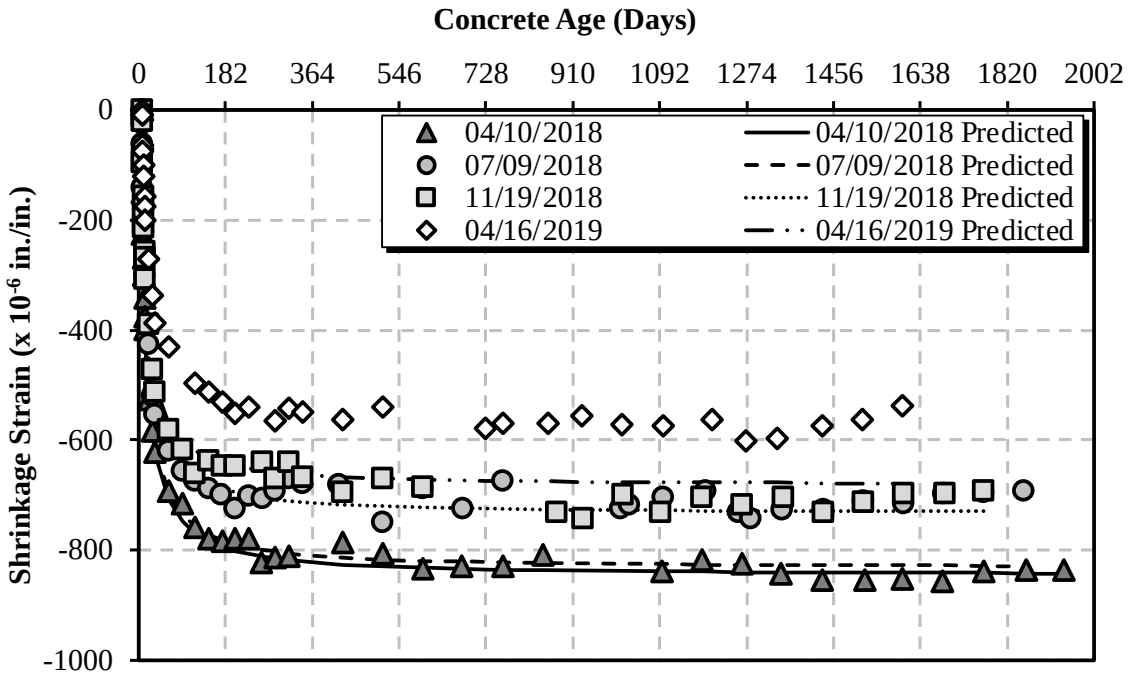

Figure B-70: Calibrated CEB MC 90-99 shrinkage for moist-cured prisms

B.11 CALIBRATED CEB MC 1990 PREDICTION MODEL

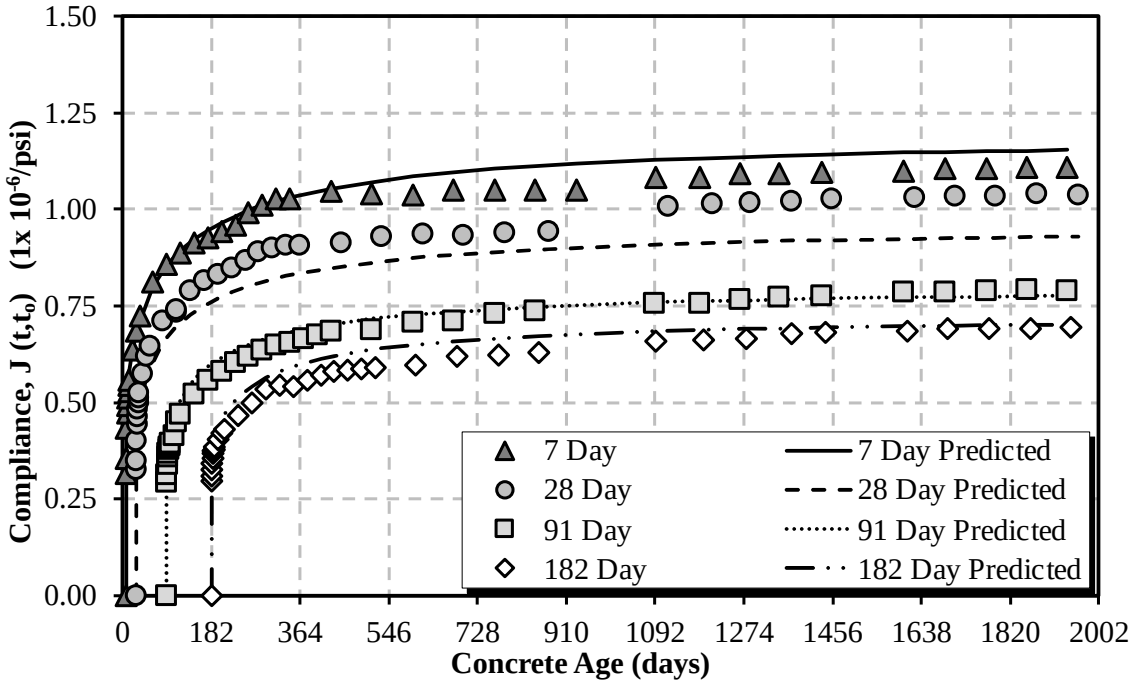

Figure B-71: Calibrated CEB MC 1990 compliance for the 04/10/2018 sampling date

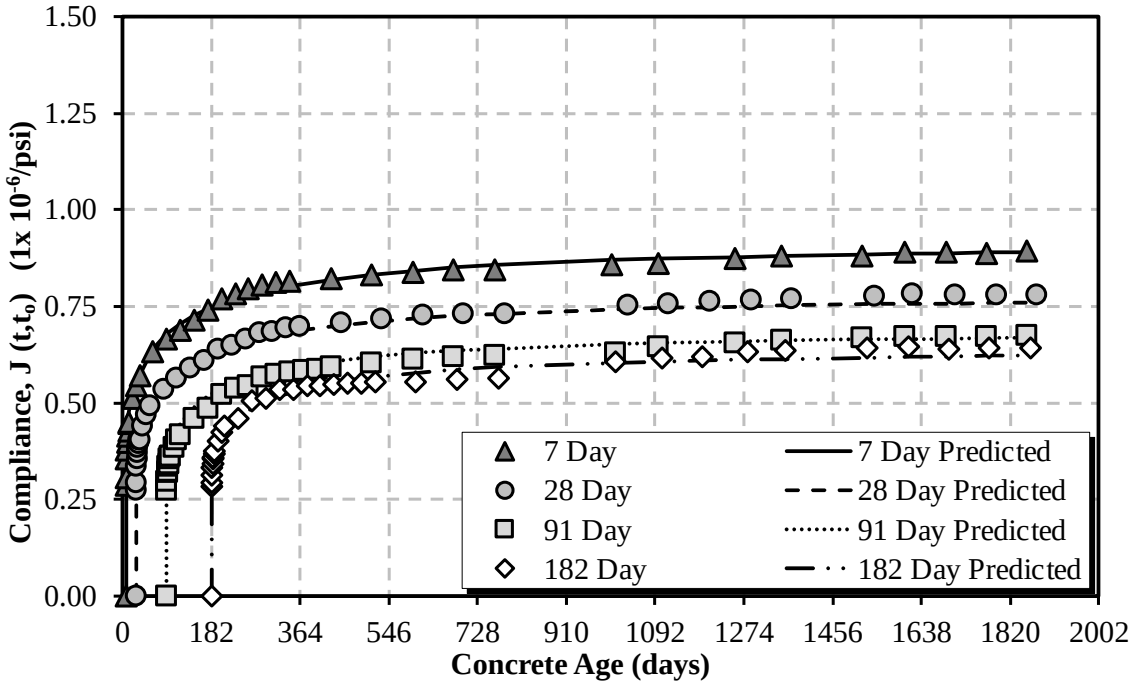

Figure B-72: Calibrated CEB MC 1990 compliance for the 07/09/2018 sampling date

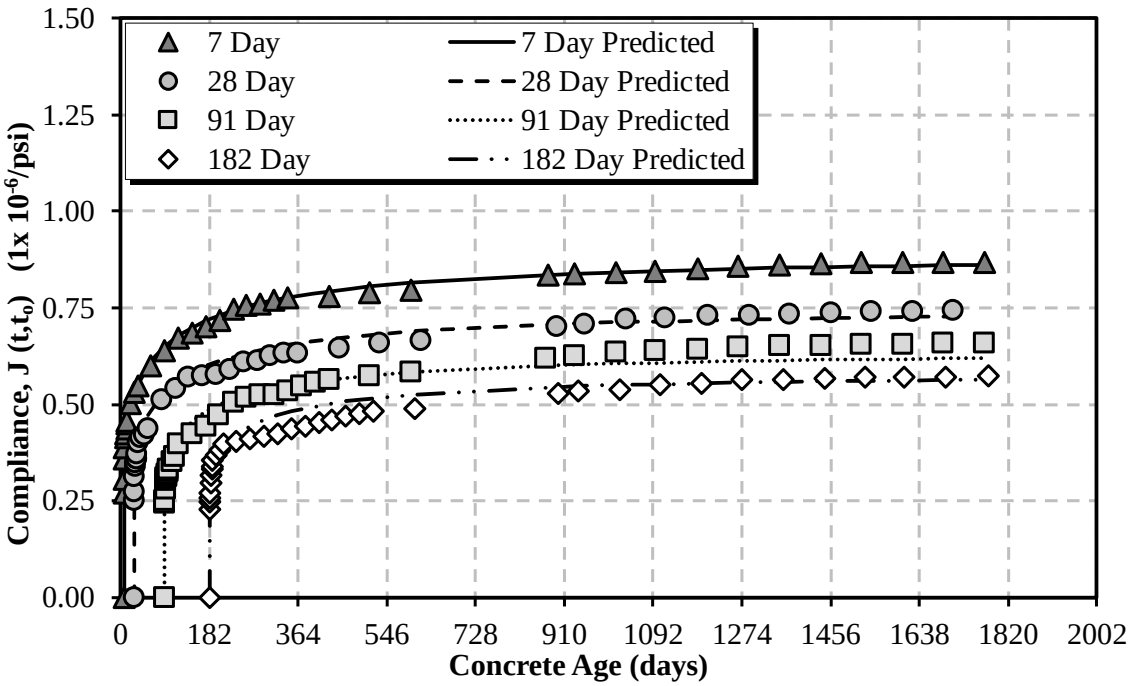

Figure B-73: Calibrated CEB MC 1990 compliance for the 11/19/2018 sampling date

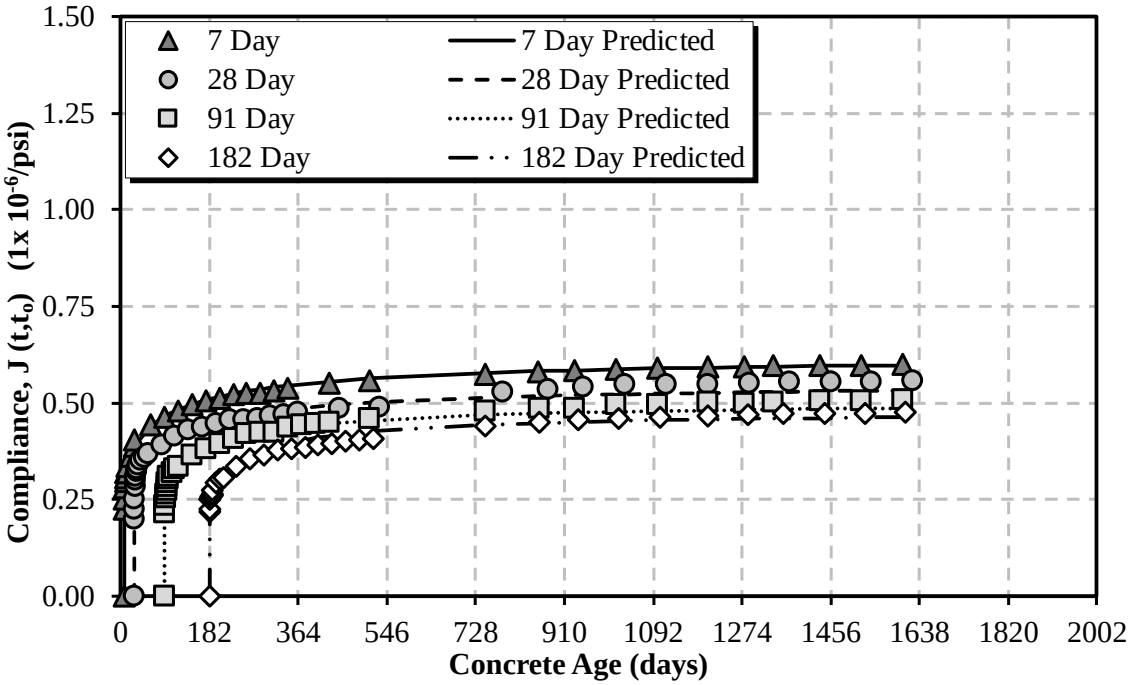

Figure B-74: Calibrated CEB MC 1990 compliance for the 04/16/2019 sampling date

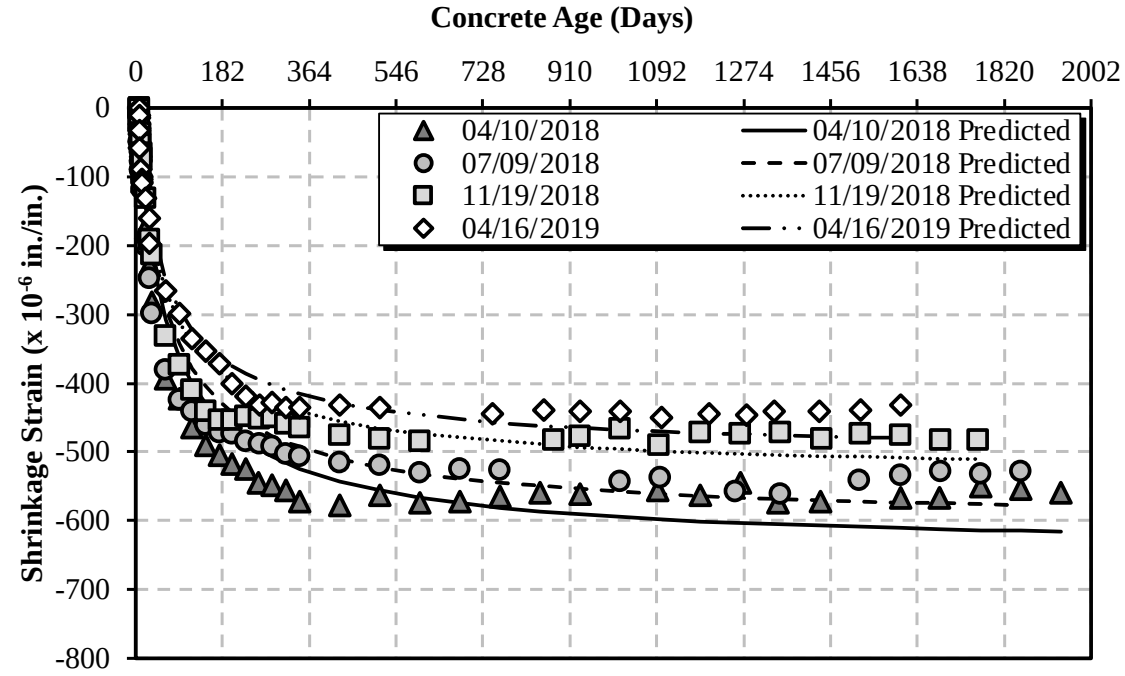

Figure B-75: Calibrated CEB MC 1990 shrinkage for cylindrical specimens

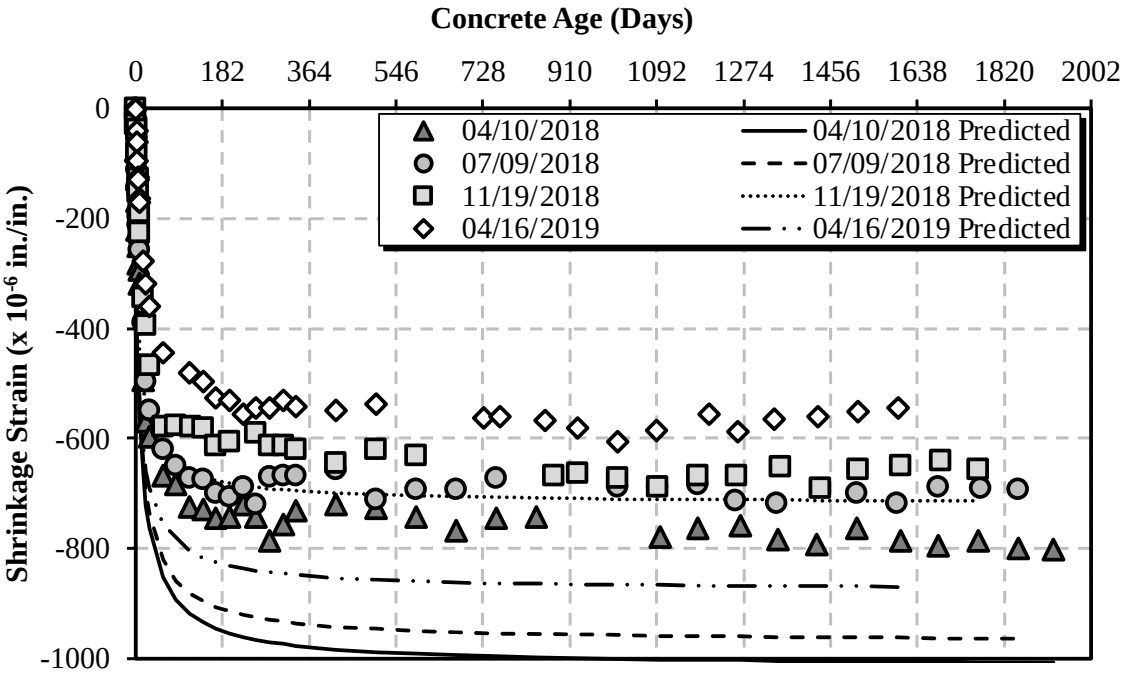

Figure B-76: Calibrated CEB MC 1990 shrinkage for air-cured prisms

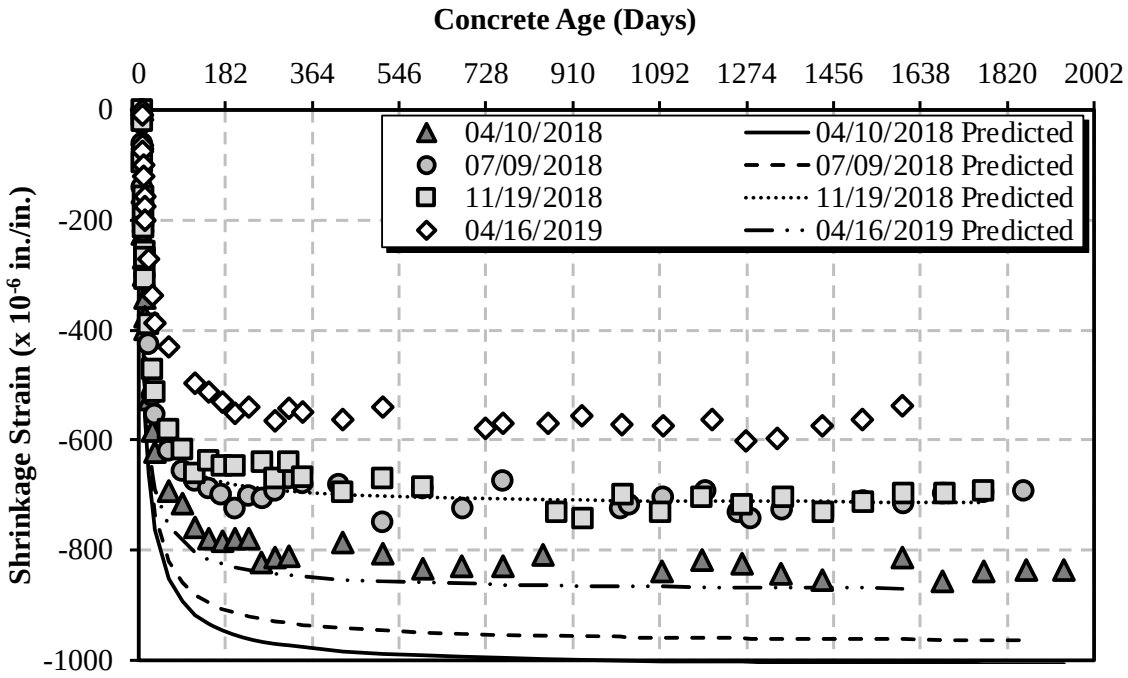

Figure B-77: Calibrated CEB MC 1990 shrinkage for moist-cured prisms

Appendix C

BIRMINGHAM I-59/I-20 SEGMENTAL BRIDGE CASTING AND ERECTION DATA

All segment designations with corresponding casting and erection dates were provided by Corven Engineering who acted as lead bridge designer for the I-59/I-20 segmental bridge project in Birmingham, Alabama. Thanks to this data presented in Table C-1, each sample collection date was able to be grouped to corresponding bridge segments, which provided the ability to better define the modified prediction models.

Table C-1: Casting and Erection Data for I-59/I-20 Bridge Segments

Span	SEGMENT Label	CAST Date	ERECT Date	Span	SEGMENT Label	CAST Date	ERECT Date
WBL-1	WBL1-EU	01/11/19	06/26/19	EBL-1	EBL1-EU	01/22/19	06/12/19
	WBL1-T1	10/27/18	06/25/19		EBL1-T1	10/16/18	06/12/19
	WBL1-T2	10/29/18	06/25/19		EBL1-T2	10/18/18	06/12/19
	WBL1-D3	10/30/18	06/25/19		EBL1-D3	10/20/18	06/11/19
	WBL1-T4	10/31/18	06/25/19		EBL1-T4	10/23/18	06/11/19
	WBL1-T5	11/01/18	06/25/19		EBL1-T5	10/24/18	06/11/19
	WBL1-T6	11/02/18	06/25/19		EBL1-T6	10/26/18	06/11/19
	WBL1-D7	11/05/18	06/25/19		EBL1-T7	10/29/18	06/11/19
	WBL1-T8	11/06/18	06/25/19		EBL1-D8	10/30/18	06/11/19
	WBL1-T9	11/08/18	06/25/19		EBL1-T9	10/31/18	06/11/19
	WBL1-T10	11/10/18	06/25/19		EBL1-T10	11/01/18	06/11/19
	WBL2-PD	11/10/18	06/26/19		EBL1-T11	11/02/18	06/15/19
WBL-2	WBL2-PU	11/08/18	06/28/19		EBL2-PD	11/05/18	06/11/19
	WBL2-T1	11/10/18	07/01/19	EBL-2	EBL2-PU	10/31/18	06/03/19
	WBL2-T2	11/13/18	07/01/19		EBL2-T1	10/15/18	06/03/19
	WBL2-T3	11/15/18	07/01/19		EBL2-T2	10/17/18	06/03/19
	WBL2-D4	11/17/18	07/01/19		EBL2-T3	10/18/18	06/03/19
	WBL2-T5	11/19/18	07/01/19		EBL2-D4	10/20/18	06/02/19
	WBL2-T6	11/20/18	07/01/19		EBL2-T5	10/23/18	06/02/19
	WBL2-T7	11/21/18	06/30/19		EBL2-T6	10/24/18	06/02/19
	WBL2-D8	11/27/18	06/29/19		EBL2-T7	10/25/18	06/02/19
	WBL2-T9	11/28/18	06/28/19		EBL2-D8	10/29/18	06/02/19
	WBL2-T10	11/29/18	06/28/19		EBL2-T9	10/30/18	06/02/19
	WBL2-T11	12/04/18	06/28/19		EBL2-T10	10/31/18	06/02/19
	WBL3-PD	10/11/18	07/03/19		EBL2-T11	11/01/18	06/01/19
WBL-3	WBL3-PU	10/09/18	07/03/19		EBL3-PD	05/15/19	06/01/19
	WBL3-T1	01/04/19	07/11/19	EBL-3	EBL3-PU	05/13/19	05/25/19
	WBL3-T2	01/07/19	07/03/19		EBL3-T1	10/02/18	05/25/19
	WBL3-T3	01/08/19	07/03/19		EBL3-T2	10/04/18	05/25/19
	WBL3-D4	01/09/19	07/03/19		EBL3-T3	10/05/18	05/25/19
	WBL3-T5	01/10/19	07/02/19		EBL3-D4	10/09/18	05/25/19
	WBL3-T6	01/11/19	07/02/19		EBL3-T5	10/11/18	05/25/19
	WBL3-T7	01/12/19	07/02/19		EBL3-T6	10/12/18	05/25/19

	WBL3-D8	01/15/19	07/02/19		EBL3-T7	10/13/18	05/24/19
	WBL3-T9	01/16/19	07/02/19		EBL3-T8	10/15/18	05/24/19
	WBL3-T10	01/17/19	07/02/19		EBL3-D9	10/17/18	05/24/19
	WBL3-T11	01/18/19	07/02/19		EBL3-T10	10/18/18	05/24/19
	WBL4-PD	10/11/18	07/08/19		EBL3-T11	10/19/18	05/24/19
WBL-4	WBL4-PU	10/08/18	07/08/19	EBL-4	EBL4-ED	05/14/19	05/28/19
	WBL4-T1	09/06/18	08/05/19		EBL4-EU	04/10/19	07/16/19
	WBL4-T2	09/07/18	08/05/19		EBL4-T1	12/10/18	07/15/19
	WBL4-T3	09/10/18	08/05/19		EBL4-T2	12/12/18	07/15/19
	WBL4-D4	09/12/18	08/05/19		EBL4-D3	12/13/18	07/15/19
	WBL4-T5	09/13/18	08/05/19		EBL4-T4	12/14/18	07/15/19
	WBL4-T6	09/14/18	08/05/19		EBL4-T5	12/15/18	07/16/19
	WBL4-T7	09/17/18	08/05/19		EBL4-T6	12/17/18	07/16/19
	WBL4-T8	09/18/18	08/05/19		EBL4-D7	12/18/18	07/16/19
	WBL4-D9	09/19/18	08/05/19		EBL4-T8	12/19/18	07/16/19
	WBL4-T10	09/20/18	08/05/19		EBL4-T9	12/20/18	07/16/19
	WBL4-T11	09/21/18	08/05/19		EBL4-T10	12/21/18	07/16/19
	WBL5-ED	01/14/19	08/06/19		EBL5-PD	01/17/19	07/17/19
WBL-5	WBL5-EU	01/09/19	08/12/19	EBL-5	EBL5-PU	01/15/19	07/20/19
	WBL5-T1	01/31/19	08/08/19		EBL5-T1	02/19/19	07/25/19
	WBL5-T2	02/01/19	08/08/19		EBL5-T2	02/21/19	07/22/19
	WBL5-D3	02/02/19	08/08/19		EBL5-T3	02/22/19	07/22/19
	WBL5-T4	02/04/19	08/08/19		EBL5-D4	02/25/19	07/22/19
	WBL5-T5	02/05/19	08/08/19		EBL5-T5	02/26/19	07/21/19
	WBL5-D6	02/06/19	08/08/19		EBL5-D6	02/27/19	07/21/19
	WBL5-T7	02/08/19	08/08/19		EBL5-T7	02/28/19	07/21/19
	WBL5-T8	02/09/19	08/08/19		EBL5-T8	03/01/19	07/21/19
	WBL5-T9	02/11/19	08/08/19		EBL5-T9	03/02/19	07/21/19
	WBL6-PD	03/04/19	08/09/19		EBL6-PD	01/30/19	07/22/19
WBL-6	WBL6-PU	02/28/19	08/10/19	EBL-6	EBL6-PU	01/26/19	07/24/19
	WBL6-T1	01/15/19	08/14/19		EBL6-T1	02/15/19	07/27/19
	WBL6-T2	01/16/19	08/11/19		EBL6-T2	02/16/19	07/24/19
	WBL6-T3	01/17/19	08/11/19		EBL6-T3	02/18/19	07/24/19
	WBL6-D4	01/18/19	08/10/19		EBL6-D4	02/20/19	07/24/19
	WBL6-T5	01/22/19	08/10/19		EBL6-T5	02/21/19	07/24/19
	WBL6-T6	01/23/19	08/10/19		EBL6-T6	02/22/19	07/24/19

	WBL6-D7	01/24/19	08/10/19		EBL6-T7	02/23/19	07/24/19
	WBL6-T8	01/25/19	08/10/19		EBL6-T8	02/25/19	07/24/19
	WBL6-T9	01/26/19	08/10/19		EBL6-D9	02/26/19	07/24/19
	WBL6-T10	01/28/19	08/10/19		EBL6-T10	02/27/19	07/24/19
	WBL7-PD	03/12/19	08/11/19		EBL6-T11	02/28/19	07/24/19
WBL-7	WBL7-PU	03/09/19	08/14/19		EBL7-ED	04/26/19	07/25/19
	WBL7-T1	05/20/19	09/09/19	EBL-7	EBL7-EU	05/30/19	08/22/19
	WBL7-T2	05/21/19	09/09/19		EBL7-T1	04/08/19	08/21/19
	WBL7-T3	05/22/19	09/09/19		EBL7-T2	04/09/19	08/21/19
	WBL7-D4	05/23/19	09/09/19		EBL7-D3	04/10/19	08/21/19
	WBL7-T5	05/24/19	09/09/19		EBL7-T4	04/12/19	08/22/19
	WBL7-T6	05/28/19	09/09/19		EBL7-T5	04/13/19	08/22/19
	WBL7-T7	05/29/19	09/09/19		EBL7-T6	04/15/19	08/22/19
	WBL7-D8	05/30/19	09/09/19		EBL7-T7	04/16/19	08/22/19
	WBL7-T9	05/31/19	09/09/19		EBL7-D8	04/18/19	08/22/19
	WBL7-T10	06/03/19	09/09/19		EBL7-T9	04/22/19	08/22/19
	WBL7-T11	06/04/19	09/09/19		EBL7-T10	04/23/19	08/22/19
	WBL8-PD	06/05/19	09/10/19		EBL7-T11	04/24/19	08/22/19
WBL-8	WBL8-PU	06/04/19	09/10/19		EBL8-PD	07/02/19	08/23/19
	WBL8-T1	06/10/19	09/13/19	EBL-8	EBL8-PU	07/01/19	08/23/19
	WBL8-T2	06/12/19	09/13/19		EBL8-T1	04/11/19	08/29/19
	WBL8-T3	06/13/19	09/12/19		EBL8-T2	04/12/19	08/28/19
	WBL8-D4	06/14/19	09/12/19		EBL8-T3	04/13/19	08/28/19
	WBL8-T5	06/17/19	09/12/19		EBL8-D4	04/15/19	08/27/19
	WBL8-T6	06/18/19	09/12/19		EBL8-T5	04/16/19	08/27/19
	WBL8-T7	06/19/19	09/12/19		EBL8-T6	04/17/19	08/27/19
	WBL8-T8	06/20/19	09/12/19		EBL8-T7	04/18/19	08/27/19
	WBL8-T9	06/21/19	09/12/19		EBL8-T8	04/22/19	08/27/19
	WBL8-D10	06/25/19	09/11/19		EBL8-D9	04/23/19	08/27/19
	WBL8-T11	06/26/19	09/11/19		EBL8-T10	04/24/19	08/27/19
	WBL8-T12	06/27/19	09/11/19		EBL8-T11	04/25/19	08/27/19
	WBL9-ED	06/12/19	09/13/19		EBL8-T12	04/26/19	08/27/19
WBL-9	WBL9-EU	11/21/18	06/13/19		EBL9-PD	12/15/18	05/08/19
	WBL9-T1	01/28/19	06/12/19	EBL-9	EBL9-PU	12/12/18	05/08/19
	WBL9-T2	01/31/19	06/12/19		EBL9-T1	11/13/18	05/06/19
	WBL9-D3	02/01/19	06/12/19		EBL9-T2	11/15/18	05/06/19

	WBL9-T4	02/04/19	06/12/19		EBL9-T3	11/16/18	05/06/19
	WBL9-T5	02/05/19	06/12/19		EBL9-D4	11/19/18	05/06/19
	WBL9-T6	02/06/19	06/12/19		EBL9-T5	11/20/18	05/06/19
	WBL9-T7	02/07/19	06/12/19		EBL9-T6	11/21/18	05/07/19
	WBL9-T8	02/08/19	06/12/19		EBL9-T7	11/26/18	05/07/19
	WBL9-D9	02/09/19	06/12/19		EBL9-T8	11/27/18	05/07/19
	WBL9-T10	02/11/19	06/13/19		EBL9-T9	11/28/18	05/07/19
	WBL9-T11	02/13/19	06/13/19		EBL9-D10	11/29/18	05/07/19
	WBL9-T12	02/14/19	06/13/19		EBL9-T11	11/30/18	05/07/19
	WBL10-PD	08/14/18	06/13/19		EBL9-T12	12/04/18	05/07/19
WBL-10	WBL10-PU	08/04/18	06/17/19		EBL10-ED	02/25/19	05/08/19
	WBL10-T1	02/07/19	06/25/19	EBL-10	EBL10-EU	12/06/18	05/24/19
	WBL10-T2	02/08/19	06/17/19		EBL10-T1	04/17/18	05/16/19
	WBL10-T3	02/09/19	06/17/19		EBL10-T2	04/25/18	05/16/19
	WBL10-D4	02/11/19	06/17/19		EBL10-D3	05/07/18	05/16/19
	WBL10-T5	02/13/19	06/17/19		EBL10-T4	05/15/18	05/16/19
	WBL10-T6	02/14/19	06/17/19		EBL10-T5	05/21/18	05/16/19
	WBL10-T7	02/15/19	06/17/19		EBL10-T6	05/25/18	05/15/19
	WBL10-T8	02/16/19	06/17/19		EBL10-T7	06/02/18	05/15/19
	WBL10-D9	02/18/19	06/16/19		EBL10-T8	06/12/18	05/15/19
	WBL10-T10	02/19/19	06/16/19		EBL10-D9	06/19/18	05/15/19
	WBL10-T11	02/21/19	06/16/19		EBL10-T10	06/29/18	05/15/19
	WBL10-T12	02/22/19	06/16/19		EBL10-T11	07/11/18	05/15/19
	WBL11-PD	05/02/19	06/18/19		EBL10-T12	07/13/18	05/15/19
WBL-11	WBL11-PU	04/30/19	06/23/19		EBL11-PD	07/27/18	05/16/19
	WBL11-T1	03/20/18	06/30/19	EBL-11	EBL11-PU	05/09/19	05/21/19
	WBL11-T2	04/29/19	06/22/19		EBL11-T1	02/27/18	05/31/19
	WBL11-T3	04/30/19	06/22/19		EBL11-T2	03/06/18	05/20/19
	WBL11-D4	05/01/19	06/22/19		EBL11-T3	03/12/18	05/20/19
	WBL11-T5	05/02/19	06/21/19		EBL11-D4	04/12/18	05/20/19
	WBL11-T6	05/03/19	06/21/19		EBL11-T5	04/21/18	05/20/19
	WBL11-T7	05/06/19	06/21/19		EBL11-T6	04/30/18	05/20/19
	WBL11-T8	05/07/19	06/21/19		EBL11-T7	05/04/18	05/20/19
	WBL11-D9	05/08/19	06/21/19		EBL11-T8	05/10/18	05/20/19
	WBL11-T10	05/10/19	06/21/19		EBL11-D9	05/23/18	05/20/19
	WBL11-T11	05/13/19	06/21/19		EBL11-T10	06/05/18	05/20/19

	WBL11-T12	05/14/19	06/21/19		EBL11-T11	06/06/18	05/20/19
	WBL12-PD	05/01/19	06/22/19		EBL11-T12	06/07/18	05/20/19
	WBL12-PU	04/29/19	06/24/19		EBL12-PD	08/10/18	05/21/19
	WBL12-T1	03/26/18	08/03/19		EBL12-PU	08/02/18	05/21/19
	WBL12-T2	05/02/19	08/03/19		EBL12-T1	04/06/18	07/11/19
	WBL12-T3	05/03/19	08/03/19		EBL12-T2	04/18/18	07/11/19
	WBL12-D4	05/06/19	08/03/19		EBL12-T3	04/24/18	07/11/19
	WBL12-T5	05/07/19	08/03/19		EBL12-D4	05/30/18	07/11/19
WBL-12	WBL12-T6	05/08/19	08/04/19		EBL12-T5	06/21/18	07/11/19
	WBL12-T7	05/09/19	08/04/19	EBL-12	EBL12-T6	06/25/18	07/12/19
	WBL12-T8	05/10/19	08/04/19		EBL12-T7	06/29/18	07/12/19
	WBL12-T9	05/13/19	08/04/19		EBL12-T8	07/09/18	07/12/19
	WBL12-D10	05/14/19	08/04/19		EBL12-T9	07/13/18	07/12/19
	WBL12-T11	05/15/19	08/04/19		EBL12-D10	07/17/18	07/12/19
	WBL12-T12	05/16/19	08/04/19		EBL12-T11	07/20/18	07/12/19
	WBL13-ED	05/28/19	08/04/19		EBL12-T12	07/24/18	07/12/19
	WBL13-EU	06/14/19	08/09/19		EBL13-ED	12/04/18	07/12/19
	WBL13-T1	03/24/18	08/09/19		EBL13-EU	05/10/19	07/23/19
	WBL13-T2	05/15/19	08/09/19		EBL13-T1	07/16/18	07/16/19
	WBL13-D3	05/16/19	08/10/19		EBL13-T2	07/18/18	07/16/19
	WBL13-T4	05/17/19	08/10/19		EBL13-D3	07/24/18	07/16/19
	WBL13-T5	05/20/19	08/10/19		EBL13-T4	07/26/18	07/16/19
WBL-13	WBL13-T6	05/21/19	08/10/19		EBL13-T5	07/30/18	07/16/19
	WBL13-T7	05/22/19	08/10/19	EBL-13	EBL13-T6	08/01/18	07/16/19
	WBL13-T8	05/23/19	08/10/19		EBL13-T7	08/03/18	07/15/19
	WBL13-D9	05/24/19	08/10/19		EBL13-T8	08/06/18	07/15/19
	WBL13-T10	05/28/19	08/11/19		EBL13-D9	08/08/18	07/15/19
	WBL13-T11	05/29/19	08/11/19		EBL13-T10	08/10/18	07/15/19
	WBL13-T12	05/30/19	08/11/19		EBL13-T11	08/11/18	07/15/19
	WBL14-PD	06/25/19	08/11/19		EBL13-T12	08/13/18	07/15/19
	WBL14-PU	06/24/19	08/17/19		EBL14-PD	06/15/19	07/16/19
	WBL14-T1	05/17/19	08/20/19		EBL14-PU	06/13/18	07/20/19
WBL-14	WBL14-T2	05/20/19	08/18/19	EBL-14	EBL14-T1	08/08/18	07/26/19
	WBL14-T3	05/21/19	08/18/19		EBL14-T2	08/10/18	07/20/19
	WBL14-D4	05/22/19	08/18/19		EBL14-T3	08/11/18	07/20/19
	WBL14-T5	05/23/19	08/18/19		EBL14-D4	08/14/18	07/20/19

	WBL14-T6	05/24/19	08/18/19		EBL14-T5	08/16/18	07/20/19
	WBL14-T7	05/28/19	08/18/19		EBL14-T6	08/17/18	07/20/19
	WBL14-T8	05/29/19	08/18/19		EBL14-T7	08/18/18	07/20/19
	WBL14-D9	05/30/19	08/18/19		EBL14-T8	08/20/18	07/20/19
	WBL14-T10	05/31/19	08/17/19		EBL14-D9	08/22/18	07/20/19
	WBL14-T11	06/03/19	08/17/19		EBL14-T10	08/23/18	07/19/19
	WBL14-T12	06/04/19	08/17/19		EBL14-T11	08/24/18	07/19/19
	WBL15-PD	06/28/19	08/19/19		EBL14-T12	08/25/18	07/19/19
WBL-15	WBL15-PU	06/27/19	08/20/19		EBL15-PD	06/29/18	07/21/19
	WBL15-T1	06/19/19	09/17/19	EBL-15	EBL15-PU	06/18/19	07/22/19
	WBL15-T2	06/20/19	09/17/19		EBL15-T1	08/07/18	08/27/19
	WBL15-T3	06/21/19	09/17/19		EBL15-T2	08/08/18	08/27/19
	WBL15-D4	06/25/19	09/17/19		EBL15-T3	08/10/18	08/27/19
	WBL15-T5	06/26/19	09/17/19		EBL15-D4	08/13/18	08/27/19
	WBL15-T6	06/27/19	09/17/19		EBL15-T5	08/14/18	08/27/19
	WBL15-T7	06/28/19	09/18/19		EBL15-T6	08/15/18	08/27/19
	WBL15-T8	06/29/19	09/18/19		EBL15-T7	08/16/18	08/27/19
	WBL15-D9	07/01/19	09/18/19		EBL15-T8	08/17/18	08/27/19
	WBL15-T10	07/02/19	09/18/19		EBL15-D9	08/20/18	08/27/19
	WBL15-T11	07/03/19	09/18/19		EBL15-T10	08/21/18	08/27/19
	WBL15-T12	07/08/19	09/18/19		EBL15-T11	08/22/18	08/27/19
	WBL16-PD	07/30/19	09/18/19		EBL15-T12	08/23/18	08/28/19
WBL-16	WBL16-PU	07/27/19	09/20/19		EBL16-PD	06/01/19	08/28/19
	WBL16-T1	07/09/19	09/24/19	EBL-16	EBL16-PU	05/30/19	09/03/19
	WBL16-T2	07/08/19	09/21/19		EBL16-T1	04/18/18	09/08/19
	WBL16-T3	07/03/19	09/21/19		EBL16-T2	04/25/18	09/05/19
	WBL16-D4	07/02/19	09/21/19		EBL16-T3	05/05/18	09/04/19
	WBL16-T5	07/01/19	09/21/19		EBL16-D4	05/18/18	09/04/19
	WBL16-T6	06/29/19	09/21/19		EBL16-T5	06/30/18	09/04/19
	WBL16-T7	06/28/19	09/21/19		EBL16-T6	07/09/18	09/04/19
	WBL16-T8	06/27/19	09/21/19		EBL16-T7	07/11/18	09/04/19
	WBL16-T9	06/26/19	09/21/19		EBL16-T8	07/13/18	09/04/19
	WBL16-D10	06/25/19	09/21/19		EBL16-T9	07/17/18	09/04/19
	WBL16-T11	06/21/19	09/21/19		EBL16-D10	07/23/18	09/04/19
	WBL16-T12	03/15/18	09/20/19		EBL16-T11	07/25/18	09/04/19
	WBL17-ED	06/25/19	09/23/19		EBL16-T12	07/26/18	09/04/19

	WBL17-EU	11/29/18	06/04/19		EBL17-ED	06/08/19	09/05/19
	WBL17-T1	01/18/19	06/04/19		EBL17-EU	01/26/19	04/01/19
	WBL17-T2	01/22/19	06/04/19		EBL17-T1	07/16/18	04/01/19
	WBL17-D3	01/24/19	06/04/19		EBL17-T2	07/17/18	04/01/19
	WBL17-T4	01/25/19	06/04/19		EBL17-D3	07/20/18	04/01/19
	WBL17-T5	01/26/19	06/05/19		EBL17-T4	07/24/18	04/01/19
WBL-17	WBL17-T6	01/28/19	06/05/19		EBL17-T5	07/25/18	04/02/19
	WBL17-T7	01/31/19	06/05/19	EBL-17	EBL17-T6	07/26/18	04/02/19
	WBL17-T8	02/01/19	06/05/19		EBL17-T7	07/27/18	04/02/19
	WBL17-D9	02/02/19	06/05/19		EBL17-T8	07/30/18	04/02/19
	WBL17-T10	02/04/19	06/05/19		EBL17-D9	08/01/18	04/02/19
	WBL17-T11	02/05/19	06/05/19		EBL17-T10	08/02/18	04/02/19
	WBL17-T12	02/06/19	06/05/19		EBL17-T11	08/03/18	04/02/19
	WBL18-PD	04/02/19	06/15/19		EBL17-T12	08/06/18	04/03/19
	WBL18-PU	03/30/19	06/15/19		EBL18-PD	04/08/19	05/05/19
	WBL18-T1	01/17/19	06/25/19		EBL18-PU	04/04/19	05/05/19
	WBL18-T2	01/18/19	06/14/19		EBL18-T1	07/25/18	05/15/19
	WBL18-T3	01/22/19	06/14/19		EBL18-T2	07/26/18	04/06/19
	WBL18-D4	01/25/19	06/14/19		EBL18-T3	07/27/18	04/06/19
	WBL18-T5	01/26/19	06/14/19		EBL18-D4	07/30/18	04/06/19
WBL-18	WBL18-T6	01/28/19	06/14/19		EBL18-T5	08/01/18	04/05/19
	WBL18-T7	01/31/19	06/13/19	EBL-18	EBL18-T6	08/02/18	04/04/19
	WBL18-T8	02/01/19	06/13/19		EBL18-T7	08/03/18	04/04/19
	WBL18-D9	02/02/19	06/13/19		EBL18-T8	08/04/18	04/04/19
	WBL18-T10	02/04/19	06/13/19		EBL18-D9	08/07/18	04/04/19
	WBL18-T11	02/05/19	06/13/19		EBL18-T10	08/10/18	04/04/19
	WBL18-T12	02/06/19	06/13/19		EBL18-T11	08/11/18	04/04/19
	WBL19-PD	02/21/19	06/20/19		EBL18-T12	08/13/18	04/04/19
	WBL19-PU	02/18/19	06/20/19		EBL19-PD	07/25/18	05/15/19
	WBL19-T1	12/31/18	06/28/19		EBL19-PU	07/16/18	05/15/19
	WBL19-T2	01/02/19	06/18/19		EBL19-T1	07/17/18	05/29/19
WBL-19	WBL19-T3	01/03/19	06/18/19	EBL-19	EBL19-T2	07/18/18	05/15/19
	WBL19-D4	01/04/19	06/18/19		EBL19-T3	07/20/18	05/15/19
	WBL19-T5	01/05/19	06/18/19		EBL19-D4	07/24/18	05/14/19
	WBL19-T6	01/07/19	06/18/19		EBL19-T5	07/26/18	05/14/19
	WBL19-T7	01/08/19	06/17/19		EBL19-T6	07/27/18	05/14/19

	WBL19-T8	01/09/19	06/17/19		EBL19-T7	07/28/18	05/14/19
	WBL19-D9	01/10/19	06/17/19		EBL19-T8	07/30/18	05/14/19
	WBL19-T10	01/11/19	06/17/19		EBL19-D9	08/02/18	05/14/19
	WBL19-T11	01/12/19	06/17/19		EBL19-T10	08/03/18	05/13/19
	WBL19-T12	01/14/19	06/17/19		EBL19-T11	08/04/18	05/13/19
	WBL20-PD	02/07/19	06/25/19		EBL19-T12	08/06/18	05/13/19
	WBL20-PU	02/05/19	06/25/19		EBL20-PD	04/01/19	05/25/19
	WBL20-T1	01/02/19	07/02/19		EBL20-PU	03/29/19	05/13/19
	WBL20-T2	01/03/19	06/26/19		EBL20-T1	07/25/18	05/30/19
	WBL20-T3	01/04/19	06/23/19		EBL20-T2	07/26/18	05/23/19
	WBL20-D4	01/07/19	06/23/19		EBL20-T3	07/30/18	05/23/19
	WBL20-T5	01/08/19	06/23/19		EBL20-D4	08/01/18	05/23/19
WBL-20	WBL20-T6	01/09/19	06/23/19		EBL20-T5	08/03/18	05/23/19
	WBL20-T7	01/10/19	06/23/19	EBL-20	EBL20-T6	08/04/18	05/23/19
	WBL20-T8	01/11/19	06/22/19		EBL20-T7	08/07/18	05/23/19
	WBL20-T9	01/12/19	06/22/19		EBL20-T8	08/10/18	05/23/19
	WBL20-D10	01/14/19	06/22/19		EBL20-T9	08/11/18	05/23/19
	WBL20-T11	01/15/19	06/22/19		EBL20-D10	08/14/18	05/23/19
	WBL20-T12	01/16/19	06/22/19		EBL20-T11	08/16/18	05/23/19
	WBL21-ED	04/17/19	06/29/19		EBL20-T12	08/18/18	05/22/19
	WBL21-EU	02/06/19	07/11/19		EBL21-ED	11/15/18	05/22/19
	WBL21-T1	12/11/18	07/10/19		EBL21-EU	04/03/19	07/22/19
	WBL21-T2	12/12/18	07/10/19		EBL21-T1	12/05/18	07/22/19
	WBL21-D3	12/14/18	07/10/19		EBL21-T2	01/04/19	07/22/19
	WBL21-T4	12/15/18	07/10/19		EBL21-D3	01/07/19	07/21/19
	WBL21-T5	12/17/18	07/10/19		EBL21-T4	01/08/19	07/21/19
WBL-21	WBL21-T6	12/18/18	07/10/19		EBL21-T5	01/09/19	07/21/19
	WBL21-T7	12/19/18	07/10/19	EBL-21	EBL21-T6	01/10/19	07/21/19
	WBL21-T8	12/20/18	07/10/19		EBL21-T7	01/11/19	07/21/19
	WBL21-D9	12/22/18	07/09/19		EBL21-T8	01/12/19	07/21/19
	WBL21-T10	01/01/19	07/09/19		EBL21-D9	01/14/19	07/20/19
	WBL21-T11	01/02/19	07/09/19		EBL21-T10	01/15/19	07/20/19
	WBL21-T12	01/03/19	07/09/19		EBL21-T11	01/16/19	07/20/19
	WBL22-PD	02/20/19	07/15/19		EBL21-T12	01/17/19	07/20/19
WBL-22	WBL22-PU	02/16/19	07/15/19		EBL22-PD	02/26/19	08/02/19
	WBL22-T1	01/02/19	07/17/19	EBL-	EBL22-PU	02/22/19	08/02/19

	WBL22-T2	01/03/19	07/02/19	22	EBL22-T1	01/09/19	08/05/19
	WBL22-T3	01/04/19	07/02/19		EBL22-T2	01/10/19	08/01/19
	WBL22-D4	01/07/19	07/02/19		EBL22-T3	01/11/19	07/31/19
	WBL22-T5	01/08/19	07/02/19		EBL22-D4	01/14/19	07/31/19
	WBL22-T6	01/09/19	07/02/19		EBL22-T5	01/15/19	07/31/19
	WBL22-T7	01/10/19	07/02/19		EBL22-T6	01/16/19	07/31/19
	WBL22-T8	01/11/19	07/02/19		EBL22-T7	01/17/19	07/31/19
	WBL22-D9	01/14/19	07/02/19		EBL22-T8	01/18/19	07/30/19
	WBL22-T10	01/15/19	07/01/19		EBL22-T9	01/22/19	07/30/19
	WBL22-T11	01/16/19	07/01/19		EBL22-D10	01/24/19	07/30/19
	WBL22-T12	01/17/19	07/01/19		EBL22-T11	01/25/19	07/30/19
	WBL23-PD	01/11/19	07/03/19		EBL22-T12	01/26/19	07/30/19
WBL-23	WBL23-PU	01/09/19	07/03/19		EBL23-ED	03/13/19	08/05/19
	WBL23-T1	01/31/19	07/19/19	EBL-23	EBL23-EU	03/16/19	08/08/19
	WBL23-T2	02/01/19	06/29/19		EBL23-T1	02/20/19	08/08/19
	WBL23-T3	02/02/19	06/29/19		EBL23-T2	02/21/19	08/08/19
	WBL23-D4	02/04/19	06/29/19		EBL23-D3	02/22/19	08/08/19
	WBL23-T5	02/05/19	06/29/19		EBL23-T4	02/23/19	08/08/19
	WBL23-T6	02/06/19	06/29/19		EBL23-T5	02/25/19	08/08/19
	WBL23-T7	02/07/19	06/29/19		EBL23-T6	02/26/19	08/08/19
	WBL23-T8	02/08/19	06/29/19		EBL23-T7	02/27/19	08/04/19
	WBL23-T9	02/09/19	06/29/19		EBL23-T8	02/28/19	08/04/19
	WBL23-D10	02/11/19	06/29/19		EBL23-D9	03/01/19	08/03/19
	WBL23-T11	02/13/19	06/28/19		EBL23-T10	03/02/19	08/03/19
	WBL23-T12	02/14/19	06/28/19		EBL23-T11	03/04/19	08/03/19
	WBL24-ED	02/14/19	07/18/19		EBL23-T12	03/05/19	08/03/19
WBL-24	WBL24-EU	05/04/19	08/17/19		EBL24-PD	03/13/19	08/24/19
	WBL24-T1	03/16/19	08/17/19	EBL-24	EBL24-PU	03/11/19	08/24/19
	WBL24-T2	03/18/19	08/17/19		EBL24-T1	04/10/19	09/11/19
	WBL24-D3	03/19/19	08/17/19		EBL24-T2	04/11/19	09/11/19
	WBL24-T4	03/20/19	08/17/19		EBL24-T3	04/12/19	09/11/19
	WBL24-T5	03/21/19	08/17/19		EBL24-D4	04/13/19	09/11/19
	WBL24-T6	03/22/19	08/17/19		EBL24-T5	04/15/19	09/11/19
	WBL24-T7	03/23/19	08/17/19		EBL24-T6	04/16/19	09/11/19
	WBL24-T8	03/25/19	08/17/19		EBL24-T7	04/17/19	09/11/19
	WBL24-D9	03/26/19	08/17/19		EBL24-T8	04/18/19	09/11/19

	WBL24-T10	03/27/19	08/17/19		EBL24-D9	04/22/19	09/11/19
	WBL24-T11	03/28/19	08/17/19		EBL24-T10	04/23/19	09/11/19
	WBL24-T12	03/29/19	08/17/19		EBL24-T11	04/24/19	09/11/19
	WBL25-PD	04/26/19	08/17/19		EBL24-T12	04/26/19	09/11/19
WBL-25	WBL25-PU	04/24/19	08/17/19		EBL25-PD	06/22/19	09/14/19
	WBL25-T1	03/25/19	08/20/19	EBL-25	EBL25-PU	05/22/19	09/14/19
	WBL25-T2	03/26/19	08/15/19		EBL25-T1	04/15/19	09/17/19
	WBL25-T3	03/27/19	08/15/19		EBL25-T2	04/16/19	09/13/19
	WBL25-D4	03/29/19	08/15/19		EBL25-T3	04/18/19	09/13/19
	WBL25-T5	03/30/19	08/15/19		EBL25-D4	04/22/19	09/13/19
	WBL25-T6	04/01/19	08/15/19		EBL25-T5	04/23/19	09/13/19
	WBL25-T7	04/02/19	08/15/19		EBL25-T6	04/24/19	09/13/19
	WBL25-T8	04/03/19	08/15/19		EBL25-T7	04/25/19	09/13/19
	WBL25-D9	04/04/19	08/15/19		EBL25-T8	04/26/19	09/13/19
	WBL25-T10	04/06/19	08/15/19		EBL25-T9	04/27/19	09/13/19
	WBL25-T11	04/08/19	08/14/19		EBL25-D10	04/29/19	09/12/19
	WBL25-T12	04/09/19	08/14/19		EBL25-T11	04/30/19	09/12/19
	WBL26-PD	05/07/19	05/16/19		EBL25-T12	05/01/19	09/12/19
WBL-26	WBL26-PU	05/06/19	05/15/19		EBL26-ED	05/21/19	09/14/19
	WBL26-T1	10/23/18	04/08/19	EBL-26	EBL26-EU	03/28/19	06/26/19
	WBL26-T2	10/25/18	04/08/19		EBL26-T1	02/13/19	06/26/19
	WBL26-T3	10/26/18	04/09/19		EBL26-T2	02/14/19	06/26/19
	WBL26-D4	10/29/18	04/09/19		EBL26-D3	02/15/19	06/25/19
	WBL26-T5	10/31/18	04/09/19		EBL26-T4	02/16/19	06/25/19
	WBL26-T6	11/01/18	04/09/19		EBL26-T5	02/18/19	06/25/19
	WBL26-T7	11/03/18	04/09/19		EBL26-T6	02/19/19	06/25/19
	WBL26-T8	11/05/18	04/09/19		EBL26-T7	02/21/19	06/25/19
	WBL26-T9	11/06/18	04/10/19		EBL26-T8	02/22/19	06/14/19
	WBL26-D10	11/08/18	04/10/19		EBL26-D9	02/23/19	06/14/19
	WBL26-T11	11/09/18	04/11/19		EBL26-T10	02/25/19	06/14/19
	WBL26-T12	11/13/18	04/12/19		EBL26-T11	02/26/19	06/14/19
	WBL27-ED	02/16/19	04/12/19		EBL26-T12	02/27/19	06/14/19
WBL-27	WBL27-EU	02/26/19	04/12/19		EBL27-PD	02/27/19	06/13/19
	WBL27-T1	09/14/18	04/13/19	EBL-27	EBL27-PU	02/25/19	06/13/19
	WBL27-T2	09/15/18	04/13/19		EBL27-T1	02/23/19	06/12/19
	WBL27-D3	09/17/18	04/13/19		EBL27-T2	02/25/19	06/21/19

	WBL27-T4	09/18/18	04/17/19		EBL27-T3	02/26/19	06/21/19
	WBL27-T5	09/19/18	04/17/19		EBL27-D4	02/27/19	06/21/19
	WBL27-T6	09/21/18	04/17/19		EBL27-T5	02/28/19	06/22/19
	WBL27-T7	09/25/18	04/17/19		EBL27-T6	03/01/19	06/22/19
	WBL27-T8	09/27/18	04/17/19		EBL27-T7	03/02/19	06/22/19
	WBL27-T9	09/28/18	04/18/19		EBL27-T8	03/04/19	06/23/19
	WBL27-D10	10/01/18	04/18/19		EBL27-D9	03/05/19	06/23/19
	WBL27-T11	10/02/18	04/18/19		EBL27-T10	03/06/19	06/23/19
	WBL27-T12	10/03/18	04/18/19		EBL27-T11	03/07/19	06/23/19
	WBL28-ED	02/22/19	04/12/19		EBL27-T12	03/08/19	06/23/19
WBL-28	WBL28-EU	06/22/19	08/02/19		EBL28-PD	03/08/19	06/24/19
	WBL28-T1	06/05/19	08/01/19	EBL-28	EBL28-PU	03/06/19	06/24/19
	WBL28-T2	06/06/19	08/01/19		EBL28-T1	05/02/19	07/18/19
	WBL28-D3	06/10/19	08/01/19		EBL28-T2	05/03/19	07/18/19
	WBL28-T4	06/11/19	08/01/19		EBL28-T3	05/06/19	07/18/19
	WBL28-T5	06/12/19	08/01/19		EBL28-D4	05/07/19	07/18/19
	WBL28-T6	06/13/19	08/01/19		EBL28-T5	05/08/19	07/18/19
	WBL28-T7	06/14/19	08/01/19		EBL28-T6	05/09/19	07/18/19
	WBL28-T8	06/17/19	08/01/19		EBL28-T7	05/10/19	07/18/19
	WBL28-D9	06/19/19	08/01/19		EBL28-T8	05/13/19	07/18/19
	WBL28-T10	06/20/19	08/01/19		EBL28-D9	05/14/19	07/18/19
	WBL28-T11	06/21/19	08/02/19		EBL28-T10	05/15/19	07/19/19
	WBL28-T12	06/25/19	08/02/19		EBL28-T11	05/16/19	07/19/19
	WBL29-PD	07/20/19	08/02/19		EBL28-T12	05/17/19	07/19/19
WBL-29	WBL29-PU	07/18/19	08/03/19		EBL29-PD	06/12/19	07/20/19
	WBL29-T1	06/05/19	08/15/19	EBL-29	EBL29-PU	06/11/19	07/20/19
	WBL29-T2	06/06/19	08/13/19		EBL29-T1	05/15/19	07/23/19
	WBL29-T3	06/07/19	08/13/19		EBL29-T2	05/17/19	07/23/19
	WBL29-D4	06/10/19	08/13/19		EBL29-T3	05/20/19	07/23/19
	WBL29-T5	06/11/19	08/13/19		EBL29-D4	05/21/19	07/23/19
	WBL29-T6	06/12/19	08/10/19		EBL29-T5	05/22/19	07/23/19
	WBL29-T7	06/13/19	08/10/19		EBL29-T6	05/23/19	07/23/19
	WBL29-T8	06/14/19	08/10/19		EBL29-T7	05/24/19	07/23/19
	WBL29-D9	06/17/19	08/10/19		EBL29-T8	05/28/19	07/23/19
	WBL29-T10	06/18/19	08/10/19		EBL29-D9	05/29/19	07/22/19
	WBL29-T11	06/19/19	08/10/19		EBL29-T10	05/30/19	07/22/19

	WBL29-T12	06/20/19	08/09/19		EBL29-T11	05/31/19	07/22/19
	WBL30-PD	07/18/19	08/13/19		EBL30-ED	06/11/19	07/23/19
WBL-30	WBL30-PU	07/16/19	08/13/19	EBL-30	EBL30-EU	06/26/19	08/27/19
	WBL30-T1	07/15/19	09/12/19		EBL30-T1	06/29/19	08/24/19
	WBL30-T2	07/16/19	09/12/19		EBL30-T2	07/01/19	08/24/19
	WBL30-T3	07/17/19	09/12/19		EBL30-D3	07/02/19	08/24/19
	WBL30-D4	07/18/19	09/12/19		EBL30-T4	07/03/19	08/24/19
	WBL30-T5	07/19/19	09/12/19		EBL30-T5	07/08/19	08/24/19
	WBL30-T6	07/20/19	09/12/19		EBL30-T6	07/09/19	08/24/19
	WBL30-T7	07/22/19	09/12/19		EBL30-D7	07/10/19	08/24/19
	WBL30-T8	07/23/19	09/12/19		EBL30-T8	07/11/19	08/24/19
	WBL30-D9	07/24/19	09/12/19		EBL30-T9	07/12/19	08/24/19
	WBL30-T10	07/25/19	09/12/19		EBL30-T10	07/13/19	08/24/19
	WBL30-T11	07/26/19	09/12/19		EBL31-PD	07/26/19	08/29/19
	WBL30-T12	07/29/19	09/12/19	EBL-31	EBL31-PU	07/24/19	08/29/19
	WBL31-PD	08/09/19	09/12/19		EBL31-T1	07/02/19	09/03/19
WBL-31	WBL31-PU	08/07/19	09/12/19		EBL31-T2	07/03/19	08/30/19
	WBL31-T1	07/20/19	09/16/19		EBL31-T3	07/08/19	08/30/19
	WBL31-T2	07/23/19	09/14/19		EBL31-D4	07/09/19	08/30/19
	WBL31-T3	07/24/19	09/14/19		EBL31-T5	07/10/19	08/30/19
	WBL31-D4	07/25/19	09/14/19		EBL31-T6	07/11/19	08/30/19
	WBL31-T5	07/26/19	09/14/19		EBL31-D7	07/13/19	08/30/19
	WBL31-T6	07/29/19	09/13/19		EBL31-T8	07/15/19	08/30/19
	WBL31-T7	07/30/19	09/13/19		EBL31-T9	07/16/19	08/30/19
	WBL31-D8	07/31/19	09/13/19		EBL31-T10	07/17/19	08/30/19
	WBL31-T9	08/01/19	09/13/19		EBL32-PD	10/17/18	05/26/19
	WBL31-T10	08/02/19	09/13/19	EBL-32	EBL32-PU	10/15/18	05/26/19
	WBL32-ED	07/11/19	09/14/19		EBL32-T1	01/18/19	05/25/19
WBL-32	WBL32-EU	05/08/19	08/22/19		EBL32-T2	01/22/19	05/25/19
	WBL32-T1	03/12/19	08/22/19		EBL32-T3	01/24/19	05/25/19
	WBL32-T2	03/13/19	08/22/19		EBL32-D4	01/25/19	05/27/19
	WBL32-D3	03/14/19	08/21/19		EBL32-T5	01/26/19	05/27/19
	WBL32-T4	03/15/19	08/21/19		EBL32-T6	01/28/19	05/27/19
	WBL32-T5	03/16/19	08/21/19		EBL32-D7	01/31/19	05/28/19
	WBL32-T6	03/18/19	08/21/19		EBL32-T8	02/01/19	05/28/19
	WBL32-T7	03/19/19	08/21/19		EBL32-T9	02/04/19	05/28/19

	WBL32-D8	03/20/19	08/21/19		EBL32-T10	02/05/19	05/28/19
	WBL32-T9	03/21/19	08/21/19		EBL33-PD	10/16/18	05/30/19
	WBL32-T10	03/22/19	08/21/19		EBL33-PU	10/13/18	05/30/19
	WBL32-T11	03/23/19	08/21/19		EBL33-T1	11/21/18	05/31/19
	WBL33-PD	04/16/19	08/02/19		EBL33-T2	11/26/18	05/31/19
	WBL33-PU	04/15/19	08/02/19		EBL33-T3	11/27/18	06/01/19
	WBL33-T1	03/12/19	07/31/19		EBL33-D4	11/28/18	06/01/19
	WBL33-T2	03/13/19	07/31/19	EBL-33	EBL33-T5	11/29/18	06/01/19
	WBL33-T3	03/14/19	07/31/19		EBL33-T6	11/30/18	06/01/19
	WBL33-D4	03/15/19	07/31/19		EBL33-T7	12/04/18	06/01/19
	WBL33-T5	03/16/19	07/31/19		EBL33-D8	12/05/18	06/02/19
WBL-33	WBL33-T6	03/18/19	07/31/19		EBL33-T9	12/06/18	06/02/19
	WBL33-T7	03/19/19	08/01/19		EBL33-T10	12/07/18	06/02/19
	WBL33-T8	03/20/19	08/01/19		EBL34-ED	02/21/19	06/02/19
	WBL33-D9	03/21/19	08/01/19		EBL34-EU	04/13/19	06/26/19
	WBL33-T10	03/22/19	08/01/19		EBL34-T1	11/20/18	06/22/19
	WBL33-T11	03/23/19	08/01/19		EBL34-T2	11/21/18	06/22/19
	WBL33-T12	03/25/19	08/01/19		EBL34-D3	11/26/18	06/22/19
	WBL34-PD	04/23/19	08/03/19		EBL34-T4	11/27/18	06/22/19
	WBL34-PU	04/18/19	08/03/19		EBL34-T5	11/28/18	06/23/19
	WBL34-T1	04/10/19	08/05/19	EBL-34	EBL34-T6	11/29/18	06/23/19
	WBL34-T2	04/11/19	08/05/19		EBL34-T7	11/30/18	06/23/19
	WBL34-T3	04/12/19	08/05/19		EBL34-T8	12/04/18	06/23/19
	WBL34-D4	04/15/19	08/05/19		EBL34-D9	12/05/18	06/23/19
	WBL34-T5	04/16/19	08/05/19		EBL34-T10	12/06/18	06/23/19
WBL-34	WBL34-T6	04/18/19	08/05/19		EBL34-T11	12/07/18	06/23/19
	WBL34-T7	04/22/19	08/05/19		EBL34-T12	12/10/18	06/23/19
	WBL34-D8	04/23/19	08/05/19		EBL35-PD	06/08/19	06/24/19
	WBL34-T9	04/24/19	08/05/19		EBL35-PU	06/07/19	06/26/19
	WBL34-T10	04/25/19	08/05/19		EBL35-T1	02/15/19	07/11/19
	WBL34-T11	04/26/19	08/06/19		EBL35-T2	02/16/19	07/11/19
	WBL35-PD	05/20/19	08/06/19	EBL-35	EBL35-T3	02/18/19	07/11/19
	WBL35-PU	05/18/19	08/07/19		EBL35-D4	02/20/19	07/11/19
WBL-35	WBL35-T1	05/01/19	09/28/19		EBL35-T5	02/21/19	07/12/19
	WBL35-T2	05/02/19	09/28/19		EBL35-T6	02/22/19	07/12/19
	WBL35-T3	05/03/19	09/28/19		EBL35-T7	02/23/19	07/20/19

	WBL35-D4	05/06/19	09/28/19		EBL35-T8	02/25/19	07/20/19
	WBL35-T5	05/07/19	09/28/19		EBL35-T9	02/26/19	07/20/19
	WBL35-T6	05/08/19	09/28/19		EBL35-D10	02/27/19	07/21/19
	WBL35-T7	05/10/19	09/28/19		EBL35-T11	02/28/19	07/21/19
	WBL35-T8	05/13/19	09/29/19		EBL35-T12	03/01/19	07/21/19
	WBL35-T9	05/14/19	09/29/19		EBL36-ED	04/24/19	07/23/19
	WBL35-D10	05/15/19	09/29/19		EBL36-EU	05/18/19	09/04/19
	WBL35-T11	05/16/19	09/29/19		EBL36-T1	03/29/19	09/04/19
	WBL35-T12	05/17/19	09/29/19		EBL36-T2	03/30/19	09/04/19
	WBL36-ED	06/04/19	09/29/19		EBL36-D3	04/01/19	09/04/19
	WBL36-EU	07/10/19	10/14/19		EBL36-T4	04/02/19	09/04/19
	WBL36-T1	07/18/19	10/14/19		EBL36-T5	04/03/19	09/04/19
	WBL36-T2	07/19/19	10/14/19	EBL-36	EBL36-T6	04/04/19	09/04/19
	WBL36-D3	07/20/19	10/14/19		EBL36-T7	04/05/19	09/04/19
	WBL36-T4	07/22/19	10/14/19		EBL36-T8	04/06/19	09/06/19
	WBL36-T5	07/23/19	10/14/19		EBL36-D9	04/08/19	09/06/19
WBL-36	WBL36-T6	07/24/19	10/14/19		EBL36-T10	04/09/19	09/06/19
	WBL36-T7	07/25/19	10/14/19		EBL36-T11	04/10/19	09/06/19
	WBL36-T8	07/26/19	10/13/19		EBL36-T12	04/11/19	09/06/19
	WBL36-D9	07/29/19	10/13/19		EBL37-PD	06/29/19	09/06/19
	WBL36-T10	07/30/19	10/13/19		EBL37-PU	06/27/19	09/06/19
	WBL36-T11	07/31/19	10/13/19		EBL37-T1	06/26/19	10/02/19
	WBL36-T12	08/01/19	10/13/19		EBL37-T2	06/27/19	10/02/19
	WBL37-PD	08/06/19	09/12/19		EBL37-T3	06/28/19	10/02/19
	WBL37-PU	08/03/19	09/12/19		EBL37-D4	06/29/19	10/02/19
	WBL37-T1	07/20/19	09/12/19		EBL37-T5	07/02/19	10/01/19
	WBL37-T2	07/22/19	09/12/19	EBL-37	EBL37-T6	07/03/19	10/01/19
	WBL37-T3	07/23/19	09/12/19		EBL37-T7	07/08/19	10/01/19
	WBL37-D4	07/24/19	09/12/19		EBL37-T8	07/09/19	10/01/19
WBL-37	WBL37-T5	07/25/19	09/11/19		EBL37-D9	07/10/19	10/01/19
	WBL37-T6	07/26/19	09/11/19		EBL37-T10	07/11/19	10/01/19
	WBL37-T7	07/29/19	09/10/19		EBL37-T11	07/12/19	10/01/19
	WBL37-D8	07/30/19	09/10/19		EBL37-T12	07/13/19	10/01/19
	WBL37-T9	07/31/19	09/10/19		EBL38-PD	01/22/19	06/08/19
	WBL37-T10	08/01/19	09/10/19	EBL-38	EBL38-PU	01/18/19	06/08/19
	WBL37-T11	08/02/19	09/10/19		EBL38-T1	01/22/19	06/06/19

	WBL38-PD	04/13/19	07/24/19		EBL38-T2	01/24/19	06/06/19
WBL-38	WBL38-PU	04/10/19	07/24/19		EBL38-T3	01/25/19	06/02/19
	WBL38-T1	02/28/19	07/19/19		EBL38-D4	01/26/19	06/02/19
	WBL38-T2	03/01/19	07/19/19		EBL38-T5	01/30/19	06/02/19
	WBL38-T3	03/02/19	07/19/19		EBL38-T6	01/31/19	06/02/19
	WBL38-D4	03/04/19	07/19/19		EBL38-T7	02/01/19	06/02/19
	WBL38-T5	03/05/19	07/19/19		EBL38-D8	02/02/19	06/02/19
	WBL38-T6	03/06/19	07/19/19		EBL38-T9	02/04/19	06/02/19
	WBL38-T7	03/07/19	07/19/19		EBL38-T10	02/05/19	06/02/19
	WBL38-D8	03/08/19	07/21/19		EBL38-T11	02/06/19	06/02/19
	WBL38-T9	03/09/19	07/21/19		EBL39-PD	01/24/19	06/08/19
	WBL38-T10	03/11/19	07/21/19	EBL-39	EBL39-PU	01/22/19	06/08/19
	WBL39-ED	04/16/19	07/21/19		EBL39-T1	04/27/19	09/11/19
WBL-39	WBL39-EU	04/18/19	08/28/19		EBL39-T2	04/29/19	09/11/19
	WBL39-T1	06/28/19	10/13/19		EBL39-T3	04/30/19	09/11/19
	WBL39-T2	06/29/19	10/13/19		EBL39-D4	05/01/19	09/11/19
	WBL39-D3	07/01/19	10/13/19		EBL39-T5	05/02/19	09/11/19
	WBL39-T4	07/02/19	10/13/19		EBL39-T6	05/03/19	09/11/19
	WBL39-T5	07/08/19	10/14/19		EBL39-T7	05/06/19	09/10/19
	WBL39-T6	07/09/19	10/14/19		EBL39-T8	05/07/19	09/10/19
	WBL39-T7	07/10/19	10/14/19		EBL39-T9	05/08/19	09/10/19
	WBL39-T8	07/11/19	10/14/19		EBL39-D10	05/10/19	09/10/19
	WBL39-D9	07/12/19	10/14/19		EBL39-T11	05/13/19	09/09/19
	WBL39-T10	07/13/19	10/14/19		EBL39-T12	05/14/19	09/09/19
	WBL39-T11	07/15/19	10/14/19		EBL40-ED	03/01/19	04/01/19
	WBL39-T12	07/16/19	10/14/19	EBL-40	EBL40-EU	03/06/19	04/01/19
	WBL40-PD	07/22/19	10/09/19		EBL40-T1	05/15/19	08/15/19
WBL-40	WBL40-PU	07/20/19	10/09/19		EBL40-T2	05/16/19	09/04/19
	WBL40-T1	07/03/19	10/08/19		EBL40-D3	05/17/19	09/04/19
	WBL40-T2	07/08/19	10/08/19		EBL40-T4	05/20/19	09/04/19
	WBL40-T3	07/09/19	10/08/19		EBL40-T5	05/21/19	09/04/19
	WBL40-D4	07/10/19	10/08/19		EBL40-T6	05/22/19	09/04/19
	WBL40-T5	07/11/19	10/08/19		EBL40-T7	05/23/19	09/04/19
	WBL40-T6	07/12/19	10/08/19		EBL40-T8	05/24/19	09/04/19
	WBL40-T7	07/13/19	10/08/19		EBL40-D9	05/28/19	09/05/19
	WBL40-T8	07/15/19	10/07/19		EBL40-T10	05/29/19	09/05/19

	WBL40-D9	07/16/19	10/07/19		EBL40-T11	05/30/19	09/05/19
	WBL40-T10	07/17/19	10/07/19		EBL40-T12	05/31/19	09/05/19
	WBL40-T11	07/18/19	10/07/19		EBL41-PD	11/17/18	06/16/19
	WBL40-T12	07/19/19	10/07/19		EBL41-PU	11/14/18	06/16/19
	WBL41-PD	04/11/19	09/20/19		EBL41-T1	11/03/18	06/15/19
	WBL41-PU	04/09/19	09/19/19		EBL41-T2	11/05/18	06/15/19
	WBL41-T1	01/08/19	09/19/19		EBL41-T3	11/06/18	06/15/19
	WBL41-T2	01/10/19	09/19/19		EBL41-D4	11/08/18	06/15/19
	WBL41-T3	01/12/19	09/19/19		EBL41-T5	11/09/18	06/13/19
	WBL41-D4	01/16/19	09/19/19	EBL-41	EBL41-T6	11/13/18	06/11/19
	WBL41-T5	01/17/19	08/28/19		EBL41-T7	11/14/18	06/11/19
WBL-41	WBL41-T6	01/18/19	08/23/19		EBL41-T8	11/15/18	06/11/19
	WBL41-T7	01/22/19	08/23/19		EBL41-D9	11/16/18	06/11/19
	WBL41-T8	01/24/19	08/23/19		EBL41-T10	11/17/18	06/11/19
	WBL41-T9	01/25/19	08/23/19		EBL41-T11	11/19/18	06/11/19
	WBL41-D10	01/26/19	08/23/19		EBL41-T12	11/20/18	06/11/19
	WBL41-T11	01/28/19	08/23/19		EBL42-PD	11/09/18	06/17/19
	WBL41-T12	01/31/19	08/22/19		EBL42-PU	11/06/18	06/17/19
	WBL42-ED	03/15/19	08/28/19		EBL42-T1	06/19/19	10/04/19
	WBL42-EU	03/25/19	09/26/19		EBL42-T2	06/20/19	10/05/19
	WBL42-T1	02/01/19	09/27/19		EBL42-T3	06/21/19	10/05/19
	WBL42-D2	02/05/19	09/27/19		EBL42-D4	06/25/19	10/05/19
WBL-42	WBL42-T3	02/06/19	09/27/19	EBL-42	EBL42-T5	06/26/19	10/05/19
	WBL42-D4	02/07/19	09/27/19		EBL42-T6	06/27/19	10/05/19
	WBL42-T5	02/09/19	09/27/19		EBL42-T7	06/28/19	10/05/19
	WBL43-ED	03/27/19	09/27/19		EBL42-D8	06/29/19	10/05/19
	WBR1-EU	12/17/18	06/17/19		EBL42-T9	07/01/19	10/05/19
	WBR1-T1	08/15/18	06/16/19		EBL42-T10	07/02/19	10/05/19
	WBR1-T2	08/16/18	06/16/19		EBL43-ED	06/29/19	10/06/19
	WBR1-D3	08/18/18	06/15/19		EBR1-EU	05/07/19	06/05/19
WBR-1	WBR1-T4	08/21/18	06/15/19		EBR1-T1	09/24/18	06/05/19
	WBR1-T5	08/22/18	06/15/19		EBR1-T2	09/25/18	06/05/19
	WBR1-T6	08/24/18	06/15/19	EBR-1	EBR1-D3	09/27/18	06/05/19
	WBR1-T7	08/27/18	06/15/19		EBR1-T4	09/28/18	06/04/19
	WBR1-D8	08/29/18	06/15/19		EBR1-T5	10/01/18	06/04/19
	WBR1-T9	08/30/18	06/15/19		EBR1-T6	10/02/18	06/04/19

	WBR1-T10	08/31/18	06/15/19		EBR1-T7	10/03/18	06/04/19
	WBR1-T11	09/05/18	06/14/19		EBR1-D8	10/05/18	06/04/19
	WBR2-PD	09/06/18	06/17/19		EBR1-T9	10/08/18	06/04/19
WBR-2	WBR2-PU	08/29/18	06/17/19		EBR1-T10	10/09/18	06/04/19
	WBR2-T1	07/30/18	06/22/19		EBR1-T11	10/11/18	06/04/19
	WBR2-T2	08/01/18	06/22/19		EBR2-PD	05/16/19	05/21/19
	WBR2-T3	08/03/18	06/21/19	EBR-2	EBR2-PU	05/14/19	05/21/19
	WBR2-D4	08/07/18	06/21/19		EBR2-T1	10/01/18	03/28/19
	WBR2-T5	08/10/18	06/21/19		EBR2-T2	10/02/18	03/28/19
	WBR2-T6	08/13/18	06/21/19		EBR2-T3	10/04/18	03/28/19
	WBR2-T7	08/15/18	06/21/19		EBR2-D4	10/06/18	03/27/19
	WBR2-D8	08/17/18	06/21/19		EBR2-T5	10/09/18	03/27/19
	WBR2-T9	08/20/18	06/21/19		EBR2-T6	10/11/18	03/27/19
	WBR2-T10	08/22/18	06/21/19		EBR2-T7	10/12/18	03/27/19
	WBR2-T11	08/24/18	06/21/19		EBR2-D8	10/16/18	03/27/19
	WBR3-PD	09/12/18	06/22/19		EBR2-T9	10/17/18	03/26/19
WBR-3	WBR3-PU	09/07/18	06/22/19		EBR2-T10	10/18/18	03/26/19
	WBR3-T1	08/24/18	06/26/19		EBR2-T11	10/19/18	03/26/19
	WBR3-T2	08/25/18	06/19/19		EBR3-PD	05/07/19	05/14/19
	WBR3-T3	08/27/18	06/19/19	EBR-3	EBR3-PU	05/04/19	05/14/19
	WBR3-D4	08/29/18	06/19/19		EBR3-T1	10/04/18	03/23/19
	WBR3-T5	08/30/18	06/19/19		EBR3-T2	10/05/18	03/22/19
	WBR3-T6	08/31/18	06/19/19		EBR3-T3	10/06/18	03/22/19
	WBR3-T7	09/04/18	06/18/19		EBR3-D4	10/08/18	03/22/19
	WBR3-D8	09/06/18	06/18/19		EBR3-T5	10/09/18	03/22/19
	WBR3-T9	09/07/18	06/18/19		EBR3-T6	10/11/18	03/22/19
	WBR3-T10	09/11/18	06/18/19		EBR3-T7	10/12/18	03/21/19
	WBR3-T11	09/12/18	06/18/19		EBR3-T8	10/13/18	03/21/19
	WBR4-PD	09/14/18	06/20/19		EBR3-D9	10/16/18	03/21/19
WBR-4	WBR4-PU	09/11/18	06/20/19		EBR3-T10	10/17/18	03/21/19
	WBR4-T1	08/21/18	07/26/19		EBR3-T11	10/18/18	03/20/19
	WBR4-T2	08/23/18	07/26/19		EBR4-ED	01/16/19	03/23/19
	WBR4-T3	08/25/18	07/26/19	EBR-4	EBR4-EU	04/06/19	07/10/19
	WBR4-D4	08/28/18	07/26/19		EBR4-T1	10/06/18	07/09/19
	WBR4-T5	08/30/18	07/26/19		EBR4-T2	10/08/18	07/09/19
	WBR4-T6	09/08/18	07/26/19		EBR4-D3	10/10/18	07/09/19

	WBR4-T7	09/11/18	07/26/19		EBR4-T4	10/11/18	07/09/19
	WBR4-T8	09/14/18	07/27/19		EBR4-T5	10/12/18	07/09/19
	WBR4-D9	09/19/18	07/27/19		EBR4-T6	10/13/18	07/09/19
	WBR4-T10	09/21/18	07/27/19		EBR4-T7	10/15/18	07/09/19
	WBR4-T11	09/24/18	07/27/19		EBR4-D8	10/16/18	07/09/19
	WBR5-ED	01/07/19	07/27/19		EBR4-T9	10/17/18	07/09/19
	WBR5-EU	12/19/18	08/04/19		EBR4-T10	10/18/18	07/10/19
	WBR5-T1	08/15/18	07/30/19		EBR4-T11	10/19/18	07/10/19
	WBR5-T2	08/17/18	07/30/19		EBR5-PD	06/17/19	07/10/19
	WBR5-D3	08/21/18	07/30/19		EBR5-PU	06/14/19	07/11/19
	WBR5-T4	08/23/18	07/30/19		EBR5-T1	10/12/18	07/17/19
WBR-5	WBR5-T5	08/24/18	07/30/19		EBR5-T2	10/13/18	07/13/19
	WBR5-T6	08/27/18	07/29/19		EBR5-T3	10/16/18	07/13/19
	WBR5-D7	08/28/18	07/29/19		EBR5-D4	10/17/18	07/12/19
	WBR5-T8	08/30/18	07/29/19	EBR-5	EBR5-T5	10/18/18	07/12/19
	WBR5-T9	08/31/18	07/29/19		EBR5-T6	10/19/18	07/12/19
	WBR5-T10	09/04/18	07/29/19		EBR5-D7	10/22/18	07/12/19
	WBR6-PD	09/20/18	07/30/19		EBR5-T8	10/24/18	07/12/19
	WBR6-PU	09/15/18	07/31/19		EBR5-T9	10/25/18	07/12/19
	WBR6-T1	08/14/18	08/07/19		EBR5-T10	10/26/18	07/12/19
	WBR6-T2	08/15/18	08/02/19		EBR6-PD	01/16/19	07/13/19
	WBR6-T3	08/16/18	08/02/19		EBR6-PU	06/19/19	07/13/19
	WBR6-D4	08/18/18	08/02/19		EBR6-T1	12/07/18	07/20/19
WBR-6	WBR6-T5	08/20/18	08/02/19		EBR6-T2	12/10/18	07/20/19
	WBR6-T6	08/21/18	08/01/19		EBR6-T3	12/12/18	07/19/19
	WBR6-D7	08/23/18	08/01/19		EBR6-D4	12/13/18	07/18/19
	WBR6-T8	08/25/18	08/01/19		EBR6-T5	12/14/18	07/18/19
	WBR6-T9	08/27/18	08/01/19	EBR-6	EBR6-T6	12/17/18	07/18/19
	WBR6-T10	08/27/18	08/01/19		EBR6-T7	12/18/18	07/18/19
	WBR7-PD	02/15/19	08/02/19		EBR6-T8	12/19/18	07/18/19
	WBR7-PU	02/13/19	08/06/19		EBR6-D9	12/20/18	07/18/19
	WBR7-T1	08/30/18	08/30/19		EBR6-T10	12/22/18	07/18/19
WBR-7	WBR7-T2	09/04/18	08/30/19		EBR6-T11	01/01/19	07/18/19
	WBR7-T3	09/06/18	08/30/19		EBR7-ED	03/26/19	07/19/19
	WBR7-D4	09/10/18	08/30/19	EBR-7	EBR7-EU	05/17/19	08/14/19
	WBR7-T5	09/12/18	08/30/19		EBR7-T1	03/16/19	08/13/19

	WBR7-T6	09/13/18	08/30/19		EBR7-T2	03/18/19	08/13/19
	WBR7-T7	09/15/18	08/30/19		EBR7-D3	03/19/19	08/13/19
	WBR7-D8	09/18/18	08/30/19		EBR7-T4	03/20/19	08/13/19
	WBR7-T9	09/19/18	08/30/19		EBR7-T5	03/21/19	08/13/19
	WBR7-T10	09/20/18	08/30/19		EBR7-T6	03/22/19	08/13/19
	WBR7-T11	09/21/18	08/30/19		EBR7-T7	03/23/19	08/13/19
	WBR8-PD	06/07/19	08/30/19		EBR7-D8	03/25/19	08/13/19
	WBR8-PU	06/04/19	09/04/19		EBR7-T9	03/26/19	08/13/19
	WBR8-T1	08/29/18	09/07/19		EBR7-T10	03/27/19	08/13/19
	WBR8-T2	08/30/18	09/06/19		EBR7-T11	03/28/19	08/13/19
	WBR8-T3	08/31/18	09/05/19		EBR8-PD	04/27/19	08/14/19
	WBR8-D4	09/05/18	09/05/19	EBR-8	EBR8-PU	04/26/19	08/15/19
	WBR8-T5	09/06/18	09/05/19		EBR8-T1	03/29/19	08/20/19
WBR-8	WBR8-T6	09/07/18	09/05/19		EBR8-T2	03/30/19	08/17/19
	WBR8-T7	09/08/18	09/05/19		EBR8-T3	04/01/19	08/17/19
	WBR8-T8	09/10/18	09/05/19		EBR8-D4	04/02/19	08/16/19
	WBR8-T9	09/12/18	09/05/19		EBR8-T5	04/03/19	08/16/19
	WBR8-D10	09/14/18	09/04/19		EBR8-T6	04/04/19	08/16/19
	WBR8-T11	09/15/18	09/04/19		EBR8-T7	04/05/19	08/16/19
	WBR8-T12	09/17/18	09/04/19		EBR8-T8	04/08/19	08/16/19
	WBR9-ED	06/05/19	09/06/19		EBR8-D9	04/09/19	08/16/19
	WBR9-EU	10/30/18	05/28/19		EBR8-T10	04/10/19	08/16/19
	WBR9-T1	08/28/18	05/24/19		EBR8-T11	04/11/19	08/16/19
	WBR9-T2	08/29/18	05/24/19		EBR8-T12	04/12/19	08/16/19
	WBR9-D3	08/31/18	05/24/19		EBR9-PD	12/19/18	04/04/19
	WBR9-T4	09/05/18	05/24/19	EBR-9	EBR9-PU	12/18/18	04/04/19
	WBR9-T5	09/06/18	05/24/19		EBR9-T1	09/27/18	04/01/19
WBR-9	WBR9-T6	09/07/18	05/25/19		EBR9-T2	09/28/18	04/01/19
	WBR9-T7	09/10/18	05/25/19		EBR9-T3	10/01/18	04/01/19
	WBR9-T8	09/11/18	05/25/19		EBR9-D4	10/04/18	04/02/19
	WBR9-D9	09/13/18	05/25/19		EBR9-T5	10/06/18	04/02/19
	WBR9-T10	09/14/18	05/25/19		EBR9-T6	10/08/18	04/02/19
	WBR9-T11	09/17/18	05/25/19		EBR9-T7	10/09/18	04/02/19
	WBR9-T12	09/18/18	05/25/19		EBR9-T8	10/11/18	04/02/19
	WBR10-PD	08/23/18	06/01/19		EBR9-T9	10/13/18	04/03/19
WBR-	WBR10-PU	08/17/18	06/01/19		EBR9-D10	10/16/18	04/03/19

10	WBR10-T1	04/09/18	06/10/19		EBR9-T11	10/18/18	04/03/19
	WBR10-T2	04/21/18	06/03/19		EBR9-T12	10/19/18	04/03/19
	WBR10-T3	04/30/18	06/03/19		EBR10-ED	01/25/19	04/03/19
	WBR10-D4	05/12/18	06/03/19		EBR10-EU	01/04/19	05/05/19
	WBR10-T5	05/16/18	06/03/19		EBR10-T1	09/19/18	05/05/19
	WBR10-T6	05/22/18	06/03/19		EBR10-T2	09/21/18	05/04/19
	WBR10-T7	05/24/18	06/03/19		EBR10-D3	04/18/19	04/27/19
	WBR10-T8	05/31/18	06/03/19		EBR10-T4	09/27/18	04/27/19
	WBR10-D9	06/05/18	06/03/19		EBR10-T5	09/28/18	04/10/19
	WBR10-T10	06/12/18	06/03/19	EBR-10	EBR10-T6	10/01/18	04/10/19
	WBR10-T11	06/14/18	06/03/19		EBR10-T7	10/02/18	04/10/19
	WBR10-T12	06/16/18	06/02/19		EBR10-T8	10/04/18	04/10/19
	WBR11-PD	08/24/18	06/03/19		EBR10-D9	10/06/18	04/10/19
	WBR11-PU	08/21/18	06/08/19		EBR10-T10	10/09/18	04/10/19
	WBR11-T1	02/21/18	06/15/19		EBR10-T11	10/11/18	04/10/19
	WBR11-T2	03/02/18	06/07/19		EBR10-T12	10/13/18	04/08/19
	WBR11-T3	03/07/18	06/07/19		EBR11-PD	12/13/18	04/26/19
	WBR11-D4	04/19/18	06/07/19		EBR11-PU	12/11/18	04/26/19
	WBR11-T5	04/27/18	06/07/19		EBR11-T1	11/15/18	05/13/19
WBR-11	WBR11-T6	05/03/18	06/07/19		EBR11-T2	11/17/18	04/16/19
	WBR11-T7	05/07/18	06/07/19		EBR11-T3	11/19/18	04/16/19
	WBR11-T8	05/09/18	06/07/19		EBR11-D4	11/20/18	04/16/19
	WBR11-D9	05/21/18	06/07/19		EBR11-T5	11/21/18	04/16/19
	WBR11-T10	05/23/18	06/07/19	EBR-11	EBR11-T6	11/26/18	04/16/19
	WBR11-T11	05/30/18	06/07/19		EBR11-T7	11/27/18	04/16/19
	WBR11-T12	05/31/18	06/07/19		EBR11-T8	11/28/18	04/15/19
	WBR12-PD	08/31/18	06/08/19		EBR11-D9	11/29/18	04/15/19
	WBR12-PU	08/28/18	06/08/19		EBR11-T10	12/04/18	04/15/19
	WBR12-T1	04/04/18	07/24/19		EBR11-T11	12/05/18	04/15/19
	WBR12-T2	04/17/18	07/24/19		EBR11-T12	12/06/18	04/15/19
	WBR12-T3	04/24/18	07/24/19		EBR12-PD	10/23/18	04/18/19
WBR-12	WBR12-D4	05/05/18	07/24/19		EBR12-PU	10/19/18	04/19/19
	WBR12-T5	05/14/18	07/24/19	EBR-12	EBR12-T1	03/21/18	06/26/19
	WBR12-T6	05/21/18	07/24/19		EBR12-T2	11/03/18	06/26/19
	WBR12-T7	06/20/18	07/24/19		EBR12-T3	11/05/18	06/26/19
	WBR12-T8	06/25/18	07/24/19		EBR12-D4	11/06/18	06/27/19

	WBR12-T9	06/29/18	07/24/19		EBR12-T5	11/08/18	06/27/19
	WBR12-D10	07/09/18	07/24/19		EBR12-T6	11/09/18	06/27/19
	WBR12-T11	07/13/18	07/24/19		EBR12-T7	11/13/18	06/27/19
	WBR12-T12	07/17/18	07/24/19		EBR12-T8	11/15/18	06/27/19
	WBR13-ED	12/11/18	07/25/19		EBR12-T9	11/16/18	06/27/19
	WBR13-EU	11/07/18	08/05/19		EBR12-D10	11/19/18	06/27/19
	WBR13-T1	06/05/18	07/27/19		EBR12-T11	11/20/18	06/27/19
	WBR13-T2	06/06/18	07/27/19		EBR12-T12	11/26/18	06/27/19
	WBR13-D3	06/11/18	07/27/19		EBR13-ED	04/27/19	06/28/19
	WBR13-T4	06/13/18	07/27/19		EBR13-EU	05/03/19	07/03/19
	WBR13-T5	06/15/18	07/27/19		EBR13-T1	10/22/18	07/02/19
WBR-13	WBR13-T6	06/18/18	07/27/19		EBR13-T2	10/24/18	07/02/19
	WBR13-T7	06/19/18	07/27/19		EBR13-D3	10/26/18	07/01/19
	WBR13-T8	06/22/18	07/27/19		EBR13-T4	10/29/18	07/01/19
	WBR13-D9	06/29/18	07/27/19		EBR13-T5	10/30/18	07/01/19
	WBR13-T10	07/09/18	07/27/19	EBR-13	EBR13-T6	10/31/18	07/01/19
	WBR13-T11	07/11/18	07/27/19		EBR13-T7	11/01/18	07/01/19
	WBR13-T12	07/13/18	07/26/19		EBR13-T8	11/02/18	07/01/19
	WBR14-PD	05/11/19	07/29/19		EBR13-D9	11/05/18	07/01/19
	WBR14-PU	05/03/19	08/06/19		EBR13-T10	11/06/18	07/01/19
	WBR14-T1	06/13/18	08/14/19		EBR13-T11	11/08/18	07/01/19
	WBR14-T2	06/14/18	08/06/19		EBR13-T12	11/09/18	07/01/19
	WBR14-T3	06/15/18	08/06/19		EBR14-PD	03/27/19	07/02/19
	WBR14-D4	06/19/18	08/06/19		EBR14-PU	03/25/19	07/09/19
	WBR14-T5	06/21/18	08/06/19		EBR14-T1	10/22/18	07/13/19
WBR-14	WBR14-T6	06/22/18	08/06/19		EBR14-T2	10/23/18	07/10/19
	WBR14-T7	06/26/18	08/06/19		EBR14-T3	10/24/18	07/10/19
	WBR14-T8	06/29/18	08/06/19		EBR14-D4	10/26/18	07/10/19
	WBR14-D9	07/09/18	08/06/19		EBR14-T5	10/29/18	07/10/19
	WBR14-T10	07/11/18	08/06/19	EBR-14	EBR14-T6	10/30/18	07/10/19
	WBR14-T11	07/13/18	08/06/19		EBR14-T7	10/31/18	07/10/19
	WBR14-T12	07/16/18	08/06/19		EBR14-T8	11/01/18	07/09/19
	WBR15-PD	06/26/19	08/06/19		EBR14-D9	11/02/18	07/09/19
WBR-15	WBR15-PU	06/25/19	08/08/19		EBR14-T10	11/03/18	07/09/19
	WBR15-T1	07/20/18	09/09/19		EBR14-T11	11/05/18	07/09/19
	WBR15-T2	07/24/18	09/10/19		EBR14-T12	11/06/18	07/09/19

	WBR15-T3	07/26/18	09/10/19		EBR15-PD	03/28/19	07/10/19
	WBR15-D4	07/30/18	09/10/19		EBR15-PU	03/26/19	07/11/19
	WBR15-T5	08/02/18	09/10/19		EBR15-T1	04/12/19	08/14/19
	WBR15-T6	08/06/18	09/10/19		EBR15-T2	04/13/19	08/14/19
	WBR15-T7	08/10/18	09/10/19		EBR15-T3	04/15/19	08/14/19
	WBR15-T8	08/14/18	09/10/19		EBR15-D4	04/16/19	08/14/19
	WBR15-D9	08/17/18	09/10/19		EBR15-T5	04/17/19	08/14/19
	WBR15-T10	08/21/18	09/10/19	EBR-15	EBR15-T6	04/22/19	08/15/19
	WBR15-T11	08/24/18	09/11/19		EBR15-T7	04/23/19	08/15/19
	WBR15-T12	08/28/18	09/11/19		EBR15-T8	04/24/19	08/15/19
	WBR16-PD	07/02/19	09/11/19		EBR15-D9	04/26/19	08/15/19
	WBR16-PU	07/01/19	09/12/19		EBR15-T10	04/27/19	08/15/19
	WBR16-T1	06/20/18	09/16/19		EBR15-T11	04/29/19	08/15/19
	WBR16-T2	06/22/18	09/14/19		EBR15-T12	04/30/19	08/15/19
	WBR16-T3	06/26/18	09/14/19		EBR16-PD	05/29/19	08/15/19
	WBR16-D4	06/30/18	09/14/19		EBR16-PU	05/24/19	08/22/19
	WBR16-T5	07/09/18	09/14/19		EBR16-T1	04/25/19	08/29/19
WBR-16	WBR16-T6	07/11/18	09/14/19		EBR16-T2	04/26/19	08/23/19
	WBR16-T7	07/12/18	09/14/19		EBR16-T3	04/27/19	08/23/19
	WBR16-T8	07/14/18	09/13/19		EBR16-D4	04/29/19	08/22/19
	WBR16-T9	07/17/18	09/13/19		EBR16-T5	04/30/19	08/22/19
	WBR16-D10	07/20/18	09/13/19	EBR-16	EBR16-T6	05/01/19	08/22/19
	WBR16-T11	07/23/18	09/13/19		EBR16-T7	05/02/19	08/22/19
	WBR16-T12	07/24/18	09/13/19		EBR16-T8	05/03/19	08/22/19
	WBR17-ED	06/15/19	09/14/19		EBR16-T9	05/06/19	08/22/19
	WBR17-EU	10/02/18	05/21/19		EBR16-D10	05/07/19	08/22/19
	WBR17-T1	08/31/18	05/20/19		EBR16-T11	05/08/19	08/22/19
	WBR17-T2	09/05/18	05/20/19		EBR16-T12	05/09/19	08/22/19
	WBR17-D3	09/10/18	05/20/19		EBR17-ED	05/24/19	08/23/19
	WBR17-T4	09/12/18	05/21/19		EBR17-EU	01/02/19	03/12/19
WBR-17	WBR17-T5	09/13/18	05/21/19		EBR17-T1	09/24/18	03/11/19
	WBR17-T6	09/17/18	05/21/19	EBR-17	EBR17-T2	09/25/18	03/11/19
	WBR17-T7	09/18/18	05/21/19		EBR17-D3	09/27/18	03/11/19
	WBR17-T8	09/20/18	05/21/19		EBR17-T4	10/01/18	03/12/19
	WBR17-D9	09/22/18	05/21/19		EBR17-T5	10/02/18	03/12/19
	WBR17-T10	09/25/18	05/21/19		EBR17-T6	10/03/18	03/13/19

	WBR17-T11	09/27/18	05/21/19		EBR17-T7	10/04/18	03/13/19
	WBR17-T12	09/29/18	05/21/19		EBR17-T8	10/05/18	03/13/19
	WBR18-PD	10/20/18	05/25/19		EBR17-D9	10/08/18	03/13/19
WBR-18	WBR18-PU	10/18/18	05/25/19		EBR17-T10	10/09/18	03/13/19
	WBR18-T1	12/07/18	06/01/19		EBR17-T11	10/11/18	03/13/19
	WBR18-T2	12/10/18	05/28/19		EBR17-T12	10/12/18	03/14/19
	WBR18-T3	12/12/18	05/28/19		EBR18-PD	09/21/18	03/14/19
	WBR18-D4	12/13/18	05/28/19	EBR-18	EBR18-PU	09/18/18	03/15/19
	WBR18-T5	12/14/18	05/28/19		EBR18-T1	09/06/18	03/23/19
	WBR18-T6	12/15/18	05/28/19		EBR18-T2	09/11/18	03/21/19
	WBR18-T7	12/17/18	05/28/19		EBR18-T3	09/12/18	03/21/19
	WBR18-T8	12/18/18	05/28/19		EBR18-D4	09/14/18	03/20/19
	WBR18-D9	12/19/18	05/26/19		EBR18-T5	09/17/18	03/20/19
	WBR18-T10	12/20/18	05/26/19		EBR18-T6	09/18/18	03/20/19
	WBR18-T11	12/21/18	05/26/19		EBR18-T7	09/20/18	03/20/19
	WBR18-T12	01/01/19	05/26/19		EBR18-T8	09/21/18	03/19/19
	WBR19-PD	01/01/19	06/02/19		EBR18-D9	09/25/18	03/19/19
WBR-19	WBR19-PU	12/19/18	06/03/19		EBR18-T10	09/27/18	03/18/19
	WBR19-T1	12/15/18	06/10/19		EBR18-T11	09/28/18	03/18/19
	WBR19-T2	12/17/18	06/02/19		EBR18-T12	10/01/18	03/18/19
	WBR19-T3	12/18/18	06/02/19		EBR19-PD	09/29/18	03/19/19
	WBR19-D4	12/19/18	06/02/19	EBR-19	EBR19-PU	09/24/18	03/19/19
	WBR19-T5	12/20/18	06/01/19		EBR19-T1	11/05/18	03/30/19
	WBR19-T6	12/22/18	06/01/19		EBR19-T2	11/06/18	03/30/19
	WBR19-T7	12/31/18	06/01/19		EBR19-T3	11/08/18	03/30/19
	WBR19-T8	01/01/19	06/01/19		EBR19-D4	11/09/18	03/30/19
	WBR19-D9	01/03/19	06/01/19		EBR19-T5	11/10/18	03/30/19
	WBR19-T10	01/04/19	06/01/19		EBR19-T6	11/13/18	03/30/19
	WBR19-T11	01/07/19	06/01/19		EBR19-T7	11/14/18	03/30/19
	WBR19-T12	01/08/19	06/01/19		EBR19-T8	11/16/18	03/30/19
	WBR20-PD	12/07/18	06/09/19		EBR19-D9	11/19/18	03/29/19
WBR-20	WBR20-PU	05/24/19	06/09/19		EBR19-T10	11/20/18	03/29/19
	WBR20-T1	11/27/18	06/13/19		EBR19-T11	11/21/18	03/29/19
	WBR20-T2	11/28/18	06/08/19		EBR19-T12	11/26/18	03/29/19
	WBR20-T3	11/29/18	06/08/19		EBR20-PD	10/06/18	04/10/19
	WBR20-D4	12/04/18	06/08/19	EBR-	EBR20-PU	10/03/18	04/10/19

	WBR20-T5	12/05/18	06/07/19	20	EBR20-T1	08/28/18	05/09/19
	WBR20-T6	12/06/18	06/07/19		EBR20-T2	09/19/18	04/23/19
	WBR20-T7	12/07/18	06/07/19		EBR20-T3	09/21/18	04/23/19
	WBR20-T8	12/10/18	06/07/19		EBR20-D4	09/24/18	04/23/19
	WBR20-T9	12/11/18	06/07/19		EBR20-T5	09/25/18	04/22/19
	WBR20-D10	12/12/18	06/07/19		EBR20-T6	09/27/18	04/22/19
	WBR20-T11	12/13/18	06/07/19		EBR20-T7	09/28/18	04/22/19
	WBR20-T12	12/14/18	06/07/19		EBR20-T8	10/01/18	04/22/19
	WBR21-ED	03/23/19	06/15/19		EBR20-T9	10/02/18	04/22/19
WBR-21	WBR21-EU	02/08/19	07/17/19		EBR20-D10	10/03/18	04/22/19
	WBR21-T1	02/07/19	07/15/19		EBR20-T11	10/04/18	04/19/19
	WBR21-T2	02/08/19	07/15/19		EBR20-T12	10/05/18	04/19/19
	WBR21-D3	02/09/19	07/14/19		EBR21-ED	12/13/18	04/19/19
	WBR21-T4	02/11/19	07/14/19	EBR-21	EBR21-EU	03/30/19	08/08/19
	WBR21-T5	02/13/19	07/14/19		EBR21-T1	02/23/19	08/08/19
	WBR21-T6	02/14/19	07/14/19		EBR21-T2	02/25/19	08/08/19
	WBR21-T7	02/15/19	07/14/19		EBR21-D3	02/27/19	08/07/19
	WBR21-T8	02/16/19	07/14/19		EBR21-T4	02/28/19	08/07/19
	WBR21-D9	02/18/19	07/14/19		EBR21-T5	03/01/19	08/07/19
	WBR21-T10	02/19/19	07/14/19		EBR21-T6	03/02/19	08/06/19
	WBR21-T11	02/21/19	07/14/19		EBR21-T7	03/04/19	08/06/19
	WBR21-T12	02/22/19	07/14/19		EBR21-T8	03/05/19	08/06/19
	WBR22-PD	02/02/19	07/25/19		EBR21-D9	03/07/19	08/06/19
WBR-22	WBR22-PU	01/31/19	07/25/19		EBR21-T10	03/08/19	08/06/19
	WBR22-T1	02/07/19	07/27/19		EBR21-T11	03/09/19	08/06/19
	WBR22-T2	02/08/19	07/23/19		EBR21-T12	03/11/19	08/06/19
	WBR22-T3	02/09/19	07/23/19		EBR22-PD	03/19/19	08/11/19
	WBR22-D4	02/11/19	07/23/19	EBR-22	EBR22-PU	03/15/19	08/11/19
	WBR22-T5	02/13/19	07/23/19		EBR22-T1	03/01/19	08/13/19
	WBR22-T6	02/14/19	07/23/19		EBR22-T2	03/02/19	08/10/19
	WBR22-T7	02/15/19	07/23/19		EBR22-T3	03/04/19	08/10/19
	WBR22-T8	02/16/19	07/23/19		EBR22-D4	03/06/19	08/10/19
	WBR22-D9	02/18/19	07/23/19		EBR22-T5	03/07/19	08/10/19
	WBR22-T10	02/21/19	07/23/19		EBR22-T6	03/08/19	08/09/19
	WBR22-T11	02/22/19	07/23/19		EBR22-T7	03/09/19	08/09/19
	WBR22-T12	02/23/19	07/23/19		EBR22-T8	03/11/19	08/09/19

	WBR23-PD	02/04/19	07/28/19		EBR22-T9	03/12/19	08/09/19
WBR-23	WBR23-PU	02/01/19	07/28/19		EBR22-D10	03/13/19	08/09/19
	WBR23-T1	03/06/19	07/30/19		EBR22-T11	03/14/19	08/09/19
	WBR23-T2	03/07/19	07/27/19		EBR22-T12	03/15/19	08/09/19
	WBR23-T3	03/08/19	07/27/19		EBR23-ED	04/12/19	08/12/19
	WBR23-D4	03/11/19	07/26/19	EBR-23	EBR23-EU	04/23/19	09/07/19
	WBR23-T5	03/12/19	07/26/19		EBR23-T1	03/02/19	09/07/19
	WBR23-T6	03/13/19	07/26/19		EBR23-T2	03/04/19	09/07/19
	WBR23-T7	03/14/19	07/26/19		EBR23-D3	03/05/19	09/07/19
	WBR23-T8	03/15/19	07/26/19		EBR23-T4	03/06/19	09/07/19
	WBR23-T9	03/16/19	07/26/19		EBR23-T5	03/07/19	09/07/19
	WBR23-D10	03/18/19	07/26/19		EBR23-T6	03/08/19	09/06/19
	WBR23-T11	03/19/19	07/26/19		EBR23-T7	03/09/19	09/06/19
	WBR23-T12	03/20/19	07/26/19		EBR23-T8	03/11/19	09/06/19
	WBR24-ED	03/08/19	07/27/19		EBR23-D9	03/12/19	09/06/19
WBR-24	WBR24-EU	05/31/19	08/22/19		EBR23-T10	03/13/19	09/06/19
	WBR24-T1	04/13/19	08/22/19		EBR23-T11	03/14/19	09/06/19
	WBR24-T2	04/15/19	08/22/19		EBR23-T12	03/15/19	09/05/19
	WBR24-D3	04/16/19	08/22/19		EBR24-PD	04/06/19	09/11/19
	WBR24-T4	04/17/19	08/22/19	EBR-24	EBR24-PU	04/03/19	09/11/19
	WBR24-T5	04/18/19	08/22/19		EBR24-T1	05/01/19	09/20/19
	WBR24-T6	04/22/19	08/21/19		EBR24-T2	05/02/19	09/20/19
	WBR24-T7	04/23/19	08/21/19		EBR24-T3	05/03/19	09/20/19
	WBR24-T8	04/24/19	08/21/19		EBR24-D4	05/06/19	09/20/19
	WBR24-D9	04/26/19	08/21/19		EBR24-T5	05/07/19	09/20/19
	WBR24-T10	04/27/19	08/21/19		EBR24-T6	05/08/19	09/20/19
	WBR24-T11	04/29/19	08/21/19		EBR24-T7	05/09/19	09/19/19
	WBR24-T12	04/30/19	08/21/19		EBR24-T8	05/10/19	09/19/19
	WBR25-PD	06/13/19	09/03/19		EBR24-D9	05/13/19	09/19/19
WBR-25	WBR25-PU	06/11/19	09/03/19		EBR24-T10	05/14/19	09/19/19
	WBR25-T1	03/30/19	09/06/19		EBR24-T11	05/15/19	09/19/19
	WBR25-T2	04/01/19	09/03/19		EBR24-T12	05/16/19	09/19/19
	WBR25-T3	04/02/19	09/03/19		EBR25-PD	06/01/19	09/21/19
	WBR25-D4	04/03/19	09/03/19	EBR-25	EBR25-PU	05/30/19	09/21/19
	WBR25-T5	04/04/19	09/03/19		EBR25-T1	05/17/19	09/26/19
	WBR25-T6	04/06/19	08/30/19		EBR25-T2	05/20/19	09/24/19

	WBR25-T7	04/08/19	08/30/19		EBR25-T3	05/21/19	09/24/19
	WBR25-T8	04/09/19	08/30/19		EBR25-D4	05/22/19	09/24/19
	WBR25-D9	04/10/19	08/30/19		EBR25-T5	05/23/19	09/24/19
	WBR25-T10	04/11/19	08/30/19		EBR25-T6	05/24/19	09/24/19
	WBR25-T11	04/12/19	08/30/19		EBR25-T7	05/28/19	09/24/19
	WBR25-T12	04/13/19	08/30/19		EBR25-T8	05/29/19	09/23/19
	WBR26-PD	01/28/19	06/19/19		EBR25-T9	05/30/19	09/23/19
	WBR26-PU	01/25/19	06/19/19		EBR25-D10	05/31/19	09/23/19
	WBR26-T1	10/19/18	06/19/19		EBR25-T11	06/03/19	09/23/19
	WBR26-T2	10/22/18	06/18/19		EBR25-T12	06/04/19	09/23/19
	WBR26-T3	10/23/18	06/18/19		EBR26-ED	05/22/19	09/24/19
	WBR26-D4	10/24/18	06/18/19		EBR26-EU	05/11/19	07/30/19
	WBR26-T5	10/25/18	06/18/19		EBR26-T1	03/09/19	07/02/19
WBR-26	WBR26-T6	10/26/18	06/18/19		EBR26-T2	03/11/19	07/02/19
	WBR26-T7	10/27/18	06/18/19		EBR26-D3	03/12/19	07/02/19
	WBR26-T8	10/29/18	06/17/19		EBR26-T4	03/13/19	07/02/19
	WBR26-T9	10/30/18	06/17/19		EBR26-T5	03/14/19	07/02/19
	WBR26-D10	10/31/18	05/23/19	EBR-26	EBR26-T6	03/15/19	07/02/19
	WBR26-T11	11/01/18	05/23/19		EBR26-T7	03/16/19	07/01/19
	WBR26-T12	11/02/18	05/23/19		EBR26-T8	03/18/19	07/01/19
	WBR27-ED	02/05/19	05/22/19		EBR26-D9	03/19/19	07/01/19
	WBR27-EU	02/19/19	05/22/19		EBR26-T10	03/20/19	07/01/19
	WBR27-T1	10/22/18	05/21/19		EBR26-T11	03/21/19	07/01/19
	WBR27-T2	10/23/18	05/21/19		EBR26-T12	03/22/19	07/01/19
	WBR27-D3	10/24/18	05/23/19		EBR27-PD	04/17/19	07/02/19
	WBR27-T4	10/25/18	06/07/19		EBR27-PU	04/16/19	07/02/19
	WBR27-T5	10/26/18	06/07/19		EBR27-T1	03/25/19	07/06/19
WBR-27	WBR27-T6	10/27/18	06/07/19		EBR27-T2	03/26/19	07/06/19
	WBR27-T7	10/29/18	06/07/19		EBR27-T3	03/27/19	07/06/19
	WBR27-T8	10/30/18	06/07/19		EBR27-D4	03/29/19	07/06/19
	WBR27-T9	10/31/18	06/08/19	EBR-27	EBR27-T5	03/30/19	07/06/19
	WBR27-D10	11/01/18	06/08/19		EBR27-T6	04/01/19	07/06/19
	WBR27-T11	11/02/18	06/08/19		EBR27-T7	04/02/19	07/06/19
	WBR27-T12	11/03/18	06/09/19		EBR27-T8	04/03/19	07/07/19
	WBR28-ED	02/13/19	06/09/19		EBR27-D9	04/04/19	07/07/19
WBR-	WBR28-EU	06/20/19	07/26/19		EBR27-T10	04/06/19	07/07/19

28	WBR28-T1	05/20/19	07/25/19		EBR27-T11	04/08/19	07/07/19
	WBR28-T2	05/21/19	07/25/19		EBR27-T12	04/09/19	07/07/19
	WBR28-D3	05/22/19	07/25/19		EBR28-PD	05/20/19	07/08/19
	WBR28-T4	05/23/19	07/25/19	EBR-28	EBR28-PU	05/17/19	07/09/19
	WBR28-T5	05/24/19	07/25/19		EBR28-T1	04/16/19	07/13/19
	WBR28-T6	05/29/19	07/25/19		EBR28-T2	04/17/19	07/12/19
	WBR28-T7	05/30/19	07/25/19		EBR28-T3	04/18/19	07/12/19
	WBR28-T8	05/31/19	07/25/19		EBR28-D4	04/22/19	07/12/19
	WBR28-D9	06/04/19	07/25/19		EBR28-T5	04/23/19	07/12/19
	WBR28-T10	06/05/19	07/26/19		EBR28-T6	04/24/19	07/12/19
	WBR28-T11	06/06/19	07/26/19		EBR28-T7	04/25/19	07/12/19
	WBR28-T12	06/07/19	07/26/19		EBR28-T8	04/26/19	07/11/19
	WBR29-PD	07/11/19	07/26/19		EBR28-D9	04/27/19	07/11/19
WBR-29	WBR29-PU	07/09/19	07/26/19		EBR28-T10	04/29/19	07/11/19
	WBR29-T1	06/03/19	07/29/19		EBR28-T11	04/30/19	07/11/19
	WBR29-T2	06/04/19	07/29/19		EBR28-T12	05/01/19	07/11/19
	WBR29-T3	06/05/19	07/29/19		EBR29-PD	05/22/19	07/13/19
	WBR29-D4	06/06/19	07/29/19	EBR-29	EBR29-PU	05/21/19	07/13/19
	WBR29-T5	06/07/19	07/29/19		EBR29-T1	04/27/19	07/16/19
	WBR29-T6	06/10/19	07/29/19		EBR29-T2	04/29/19	07/15/19
	WBR29-T7	06/11/19	07/29/19		EBR29-T3	04/30/19	07/15/19
	WBR29-T8	06/12/19	07/27/19		EBR29-D4	05/01/19	07/15/19
	WBR29-D9	06/13/19	07/27/19		EBR29-T5	05/02/19	07/15/19
	WBR29-T10	06/14/19	07/27/19		EBR29-T6	05/03/19	07/15/19
	WBR29-T11	06/17/19	07/27/19		EBR29-T7	05/06/19	07/15/19
	WBR29-T12	06/18/19	07/27/19		EBR29-T8	05/07/19	07/15/19
	WBR30-PD	07/17/19	07/30/19		EBR29-T9	05/08/19	07/15/19
WBR-30	WBR30-PU	07/13/19	07/30/19		EBR29-D10	05/10/19	07/15/19
	WBR30-T1	07/10/19	09/05/19		EBR29-T11	05/13/19	07/15/19
	WBR30-T2	07/11/19	09/05/19		EBR29-T12	05/14/19	07/15/19
	WBR30-T3	07/12/19	09/05/19		EBR30-ED	06/01/19	07/16/19
	WBR30-D4	07/15/19	09/05/19	EBR-30	EBR30-EU	06/22/19	08/19/19
	WBR30-T5	07/16/19	09/05/19		EBR30-T1	06/18/19	08/17/19
	WBR30-T6	07/17/19	09/05/19		EBR30-T2	06/19/19	08/17/19
	WBR30-T7	07/18/19	09/06/19		EBR30-D3	06/20/19	08/17/19
	WBR30-T8	07/19/19	09/06/19		EBR30-T4	06/21/19	08/17/19

	WBR30-D9	07/22/19	09/06/19		EBR30-T5	06/25/19	08/17/19
	WBR30-T10	07/23/19	09/06/19		EBR30-T6	06/26/19	08/17/19
	WBR30-T11	07/24/19	09/06/19		EBR30-D7	06/27/19	08/17/19
	WBR30-T12	07/25/19	09/06/19		EBR30-T8	06/28/19	08/18/19
	WBR31-PD	07/31/19	09/06/19		EBR30-T9	06/29/19	08/18/19
	WBR31-PU	07/29/19	09/07/19		EBR30-T10	07/01/19	08/18/19
	WBR31-T1	07/17/19	09/12/19		EBR31-PD	07/25/19	08/19/19
	WBR31-T2	07/18/19	09/09/19		EBR31-PU	07/23/19	08/19/19
	WBR31-T3	07/19/19	09/09/19		EBR31-T1	06/21/19	08/22/19
	WBR31-D4	07/20/19	09/09/19		EBR31-T2	06/25/19	08/21/19
WBR-31	WBR31-T5	07/22/19	09/09/19		EBR31-T3	06/26/19	08/21/19
	WBR31-T6	07/23/19	09/09/19		EBR31-D4	06/27/19	08/21/19
	WBR31-T7	07/24/19	09/09/19	EBR-31	EBR31-T5	06/28/19	08/21/19
	WBR31-D8	07/25/19	09/09/19		EBR31-T6	06/29/19	08/21/19
	WBR31-T9	07/26/19	09/09/19		EBR31-D7	07/01/19	08/21/19
	WBR31-T10	07/29/19	09/09/19		EBR31-T8	07/02/19	08/21/19
	WBR32-ED	07/03/19	09/09/19		EBR31-T9	07/03/19	08/21/19
	WBR32-EU	04/30/19	08/14/19		EBR31-T10	07/08/19	08/21/19
	WBR32-T1	02/25/19	08/14/19		EBR32-PD	09/27/18	05/08/19
	WBR32-T2	02/26/19	08/13/19		EBR32-PU	09/22/18	05/08/19
	WBR32-D3	02/28/19	08/13/19		EBR32-T1	07/14/18	04/24/19
	WBR32-T4	03/01/19	08/13/19		EBR32-T2	07/17/18	04/24/19
	WBR32-T5	03/02/19	08/13/19		EBR32-T3	07/20/18	04/24/19
WBR-32	WBR32-T6	03/04/19	08/13/19		EBR32-D4	07/26/18	04/24/19
	WBR32-T7	03/05/19	08/13/19	EBR-32	EBR32-T5	07/30/18	04/24/19
	WBR32-D8	03/06/19	08/13/19		EBR32-T6	08/01/18	04/25/19
	WBR32-T9	03/07/19	08/13/19		EBR32-D7	08/04/18	04/25/19
	WBR32-T10	03/08/19	08/13/19		EBR32-T8	08/07/18	04/25/19
	WBR32-T11	03/09/19	08/13/19		EBR32-T9	08/10/18	04/25/19
	WBR33-PD	03/22/19	07/18/19		EBR32-T10	08/13/18	04/26/19
	WBR33-PU	03/20/19	07/18/19		EBR33-PD	10/04/18	05/09/19
	WBR33-T1	03/04/19	07/15/19		EBR33-PU	10/02/18	05/09/19
WBR-33	WBR33-T2	03/05/19	07/15/19	EBR-33	EBR33-T1	11/05/18	05/02/19
	WBR33-T3	03/06/19	07/15/19		EBR33-T2	11/06/18	05/02/19
	WBR33-D4	03/07/19	07/16/19		EBR33-T3	11/07/18	05/02/19
	WBR33-T5	03/08/19	07/16/19		EBR33-D4	11/08/18	05/02/19

	WBR33-T6	03/09/19	07/16/19		EBR33-T5	11/09/18	05/02/19
	WBR33-T7	03/11/19	07/16/19		EBR33-T6	11/10/18	05/02/19
	WBR33-D8	03/12/19	07/16/19		EBR33-T7	11/13/18	04/30/19
	WBR33-T9	03/13/19	07/16/19		EBR33-D8	11/15/18	04/30/19
	WBR33-T10	03/14/19	07/17/19		EBR33-T9	11/16/18	04/30/19
	WBR33-T11	03/15/19	07/17/19		EBR33-T10	11/19/18	04/30/19
	WBR34-PD	03/23/19	07/19/19		EBR34-ED	02/09/19	05/20/19
WBR-34	WBR34-PU	03/21/19	07/19/19	EBR-34	EBR34-EU	02/27/19	06/10/19
	WBR34-T1	03/16/19	07/29/19		EBR34-T1	12/05/18	06/09/19
	WBR34-T2	03/18/19	07/29/19		EBR34-T2	12/10/18	06/09/19
	WBR34-T3	03/19/19	07/29/19		EBR34-D3	12/12/18	06/09/19
	WBR34-D4	03/20/19	07/29/19		EBR34-T4	12/14/18	06/09/19
	WBR34-T5	03/21/19	07/29/19		EBR34-T5	12/15/18	06/09/19
	WBR34-T6	03/22/19	07/29/19		EBR34-T6	12/17/18	06/10/19
	WBR34-T7	03/23/19	07/29/19		EBR34-T7	12/18/18	06/10/19
	WBR34-T8	03/25/19	07/29/19		EBR34-T8	12/19/18	06/10/19
	WBR34-D9	03/26/19	07/29/19		EBR34-D9	12/21/18	06/10/19
	WBR34-T10	03/27/19	07/30/19		EBR34-T10	01/01/19	06/10/19
	WBR34-T11	03/29/19	07/30/19		EBR34-T11	01/02/19	06/10/19
	WBR34-T12	03/30/19	07/30/19		EBR34-T12	01/03/19	06/10/19
	WBR35-PD	05/10/19	07/30/19		EBR35-PD	02/14/19	06/13/19
WBR-35	WBR35-PU	05/02/19	07/30/19	EBR-35	EBR35-PU	02/11/19	06/13/19
	WBR35-T1	03/26/19	09/24/19		EBR35-T1	01/09/19	06/20/19
	WBR35-T2	03/29/19	09/24/19		EBR35-T2	01/10/19	06/15/19
	WBR35-T3	03/30/19	09/24/19		EBR35-T3	01/11/19	06/15/19
	WBR35-D4	04/01/19	09/24/19		EBR35-D4	01/14/19	06/15/19
	WBR35-T5	04/02/19	09/24/19		EBR35-T5	01/15/19	06/15/19
	WBR35-T6	04/03/19	09/24/19		EBR35-T6	01/17/19	06/15/19
	WBR35-T7	04/04/19	09/24/19		EBR35-T7	01/18/19	06/15/19
	WBR35-T8	04/05/19	09/24/19		EBR35-T8	01/22/19	06/15/19
	WBR35-T9	04/06/19	09/25/19		EBR35-T9	01/24/19	06/14/19
	WBR35-D10	04/08/19	09/25/19		EBR35-D10	01/25/19	06/14/19
	WBR35-T11	04/09/19	09/25/19		EBR35-T11	01/28/19	06/14/19
	WBR35-T12	04/10/19	09/25/19		EBR35-T12	01/30/19	06/14/19
	WBR36-ED	05/15/19	09/25/19		EBR36-ED	03/20/19	06/21/19
WBR-	WBR36-EU	06/28/19	10/10/19	EBR-	EBR36-EU	06/18/19	07/22/19

36	WBR36-T1	07/09/19	10/10/19	36	EBR36-T1	05/29/19	07/22/19
	WBR36-T2	07/10/19	10/10/19		EBR36-T2	05/30/19	08/18/19
	WBR36-D3	07/11/19	10/10/19		EBR36-D3	05/31/19	08/18/19
	WBR36-T4	07/12/19	10/09/19		EBR36-T4	06/03/19	08/18/19
	WBR36-T5	07/13/19	10/09/19		EBR36-T5	06/04/19	08/18/19
	WBR36-T6	07/15/19	10/09/19		EBR36-T6	06/05/19	08/18/19
	WBR36-T7	07/16/19	10/09/19		EBR36-D7	06/06/19	08/19/19
	WBR36-D8	07/17/19	10/09/19		EBR36-T8	06/07/19	08/21/19
	WBR36-T9	07/18/19	10/09/19		EBR36-T9	06/10/19	08/21/19
	WBR36-T10	07/19/19	10/09/19		EBR36-T10	06/11/19	08/21/19
	WBR36-T11	07/20/19	10/09/19		EBR37-PD	06/22/19	08/21/19
	WBR37-PD	08/05/19	09/21/19	EBR-37	EBR37-PU	06/20/19	08/22/19
WBR-37	WBR37-PU	08/01/19	09/21/19		EBR37-T1	06/03/19	09/25/19
	WBR37-T1	07/15/19	09/21/19		EBR37-T2	06/04/19	09/25/19
	WBR37-T2	07/16/19	09/21/19		EBR37-T3	06/05/19	09/25/19
	WBR37-T3	07/17/19	09/21/19		EBR37-D4	06/06/19	09/25/19
	WBR37-D4	07/18/19	09/21/19		EBR37-T5	06/07/19	09/25/19
	WBR37-T5	07/19/19	09/20/19		EBR37-T6	06/10/19	09/25/19
	WBR37-T6	07/20/19	09/20/19		EBR37-T7	06/11/19	09/26/19
	WBR37-T7	07/22/19	09/20/19		EBR37-D8	06/12/19	09/26/19
	WBR37-T8	07/23/19	09/20/19		EBR37-T9	06/13/19	09/26/19
	WBR37-D9	07/25/19	09/20/19		EBR37-T10	06/15/19	09/26/19
	WBR37-T10	07/26/19	09/20/19		EBR37-T11	06/18/19	09/26/19
	WBR37-T11	07/29/19	09/20/19		EBR38-PD	11/29/18	05/20/19
	WBR37-T12	07/30/19	09/20/19	EBR-38	EBR38-PU	11/27/18	05/10/19
	WBR38-PD	02/09/19	07/09/19		EBR38-T1	12/15/18	05/10/19
WBR-38	WBR38-PU	02/06/19	07/09/19		EBR38-T2	12/17/18	05/10/19
	WBR38-T1	02/06/19	07/02/19		EBR38-T3	12/18/18	05/10/19
	WBR38-T2	02/07/19	07/02/19		EBR38-D4	12/19/18	05/11/19
	WBR38-T3	02/08/19	07/02/19		EBR38-T5	12/20/18	05/12/19
	WBR38-D4	02/09/19	07/02/19		EBR38-T6	12/22/18	05/12/19
	WBR38-T5	02/11/19	07/03/19		EBR38-T7	12/31/18	05/12/19
	WBR38-T6	02/13/19	07/03/19		EBR38-T8	01/01/19	05/12/19
	WBR38-T7	02/14/19	07/03/19		EBR38-D9	01/03/19	05/12/19
	WBR38-D8	02/15/19	07/03/19		EBR38-T10	01/04/19	05/12/19
	WBR38-T9	02/16/19	07/03/19		EBR38-T11	01/07/19	05/12/19

	WBR38-T10	02/18/19	07/03/19		EBR38-T12	01/08/19	05/12/19
	WBR39-ED	04/02/19	07/10/19		EBR39-PD	11/28/18	05/13/19
WBR-39	WBR39-EU	04/09/19	08/29/19	EBR-39	EBR39-PU	11/21/18	05/13/19
	WBR39-T1	06/05/19	10/03/19		EBR39-T1	03/11/19	08/13/19
	WBR39-T2	06/06/19	10/03/19		EBR39-T2	03/12/19	08/13/19
	WBR39-D3	06/07/19	10/04/19		EBR39-T3	03/14/19	08/13/19
	WBR39-T4	06/10/19	10/04/19		EBR39-D4	03/15/19	08/13/19
	WBR39-T5	06/11/19	10/04/19		EBR39-T5	03/16/19	08/13/19
	WBR39-T6	06/12/19	10/05/19		EBR39-T6	03/18/19	08/12/19
	WBR39-T7	06/13/19	10/05/19		EBR39-T7	03/20/19	08/12/19
	WBR39-T8	06/14/19	10/05/19		EBR39-T8	03/21/19	08/12/19
	WBR39-D9	06/17/19	10/05/19		EBR39-T9	03/22/19	08/12/19
	WBR39-T10	06/18/19	10/05/19		EBR39-D10	03/25/19	08/12/19
	WBR39-T11	06/19/19	10/05/19		EBR39-T11	03/26/19	08/12/19
	WBR39-T12	06/20/19	10/05/19		EBR39-T12	03/27/19	08/12/19
	WBR40-PD	07/15/19	09/17/19		EBR40-ED	03/05/19	04/02/19
WBR-40	WBR40-PU	07/13/19	09/16/19	EBR-40	EBR40-EU	03/02/19	04/02/19
	WBR40-T1	06/12/19	09/16/19		EBR40-T1	04/01/19	07/11/19
	WBR40-T2	06/13/19	09/16/19		EBR40-T2	04/02/19	07/11/19
	WBR40-T3	06/14/19	09/16/19		EBR40-D3	04/03/19	07/12/19
	WBR40-D4	06/17/19	09/16/19		EBR40-T4	04/04/19	07/12/19
	WBR40-T5	06/18/19	09/15/19		EBR40-T5	04/06/19	07/13/19
	WBR40-T6	06/19/19	09/15/19		EBR40-T6	04/08/19	07/13/19
	WBR40-T7	06/20/19	09/15/19		EBR40-T7	04/09/19	07/13/19
	WBR40-T8	06/21/19	09/15/19		EBR40-T8	04/10/19	07/13/19
	WBR40-D9	06/25/19	09/15/19		EBR40-D9	04/11/19	07/13/19
	WBR40-T10	06/26/19	09/15/19		EBR40-T10	04/12/19	07/13/19
	WBR40-T11	06/27/19	09/15/19		EBR40-T11	04/13/19	07/13/19
	WBR40-T12	06/28/19	09/15/19		EBR40-T12	04/15/19	07/13/19
	WBR41-PD	06/20/19	08/02/19		EBR41-PD	11/20/18	06/01/19
WBR-41	WBR41-PU	03/02/19	08/01/19	EBR-41	EBR41-PU	11/16/18	06/01/19
	WBR41-T1	12/10/18	08/01/19		EBR41-T1	11/27/18	06/01/19
	WBR41-T2	12/12/18	08/01/19		EBR41-T2	11/28/18	06/01/19
	WBR41-T3	12/14/18	08/01/19		EBR41-T3	11/29/18	06/01/19
	WBR41-D4	12/17/18	07/29/19		EBR41-D4	12/04/18	06/01/19
	WBR41-T5	12/19/18	07/29/19		EBR41-T5	12/05/18	05/29/19

	WBR41-T6	12/20/18	07/29/19		EBR41-T6	12/06/18	05/29/19
	WBR41-T7	12/22/18	07/28/19		EBR41-T7	12/07/18	05/29/19
	WBR41-T8	12/31/18	07/28/19		EBR41-T8	12/10/18	05/29/19
	WBR41-D9	01/02/19	07/28/19		EBR41-D9	12/11/18	05/29/19
	WBR41-T10	01/04/19	07/27/19		EBR41-T10	12/12/18	05/29/19
	WBR41-T11	01/05/19	07/26/19		EBR41-T11	12/13/18	05/28/19
	WBR42-ED	03/12/19	07/31/19		EBR41-T12	12/14/18	05/28/19
WBR-42	WBR42-EU	03/18/19	09/30/19		EBR42-PD	12/06/18	06/04/19
	WBR42-T1	08/02/19	09/30/19	EBR-42	EBR42-PU	12/04/18	06/04/19
	WBR42-D2	08/01/19	09/30/19		EBR42-T1	07/09/19	10/12/19
	WBR42-T3	02/14/19	09/30/19		EBR42-T2	07/10/19	10/12/19
	WBR42-D4	02/15/19	09/30/19		EBR42-T3	07/11/19	10/13/19
	WBR42-T5	02/16/19	10/01/19		EBR42-D4	07/12/19	10/13/19
	WBR43-ED	03/21/19	10/01/19		EBR42-T5	07/13/19	10/13/19
B26-1	B26-1-EU	05/01/19	09/18/19		EBR42-T6	07/15/19	10/14/19
	B26-1-T1	03/21/19	09/17/19		EBR42-T7	07/16/19	10/14/19
	B26-1-T2	03/22/19	09/17/19		EBR42-D8	07/17/19	10/14/19
	B26-1-D3	03/25/19	09/17/19		EBR42-T9	07/18/19	10/14/19
	B26-1-T4	03/26/19	09/17/19		EBR42-T10	07/19/19	10/14/19
	B26-1-T5	03/27/19	09/17/19		EBR43-ED	07/02/19	10/14/19
	B26-1-T6	03/29/19	09/17/19	B22-1	B22-1-EU	01/30/19	03/28/19
	B26-1-T7	03/30/19	09/18/19		B22-1-T1	11/08/18	03/28/19
	B26-1-T8	04/01/19	09/18/19		B22-1-T2	11/13/18	03/28/19
	B26-1-D9	04/02/19	09/18/19		B22-1-D3	11/15/18	03/28/19
	B26-1-T10	04/03/19	09/18/19		B22-1-T4	11/16/18	03/28/19
	B26-1-T11	04/04/19	09/18/19		B22-1-T5	11/19/18	03/29/19
	B26-1-T12	04/05/19	09/18/19		B22-1-T6	11/20/18	03/29/19
	B26-2-PD	04/24/19	09/20/19		B22-1-T7	11/26/18	03/29/19
B26-2	B26-2-PU	04/22/19	09/20/19		B22-1-T8	11/27/18	03/29/19
	B26-2-T1	05/10/19	09/26/19		B22-1-T9	11/28/18	03/29/19
	B26-2-T2	05/13/19	09/26/19		B22-1-D10	12/04/18	03/29/19
	B26-2-T3	05/14/19	09/26/19		B22-1-T11	12/05/18	03/29/19
	B26-2-D4	05/15/19	09/26/19		B22-1-T12	12/07/18	03/30/19
	B26-2-T5	05/16/19	09/26/19		B22-2-ED	02/01/19	03/30/19
	B26-2-T6	05/17/19	09/26/19				
	B26-2-T7	05/20/19	09/26/19				

	B26-2-T8	05/21/19	09/26/19	
	B26-2-D9	05/22/19	09/26/19	
	B26-2-T10	05/23/19	09/25/19	
	B26-2-T11	05/24/19	09/25/19	
	B26-2-T12	05/28/19	09/25/19	
	B26-3-PD	07/11/19	10/01/19	
B26-3	B26-3-PU	07/09/19	10/01/19	
	B26-3-T1	05/31/19	10/03/19	
	B26-3-T2	06/03/19	10/03/19	
	B26-3-T3	06/04/19	10/03/19	
	B26-3-D4	06/05/19	10/03/19	
	B26-3-T5	06/06/19	10/03/19	
	B26-3-T6	06/07/19	10/02/19	
	B26-3-T7	06/10/19	10/02/19	
	B26-3-T8	06/11/19	10/02/19	
	B26-3-T9	06/12/19	10/02/19	
	B26-3-D10	06/13/19	10/02/19	
	B26-3-T11	06/14/19	10/02/19	
	B26-3-T12	06/17/19	10/02/19	
	B26-4-ED	06/08/19	10/03/19	